

Hybrid Simulation to Assess Performance of Seismic Isolation in Nuclear Power Plants

**IAEA**

International Atomic Energy Agency

IAEA SAFETY STANDARDS AND RELATED PUBLICATIONS

IAEA SAFETY STANDARDS

Under the terms of Article III of its Statute, the IAEA is authorized to establish or adopt standards of safety for protection of health and minimization of danger to life and property, and to provide for the application of these standards.

The publications by means of which the IAEA establishes standards are issued in the **IAEA Safety Standards Series**. This series covers nuclear safety, radiation safety, transport safety and waste safety. The publication categories in the series are **Safety Fundamentals**, **Safety Requirements** and **Safety Guides**.

Information on the IAEA's safety standards programme is available on the IAEA Internet site

<http://www-ns.iaea.org/standards/>

The site provides the texts in English of published and draft safety standards. The texts of safety standards issued in Arabic, Chinese, French, Russian and Spanish, the IAEA Safety Glossary and a status report for safety standards under development are also available. For further information, please contact the IAEA at: Vienna International Centre, PO Box 100, 1400 Vienna, Austria.

All users of IAEA safety standards are invited to inform the IAEA of experience in their use (e.g. as a basis for national regulations, for safety reviews and for training courses) for the purpose of ensuring that they continue to meet users' needs. Information may be provided via the IAEA Internet site or by post, as above, or by email to Official.Mail@iaea.org.

RELATED PUBLICATIONS

The IAEA provides for the application of the standards and, under the terms of Articles III and VIII.C of its Statute, makes available and fosters the exchange of information relating to peaceful nuclear activities and serves as an intermediary among its Member States for this purpose.

Reports on safety in nuclear activities are issued as **Safety Reports**, which provide practical examples and detailed methods that can be used in support of the safety standards.

Other safety related IAEA publications are issued as **Emergency Preparedness and Response** publications, **Radiological Assessment Reports**, the International Nuclear Safety Group's **INSAG Reports**, **Technical Reports** and **TECDOCs**. The IAEA also issues reports on radiological accidents, training manuals and practical manuals, and other special safety related publications.

Security related publications are issued in the **IAEA Nuclear Security Series**.

The **IAEA Nuclear Energy Series** comprises informational publications to encourage and assist research on, and the development and practical application of, nuclear energy for peaceful purposes. It includes reports and guides on the status of and advances in technology, and on experience, good practices and practical examples in the areas of nuclear power, the nuclear fuel cycle, radioactive waste management and decommissioning.

HYBRID SIMULATION TO ASSESS
PERFORMANCE OF SEISMIC ISOLATION
IN NUCLEAR POWER PLANTS

The following States are Members of the International Atomic Energy Agency:

AFGHANISTAN	GERMANY	PAKISTAN
ALBANIA	GHANA	PALAU
ALGERIA	GREECE	PANAMA
ANGOLA	GRENADA	PAPUA NEW GUINEA
ANTIGUA AND BARBUDA	GUATEMALA	PARAGUAY
ARGENTINA	GUYANA	PERU
ARMENIA	HAITI	PHILIPPINES
AUSTRALIA	HOLY SEE	POLAND
AUSTRIA	HONDURAS	PORTUGAL
AZERBAIJAN	HUNGARY	QATAR
BAHAMAS	ICELAND	REPUBLIC OF MOLDOVA
BAHRAIN	INDIA	ROMANIA
BANGLADESH	INDONESIA	RUSSIAN FEDERATION
BARBADOS	IRAN, ISLAMIC REPUBLIC OF	RWANDA
BELARUS	IRAQ	SAINT LUCIA
BELGIUM	IRELAND	SAINT VINCENT AND THE GRENADINES
BELIZE	ISRAEL	SAN MARINO
BENIN	ITALY	SAUDI ARABIA
BOLIVIA, PLURINATIONAL STATE OF	JAMAICA	SENEGAL
BOSNIA AND HERZEGOVINA	JAPAN	SERBIA
BOTSWANA	JORDAN	SEYCHELLES
BRAZIL	KAZAKHSTAN	SIERRA LEONE
BRUNEI DARUSSALAM	KENYA	SINGAPORE
BULGARIA	KOREA, REPUBLIC OF	SLOVAKIA
BURKINA FASO	KUWAIT	SLOVENIA
BURUNDI	KYRGYZSTAN	SOUTH AFRICA
CAMBODIA	LAO PEOPLE'S DEMOCRATIC REPUBLIC	SPAIN
CAMEROON	LATVIA	SRI LANKA
CANADA	LEBANON	SUDAN
CENTRAL AFRICAN REPUBLIC	LESOTHO	SWEDEN
CHAD	LIBERIA	SWITZERLAND
CHILE	LIBYA	SYRIAN ARAB REPUBLIC
CHINA	LIECHTENSTEIN	TAJIKISTAN
COLOMBIA	LITHUANIA	THAILAND
CONGO	LUXEMBOURG	TOGO
COSTA RICA	MADAGASCAR	TRINIDAD AND TOBAGO
CÔTE D'IVOIRE	MALAWI	TUNISIA
CROATIA	MALAYSIA	TURKEY
CUBA	MALI	TURKMENISTAN
CYPRUS	MALTA	UGANDA
CZECH REPUBLIC	MARSHALL ISLANDS	UKRAINE
DEMOCRATIC REPUBLIC OF THE CONGO	MAURITANIA	UNITED ARAB EMIRATES
DENMARK	MAURITIUS	UNITED KINGDOM OF GREAT BRITAIN AND NORTHERN IRELAND
DJIBOUTI	MEXICO	UNITED REPUBLIC OF TANZANIA
DOMINICA	MONACO	UNITED STATES OF AMERICA
DOMINICAN REPUBLIC	MONGOLIA	URUGUAY
ECUADOR	MONTENEGRO	UZBEKISTAN
EGYPT	MOROCCO	VANUATU
EL SALVADOR	MOZAMBIQUE	VENEZUELA, BOLIVARIAN REPUBLIC OF
ERITREA	MYANMAR	VIET NAM
ESTONIA	NAMIBIA	YEMEN
ESWATINI	NEPAL	ZAMBIA
ETHIOPIA	NETHERLANDS	ZIMBABWE
FIJI	NEW ZEALAND	
FINLAND	NICARAGUA	
FRANCE	NIGER	
GABON	NIGERIA	
GEORGIA	NORTH MACEDONIA	
	NORWAY	
	OMAN	

The Agency's Statute was approved on 23 October 1956 by the Conference on the Statute of the IAEA held at United Nations Headquarters, New York; it entered into force on 29 July 1957. The Headquarters of the Agency are situated in Vienna. Its principal objective is "to accelerate and enlarge the contribution of atomic energy to peace, health and prosperity throughout the world".

IAEA-TECDOC-1888

HYBRID SIMULATION TO ASSESS
PERFORMANCE OF SEISMIC ISOLATION
IN NUCLEAR POWER PLANTS

INTERNATIONAL ATOMIC ENERGY AGENCY
VIENNA, 2019

COPYRIGHT NOTICE

All IAEA scientific and technical publications are protected by the terms of the Universal Copyright Convention as adopted in 1952 (Berne) and as revised in 1972 (Paris). The copyright has since been extended by the World Intellectual Property Organization (Geneva) to include electronic and virtual intellectual property. Permission to use whole or parts of texts contained in IAEA publications in printed or electronic form must be obtained and is usually subject to royalty agreements. Proposals for non-commercial reproductions and translations are welcomed and considered on a case-by-case basis. Enquiries should be addressed to the IAEA Publishing Section at:

Marketing and Sales Unit, Publishing Section
International Atomic Energy Agency
Vienna International Centre
PO Box 100
1400 Vienna, Austria
fax: +43 1 26007 22529
tel.: +43 1 2600 22417
email: sales.publications@iaea.org
www.iaea.org/publications

For further information on this publication, please contact:

External Events Safety Section
International Atomic Energy Agency
Vienna International Centre
PO Box 100
1400 Vienna, Austria
Email: Official.Mail@iaea.org

© IAEA, 2019
Printed by the IAEA in Austria
December 2019

IAEA Library Cataloguing in Publication Data

Names: International Atomic Energy Agency.
Title: Hybrid simulation to assess performance of seismic isolation in nuclear power plants / International Atomic Energy Agency.
Description: Vienna : International Atomic Energy Agency, 2019. | Series: IAEA TECDOC series, ISSN 1011-4289 ; no. 1888 | Includes bibliographical references.
Identifiers: IAEAL 19-01279 | ISBN 978-92-0-162719-3 (paperback : alk. paper) | ISBN 978-92-0-162819-0 (pdf)
Subjects: LCSH: Nuclear power plants — Safety measures. | Hybrid computer simulation. | Earthquake resistant design.

FOREWORD

Seismic isolation technology has proved to be a reliable option for engineers designing structures in areas of the world with a moderate to large seismic hazard. Nevertheless, the use of this technology for nuclear safety related buildings poses a series of challenges, and only a few such structures designed using this technology are currently in operation worldwide.

In the recent years, it has been found that the seismic hazard at a significant number of prospective sites in embarking countries results in a design basis earthquake which exceeds that used for developing most of the standard nuclear power plant designs available on the market. At many sites, the seismic hazard can be an important contributor to the overall risk posed by the nuclear power plant. Seismic isolation technology has the potential to significantly reduce this contribution. This context has renewed interest in the use of seismic isolation technology within the nuclear industry.

A testing programme is an integral part of a seismic isolation project. Not only do the isolating devices have to be characterized for design purposes, but validation of the analytical procedures used in design is also normally required by the safety authorities in Member States. Since the behaviour of the isolating devices is non-linear for the large seismic demands set on them, this poses a considerable challenge to the engineering community.

Hybrid simulation is a testing technique which is a good candidate to experimentally assess the behaviour of an isolation system. The method combines computation of the response of the isolated structure with experimental determination of the behaviour of full scale isolating devices under the demand imposed by the movement of ground and structure. The present publication was prepared as a contribution to the assessment of this method as a tool for the design and safety demonstration of base-isolated nuclear structures, systems and components. It was developed using funding from Member States voluntarily contributing to, and participating in, the extrabudgetary programme of the External Events Safety Section.

The present publication is a compilation of the benchmark's main results, findings, conclusions and suggestions; the supplementary files available on-line present the data package of the benchmark, results of the characterization tests of isolating devices and all benchmark participant results.

The IAEA would like to express its appreciation to all the contributors to the development and review of this publication. In particular, the IAEA gratefully acknowledges the contributions of Sanghoon Lee (Republic of Korea). The IAEA officer responsible for this publication was A. Altinyollar of the Division of Nuclear Installation Safety.

EDITORIAL NOTE

This publication has been prepared from the original material as submitted by the contributors and has not been edited by the editorial staff of the IAEA. The views expressed remain the responsibility of the contributors and do not necessarily represent the views of the IAEA or its Member States.

Neither the IAEA nor its Member States assume any responsibility for consequences which may arise from the use of this publication. This publication does not address questions of responsibility, legal or otherwise, for acts or omissions on the part of any person.

The use of particular designations of countries or territories does not imply any judgement by the publisher, the IAEA, as to the legal status of such countries or territories, of their authorities and institutions or of the delimitation of their boundaries.

The mention of names of specific companies or products (whether or not indicated as registered) does not imply any intention to infringe proprietary rights, nor should it be construed as an endorsement or recommendation on the part of the IAEA.

The authors are responsible for having obtained the necessary permission for the IAEA to reproduce, translate or use material from sources already protected by copyrights.

The IAEA has no responsibility for the persistence or accuracy of URLs for external or third party Internet web sites referred to in this publication and does not guarantee that any content on such web sites is, or will remain, accurate or appropriate.

CONTENTS

1	INTRODUCTION.....	1
1.1	Background	1
1.2	Objective	1
1.3	Scope	1
1.4	Structure	3
2	OVERVIEW ON SEISMIC ISOLATION SYSTEMS AND HYBRID SIMULATION	3
2.1	Seismic isolation in nuclear power plants	3
2.1.1	Overview and current state of practice.....	3
2.1.2	Role of testing in the design of seismic isolation systems	6
2.1.3	Present challenges	7
2.2	Hybrid simulation.....	7
2.2.1	Overview and history	7
2.2.2	Components and procedure	10
3	INTERNATIONAL BENCHMARK PRESENTATION.....	13
3.1	Purpose of benchmark.....	13
3.2	Overview of benchmark activities.....	13
3.3	List of participants.....	14
3.4	Specification of the benchmark.....	15
3.4.1	Archetype plant models.....	15
3.4.2	Isolator properties and models.....	24
3.4.3	Seismic motion.....	31
3.4.4	Required output	33
3.4.5	Matrix of benchmark analyses.....	34
4	NUMERICAL APPROACHES AND RESULTS BY PARTICIPANTS.....	34
4.1	Computational approaches and models	34
4.1.1	Superstructure models	34
4.1.2	LRB isolation system models.....	36
4.1.3	EQSB isolation system models	40
4.1.4	TPFB isolation system models	42
4.1.5	Time history analyses methods and tools.....	42
4.2	Computed responses for LRB isolator	43
4.2.1	Available results and selection of representative data.....	43
4.2.2	Results of Case 1 – LRB system – Comparison of computed responses	44
4.2.3	Results of Case 2 – LRB system – Effect of increased seismic excitation.....	55
4.2.4	Results of Case 6 – LRB system – Effect of representation of all isolators.....	64
4.2.5	Results of Case 12 – LRB system – Effect of EUR ground motion spectra	68
4.3	Computed responses for EQSB isolator.....	74
4.3.1	Available results and selection of representative data.....	74
4.3.2	Results of Case 1 – EQSB system – Comparison of computed responses.....	77
4.3.3	Results of Case 2 – EQSB system – Effect of increased seismic excitation	82
4.4	Computed responses for TPFB isolator.....	87
4.5	Conclusions from the analysis of the results by participants.....	87
4.5.1	Maximum global acceleration of the isolated superstructure.....	87
4.5.2	Maximum displacements and hysteresis curves.....	87
4.5.3	Floor response spectra at higher elevations.....	89
4.5.4	Effect of seismic isolation system models.....	90
4.5.5	Remarks on the dispersion of results.....	90

4.6	Parametric studies with larger seismic input	91
5	EXPERIMENTAL RESULTS	99
5.1	SRMD-UCSD testing facility	99
5.2	Isolator test specimens	100
5.3	Isolator characterization tests	102
5.3.1	LRB isolator	102
5.3.2	Horizontal (effect of axial load)	103
5.3.3	EQSB isolator	107
5.3.4	TPFB isolator	112
5.3.5	Numerical bearing model parameters calibrated from characterization tests	118
5.4	Hybrid models of archetype plant	119
5.4.1	Material and damping properties	119
5.4.2	Development of ANT 3D model in OpenSees	120
5.5	Ground motions	127
5.6	Implementation of hybrid simulation	127
5.6.1	Hardware configuration	127
5.6.2	Software configuration	128
5.6.3	Special Settings for Testing Triple Friction Pendulum Bearings	128
5.6.4	Test Setup	128
5.7	Test results	131
5.7.1	LRB isolator	133
5.7.2	EQSB isolator	148
5.7.3	TPFB isolator	160
5.7.4	Comparison of results for all bearing types	168
5.8	Remarks and conclusions	174
6	COMPARISON BETWEEN HYBRID TESTS AND BENCHMARK RESULTS	175
6.1	Comparison for LRB isolators	175
6.1.1	Available data and selection of representative results	175
6.1.2	Comparison of displacement time histories	175
6.1.3	Comparison of floor response spectra at centre of upper basemat	177
6.1.4	Comparison of floor response spectra at top of buildings	177
6.1.5	Comparison of hysteresis loops	182
6.2	Comparison for EQSB isolators	184
6.2.1	Available data and selection of representative results	184
6.2.2	Comparison of displacement time histories	184
6.2.3	Comparison of floor response spectra at centre of upper basemat	186
6.2.4	Comparison of floor response spectra at top of buildings	189
6.2.5	Comparison of hysteresis loops	189
6.3	Comparison for TPFB isolators	194
6.4	Conclusions	194
7	CONCLUSIONS AND SUGGESTIONS	197
7.1	Conclusions	197
7.1.1	General conclusions	197
7.1.2	Specific conclusions	197
7.2	Suggestions	199
7.2.1	General suggestions	199
7.2.2	Specific suggestions	200
	REFERENCES	201
	ABBREVIATIONS	203

ANNEX: SUPPLEMENTARY FILES.....205
CONTRIBUTORS TO DRAFTING AND REVIEW.....206

1 INTRODUCTION

1.1 BACKGROUND

Currently, there exist worldwide only a few instances of base-isolated nuclear safety-related buildings. However, present seismic base isolation technology has demonstrated its capacity to improve the seismic performance in conventional buildings located in earthquake prone areas. As a result, it is generally considered that the technology has reached a degree of maturity that would allow general application in nuclear safety related projects.

As commonly used in practice, seismic base-isolation reduces the seismic response of a structure to the horizontal ground motion by means of a horizontally ‘flexible’ layer of seismic isolation devices (‘isolators’ or ‘bearings’), located between the superstructure and its substructure. The horizontal stiffness of the isolators is selected so that the fundamental vibration frequency of the isolated structural system is significantly smaller than that of the non-isolated structure, and away from the frequency band at which the ground motion has most of its energy. Only in a few known cases isolation systems can provide isolation of vertical seismic component and mitigate vertical seismic amplification of a structure.

In contrast with conventional buildings, in a nuclear project, seismic isolation is primarily intended to protect the systems and components located in the buildings. The robustness of nuclear plant structures normally makes systems and components the most vulnerable items from a seismic standpoint.

A testing programme is an integral part of a seismic isolation project. Not only have the isolating devices to be characterized for design purposes, but also validation of the analytical procedures used in design is normally required by the safety authorities in the Member States. Since the behaviour of the isolators is non-linear for the large seismic demands set on them, this poses a big challenge to the engineering community.

Hybrid simulation is a method intended to experimentally assess the behaviour of a structure by a combination of analysis of the parts which are easily modelled and testing of the parts with complex behaviour. In the case of a non-linear isolation system supporting a standard linear structure, it combines the computation of the response of the isolated structure with the experimental real-time determination of the behaviour of full-scale isolators under the demand imposed by the movement of ground and structure.

The present publication reports on the analytical and experimental activities developed in the framework of an international benchmark launched by the IAEA in March 2015. The publication describes the background of hybrid simulation, the work performed by the benchmark participants, experimental test results, and the main conclusions and suggestions for practical application.

1.2 OBJECTIVE

The objective of this publication is to introduce hybrid simulation to the uninformed reader, to present the results of the benchmark exercise and to demonstrate the use of hybrid simulation to further validate the applicability of seismic isolation to nuclear structures.

With respect to other test methods, hybrid simulation has its own strengths and limitations, though it is probably less known and less used by the engineering community worldwide. The present publication is intended to be a contribution to fill in this gap.

1.3 SCOPE

This publication addresses the current ability of hybrid simulation to assess the performance of seismic isolation for NPPs, based on:

- (1) International benchmark for computing the seismic response of a real size nuclear power plant with isolators, for different levels of seismic excitation;

- (2) Hybrid simulation testing, consistent with the building models, isolators and earthquake excitation levels used in the benchmark definition;
- (3) Analysis of test results and comparison with benchmark results.

These activities are described in detail in the following Sections. The general workflow is shown in Figure 1.

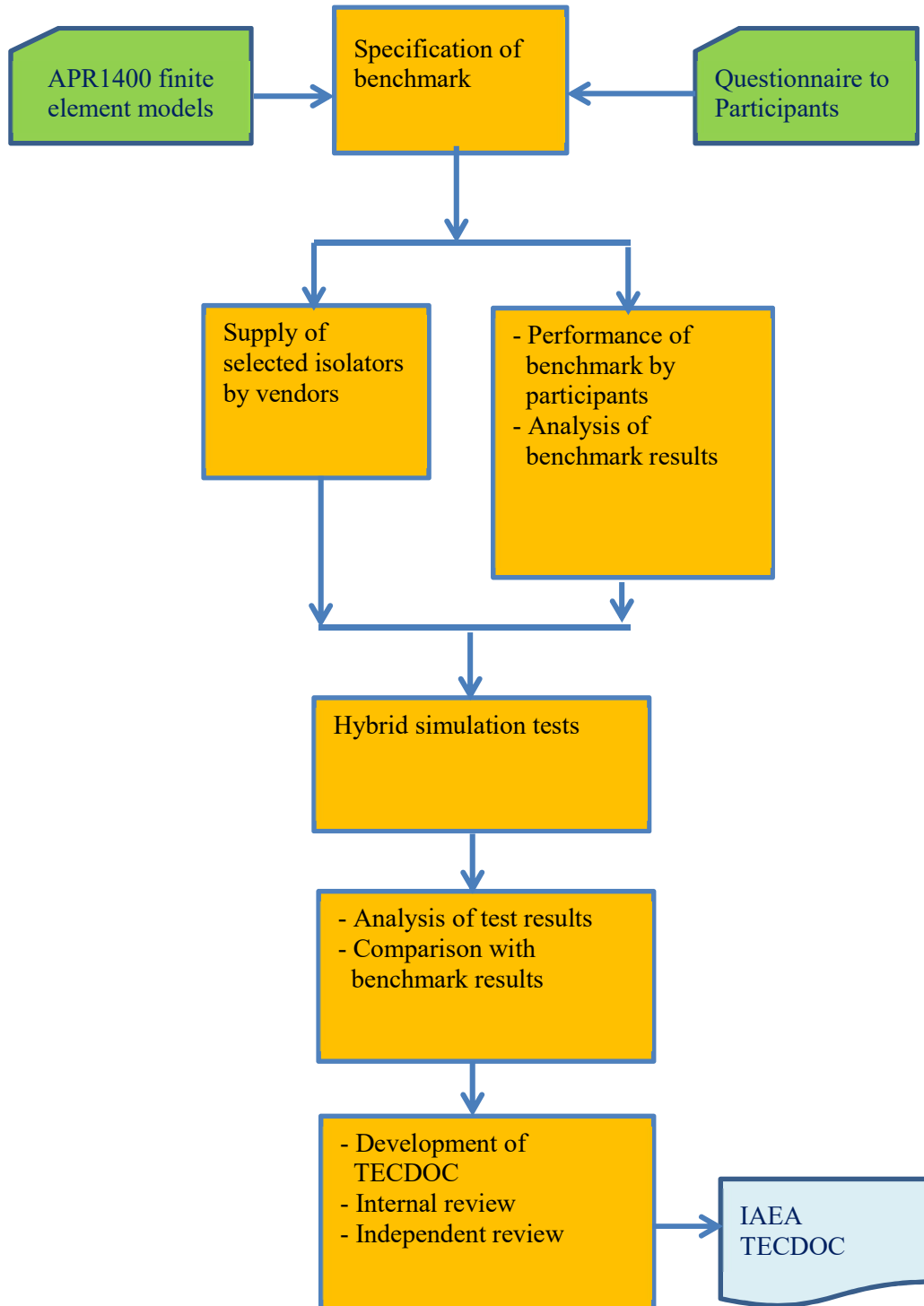


FIG. 1. International benchmark - General workflow of activities.

1.4 STRUCTURE

Section 2 provides an overview on seismic isolation systems and hybrid simulation. Section 3 introduces the international benchmark, including an overview of the benchmark activities, the list of participants, and the statement of the benchmark, in terms of structural models, isolators, seismic input motions and required output. Section 4 summarizes the analytical results of the international benchmark. It describes the computational approaches and models used by the participants and the computed responses for each type of isolator. At the end of the section, an assessment of the consistency of approaches and results is also presented. Section 5 gathers the experimental results obtained using hybrid simulation for the same isolators and seismic input used for the international benchmark. A description of the testing facility and isolator test specimens is given first. Then, the results of the isolator characterization tests are reported. The rest of the section is dedicated to the hybrid computational models, the implementation of the hybrid simulation and the results obtained from the hybrid testing for each type of isolator. Section 6 provides the comparison between hybrid test results and the results from the analyses performed by the participants within the international benchmark. Both the response of the isolators and the overall structural response are compared. Conclusions are drawn from the comparison. Finally, Section 7 presents the conclusions and suggestions derived from the whole exercise. Conclusions address the degree of applicability and reliability of purely analytical approaches in the performance of seismic isolation systems, especially when non-linear behaviour of isolators is expected. In addition, the conclusions assess the role of hybrid simulation to increase confidence in the performance of seismic isolation systems in nuclear power plants (NPPs), which is one of the issues which motivated the present work. Suggestions are also provided in this section, as a result of shared views of the participants after activities were completed.

On an attached CD-ROM, the following information is organized in 3 Annexes:

Annex I Data package of the benchmark

Annex II Results of the characterization tests

Annex III All participant results

2 OVERVIEW ON SEISMIC ISOLATION SYSTEMS AND HYBRID SIMULATION

2.1 SEISMIC ISOLATION IN NUCLEAR POWER PLANTS

2.1.1 Overview and current state of practice

2.1.1.1 Overview of seismic isolation

The basic concept of seismic isolation is to decouple the movement of the ground and the movement of the structure by introducing flexible elements (isolators) between the structure and its foundation. As a result, inertial forces caused by the earthquake can be substantially reduced with respect to the non-isolated structure.

The isolation system is generally formed by a number of individual elements (isolators) with low stiffness and, possibly, some additional damping directly integrated in the isolator or on a separate damping device. Generally, building structures are isolated only for horizontal motion, not for vertical motion. In most common systems, each isolator provides flexibility in horizontal direction and it is significantly stiffer in the vertical direction, in which it provides the required bearing capacity for the isolated structure. This scheme can be provided by rubber bearings, such as those used in bridge construction, or by a sliding device.

With respect to a non-isolated structure, the seismic response of an isolated structure incorporates two beneficial effects. On the one hand, the flexibility introduced by the isolation system shifts the

fundamental frequencies of the isolated structure to values one order of magnitude smaller, away from the frequency band at which the ground motion usually has the largest portion of its energy. Thus, the fundamental frequencies in nuclear safety related buildings, which are normally between 2 and 8 Hz, can be shifted to values under 0.5 Hz, and the in-structure horizontal response spectra are generally greatly reduced. Some systems including vertical isolation have been developed in Europe and Japan.

On the other hand, the flexibility of the isolation system leads to potentially large relative displacements of the superstructure relative to the ground. The resulting drift is concentrated at the elevation of the isolators. The main component of the motion of the superstructure is similar to a rigid body motion. As a result, a space (moat) needs to be allocated for these displacements to take place and the subsystems entering the superstructure from the outside (umbilical) need to be designed accordingly. The inter-story displacements, which are a potential source of damage for the systems housed by the structure, are significantly reduced with respect to the non-isolated structure.

The use of an isolation system also brings some specific issues for the assessment of the seismic response that require careful attention. In case of significantly dissipative isolation systems, the most important is the generally non-linear behaviour of such systems, which need to be both properly characterized and represented in analytical models. In addition, in slender structures, the response can induce large variations in vertical forces from one isolator to the other, causing variations in lateral stiffness and including uplift at the perimeter isolators, which is normally an undesirable effect. It can also be the case that aspects with small relevance in the response of non-isolated structures, or enveloped by other considerations, become significant for the response of an isolated structure. These include the variation of ground motion within the footprint of the structure, or the amplified coupling between horizontal and vertical modes of vibration in the superstructure.

Finally, isolated configuration provides flexibility for future changes, by means of the modification of the isolators and/or the addition of damping devices, if necessary. This flexibility may allow accommodating changes in the seismic conditions of a site.

2.1.1.2 Basic considerations for design

With respect to a similar non-isolated structure, seismic isolation introduces some complexity in the design and in the construction schedule. In a typical base-isolated structure, the design includes two basemats, one is in contact with the ground (lower basemat) and the other is supported by the isolators (upper basemat). The isolator pedestals or plinths, coming out of the lower basemat, are structural components that do not exist in the non-isolated structure. In addition, a “seismic pit” or volume to allow for the displacements of the superstructure needs to be introduced in the design. This space needs to be protected from the external influences and its boundaries need to be seismically designed. These four elements, lower and upper basemat, plinths and seismic pit, are the specific attributes of base-isolated structures. In nuclear projects, easy access to each isolator needs to be taken into account in the design in case of inspection of them and replacement of individual devices are necessary during the life time of the structure.

The design process is more complex as well. The structural design cannot be separated from the design and spatial layout of the isolators, which is a highly specialized discipline normally in the hands of the isolator suppliers. Hence, the design team needs to combine structural engineers and specialists from the selected isolation technology. In addition, the design is normally very much coupled with the qualification program of the isolators, since testing provides the input for the design characterization of the devices. Hence, for ad-hoc devices, not previously submitted to a qualification programme that meets the specific project requirements, the development of such a programme can result in a time schedule for the design process significantly larger than in the case of a non-isolated structure.

Without giving too much detail, the design of a base-isolated structure includes the following activities:

- (1) *Selection of a type of isolation system.* The selection of an isolation system is a function of the level of the seismic demand, the site parameters (ground conditions, environment), the weight of the structure to be isolated and its expected seismic response. The selection needs to consider the objective of the isolation and the industry experience in the Member State and in the country where the isolators are to be manufactured.

- (2) *Definition of the layout of isolators.* Definition of the layout normally requires several loops of iteration, targeted to meet the following conditions:
- Vertical loads on the isolators are as uniformly distributed as possible for all load combinations;
 - The offset of the rigidity centre of the isolators and the projection of the centre of gravity of the superstructure is as small as possible;
 - Isolators are located under the vertical elements (walls, columns) of the superstructure, as far as reasonably achievable;
 - Access to all isolators needs to be granted, for inspection and potential replacement, if necessary, during the life time of the structure.
- (3) *Pre-sizing of structural elements.* Lower basemat, plinths, upper basemat and the rest of the structural components of the superstructure are pre-sized according to the expected structural response.
- (4) *Structural response analysis.* Structural response is obtained for all applicable load combinations, using the specified codes and standards, and including a proper representation of isolators in the structural model. The isolator model is calibrated using the results of calibration tests. Nonlinear response history analyses are usually required.
- (5) *Capacity checks.* The computed structural response is used to verify the capacity of the isolators, consistent with the isolator qualification programme, and the structural capacity, according to the specified codes and standards. Note that, because the low frequency content of the seismic excitation transmitted to the superstructure, the ductility demand would be very large if the elastic limits were exceeded. For this reason, the superstructure normally needs to be designed to remain in its elastic range for the design basis earthquake and, as far as possible, for beyond design basis scenarios as well.

The design and analysis of equipment installed in the superstructure follow the same procedures as for non-isolated structures, noting that the use of an isolation system will result in peaks at the frequencies of the isolated structure, normally under 1 Hz. Although the use of isolation will generally substantially reduce horizontal spectral demands, longer period parts of equipment such as arms on fuel handling machines may experience demands greater than those corresponding to the non-isolated structure. In addition, modal combination may be modified by the low frequency content of the isolated floors.

Particularly, fluid in spent fuel pools and tanks excited by earthquakes may slosh, with wave heights varying as a function of pool/tank geometry, use of baffles, and seismic input. Since sloshing frequencies are normally smaller than 1 Hz, wave heights may be larger when seismic isolation is used, and more freeboard may be required.

Finally, ductility or inelastic energy absorption factors need to be used with great care in the estimation of beyond design basis behaviour of structures, systems and components housed by the superstructure. This is because a significant part of the seismic demand is at very low frequency and it can be considered as pseudo-static for most components.

In general, when the design earthquake exceeds a limit (e.g. the standard design assumptions), design alternatives are assessed by comparing the base-isolated solution (and the possible isolation technologies) with a reinforced conventional design solution. Multi-criteria analysis is performed, which accounts not only for structural response and design complexities, but also for project schedule, including qualification of isolators, licensing and construction extra-time, impact on other external hazards load cases, etc.

2.1.1.3 Base-isolated nuclear projects

Even though base-isolation technology can be considered to be mature, there are very few base-isolated operating nuclear reactors in the World. Table 1, adapted from Ref. [1], provides a summary of base-isolated nuclear reactor buildings worldwide. As it can be seen, the first projects are dated back in the

1980s and the size of isolators has increased in the more recent projects, due to the improvements introduced in the manufacturing process (Ref. [1]). At the same time, and as an improvement made possible by the larger isolators accommodating larger displacements, the isolation frequency has decreased over time.

TABLE 1. MAJOR BASE-ISOLATED SAFETY-RELATED NUCLEAR REACTOR BUILDING IN THE WORLD (Adapted from Ref. [1])

Facility	Start of operation	Design PGA (g)	Design isolation frequency (Hz)	Size of isolators
Cruas NPP, France 4 × 900 MW(e) PWR	1984	0.30	1.00	500 × 500 × 66.5 mm square low damping rubber bearings
Koeberg NPP, South Africa 2 × 900 MW(e) PWR	1985	0.30	1.00	700 × 700 × 130 mm square low damping rubber bearings on sliders
Jules Horowitz research reactor, France 100 MW tank pool reactor	Under construction	0.32	0.60	900 × 900 × 181 mm square low damping rubber bearings
Int. Thermonuc. Experim. Reactor, ITER, France Tokamak fusion reactor	Under construction	0.32	0.55	900 × 900 × 181 mm square low damping rubber bearings

All projects shown in the table correspond to French technology, which traditionally uses laminated polychloroprene (neoprene) rubber bearings, which today are designated as Low Damping Rubber Bearings (LDRB).

2.1.2 Role of testing in the design of seismic isolation systems

A testing programme is an integral part of the seismic isolation project. The nature and extent of the programme depend on the regulation and practice in each Member State. In general, there exist two broad categories of tests:

- (1) *Characterization tests*. These are tests performed on individual prototype isolators. The objective is to determine or to verify static and dynamic properties assumed in the design, including the variation of these properties with aging.

For nuclear safety applications, isolators need normally to be characterized not only for the design conditions, but also for extended design conditions (e.g. 1.67 times the design basis earthquake), where non-linear phenomena can be very relevant.

- (2) *Validation tests*. The scope of these tests is not a single isolator, but the whole isolation system. The objective is to verify that the structural response computed based on the results of the characterization tests is an acceptable approximation to the real behaviour.

These tests may be not necessary when the isolators have basically a linear behaviour for the design loads (e.g. LD isolators). However, in other cases, given the complexity of non-linear modelling and analysis methods, it is normally required that experimental validation supports the results in which the design will be based.

In theory, shake table testing of full-scale models would provide such a validation. However, at the current state of the technology, those tests are physically impossible given the size of the structures¹. Hence, testing would need to be done on scale model isolators and a scaled model structure. In this case, scaling effects might have a strong influence in the response and the correspondence to the real structure needs to be carefully evaluated. Excessive simplifications would therefore raise questions about the accuracy and realism of the tests due to issues with size, scale and rate-of-

¹ The largest shake table in the World is 20 × 15 m and it has a payload up to 1200 ton. A typical modern reactor building can weight in the order of 150000 tons and it has a footprint of about 70 × 70 m.

loading effects. Therefore, scaled prototypes cannot be very small and this results in an important practical limitation, since very few shake tables in the World are able of testing the resulting prototypes.

Hybrid simulation, the main subject of the present report, is a technique that combines full scale testing and analysis. This technique can be used to validate purely analytical approaches, as discussed in the following sections.

In any case, given the size of the isolators that can nowadays be manufactured for nuclear safety applications, the designer needs to bear in mind the physical limitations of the available testing facilities. Large isolators will normally require load capacities and load rates which are currently available at only a few laboratories in the World.

2.1.3 Present challenges

In the current international context, a small number of nuclear plant vendors market their standard plant designs for new nuclear power plant projects. Most of these designs were developed for a design basis earthquake with peak ground acceleration in the order of 0.30 g.

Once a particular site is selected, the standard designs need to be assessed, and sometimes adapted, for site conditions, including the seismic hazard (Ref. [2]). In the recent years, it has been found that the seismic hazard in a significant number of prospective sites in embarking countries could result in a design basis earthquake which exceeds the one used for developing most of the standard designs. In these cases, the vendor needs to revisit the design and to introduce changes for increasing the seismic capacity. This is exactly the kind of situation which motivated the first base-isolated nuclear projects shown in Table 1. Introducing base-isolation is a very efficient way of achieving a large increase in the seismic capacity of a standard design.

In many sites, the seismic hazard can be an important contributor to the overall risk posed by the nuclear plant. In the current licensing environment, the designer needs to show that the design has a large enough margin so that this contribution remains within acceptable limits. Seismic isolation technology has the potential to significantly reduce the seismic contribution to risk and, consequently, it is a powerful design tool to address this challenge.

In sites with design basis earthquake with peak ground accelerations significantly larger than 0.30 g and with a large displacement demand at low frequencies, the use of Low Damping Rubber Bearings (LDRB), such as the ones used in the projects shown in Table 1, is not the optimal technical solution, because of the large deformations induced in the isolators. Applications in the conventional building industry suggest that energy dissipation devices need to be introduced. There are different mature technologies available, such as the Lead plug Rubber Bearings (LRB), but none has been used so far in nuclear safety-related buildings. This is a significant design challenge, since the behaviour of these energy dissipating devices is highly non-linear, and the characterization of the behaviour requires an extensive experimental program. Validation of the analytical procedures used in design to justify safety, based on experimental results, is normally required by the safety authorities.

In addition, in the current worldwide regulatory environment, the design needs to be assessed for beyond design basis external events, with the purpose of showing that there is enough safety margin for extreme events that could exceed those considered in the design and that no cliff-edge effects would appear for small exceedances of the design levels. Since the seismic isolation system is the key component for the overall seismic resistance, the margin beyond design will be very much dependent on the margin of this system and the tools used to assess this margin will also need to be validated, this time for earthquakes between 1.40 and 1.67 stronger than the design earthquake. This is an even more significant challenge.

2.2 HYBRID SIMULATION

2.2.1 Overview and history

Results from experimental tests are essential in developing numerical models and validating the accuracy of simulations used by engineers to predict the behaviour of complex civil structures or

mechanical components. For seismic loading conditions there exist three well-established methods to perform dynamic testing in a laboratory and assess the behaviour of structural systems and components.

The first method is a cyclic characterization test, where the test specimen is subjected to a predefined history of displacements or loads applied through actuators. The effect of systematic changes in material properties, loading rates, details, boundary conditions, and other factors can be characterized by imposing the same displacement or load history on a series of specimens. While such tests are relatively easy and economical to execute, the overall demands imposed on the test specimens are not directly related to the constantly changing load distributions that a structure undergoes during an actual seismic event. Furthermore, in the case of testing seismic isolation bearings this method only assesses the behaviour of the device itself without the ability to investigate the behaviour and response of the isolated superstructure including the in-structure response.

The second method is a dynamic test using a shake table, where the test specimen is subjected to a predefined (recorded or synthetic) base motion. Shake table tests try to simulate conditions that closely resemble those that would exist during a particular earthquake. Therefore, they are able to assess the dynamic response caused by specific ground motions, considering the inertial and energy-dissipation characteristics of the test specimen and the consequences of geometric nonlinearities, localized yielding and damage, and component failure on the structural response. Full-scale shake table tests are generally viewed as the most realistic method for the seismic evaluation of structural systems. However, as mentioned above, full-scale testing of nuclear buildings is currently impossible.

In the third method, physical test specimens are combined with numerically modelled parts of a structural system to assess the behaviour of the ensemble in an integrated simulation. This experimental testing method has become increasingly more popular and over the years has been referred to as online computer-controlled test method, pseudo-dynamic test method, hybrid simulation test method, and more recently as cyber-physical systems test method. In this method, conceptually shown in Figure 2, a hybrid model of the structural system is created by partitioning the structure into two different classes. One class includes the parts of the structure that are well understood or can be modelled and simulated with confidence in structural analysis software. The other class consists of the parts that are difficult to be simulated well using computational approaches and are thus physically tested in one or more laboratories. Consequently, hybrid simulation can combine recent advancements in numerical simulation techniques with laboratory testing that requires fewer resources than shake table testing. The method removes a large source of uncertainty by replacing parts of the structure that are difficult to model numerically with real physical components that can more easily be tested in full-scale than a complete structural system.

Given these capabilities, hybrid simulation provides an excellent opportunity to assess the performance of seismically isolated nuclear power plants with full-scale seismic isolation bearings under realistic seismic loading conditions. Because seismic isolation bearings typically exhibit uncertain nonlinear behaviour that is significantly affected by bearing scale, rate-of-loading, and vertical-horizontal coupling effects, full-scale bearings need to be tested physically in the laboratory (preferably in real time) to obtain a realistic bearing behaviour. On the other hand, the nuclear power plant superstructure is expected to remain linear-elastic because of the protection provided by the seismic isolation system. Hence, the superstructure can be modelled and simulated numerically with confidence using linear approaches in existing structural analysis software.

Hybrid simulation has come a long way since its inception in the early 1960s. The concept of combining numerical and physical parts of a system originated in the field of aerospace and control engineering. These first implementations [3] and [4] combined digital computers (numerical sub-assemblies) with analogue subsystems that included controllers (physical subassemblies). Soon thereafter hybrid simulation concepts also started being developed in the field of structural engineering. While seeking new experimental testing methods for evaluating the dynamic, especially seismic, behaviour of large-scale structures, structural engineering researchers initiated the development of the online computer-controlled test method. However, the first official publication did not appear until 1975 when hybrid simulation was proposed as an alternative experimental testing technique to shake table testing [5]. Since then a vast number of variations of this experimental method and the necessary computational techniques have been developed to improve efficiency, accuracy, and versatility.

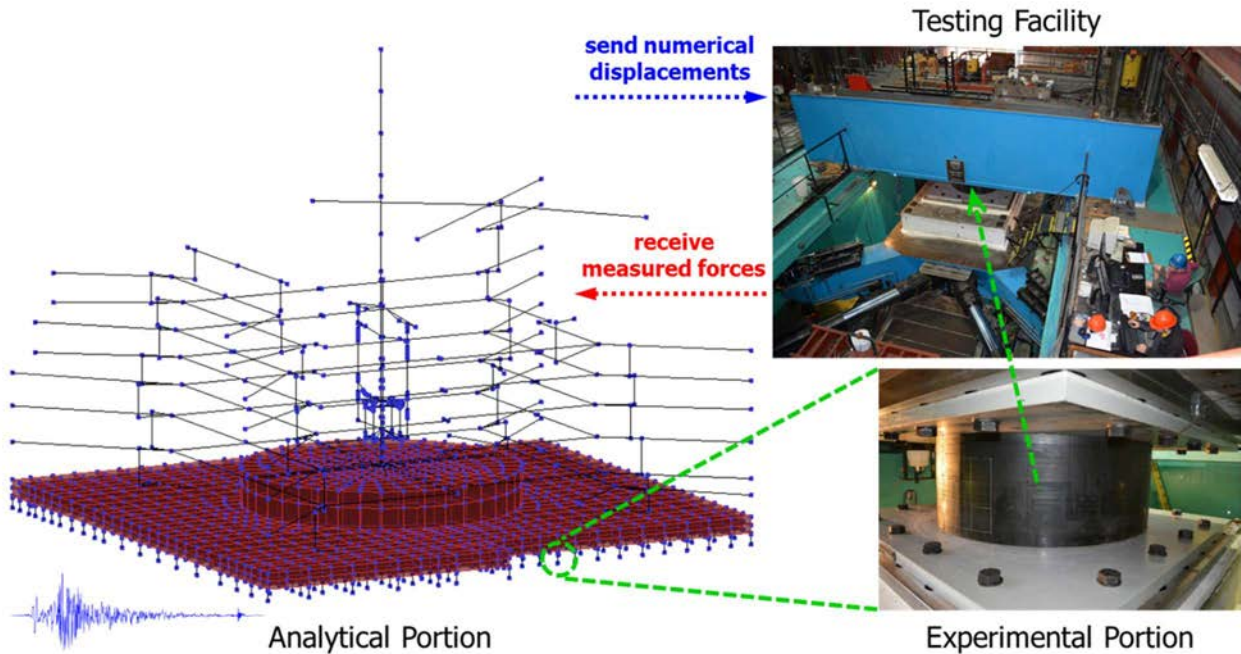


FIG. 2. Concept of hybrid simulation based on seismically isolated NPP.

Generally, the developments in hybrid simulation have been strongly related to the advancements in the fields of digital control theory and high-performance computing, due to the cyber-physical nature of this testing method. After the initial application of the method to structural testing, it was further developed in the early 1980s. During this time period the method was referred to as pseudo-dynamic testing method, because the physical components of the simulation were tested at very slow rates capturing only quasi-static restoring forces while inertia and energy dissipation were entirely modelled in the numerical portions of the hybrid simulation. As such, pseudo-dynamic testing was used in combination with reaction walls to test large structural specimens at slow testing rates. In the late 1980s, error and rate-of-loading effects were studied [6] [7]. It was shown that hybrid simulation tests can produce results comparable to shake table tests as long as experimental errors are effectively mitigated. Detailed explanations and summaries on errors in hybrid simulations, including lead and lag errors which play an essential role in evaluating hybrid simulation results in Section 5.7, can be found in references [8] and [9].

An important milestone in the development of hybrid simulation was driven by the need to assess the dynamic behaviour and performance of rate-dependent structural components (e.g. seismic isolation bearings for civil structures, energy dissipation devices, and high-performance materials). This need combined with advances in embedded control systems with hard real-time computing capabilities eventually led to the development of fast and real-time hybrid simulations (RTHS). In a real-time hybrid simulation, the physical parts of the structure are loaded with the real, calculated velocities and accelerations, meaning that inertia and energy dissipation contribute to the measured forces and rate dependent behaviour is captured correctly. The first implementation of a real-time hybrid simulation was achieved by the use of improved hardware, including a dynamic actuator and a digital servo-mechanism instead of an analogue one [10].

For many years, implementations of hybrid simulation have been problem specific and highly dependent on the equipment, software, and hardware at a particular testing facility. Due to the lack of a more unified, repeatable, and extensible approach to hybrid simulation several research projects [11], [12], and [13] initiated the development of frameworks for hybrid testing. One of these software frameworks, namely the Open Framework for Experimental Setup and Control (OpenFresco) [14], was deployed herein (see Section 5.6) to perform hybrid simulations for seismically isolated nuclear power plants. Another, less active area of research in hybrid simulation is related to the development of different

methods of control, such as force control [15], switch control [16], and mixed control [17]. The mixed control strategy was utilized for the 3D hybrid simulations carried out in the present work, where the two horizontal degrees of freedom of the isolator were displacement controlled and the axial degree of freedom of the isolator was force controlled.

For a more detailed history of hybrid simulation, see reference [18].

2.2.2 Components and procedure

In its most basic form, a cyber-physical simulation requires a hybrid model of the system to be investigated consisting of a numerically modelled portion of the system combined with at least one physically tested component. In the case of a cyber-physical system for structural testing, several key components consisting of software and hardware that need to interact with each other during a hybrid simulation can be identified. These key components are shown in Figure 3 and are described next. For a more detailed summary on the components required to perform a hybrid simulation see [18].

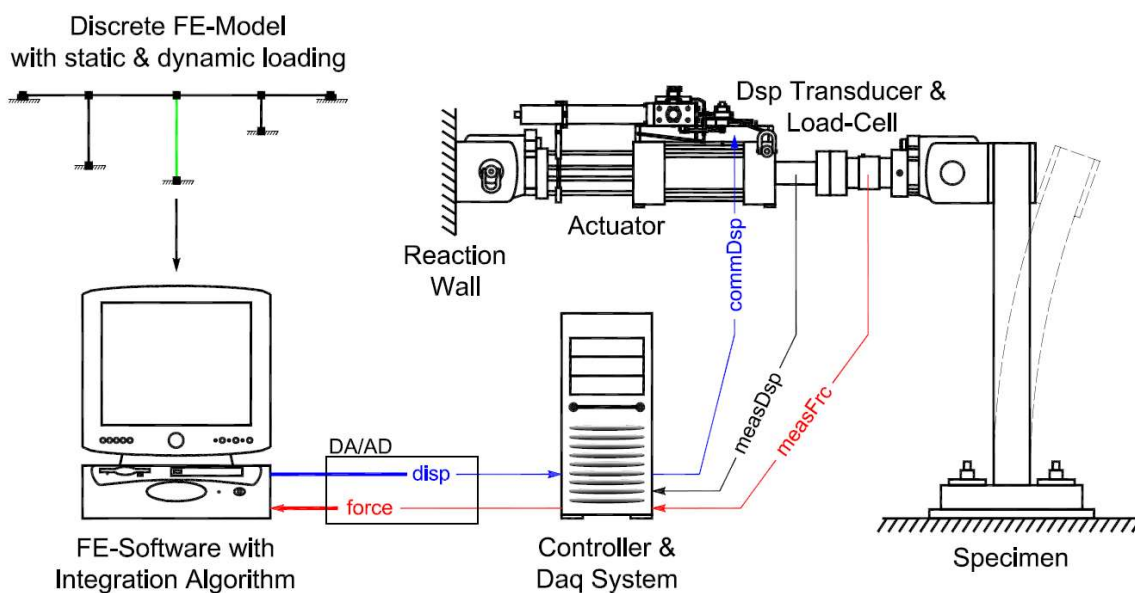


FIG. 3. Key components of a hybrid simulation for structural testing.

The purpose and function of each component are as follows:

- (1) A discrete numerical computer analysis model of the structure to be investigated. This model includes static and dynamic loading conditions that are typically defined purely numerical but can also include physical loads. The dynamic loading conditions that can be considered include seismic events, hydrodynamic loads created by waves and storm surges, traffic and impact loads due to moving vehicles, and aerodynamic loads generated by wind and blast. The portion of the structure that is to be tested in the laboratory is embedded as a subassembly into the numerical computer analysis model [19]. In most cases, the finite element method is then deployed to discretize the problem spatially and a time-stepping integration algorithm is used to discretize and advance the solution in time.
- (2) A transfer system consisting of a controller and static or dynamic actuators. The transfer system connects the numerical portions with the physical portion of the structure by applying to the experimental specimen incremental displacements (or forces) determined by the time-stepping integration algorithm in (1). Any control system and testing equipment that provides a means to receive external command signals can be used to act as the transfer system. However, for real-time hybrid simulation, advanced high-fidelity controllers [20], delay compensation techniques [21], and

dynamic actuators are required to obtain the best possible tracking performance. Furthermore, dynamic effects play an important role in real-time hybrid simulation and need to be considered and compensated for to minimize systematic experimental errors and ultimately prevent instability.

- (3) The physical specimen that is being tested in the laboratory. The experimental laboratory setup is configured such that the computed response from the numerical portion of the hybrid model can be imposed at the desired interface degrees of freedom using the transfer system described in (2). The specimen needs to be securely anchored to a stiff reaction wall or strong floor so that the desired response can be imposed accurately, and the corresponding measurements can be acquired correctly. Careful attention is needed to choose the most effective interface degrees of freedom and boundary conditions, and to determine appropriate scaling factors.
- (4) A data acquisition system (DAQ) including sensors such as load cells, displacement transducers, and accelerometers. The data acquisition system with its sensors is responsible for measuring the response of the test specimen, digitizing it, and returning such experimental information to the time-stepping integration algorithm in (1) in order to advance the solution to the next analysis step. The response of the physical specimen can be measured directly at co-located transfer system degrees of freedom, or it can be computed from other sensor measurements using observer techniques. Oftentimes the data acquisition system is an independent system but in fast and real-time applications it can be beneficial to have it integrated with the control system to eliminate synchronization issues.

Similar to a purely numerical simulation, in the finite element approach to hybrid simulation a time-stepping integration algorithm is used to discretize and advance the solution in time. Hence, the testing procedure can be summarized in terms of the required steps to perform such time-stepping analysis. As has been mentioned before, significant research has been conducted over the years to develop time integration methods that are specialized for hybrid simulation. Due to its straightforwardness, the explicit Newmark method was one of the first methods employed to integrate the equations of motion and is thus also used here to explain the solution process. As explained in detail in [22] the explicit Newmark method is a conditionally stable direct integration method and requires that the selected integration time step size is smaller than the shortest period of the structure divided by pi. The three steps of the testing procedure are illustrated in Figure 4 and can be summarized as follows:

- (1) For each time step of the direct integration analysis, the first operation is to compute the new trial response consisting of displacements, velocities and accelerations. The new response is computed from the response at the previous time step and factors that depend on the type of the integration method. In addition, the loads and the analysis time are incremented, and the new trial response is sent to the analytical and experimental subassemblies. The analytical subassemblies store this response so that they can later determine the corresponding unbalanced load. The experimental subassemblies, on the other hand, send this response to the transfer system in the laboratory, which immediately starts imposing the new trial response on the test specimen.
- (2) The next operation in the direct integration analysis is to solve the linear system of equations:

$$\mathbf{A} \times \mathbf{x} = \mathbf{b} \tag{1}$$

at the current time step for the solution vector \mathbf{x} . Since explicit integration methods, such as the explicit Newmark method, do not perform any equilibrium iterations a linear equilibrium solution algorithm is required to compute the solution vector \mathbf{x} . The linear algorithm executes the following four substeps:

- a. First, the tangent, mixed or initial Jacobian \mathbf{A} (also referred to as effective stiffness matrix) needs to be assembled from the different portions of the structure. For the explicit Newmark method the Jacobian \mathbf{A} has only mass and damping matrix contributions, meaning that no stiffness matrices need to be obtained from the analytical and experimental subassemblies (hence these operations are greyed out in Figure 4). However, for other integration methods the analytical subassemblies need to calculate and return their tangent or initial stiffness matrices and the experimental subassemblies need to return their initial stiffness matrices that have been determined numerically or analytically prior to the start of the hybrid simulation.

- b. Next, the linear equilibrium solution algorithm needs to assemble the unbalanced force vector \mathbf{b} . When queried, the analytical subassemblies retrieve the response that was received and stored in step (1) to calculate and return their resisting forces and dynamic contributions to the unbalanced force vector. In contrast, the experimental subassemblies communicate with the data acquisition systems in the laboratory which measure the resisting forces as soon as the previously received target response is achieved. The measured resisting forces combined with dynamic contributions to the unbalanced force vector are then returned to the linear algorithm.
 - c. Once the assembly processes of the Jacobian and the unbalanced forces are completed, the equilibrium solution algorithm can solve the linear system of equations (1) for the solution vector \mathbf{x} . For the explicit Newmark method, the solution vector consists of the accelerations at the new time step.
 - d. In the last step the response of the structure is updated by applying the computed solution vector. For the explicit Newmark method this means that velocities at the new time step are updated based on the computed accelerations.
- (3) In the last operation of the procedure, the solution state of the structure is committed, and the direct integration analysis can be advanced to the next time step. The analysis steps are repeated until the desired number of integration steps has been reached.

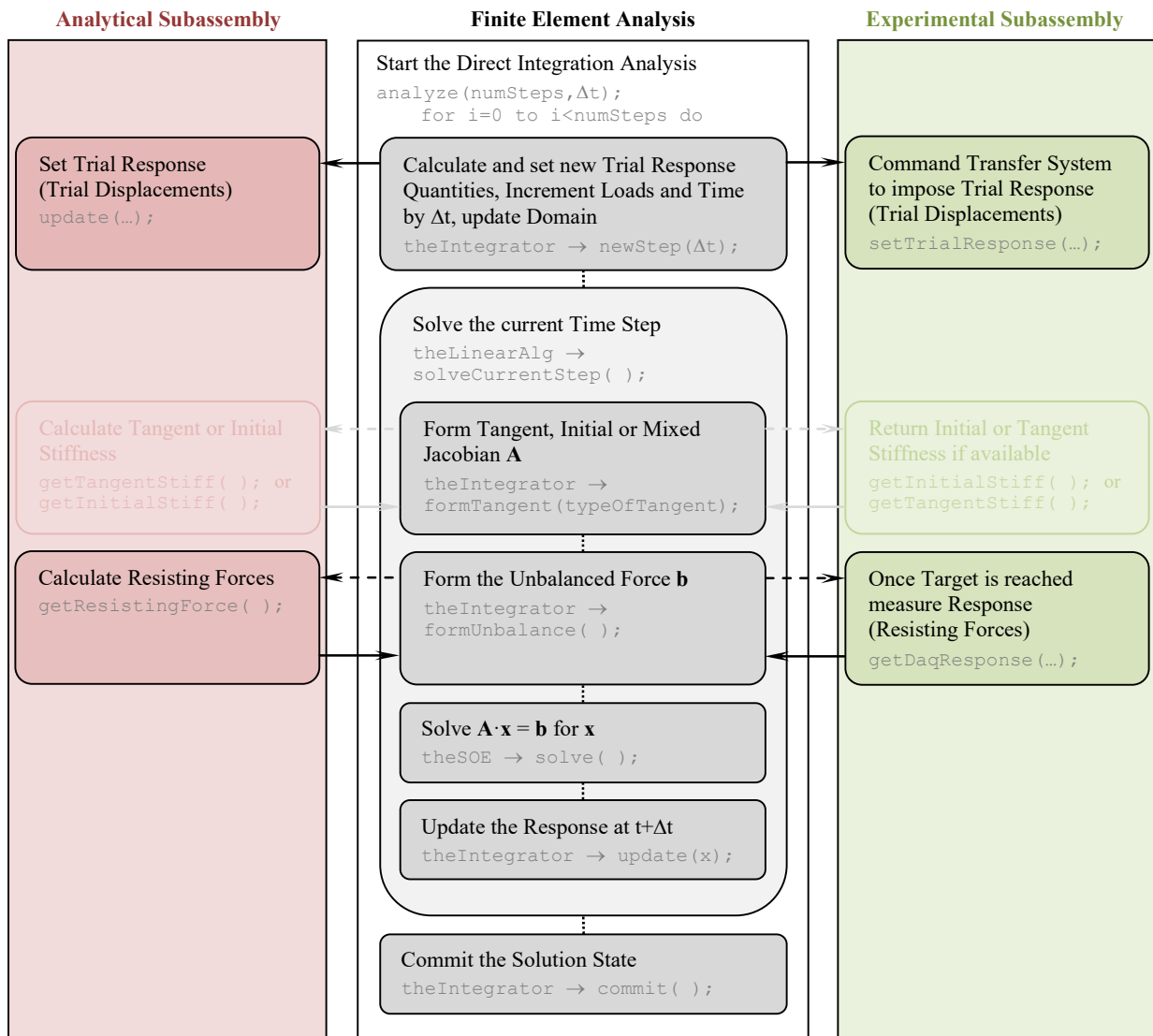


FIG. 4. Hybrid simulation testing procedure.

3 INTERNATIONAL BENCHMARK PRESENTATION

3.1 PURPOSE OF BENCHMARK

The main purpose of the benchmark was to assess the current prediction capabilities for the behaviour of an isolated nuclear structure subjected to a large seismic excitation.

Participants were asked to obtain the response of a base isolated nuclear island to different levels of seismic input motion. This was intended to be a blind exercise. The results computed by the participants have afterwards been compared with the results obtained from the hybrid simulation testing. From the comparison, conclusions have been derived about prediction capabilities and the consistency between purely computational methods and hybrid simulations.

The target of the benchmark was the behaviour of the isolators, not the modelling of the superstructure. Hence, all participants were requested to use the same computational models for the superstructure, provided in SAP 2000 format and adapted to their computer codes with as few changes as possible. The models provided to the participants corresponded to the base-isolated design of the APR-1400 nuclear island (Reactor, Fuel and Auxiliary buildings, Figure 5).

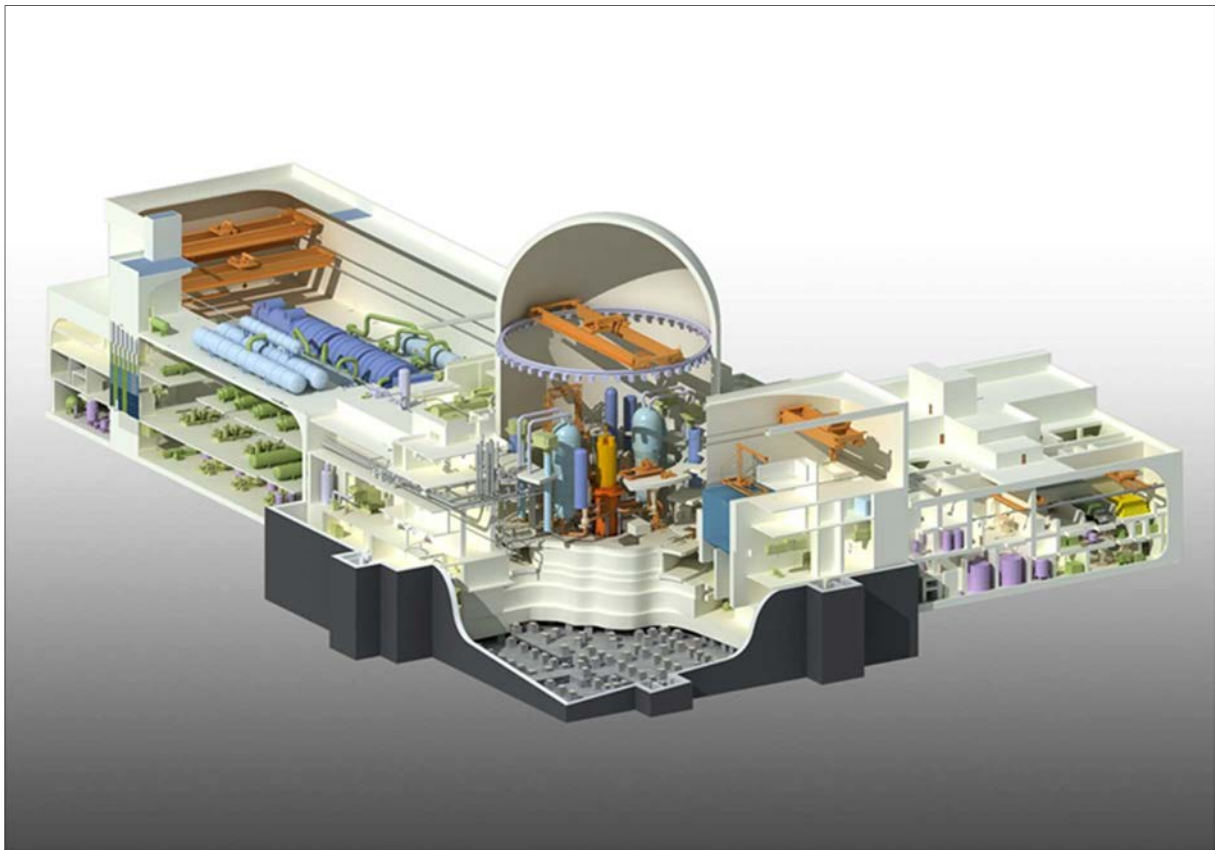


FIG. 5. General perspective of the base-isolated APR-1400 plant.

The participants were asked to model the isolators according to their practice and to compute the required response parameters for, at least, the design basis earthquake (DBE, 0.50 g) and for 1.67 times the DBE. The analyses required by this benchmark were resource intensive and time consuming. Hence, it was foreseen that some participants would not be able to assign resources for producing all required output. Therefore, a priority order was then given for the analyses, so that high priority analyses were performed by as many as possible participants.

3.2 OVERVIEW OF BENCHMARK ACTIVITIES

Benchmark activities developed by the participants consisted in the sequence of tasks described below:

- (1) Assimilation of benchmark information. The same package of information was supplied to every nominated participant by the IAEA Secretariat.
- (2) Adaptation of computational models to participant's computer programs. The computational models described in Section 3.4.1 below were supplied in SAP 2000 format within the benchmark package. When the participant was not using this computer software he/she needed to convert the models into the format required by his/her software.
- (3) Check adapted models. Once the models were adapted, basic checks were performed, to make sure that no errors were introduced during the conversion and that the basic dynamic behaviour was the same as in the SAP 2000 models. For this purpose, the information supplied to the participants included the following basic model parameters:
 - Total mass and tensor of inertia;
 - Position of the centre of gravity;
 - First natural frequencies (fixed base model);
 - Corresponding modal shapes and participation factors.
- (4) Select computational model for isolator behaviour. Based on the information provided about the seismic isolators, the participants selected a numerical model to represent the behaviour of the isolators within his/her models and defined the appropriate values for the parameters of the numerical model. This was the key point of the benchmark exercise.
- (5) Run models for given seismic input motions. Once the computational models included the intended representation of the isolators, the participant carried out the computer analyses and produced the different outputs.
- (6) Prepare and submit required output. In a final step, the participant post-processed the computer results to produce the required output.

3.3 LIST OF PARTICIPANTS

Table 2 gives the list of organizations participating in the international benchmark. Participants are given in alphabetic order. The code assigned to participants when results are presented in the following sections has been assigned to the Secretariat, in order to keep the results anonymous. A total of eight organizations, from six Member States took part in the exercise.

TABLE 2. PARTICIPANTS IN THE INTERNATIONAL BENCHMARK

Organization	Member State
CEA	France
Framatome	France
IEM & NSC	China
KEPCO	Korea
KINS	Korea
PAEC	Pakistan
SNERDI	China
Wölfel Engineering	Germany

On the other hand, Table 3 lists the organizations supplying the three isolators considered in the benchmark. Prototype isolators of each type were supplied for testing in the hybrid simulations described in Section 5.

TABLE 3. SEISMIC ISOLATION DEVICES CONSIDERED IN THE BENCHMARK EXERCISE

Name of Device	Supplier	Member State	Remarks
Eradi Quake System (EQSB)	ESCO RTS	Korea	Patented system based on a plane sliding surface and self-centering springs
Multi Lead-core Rubber Bearing (LRB)	UNISON ETECH	Korea	Lead-rubber bearing with four lead cores
Triple Pendulum Friction Bearing (TPFB)	EPS	United States of America	Friction pendulum bearing, with two pairs of sliding surfaces with different radii and coefficients of friction.

3.4 SPECIFICATION OF THE BENCHMARK

3.4.1 Archetype plant models

3.4.1.1 Description of isolated structure and isolation system

This numerical model supplied to the participants was based on the base-isolated design of the APR-1400, which stands for Advanced Power Reactor. The APR-1400 is a pressurized water reactor design developed in Korea that produces 1400 MW(e). Figure 6 shows vertical and horizontal cross sections of the nuclear island.

As can be seen in Figure 6, the structure is a relatively conventional reinforced concrete shear wall structure, including a cylindrical containment with a hemispherical dome. The distinct feature is that the basemat (drawn in orange in Figure 6) is placed on seismic isolators, installed on top of plinths (short columns). In turn, the base of the plinths is connected to the foundation basemat (drawn in purple in Figure 6), which is at the bottom of a 'seismic pit', embedded in the foundation ground.

For the purposes of this benchmark exercise, data from the preliminary seismic isolation design was provided to the participants. Main parameters are as follows:

Weight (W) of isolated structure
485500 ton-force

Geometry of the isolated structure
Dimensions in plan: 103.6 m × 102.4 m
Number of plinths: 445
Plinth dimensions (W × D × H): 2.44 × 2.44 × 1.80 m

3.4.1.2 Superstructure model

To reduce scatter in the results due to causes other than modelling of the isolators, it was considered desirable that all participants used the same numerical model for the superstructure (i.e. the APR-1400 nuclear island). For this purpose, a simplified stick model was provided to the participants (Archetype Nuclear Test model, ANT). An overall perspective of this model can be seen in Figure 7.

The ANT numerical model includes the nuclear island buildings, the bearings supporting the nuclear island, the plinths, and a lower basemat in contact with the ground. The nuclear island includes reactor systems, internal structures and containment structures of the reactor containment building (RCB), the auxiliary complex building (ACB), and an upper basemat supporting the RCB and ACB. For the purposes of this benchmark, the upper basemat was considered to be rigid.

The RCB, the containment internal structures with reactor systems and the ACB are modelled by separate stick models (beam elements plus lumped masses) within the overall ANT model. The ANT numerical model does not consider the moat wall, the backfill, or the soil foundation. The hybrid tests will additionally ignore the lower basemat and the plinths are modelled as being fixed-base. The hybrid

test theoretically can consider soil-structure interaction (SSI) effects, but they were not covered in the current program.

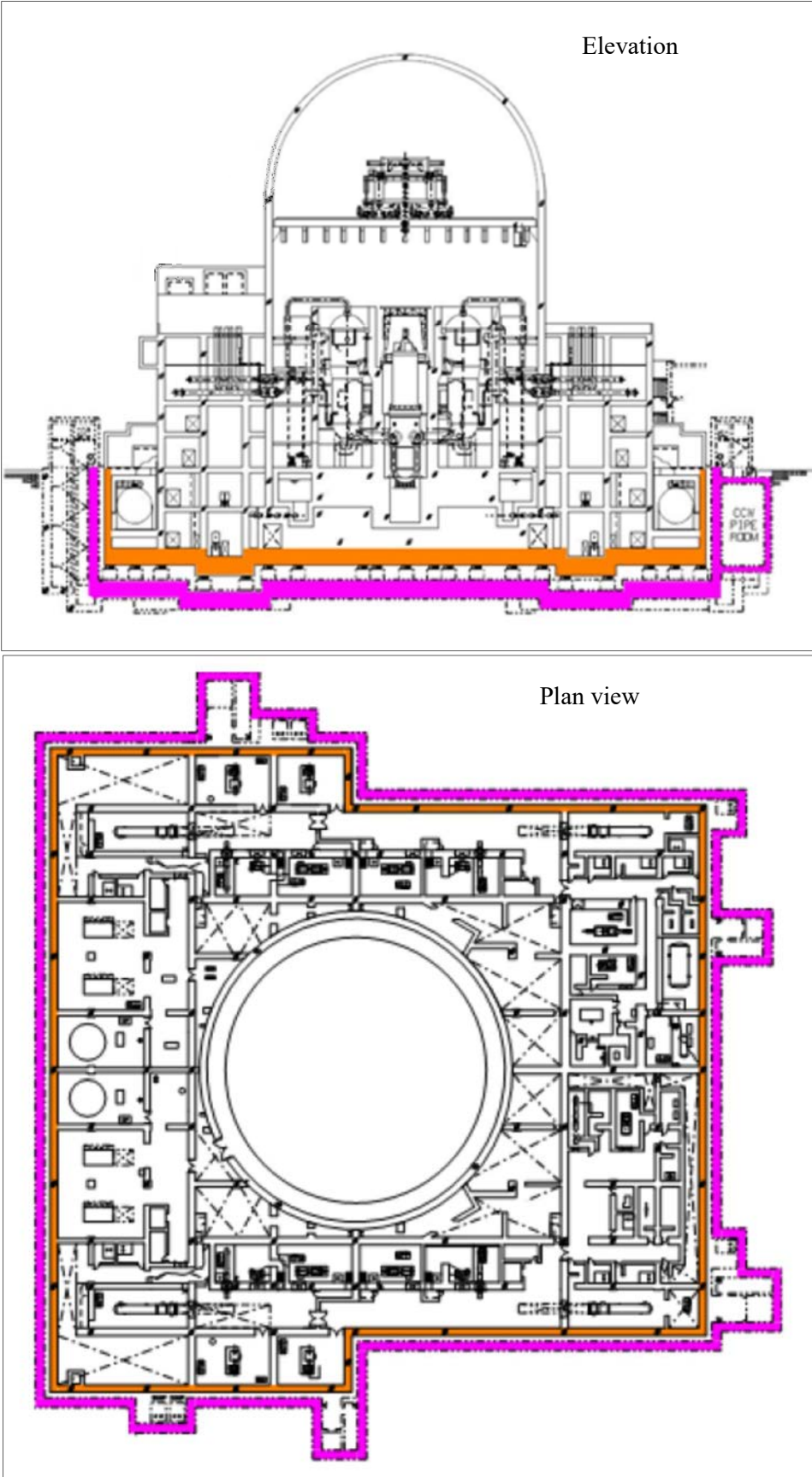


FIG. 6. Cross sections of the nuclear island of the base-isolated APR-1400 plant.

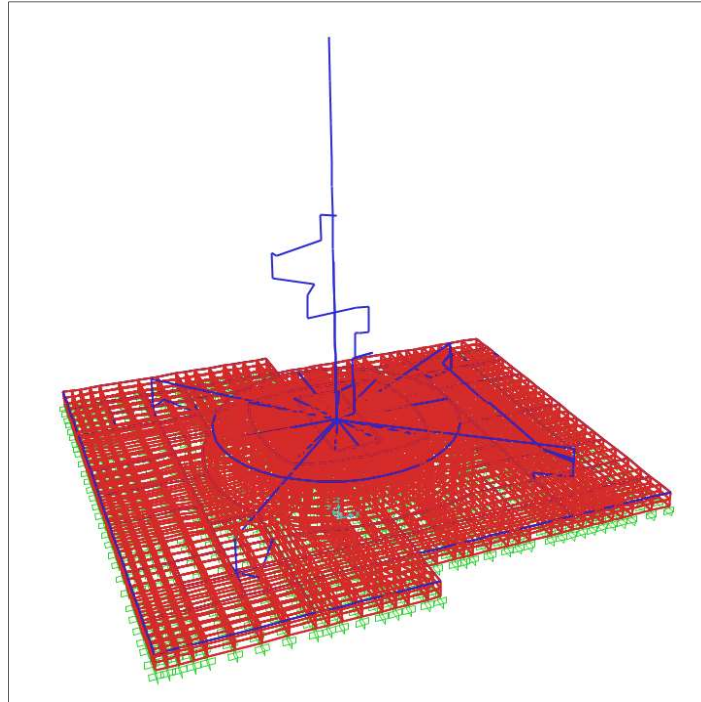


FIG. 7. Stick model representing the nuclear island of APR-1400 plant.

Figure 8 shows the different parts of the stick model. Figure 7 corresponds to the complete model, once connected to the upper basemat. Nodal coordinates of RCB, internal structure and ACB submodels, together with lumped mass values of the ANT model and structural section properties for the three stick submodels, can be found in Annex I.

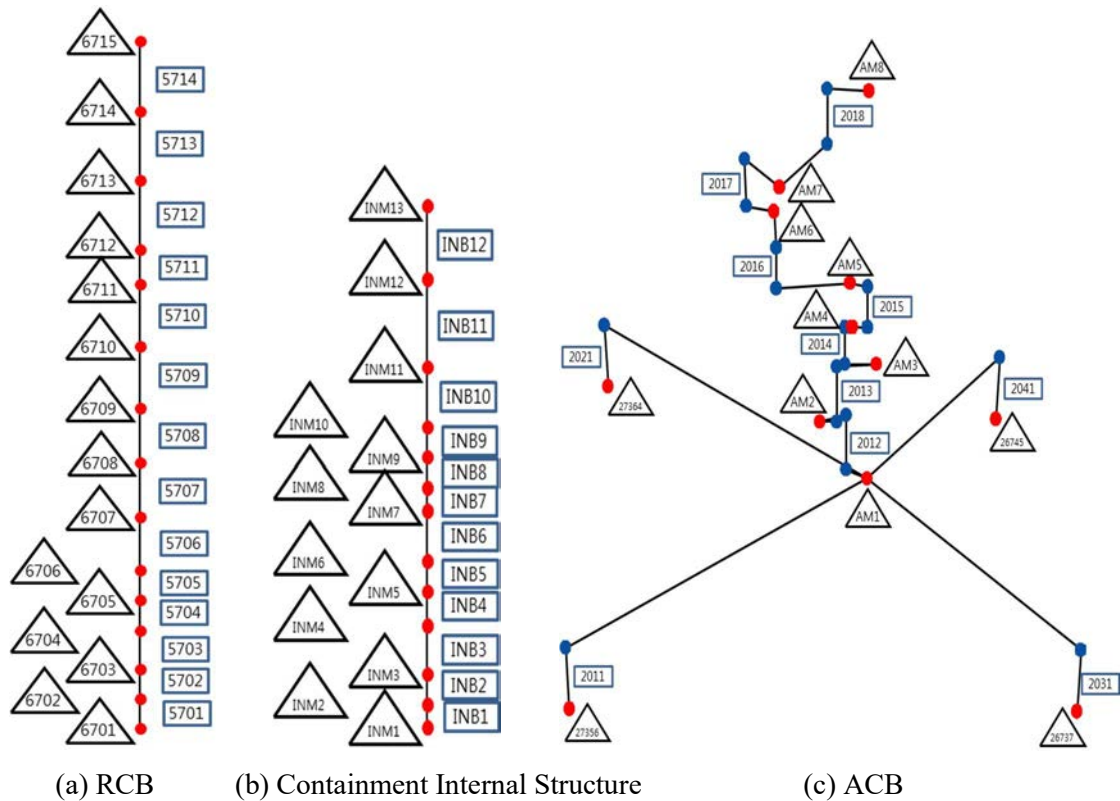


FIG. 8. Detail of the different components of the stick model representing the nuclear island of APR-1400 plant.

Table 4 gives material properties used for the different portions of the ANT model. For simplicity, structural damping was assumed to be 5% in all cases.

TABLE 4. MATERIAL PROPERTIES FOR THE SUPERSTRUCTURE MODEL

Model	Elastic Modulus (GPa)	Mass Density (kg/m ³)	Poisson's Ratio	Damping Ratio
RCB Internal Structures	30.45	0.00	0.170	0.05
ACB	27.77	0.00	0.169	0.05
Rigid Beam	277700.00	0.00	0.000	0.05

Natural frequencies of the RCB, internal structure and ACB, obtained from an eigenvalue analysis using the ANT model without isolators (fixed base analysis, model fixed at top of isolators) are listed in Table 5, and modal shapes corresponding to the lower natural frequencies of each structure are shown in Figures 9 through 11. An input file in SAP2000 format (Ref. [23]), for the ANT model, "ANT.s2k", is included in Annex I.

TABLE 5. SUPERSTRUCTURE MODEL – NATURAL FREQUENCIES

	First Natural Frequency (Hz)
RCB X-direction mode	3.710
RCB Y-direction mode	3.715
Containment Internal Structure X-direction mode	9.875
Containment Internal Structure Y-direction mode	11.445
ACB X-direction mode	6.049
ACB Y-direction mode	5.648

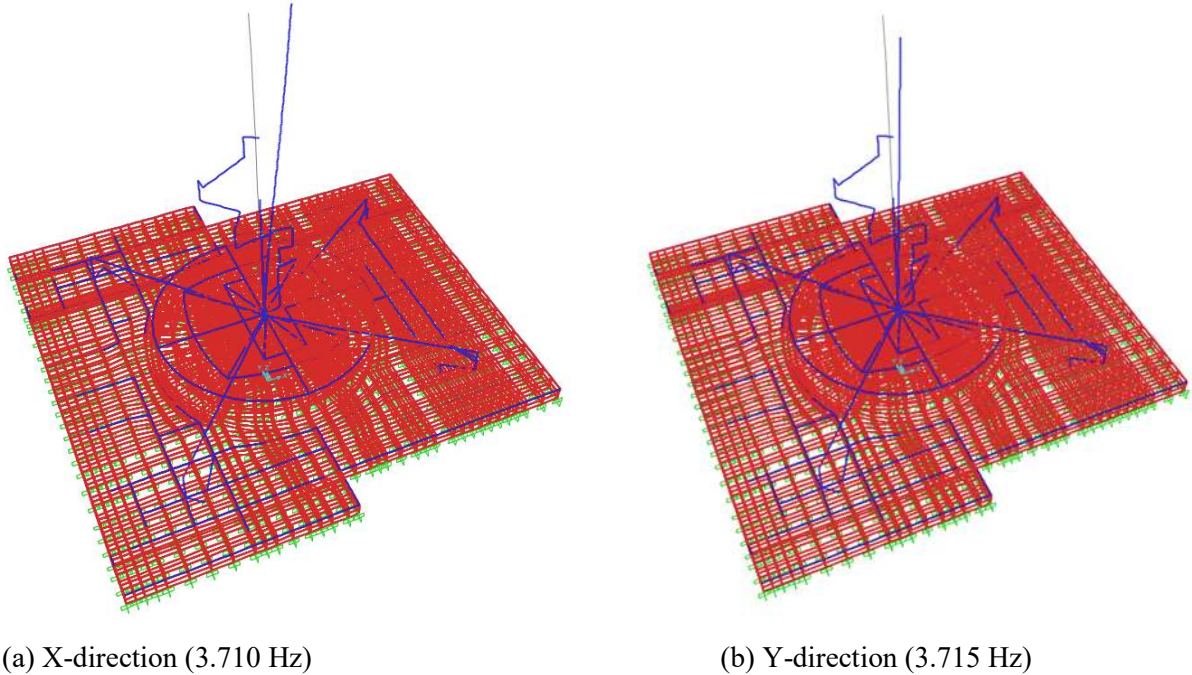
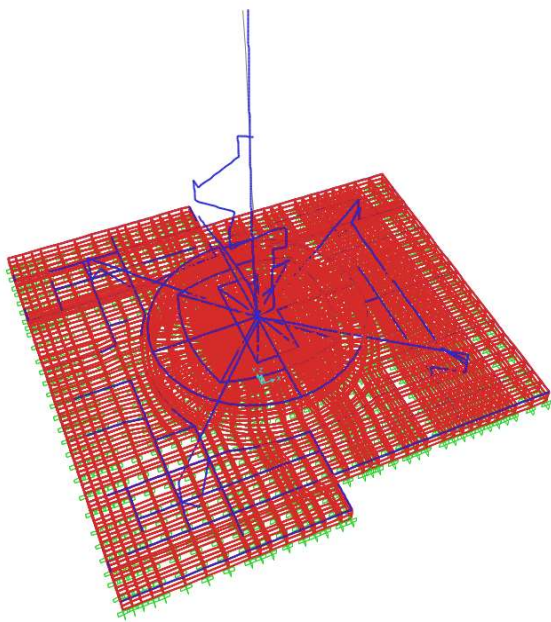
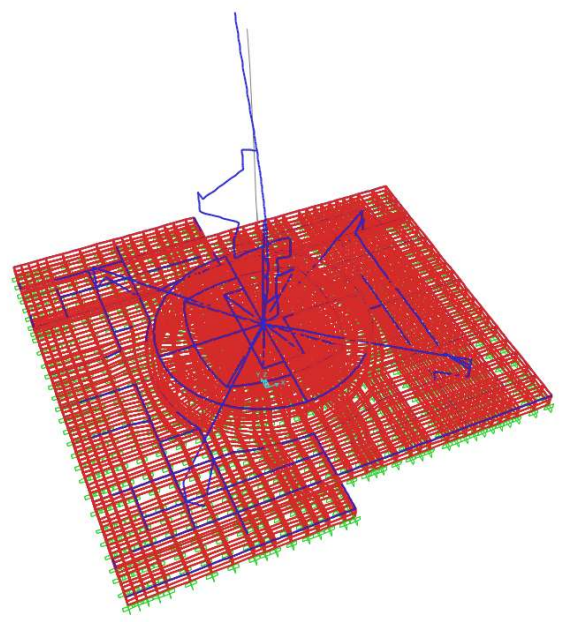


FIG. 9. Fundamental mode shapes of the stick model representing the RCB.

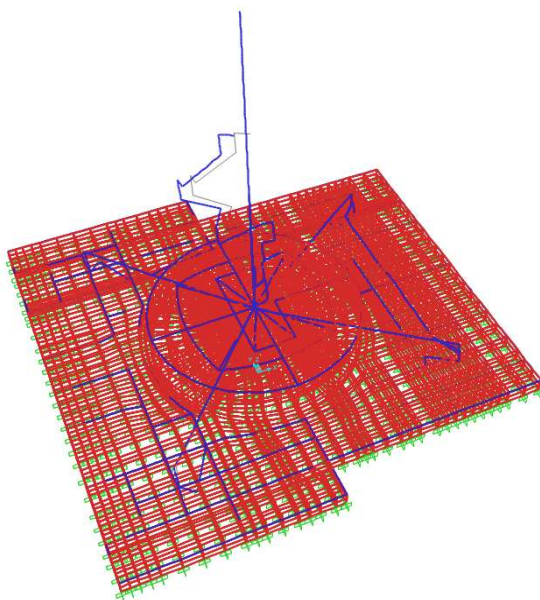


(a) X-direction (9.875 Hz)

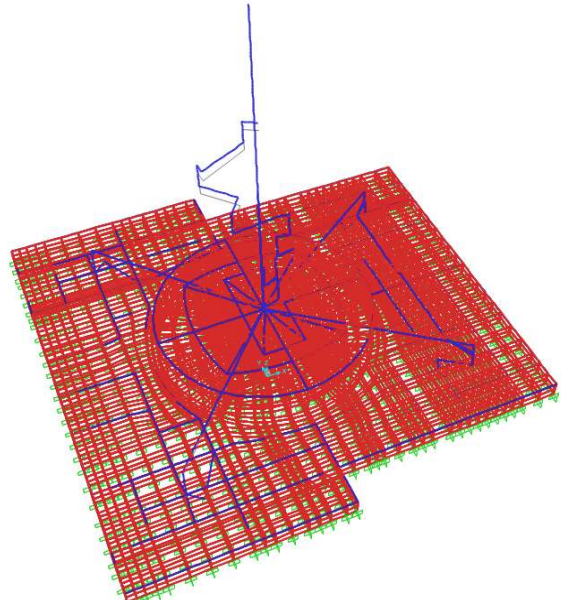


(b) Y-direction (11.445 Hz)

FIG. 10. Fundamental mode shapes of the stick model representing the containment internal structures



(a) X-direction (6.049 Hz)



(b) Y-direction (5.648 Hz)

FIG. 11. Fundamental mode shapes of the stick model representing the ACB.

3.4.1.3 Models of isolation system

The stick model representing the nuclear island of APR-1400 plant (Figure 7) is connected to three different representations of the isolation system which, in turn gives three different computational models:

- (1) 486-bearing model, in which all bearings are included. Figures 12 and 13 show the arrangement of bearings and its representation in the finite element model, respectively. The lower end of each bearing is fixed, and the upper end is connected to the upper basemat, which is modelled by solid elements. Bearing properties used for model checking purposes and an input file in SAP2000 format (Ref. [23]), “ANT_nonlinear_simple_486.s2k”, are included in Annex I.

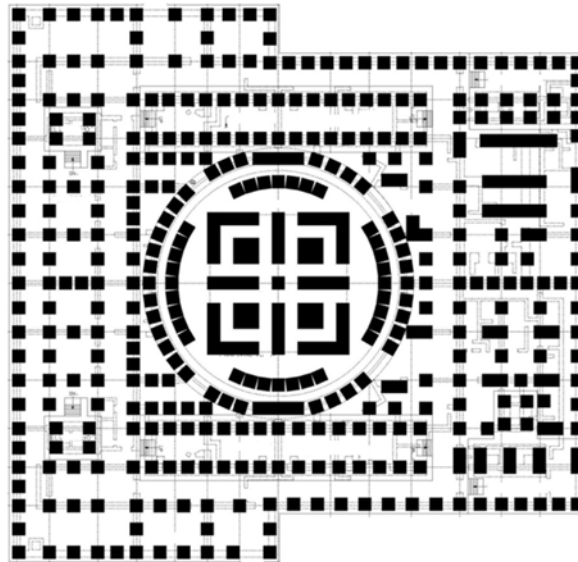


FIG. 12. Arrangement of bearings under the nuclear island of APR-1400 plant.

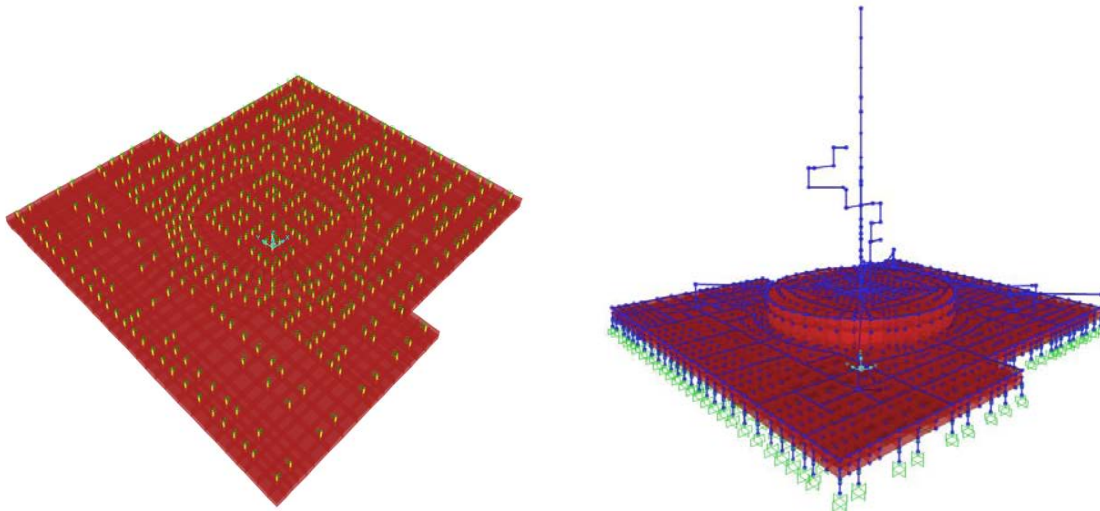


FIG. 13. Perspective of the 486-bearing model.

- (2) Five-bearing equivalent model, in which only five equivalent bearings are used, trying to represent the basic parameters of the isolation system with influence in the translational and rotational response. To obtain the equivalent properties, the 486 bearings are subdivided into five sets of isolators as shown in Figure 14, and then the total stiffness of each set of bearings are substituted by

the stiffness of the corresponding equivalent bearing. The vertical, horizontal, and torsional stiffness of the equivalent bearing is calculated by the following equations:

$$k_v = num_{Iso} \times k_{v,Iso} \quad (2)$$

$$k_{Fy} = num_{Iso} \times k_{h,Iso} \quad (3)$$

$$k_{Fz} = num_{Iso} \times k_{h,Iso} \quad (4)$$

$$k_T = \sum_{i=1}^{num_{Iso}} k_{h,Iso} \times R_i^2 \quad (5)$$

where k_v is the equivalent vertical stiffness; num_{Iso} is the number of bearing; $k_{v,Iso}$ is the vertical stiffness of each bearing; k_{Fy} and k_{Fz} are the equivalent horizontal stiffness; k_T is the equivalent torsional stiffness; $k_{h,Iso}$ is the equivalent horizontal stiffness; and R is the distance between the centre of each bearing and the centroid of all bearings.

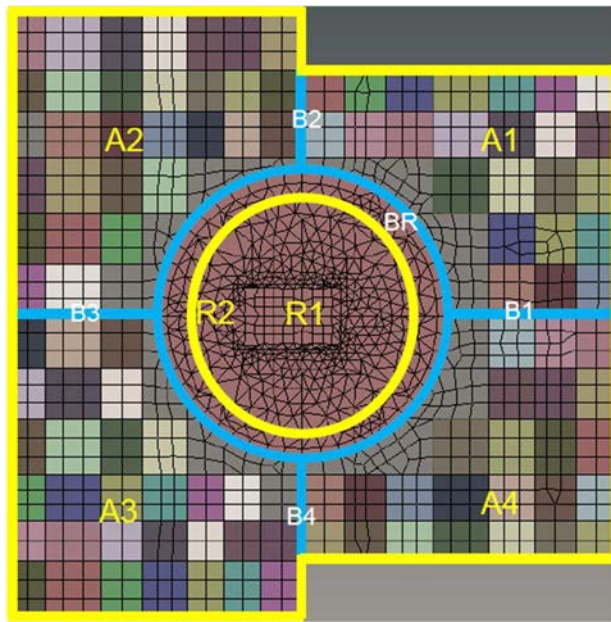


FIG. 14. Tributary areas for the 5-bearing equivalent model.

Figure 15 shows the arrangement of the five bearings representing the actual set of 486 bearings.

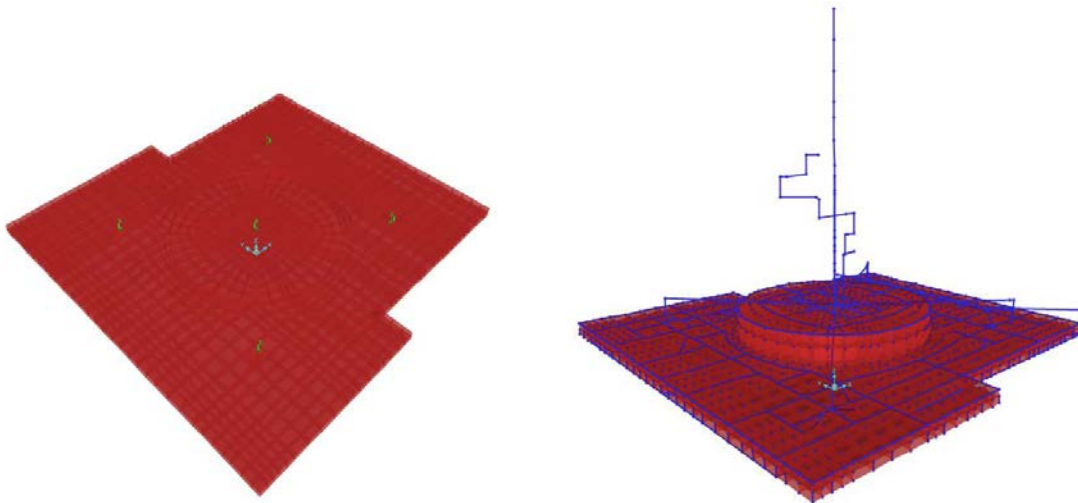


FIG. 15. Perspective of the 5-bearing equivalent model.

The rigid links are connected between the five equivalent bearings and the upper basemat as shown in red lines in Figure 16. Bearing equivalent properties used for model checking purposes and an input file in SAP2000 format (Ref. [23]), “ANT_nonlinear_simple_486to5.s2k”, is included in Annex I.

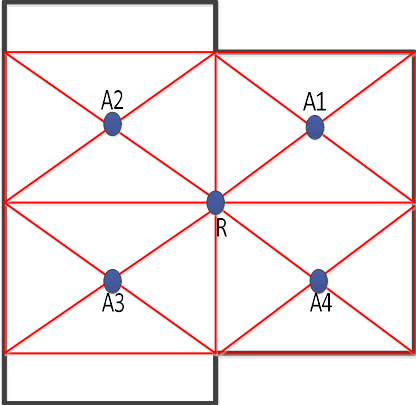


FIG. 16. Connection with rigid links and isolators for the 5-bearing equivalent model.

- (3) One-bearing equivalent model, in which just one bearing is introduced, with the intent of representing mainly the translational response of the system. Figure 17 shows the arrangement of the bearing that represents the actual 486 bearings. The total stiffness of 486 bearings is substituted by the stiffness of the corresponding one equivalent bearing. The same procedure with the five-bearing equivalent model is applied to calculate the vertical, horizontal, and torsional stiffness values for the one equivalent bearing.

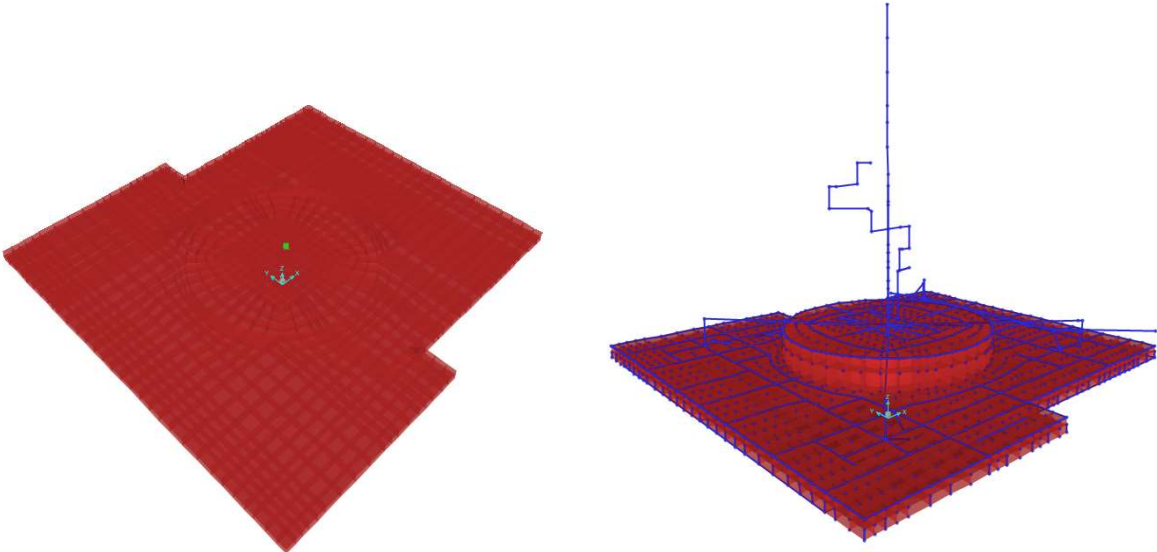


FIG. 17. Perspective of the 1-bearing equivalent model.

The rigid links are connected between the one equivalent bearing and the upper basemat as shown in red lines in Figure 18. One-bearing properties used for model checking purposes and an input file in SAP2000 format (Ref. [23]), “ANT_nonlinear_simple_486to1.s2k”, is included in Annex I.

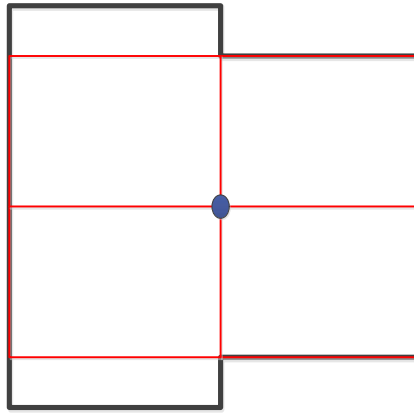


FIG. 18. Connection with rigid links and isolators for the 1-bearing equivalent model.

The modal analysis of the resulting three models was done with the SAP2000 software (Ref. [23]) and the results were supplied to participants with the intent of facilitating their checking of the models to be used for the benchmark analyses. First frequencies in each direction are summarized in Table 6. Figures from 19 through 21 show modal shapes corresponding to these frequencies.

TABLE 6. MODAL ANALYSIS INCLUDING BEARINGS – NATURAL FREQUENCIES

Mode	Frequency (Hz)		
	486 bearing model	Five-bearing model	One-bearing model
1st translational	0.477	0.476	0.476
2nd translational	0.477	0.477	0.476
1st torsional	0.710	0.710	0.710

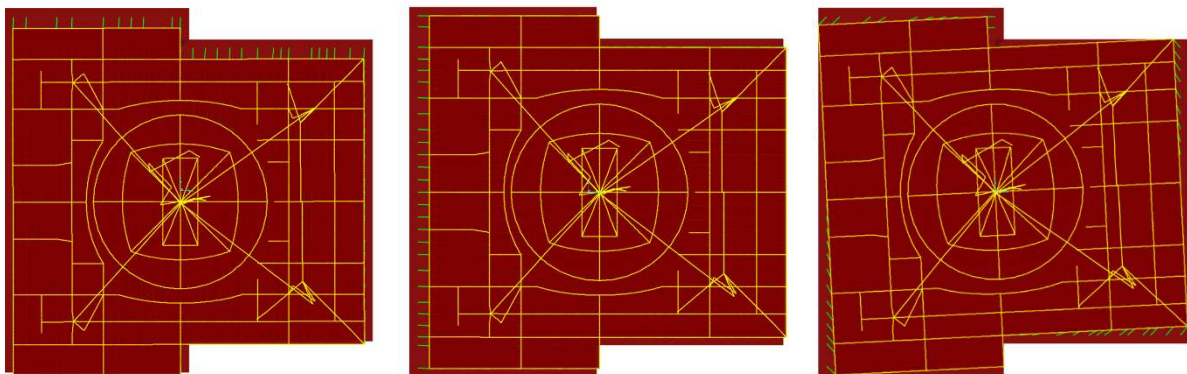


FIG. 19. First mode shapes – ANT model with 486 bearings.

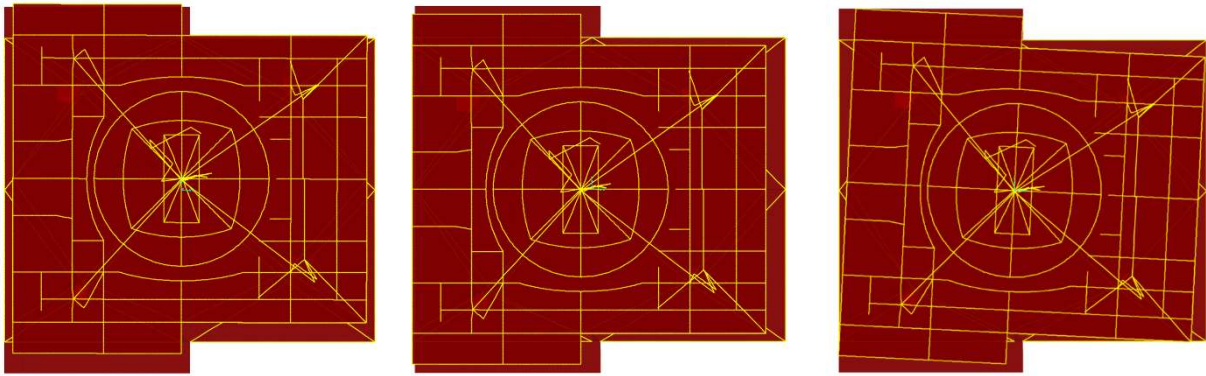


FIG. 20. First mode shapes – ANT model with 5 equivalent bearings.

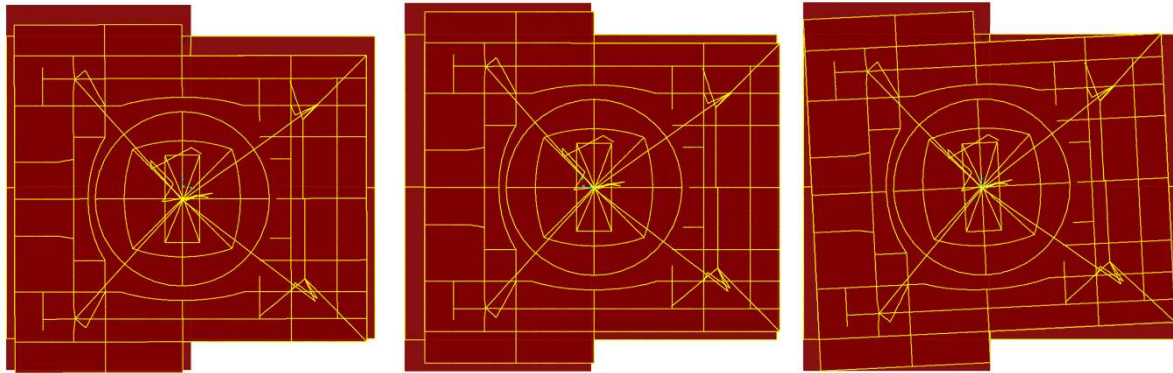


FIG. 21. First mode shapes – ANT model with 1 equivalent bearing.

3.4.1.4 Modelling of damping

Participants were asked to use the Rayleigh approach for modelling of damping, with no mass proportional damping ($\alpha=0$) and stiffness proportional damping (β) computed so that 0.6% damping is obtained at 0.5 Hz.

Participants were asked not to use stiffness proportional damping for the isolators ($\beta=0$ in the isolators).

3.4.2 Isolator properties and models

The following sections gather the information about the isolators that was provided to the participants in the benchmark.

3.4.2.1 Eradi Quake System bearing (EQSB)

The Eradi Quake System bearing (EQSB) consists of a top plate, a lower plate, the centre friction material, MER-springs, and a Polytron disk. Figure 22 shows the layout of these components within the EQSB assembly.

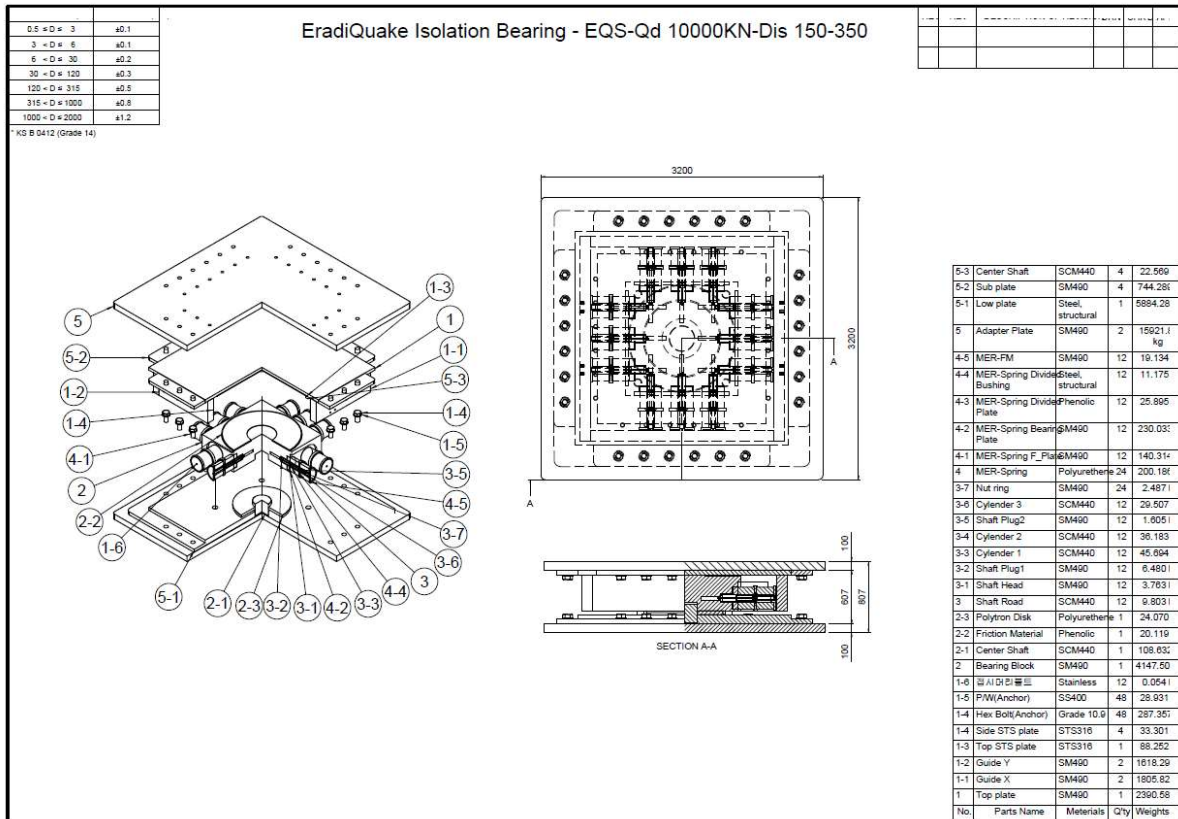
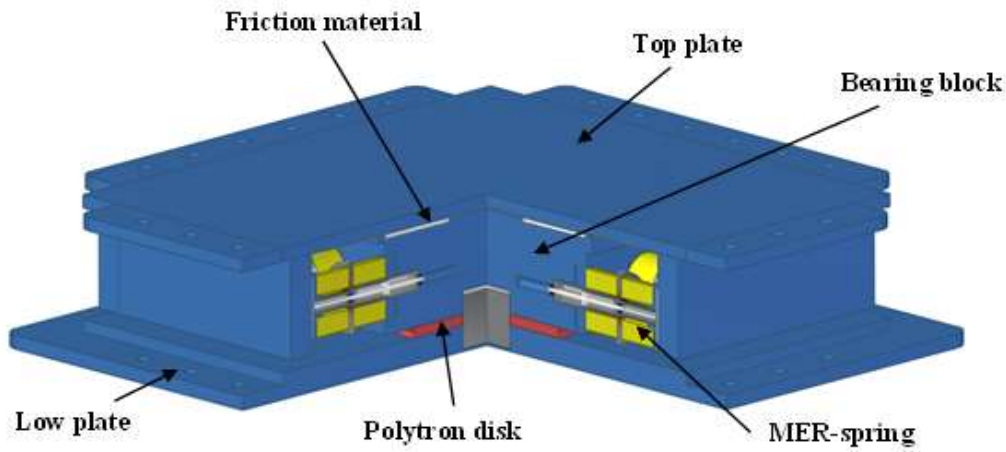


FIG. 22. Components of the EQSB bearing (courtesy of ESCO RTS).

The design vertical stress in the friction material used in the EQSB is 10.29 MPa under a specified 10000 kN vertical load. The top and lower plates are 2900 mm × 2900 mm and the height of whole EQSB is 607 mm. Outer and inner diameters of friction material are 1200 mm and 450 mm respectively. Outer and inner diameters of MER-spring are 240 mm and 90 mm. Length of MER-Spring is 200 mm each. Two MER-springs consist of one module. Total length of MER-spring module is 400 mm. Three MER-spring modules are assembled on side bearing block per side. Outer diameter, inner diameter and height of Polytron disk are 860 mm, 287 mm and 43 mm, respectively. Design shear strain limit (41.5%) of MER-Spring produces a design displacement capacity of 150 mm. Table 7 gives further dimensional parameters of EQSB.

TABLE 7. EQSB BEARING – DIMENSIONAL SPECIFICATIONS

Item	Symbol	Unit	Value
Top plate - transversal	TB	mm	2,900
Top plate - longitudinal	TL	mm	2,900
Low plate - transversal	LB _c	mm	2,900
Low plate - longitudinal	LL	mm	2,900
Overall height of bearing	h	mm	607
Friction material	F-OD	mm	1200
	F-ID	mm	450
MER-spring	M-OD	mm	240
	M-ID	mm	90
	M-H	mm ²	400
	M-n	EA	3
	Divided	EA	2
	Pre-compression	%	4
Polytron disk	Pd-OD	mm	860
	Pd-ID	mm	287
	Pd-H	mm	43

As shown Table 8, the characteristic strength (Q_d) is specified as 1092 kN at 150 mm. Second slope stiffness (K_2) and Effective stiffness calculated by the supplier are 11.56 kN/mm and 18.84 kN/mm respectively. The detailed design characteristics of the EQSB bearing are listed in Table 8. Figure 23 shows the load-displacement hysteresis curve for a maximum horizontal displacement of 150 mm.

TABLE 8. EQSB BEARING – DESIGN PARAMETERS

Displacement	150 mm
Design vertical load	10000 kN
Second slope stiffness (K_2)	11.56 kN/mm
Effective Stiffness (K_e)	18.84 kN/mm
Characteristic strength (Q_d)	1092 kN
Coefficient of friction	0.1092

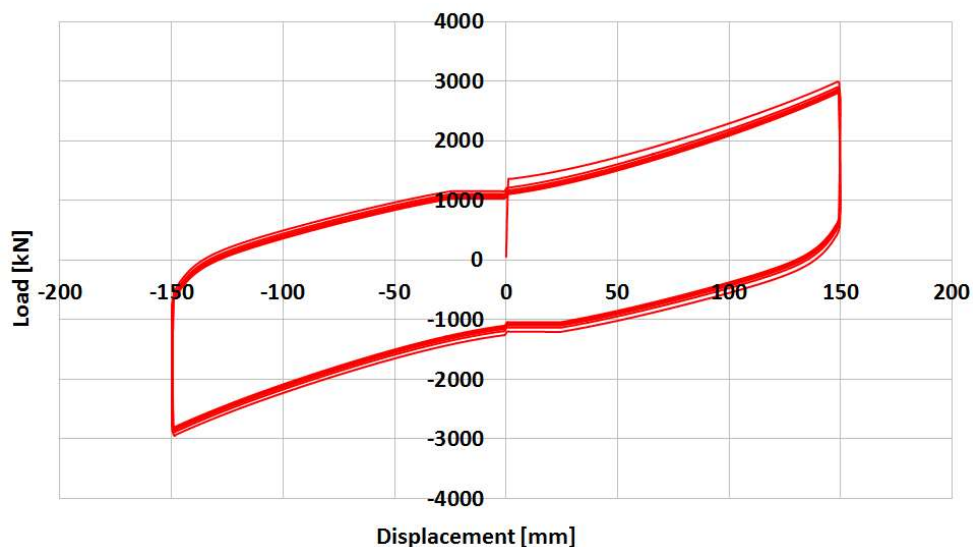


FIG. 23. Load-displacement hysteresis curve for 150 mm horizontal design displacement.

3.4.2.2 Lead Rubber Bearing (LRB)

The Lead Rubber Bearing (LRB) used for the benchmark has a lead core distributed in four cylinders (Figure 24).

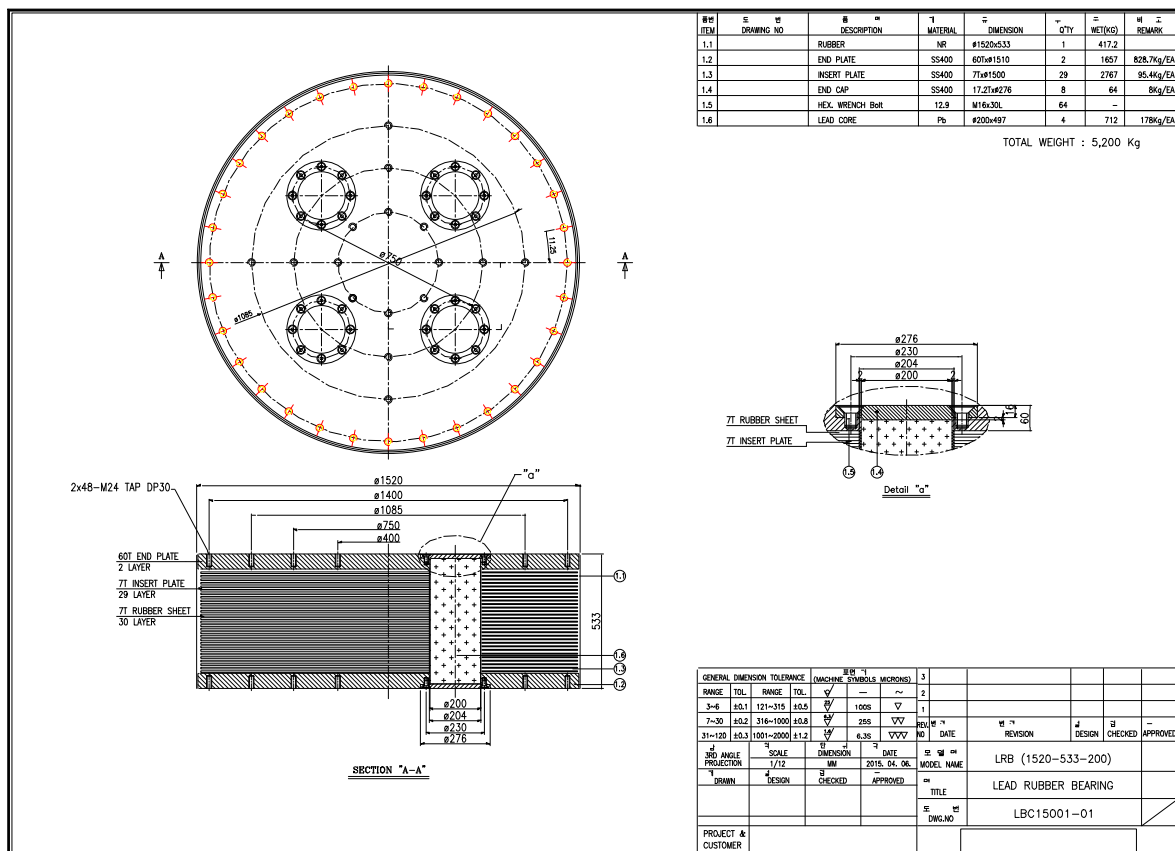
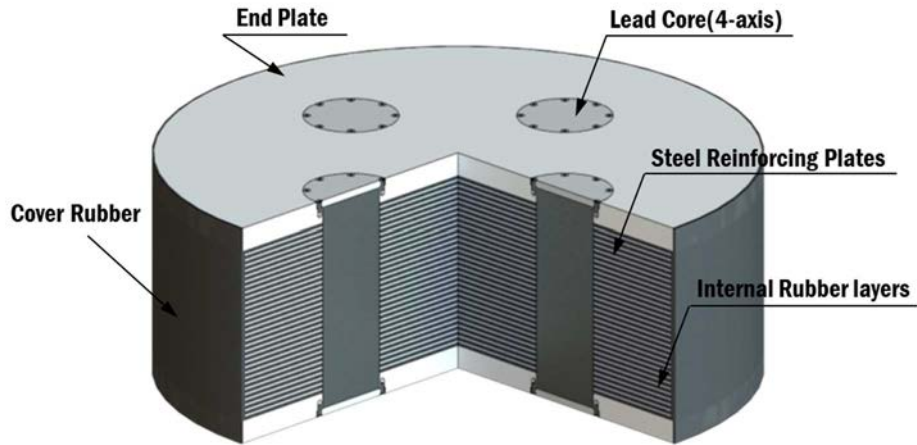


FIG. 24. Components of the LRB bearing (courtesy of UNISON ETECH).

The shear modulus of the LRB bearing is 0.5 MPa under the shear strain of 100% and compressive stress of 13 MPa. The diameter of bearing is 1520 mm, including the 10 mm thickness of cover rubber. Four lead cores with 200 mm diameter are installed inside the bearing as shown in Figure 24. Thirty rubber layers with 7 mm thickness are laminated inside the bearing's body. These are sandwiched between 29 steel plates, also with 7 mm thickness, and 60 mm thick end plates, which form the top and bottom of the bearing. Total height of LRB is 533 mm. Primary and secondary shape factors of LRB are 53.6 and 7.1, respectively. Design displacement corresponding to the design shear strain of 100% is 210 mm. More specifications are listed in Table 9.

TABLE 9. LRB BEARING – DIMENSIONAL SPECIFICATIONS

Item	Symbol	Unit	Value
External diameter	D	mm	1520
Diameter of steel reinforcing plate	D _s	mm	1500
Thickness of cover rubber	T _c	mm	10
Diameter of lead plug	D _p	mm	200
Number of lead core	L _n	-	4
Thickness of rubber	t _r	mm	7
Number of rubber layers	n	-	30
Thickness of total rubber layer	T _r	mm	210
Thickness of steel reinforcing plate	t _s	mm	7
Net sectional area of rubber	A _r	mm ²	1641482
Area of lead core	A _p	mm ²	125664
Primary shape factor	S ₁	-	53.6
Secondary shape factor	S ₂	-	7.1
Thickness of end plate	t _e	mm	60
Total height of bearing	H	mm	533

As shown Table 10, the characteristic strength (Q_d) is specified as 1001.77 kN. Initial stiffness (K_1) and second slope stiffness (K_2) calculated by the supplier are 544.93 kN/mm and 4.20 kN/mm, respectively. The other design parameters are listed in Table 10. Design shear force-displacement bilinear curve is shown in Figure 25.

TABLE 10. LRB BEARING – DESIGN PARAMETERS

Design characteristics (20°C, $\gamma=100\%$)	
Vertical stiffness (K_v)	12896 kN/mm
Initial stiffness (K_1)	544.93 kN/mm
Second slope stiffness (K_2)	4.20 kN/mm
Characteristic strength (Q_d)	1001.77 kN
Equivalent stiffness (K_{eq})	8.97 kN/mm
Equivalent damping ratio (H_{eq})	0.335

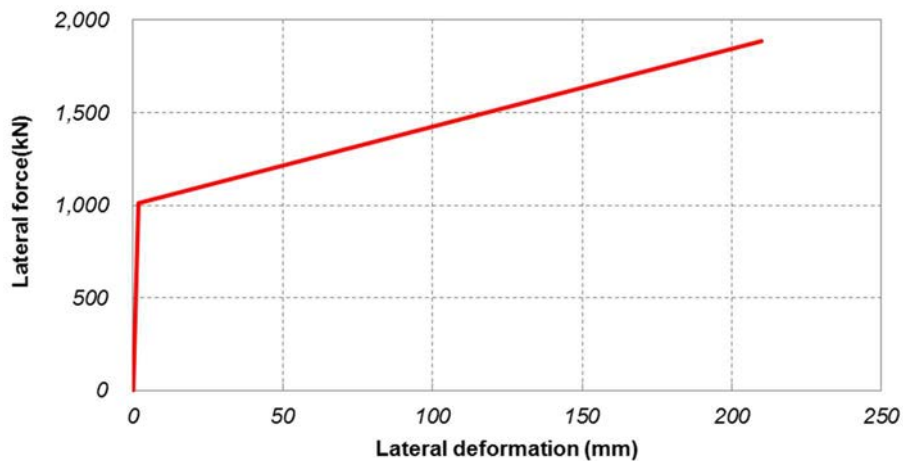


FIG. 25. LRB lateral load-displacement curve (computed by supplier).

3.4.2.3 Triple Pendulum Friction Bearing (TPFB)

The Triple Pendulum Friction Bearing (TPFB) used for the benchmark contains four pendulum systems working in series on four sliding surfaces (upper outer, upper inner, lower outer, lower inner), as seen in Figure 26. The device is made of carbon steel. The sliding concave dishes are lined with stainless steel and Teflon (PTFE) liners coat the convex sliders.

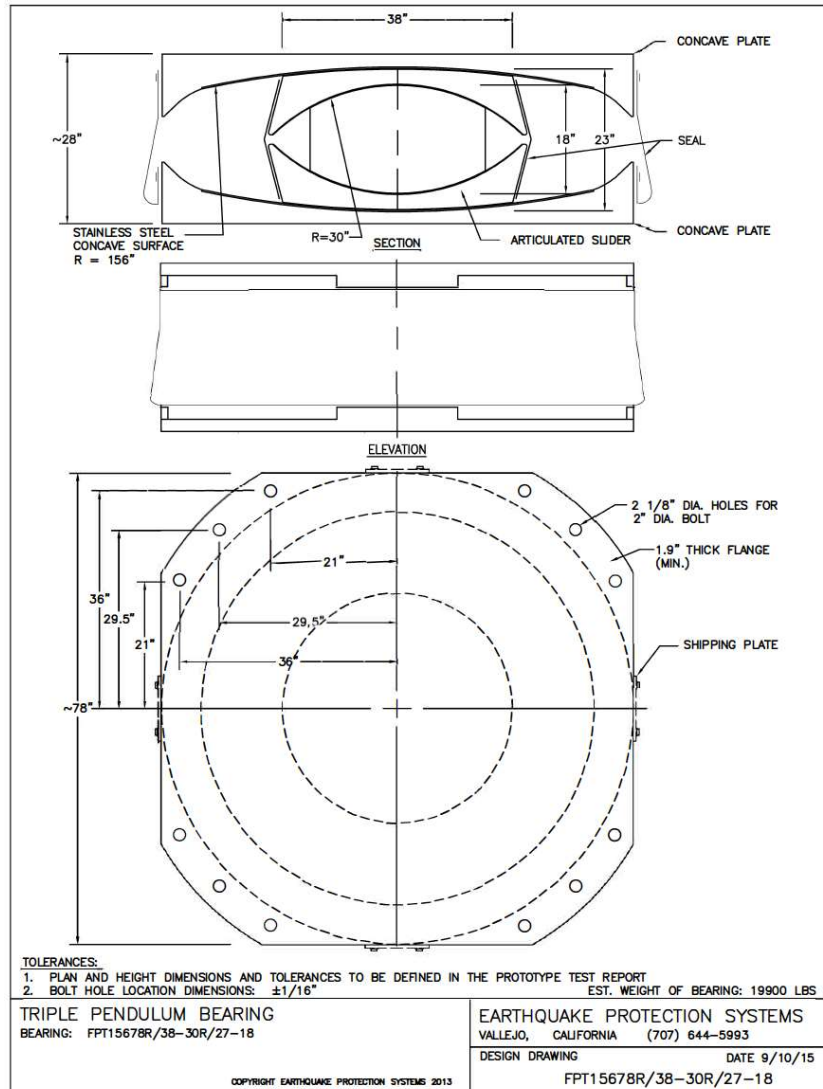


FIG. 26. TPFB production specifications (courtesy of EPS).

The geometric and mechanical properties of the bearing are summarized in Table 11. The bearing is about 2×2 m, with a height of 711 mm.

TABLE 11. TPFB GEOMETRIC AND MECHANICAL PROPERTIES (PROVIDED BY MANUFACTURER)

Geometric Properties		Mechanical Properties	
Radius (outer concave)	3962 mm	Coefficient of friction (inner surface)	2%
Radius (inner concave)	762 mm	Coefficient of friction (outer surface)	9%
Diameter (outer concave)	1981 mm	Characteristic strength (Q_d)	780 kN
Diameter (inner concave)	965 mm	Second slope stiffness (K_2)	1.33 kN/mm
Total height	711 mm		

Multilinear horizontal force-displacement behaviour can be achieved with this bearing because sliding occurs on different sliding surface combinations at different horizontal displacement ranges, as illustrated in Figure 27. The hardening stage provides a “soft stop” mechanism with additional horizontal displacement and shear capacity for the bearing. Unlike the traditional TPFB bearing, the hardening is achieved by yielding of a specially designed steel lip on the perimeter of the inner slider when it moves onto the stiffening stage of the concave sliding dish. This results in a more gradual hardening behaviour and more energy dissipation upon unloading.

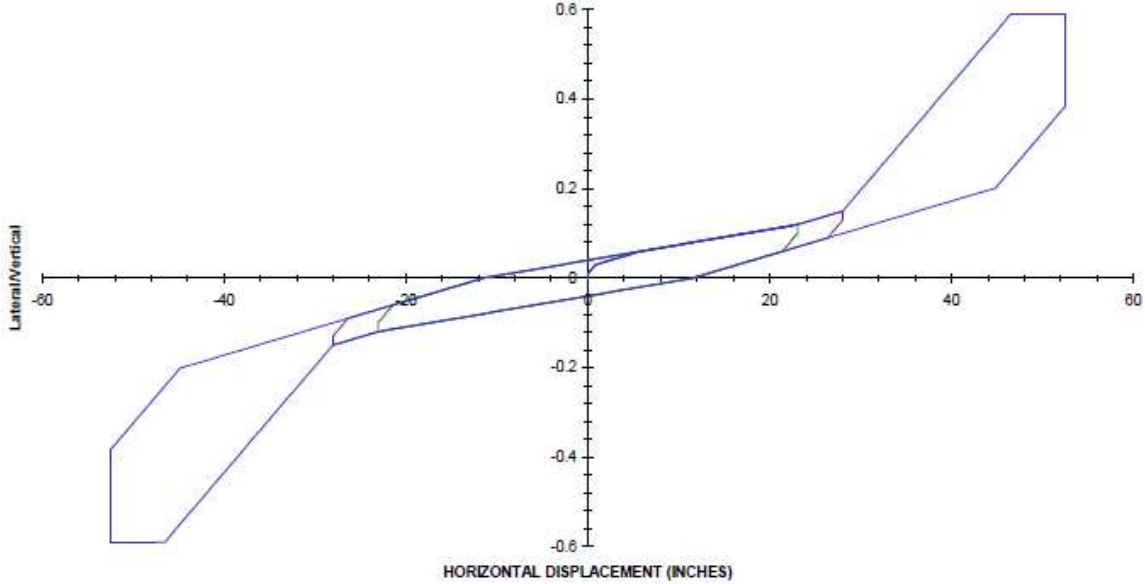


FIG. 27. Multilinear horizontal force-displacement behaviour in a TPFB (computed from geometry)

For the specific configuration of the TPFB utilized in this program, the design displacement was 584 mm. A quality control test was conducted by the manufacturer with an axial load of 11150 kN. The horizontal force-displacement relation from the quality control test is shown in Figure 28.

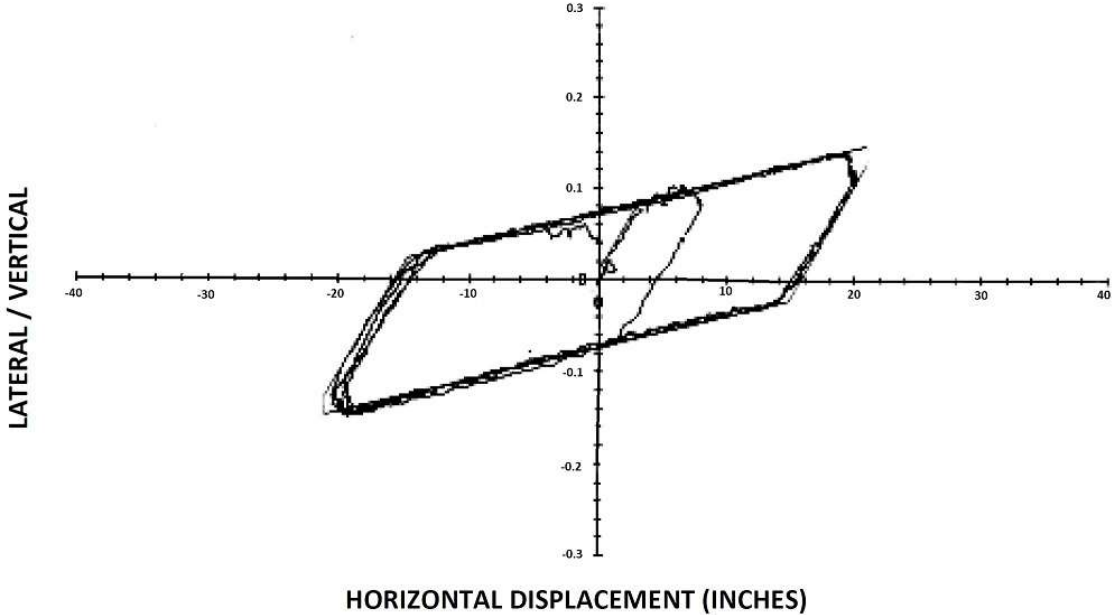


FIG. 28. TPFB manufacturer quality control test results for the horizontal force-displacement behaviour.

3.4.3 Seismic motion

3.4.3.1 Spectral shapes

Two broad band spectral shapes were given in the benchmark specification, the shape of the US-NRC Regulatory Guide 1.60 (Ref. [24]), shown in Figure 29, and the shape of the European Utility Requirements (EUR) 2.4.6 for hard soil (Ref. [25]), shown in Figure 30.

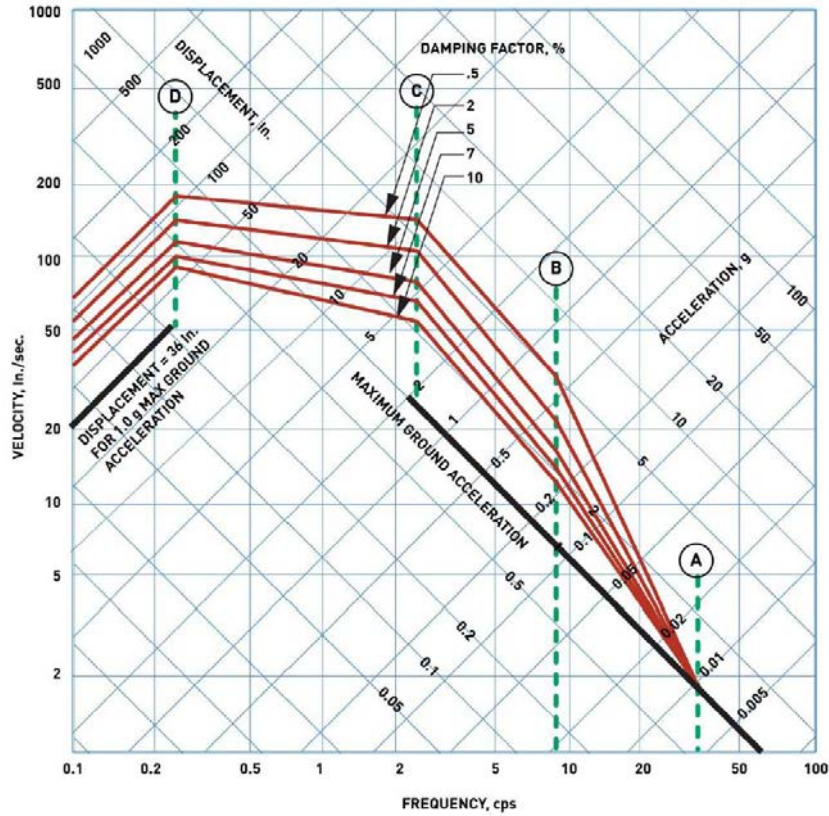


FIG. 29. Spectral shape of US-NRC RG 1.60 – Horizontal motion (Ref. [24]).

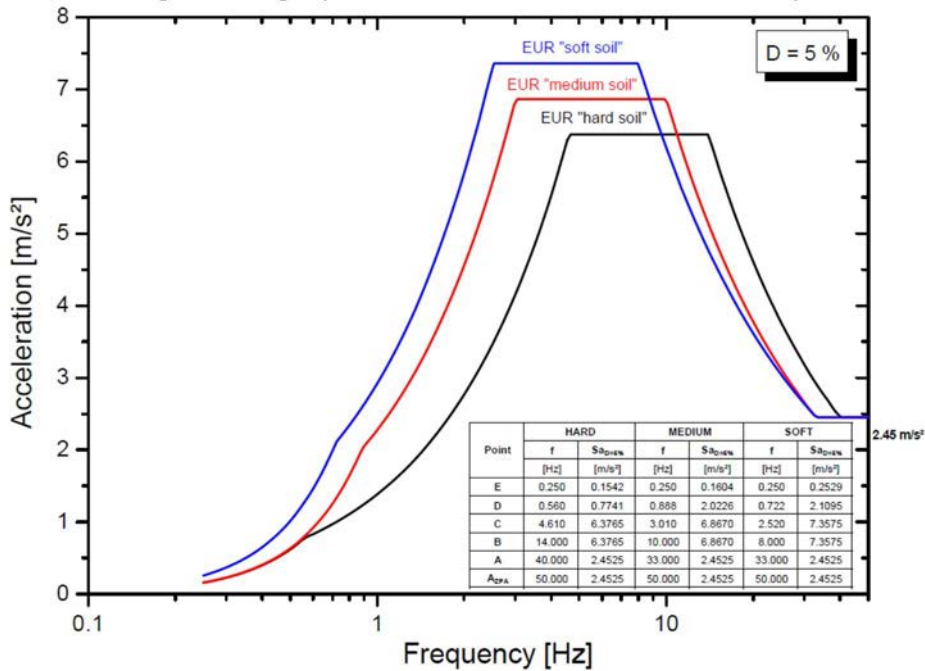


FIG. 30. Spectral shapes of EUR 2.4.6 – Horizontal motion (Ref. [25]).

These two references define the spectral shapes both for horizontal and for vertical motion. Both needed to be considered, since the computations needed to take into account the three-dimensional nature of the ground motion.

3.4.3.2 *Ground motion levels*

The Design Basis Earthquake (DBE) of the isolation system was assumed to be at a peak ground acceleration of 0.50 g, in both horizontal and vertical directions, and two ground motion levels were considered for the benchmark:

- Motion at the design level earthquake (DBE);
- Motion at 1.67 times the design level earthquake ($1.67 \times \text{DBE}$).

3.4.3.3 *Time history generation*

For each type of spectral shape (RG 1.60 and EUR hard soil) a set of three statistically independent acceleration time histories XYZ matching the spectra at the DBE level was obtained using appropriate real earthquake records as seeds. Resulting acceleration time histories are shown in Figure 31 and Figure 32. Acceleration time histories supplied to the participants are included in Annex I.

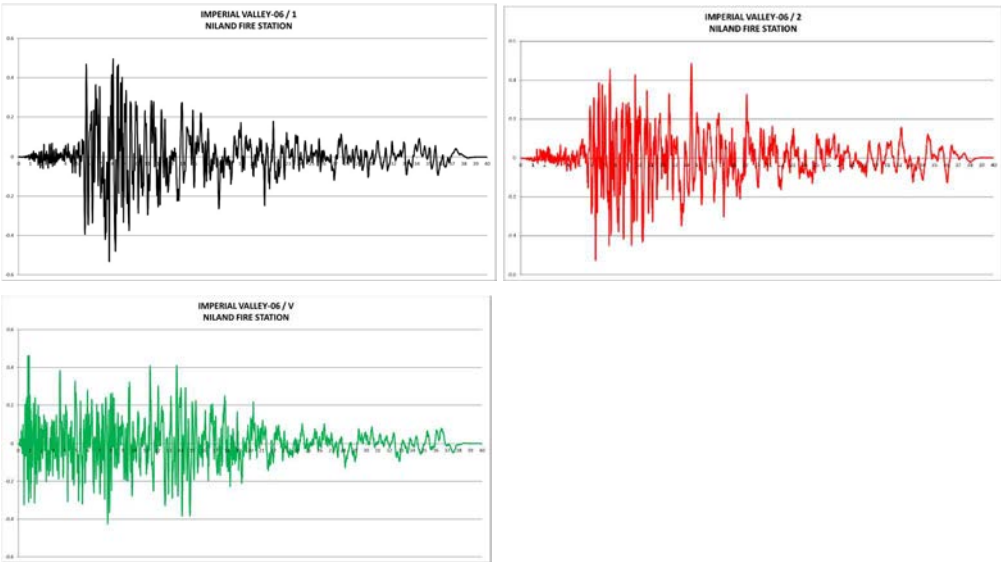


FIG. 31. Acceleration time histories matching RG 1.60 spectra at DBE level (units in g and seconds).

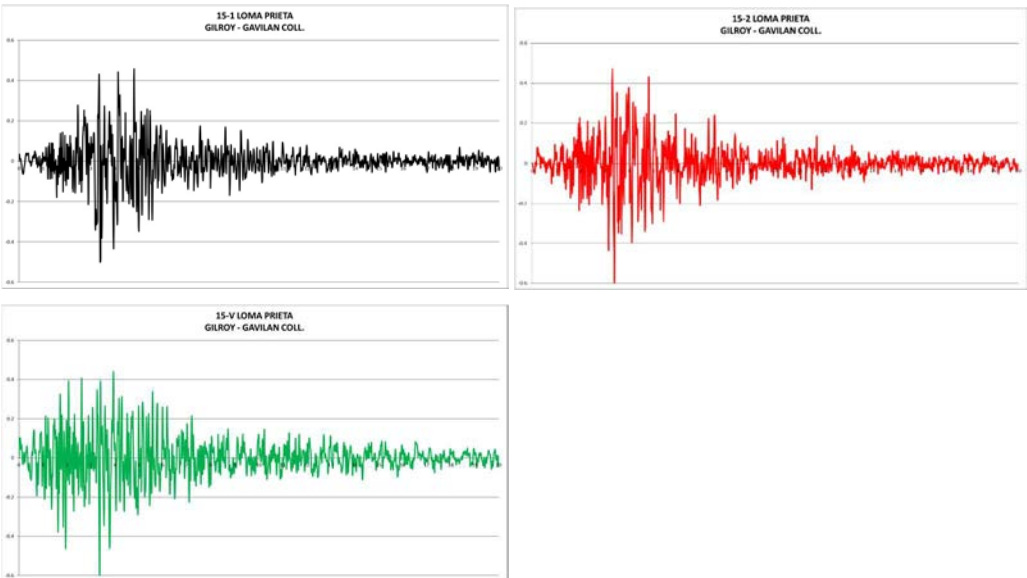


FIG. 32. Acceleration time histories matching EUR spectra at DBE level (units in g and seconds).

3.4.4 Required output

The participants were requested to describe the computational models and to give their basic dynamic parameters: total mass, position of centre of gravity, inertia tensor, natural frequencies and mode shapes, participation factors, etc. The participants were also requested to provide the details of the mathematical model used to represent the behaviour of the isolators and the procedure used for integration of the equations of motion.

Responses obtained from the analyses were requested at the following locations, for comparison with the hybrid test results. At each location, absolute acceleration and relative displacement time histories (three components), together with the floor response spectra were requested.

- Centre of upper basemat (node #24718)
- One corner of upper basemat (nodes #25270, #24189, #24275, #25235)
- Top of internal structure at RCB (node INM13)
- Top of containment at RCB (node #6715)
- Top of ACB (node AM8)
- Bearing response
 - 486 bearing model: element #253, i-node #23939, j-node #24718
 - 5-bearing equivalent model: element #5, i-node #13079, j-node #24718
 - 1-bearing equivalent model: element #1, i-node #13079, j-node #24718
- Shear force – lateral displacement hysteresis (2 components)
 - 486 bearing model: element #253, i-node #23939, j-node #24718
 - 5-bearing equivalent model: element #5, i-node #13079, j-node #24718
 - 1-bearing equivalent model: element #1, i-node #13079, j-node #24718
- Axial force – axial displacement hysteresis
 - 486 bearing model: element #253, i-node #23939, j-node #24718
 - 5-bearing equivalent model: element #5, i-node #13079, j-node #24718
 - 1-bearing equivalent model: element #1, i-node #13079, j-node #24718
- Horizontal displacement orbits (node #24718)

At each location, absolute acceleration and relative displacement time histories (three components) were requested. Floor response spectra at each location were also requested. Figure 34 shows the locations of nodes to obtain the requested output at the basemat, reactor building internal structure, RCB, and ACB.

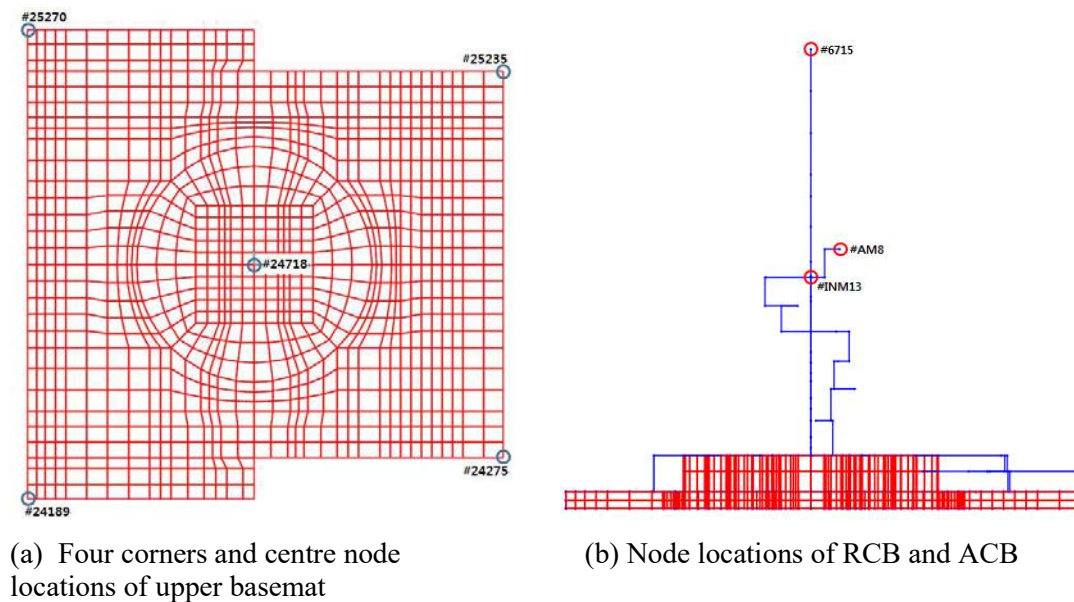
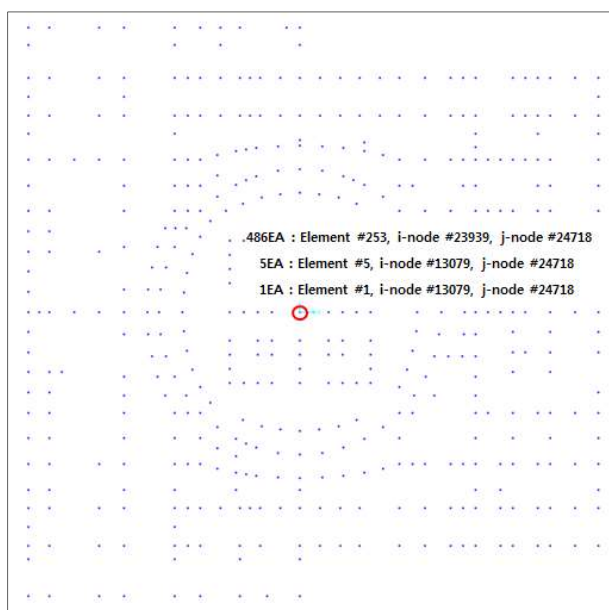


FIG. 33. Locations of nodes to obtain output.



(c) Node locations of three bearing models

FIG. 34. Locations of nodes to obtain output (Continued)

3.4.5 Matrix of benchmark analyses

As a result of the different alternatives described in the previous sections, Table 12 gives the matrix of analyses for each type of isolator. Numbers and colours give the order of priority given to participants (red colour meaning highest priority, white meaning lowest priority).

TABLE 12. MATRIX OF ANALYSES FOR EACH TYPE OF ISOLATOR

Seismic Motion	Computational Model		
	1 equivalent bearing	5 equiv. bearings	486 bearings
DBE – RG 1.60	Case 1	Case 3	Case 5
1.67 DBE – RG 1.60	Case 2	Case 4	Case 6
DBE - EUR	Case 7	Case 9	Case 11
1.67 DBE - EUR	Case 8	Case 10	Case 12

4 NUMERICAL APPROACHES AND RESULTS BY PARTICIPANTS

4.1 COMPUTATIONAL APPROACHES AND MODELS

The present section gives an overview of the different strategies adopted by benchmark participants for modelling the superstructure, modelling the isolation systems and running the analyses.

4.1.1 Superstructure models

The ANT super structure model was provided to all participants as node coordinates, lumped masses and section properties, as described in Section 3. Each participant was then free to reconstruct the super structure model in the calculation environment of his/her choice. Besides, participants were also provided some ready-to-use SAP2000 scripts to generate the super-structure model.

Table 13 summarizes the environments that were selected by the participants to build the super-structure finite element model, as well as the modelling hypotheses that were made to represent the basemat.

TABLE 13. MODEL CONSTRUCTION ENVIRONMENT

	P0	P1	P2	P3	P4	P5	P6	P7	P8
Software	OPENSEES	OPENSEES+MATLAB	ANSYS+MATLAB	SAP2000	ABAQUS	SAP2000	SAP2000	OPENSEES	SAP2000
Basemat modelling hypothesis	Large equivalent beams for different zones	2*6-degree of freedom equivalent system	Fully rigid	SAP2000 model with increased stiffness	Fully rigid	Original SAP2000 model	Original SAP2000 model	SAP2000 model with increased stiffness	Original SAP2000 model

All participants but P2 decided to use the SAP2000 model as input. Among those, several participants changed the representation of the basemat, some for calculation efficiency purposes and some after realizing that the SAP2000 basemat model was not rigid enough for not interfering with the building modes:

- Participant P0, who developed the model used in the hybrid testing, used different basemat models depending on the number of isolators modelled. A detailed description of the modelling hypotheses is given in Section 5.4.
- Participant P1 represented the basemat as two connected rigid parts with 6 degrees of freedom each. The first is the central part, supporting the reactor building internal structures and RCB, and the second is the peripheral part, supporting the auxiliary building. The mass and inertia associated with the two rigid parts as well as the stiffness between them are obtained by static condensation of a 3D basemat model into a 12×12 matrix super element. This basemat model is illustrated in Figure 35.
- Participants P2 and P4 defined the basemat as a rigid body with only 6 degrees of freedom.
- Participant P3 kept the original basemat elements but multiplied their Young modulus by 1000, so as to make fully rigid.
- Participant P7 kept the original basemat elements but added some stiffening massless beams to the model.

Participants P5, P6 and P8 used the initially provided model, without stiffening the basemat.

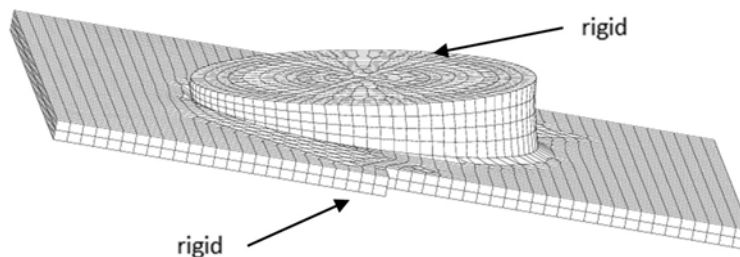


FIG. 35. Participant P1 – 2 x 6 degrees of freedom representation of the basemat.

Participant P1 represented all buildings using dynamic super elements containing their modal basis and connected to the basemat. The use of super elements increases the calculation efficiency and allows the use of modal damping instead of a truncated Rayleigh damping. Since a truncated Rayleigh damping was specified as input data for the benchmark, participant P1 could not benefit from this possibility. None of the other participant used such projection on modal basis.

As presented in Section 3, in order to check the adequacy of the models used by participant before the introduction of the isolation system, the results of a modal analysis of the superstructure alone was provided within the benchmark specification package. This modal analysis was conducted with the base of the stick models representing the superstructure fixed. As illustrated in Table 14, all but participant P4 obtained very similar modal analysis results.

TABLE 14. NATURAL FREQUENCY RESULTS OF FIXED BASE MODAL ANALYSES (IN Hz)

	P0	P1	P2	P3	P4	P5	P6	P7	P8
RCB 1st mode X	3.73	-	3.68	3.71	3.83	3.71	3.71	3.71	3.86
RCB 1st mode Y	3.73	-	3.68	3.71	3.83	3.71	3.71	3.71	3.86
ACB 1st mode X	5.85	-	6.04	6.05	8.70	6.05	6.05	6.05	6.13
ACB 1st mode Y	5.48	-	5.73	5.65	7.50	5.65	5.65	5.65	5.72
IS 1st mode X	9.96	-	9.95	9.88	11.17	9.87	9.87	9.87	10.35
IS 1st mode Y	11.50	-	11.29	11.45	10.30	11.45	11.45	11.45	11.63

As a conclusion concerning the superstructure, all but one participant seems to have equivalent models of the three different buildings, at least concerning their dynamic behaviour in the horizontal directions, but some non-negligible differences exist in the different basemat representation that were adopted by the different participants. Such differences may affect the vertical and the rocking behaviour of the complete superstructure.

4.1.2 LRB isolation system models

A Lead Rubber Bearing (LRB) model was developed by all participants to the benchmark.

The dynamic behaviour of an LRB being very non-linear, it is generally defined based on characterisations tests, such as the ones described in Section 5.3.

Numerical models are then calibrated to represent the characterization test results as closely as possible. This work was performed by participant P0, when developing the isolators numerical model used in hybrid simulation tests with 5 or 486 bearings.

For all other participants, this calibration was not performed. Indeed, it was decided to evaluate the participants capacity to predict the LRB system behaviour without allowing them to calibrate their models on characterisation tests results. It was up to the participant to define their LRB model behaviour. Manufacturer's data, as described in Section 3, were used as input. The single exception to this rule was the use by participants P1 and P2 of a vertical stiffness value different from the one given by the manufacturer. This decision was made because the discrepancy between the manufacturer's value and the characterization tests results was found to be very significant on the simulation results in the vertical direction.

Different LRB isolation system models were used by participants, with various degrees of complexity. In general, an LRB model is designed to represent the bearing dynamic behaviour in both the horizontal and vertical directions. In the horizontal direction, a LRB expected behaviour can be summarized as follows:

- Linear domain. For very limited distortion, corresponding to shear stresses in the lead core(s) lower than its yielding value, the bearing behaves linearly, with reaction forces proportional to its in-plane horizontal distortion. The bearing apparent stiffness is then mainly the one of the lead in shear, with a small contribution of the rubber in shear.
- Lead yield domain. As the lead core(s) material progressively reaches its yield value, a change of apparent stiffness is observed on the force-distortion curve representative of the bearing behaviour. The occurrence of yield is due to simultaneous distortions in both horizontal directions. Beyond the yielding point, the lead deforms without significant increase of associated yield force. The bearing force-displacement slope in the direction of maximum distortion is then mainly defined by the rubber stiffness in shear, which remains roughly constant in this domain.

- Rubber hardening domain. For extreme bearing distortion, the rubber compound hardens, leading to slope increase on the bearing forces-displacement curve, before the ultimate bearing break distortion is reached.

Additionally, three types of effect can influence the LRB horizontal behaviour:

- Load cycling effect. With increased number of distortion cycles, the lead core(s) heats up as it dissipates energy. Although some energy can be conducted away from the lead through the metallic shim plates in the laminated rubber, most of it remains trapped in the yield for the duration of the earthquake. This increase of temperature has the effect of reducing the apparent yield force for the bearing.
- Compressive load effect. When submitted to high compressive stresses, the rubber apparent shear stiffness is reduced, eventually going to zero for a compressive stress equal to its buckling stress
- Scragging effect. The apparent stiffness of an LRB bearing is sometimes observed to be higher for the first load cycle than for the following ones. This happens due to additional connections that build up in the rubber compound with time and which are broken during the first loading cycle.

In the vertical direction, the lead core(s) is (are) not supposed to play a role and the LRB expected behaviour can be described as follows:

- In compression: the isolator behaviour is expected to be roughly linear and defined by the rubber layers stiffness in compression.
- In tension with small deformations: the isolator behaviour is expected to be roughly linear and defined by the rubber layers stiffness in tension.

Additionally, two types of effect can influence the LRB vertical behaviour:

- Shear distortion effect on vertical compressive stiffness. As the bearing is distorted in the horizontal plane, the effective rubber section resisting vertical loads is reduced and the apparent vertical stiffness is reduced as well.
- Cavitation effect on tension behaviour. As the rubber reaches its cavitation limit, either for the whole bearing area in pure tension or for a localized tensioned area in shear-tension, micro-cracks form in the rubber material leading to a steep reduction of apparent tensile stiffness. This effect is non-reversible: once the micro-cracks have appeared, the tension apparent stiffness is reduced even for tension deformation smaller than the ones originally necessary to initiate the cracking.

Table 15 synthesizes the participants modelling choices concerning the representation of the LRB isolation system for the benchmark. The column corresponding to participant P0 relates to the modelling adopted for the numerically simulated isolators for the hybrid test cases where part of the isolation system was simulated.

TABLE 15. LRB ISOLATION SYSTEM MODELS

	P0	P1	P2	P3	P4	P5	P6	P7	P8
Shear behavior	Bouc-Wen model	Elasto-plastic model	Bouc-Wen model	Bouc-Wen model	Unidirect bilinear model	Bouc-Wen model	Bouc-Wen model	Elasto-plastic model	Bouc-Wen model
Rubber hardening	None	None	None	None	None	None	None	None	None
Cycling effect	Kalpakidis model	Kalpakidis model	Kalpakidis model	None	None	None	None	None	None
Compression effect	Kumar et al model	Kumar et al model	Kumar et al model	None	None	None	None	None	None
Scragging effect	None	None	None	None	None	None	None	None	None
Compression stiffness	Non-linear test-fitted value	Linear - updated values	Linear - updated values	Linear - original values					
Tension stiffness	Linear - updated values	Linear - updated values	Linear - updated values	Linear - original values					
Shear distort. effect	Warn et al model	Warn et al model	Warn et al model	None	None	None	None	None	None
Effect of cavitation	Kumar et al model	Kumar et al model	Kumar et al model	None	None	None	None	None	None

All participants represented the pre- and post-yield shear behaviour of LRB under shear distortion, most of them using an elastoplastic model and participants P0 and P2 using Bouc-Wen model (Ref. [26]). Participant P4 used a bilinear model acting separately in X and Y directions. Hysteresis curves obtained with pseudo-static unidirectional loading of some participant models are illustrated in Figure 36. In this figure, values for participant P0 are the experimentally observed ones, not the ones resulting from participant P0 numerical model. It is noticeable that the experimental curve does not have exactly the same secondary stiffness as the participants uncalibrated models, which corresponds to the manufacturers value. Still, this difference is not expected to have a very strong impact on the analysis.

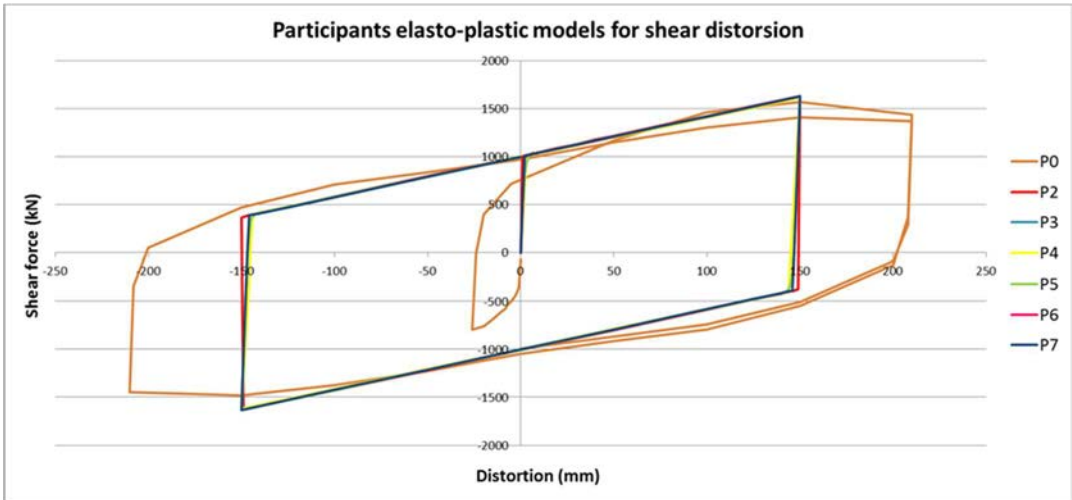


FIG. 36. Elastic-plastic models for LRB used by different participants.

All participant represented tension and compressive stiffness by a linear model except participant P0, who fitted a non-linear model on experimentally observed force-compression curves. For participants P3, P4, P5, P6, P7 and P8, the vertical stiffness was based on the compressive stiffness provided by the manufacturer (12896 kN/mm). For participants P0, P1 and P2, the vertical stiffness was adapted to the one measured during the characterization tests (5100 kN/mm).

Participants P0, P1 and P2 represented:

- The compressive effect on LRB shear stiffness according to Kumar et al model (Ref. [27]). Figure 37 illustrates the hysteresis loop modification resulting from application of vertical loads with this model.
- The lead core(s) heating with repeated load cycle using the Kalpakidis model (Ref. [28]). Figure 38 illustrates the hysteresis loop modification resulting from repeated cycles with this model.
- The cavitation effect based on Kumar et al model (Ref. [27]). Figure 39 illustrates the behaviour of this model, with effective stiffness reduction after the first onset of cavitation and further reduction as more axial deformation is observed.
- The shear distortion effect on compressive stiffness based on Warn et al model (Ref. [29]).

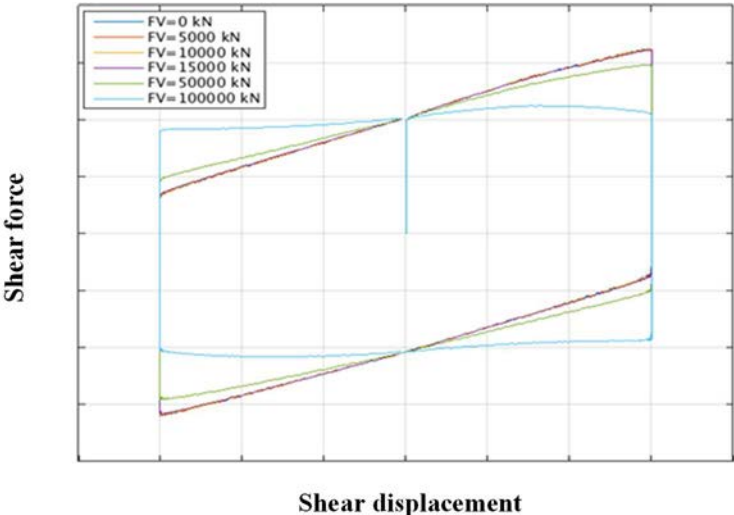


FIG. 37. Illustration of application of Kumar et al model to represent compressive stress effect on the rubber shear stiffness - Model of participant P2.

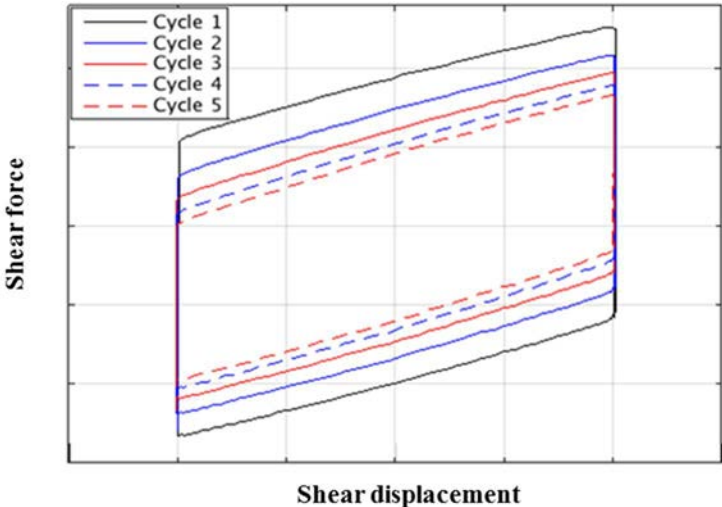


FIG. 38. Illustration of application of Kalpakidis model to represent heating effect on the lead core(s) yield strength - Model of participant P2.

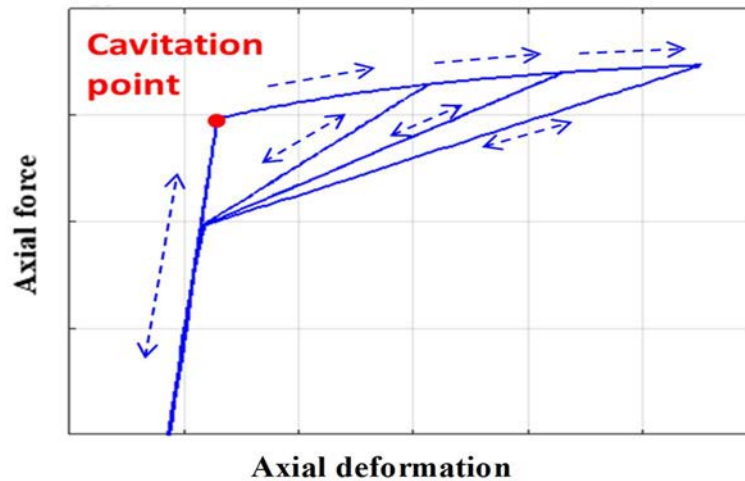


FIG. 39. Illustration of application of Kumar et al model to represent cavitation in tension - Model of participant P2.

Other participants did not include these effects in their model.

None of the participants represented rubber hardening effect. This is understandable since the prescribed benchmark loadings are not expected to distort the rubber so much as to reach the rubber hardening domain. None of the participants represented the scragging effect, which was considered to have negligible influence on the analysis results.

4.1.3 EQSB isolation system models

The EQSB system was modelled by three participants: P3, P5 and P7.

As for LRB system, the behaviour of the EQSB system is fundamentally non-linear and generally requires a calibration based on characterisation test results, as presented in Section 5.3. Participant P0 performed such a calibration when defining its EQSB model for use in the hybrid simulation tests with 5 or 486 bearings. Other participants were not allowed to calibrate their model for the present benchmark and therefore simply relied on values provided by the manufacturer. One exception to this rule is the adaptation by participant P7 of its vertical isolator stiffness to the experimentally observed one, whereas other participant simply considered the bearings as rigid in the vertical direction.

As for the LRB, it was up to the participant to define their EQSB model behaviour. In practice, the behaviour of such isolator could be summarized as follows:

- Shear linear domain. For a very limited horizontal force applied to the bearing, the friction forces are not overcome and the bearing stiffness is high and defined by the stiffness of its constitutive parts.
- Horizontal sliding domain. Once the horizontally applied force exceeds the friction forces, sliding occurs and dissipate energy. The equivalent stiffness of the bearing is then defined by the compressive stiffness of the MER springs.
- Springs hardening in sliding domain. The “secondary stiffness” of the EQSB bearing, which is activated when it starts sliding, is not fully linear. The further the MER springs are compressed, the stiffer they behave.
- Horizontal friction dependency on the vertically applied loads. The friction forces themselves are dependent on the equivalent friction coefficient between the bearing block and the top plate and on the vertically applied load on the bearing. Variation of vertically applied load on the bearing produces significant variation of the force-displacement curves in the horizontal direction as well.

- Horizontal friction dependency on variation of friction coefficient. As studied in the characterization tests, Section 5.3, the coefficient of friction can itself be subject to changes depending on the distortion velocities, the increase of temperature of the friction surface or the vertically applied load.

All participants represented the linear and horizontal sliding domains of the EQSB. The resulting bilinear force-distortion curves are illustrated on Figure 40 for a quasi-static shear loading and with the nominal vertical load applied. From this figure, it appears that the three uncalibrated models of participants P3, P5 and P7 are totally equivalent and present a distinctly higher second stiffness than the one experimentally recorded by participant P0.

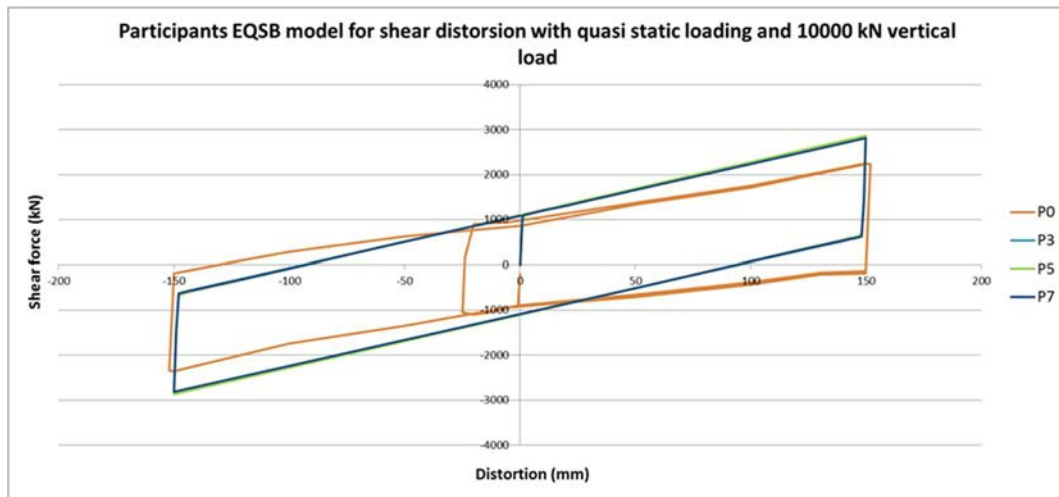


FIG. 40. Shear distortion model for EQSB used by different participants – Static shear loading and nominal vertical load.

Participants P5 represented the horizontal friction dependency on the vertically applied load whereas participants P3 and P7 did not. Figure 41 shows the variations of participant P5 hysteresis loop with variation of vertical loads against those experimentally observed ones. From this figure, it seems that the experimentally observed variation is lower than the one predicted by participant P5 model. Participant P5 model also predicts a change of secondary stiffness with increased vertical load which is not observed in the experiment.

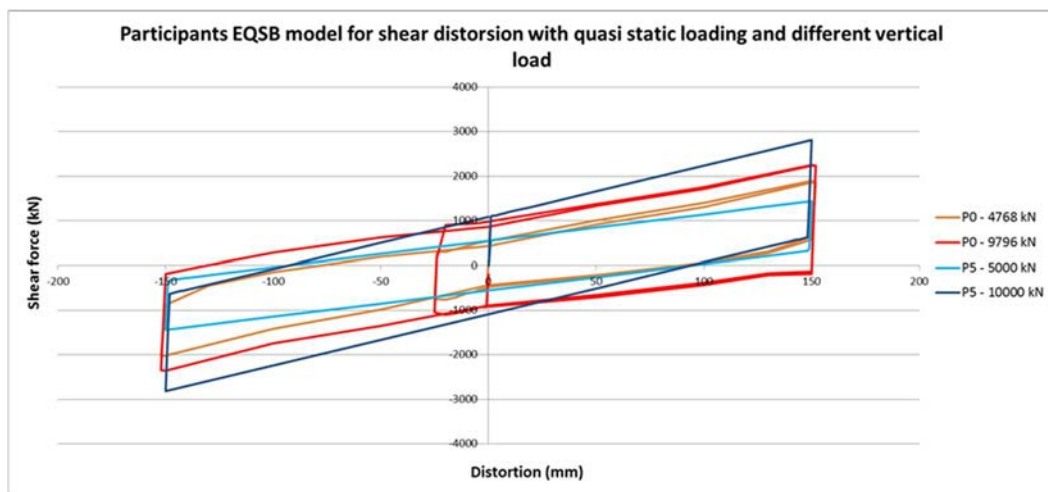


FIG. 41. Shear distortion model for EQSB for participant P5 – Static shear loading and variable vertical load.

Participant P5 further represented a variation of the isolator coefficient of friction with the distortion velocity. Hysteresis curves obtained for quasi-static and 500 mm/s distortion tests are compared with the experimentally observed ones on Figure 42. Participant P5 variation is significantly larger than the experimentally observed one.

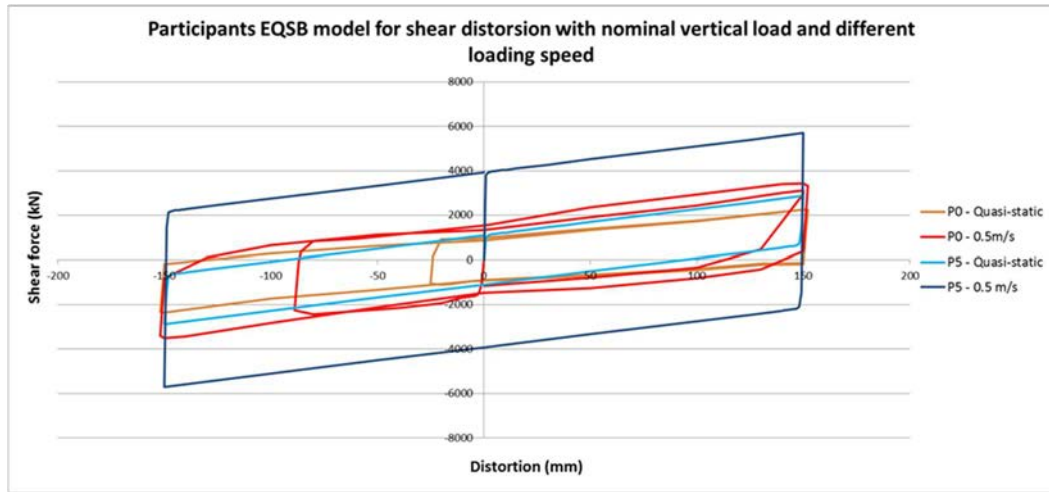


FIG. 42. Shear distortion model for EQSB for participant P5 – Static shear loading and variable loading speed.

None of the participants represented the spring hardening effects.

In the vertical direction, the behaviour of the EQSB system can be summarized as follows:

- Linear domain. As long as the bearing remains under compression, its vertical stiffness is theoretically constant and defined by the stiffness of its different constitutive parts.
- Uplift domain. In the tensile direction, the bearing has theoretically no resistance at all and uplift of the top plate can occur, generating impacts during the following fall back into compression.

For this benchmark, all participants used a simple linear model for the EQSB vertical stiffness, albeit with different stiffness values. As no vertical stiffness value was provided in the benchmark specification, different participants made some very different choices of stiffness values. Participants P0 and P7 chose values that are close or identical to the ones observed in the characterization tests, whereas participants P3 and P5 used some much higher stiffness values.

4.1.4 TPFB isolation system models

The TPFB isolation system was modelled only by participant P5. Its behaviour in the horizontal plane was assimilated to the one of a simple friction pendulum with a bilinear shear force versus displacement curve. The friction coefficient was made dependent on the loading velocity. In the vertical direction, participant P5 model is infinitely stiff.

4.1.5 Time history analyses methods and tools

All participant used direct time integration to determine the isolated structure response to seismic excitation. Different tools were used by the participants.

- SAP2000 was the most widely used tool, being selected by participants P3, P5, P6 and P8,
- OPENSEES was used by participant P7 and by participant P0 for the hybrid simulation testing,
- ABAQUS was used by participant P4,
- In-house tools, both developed on Matlab, were used by participants P1 and P2.

For such very non-linear problem, several participants identified the fact that the use of explicit time integration schemes allowed a much faster time integration process without loss of accuracy.

4.2 COMPUTED RESPONSES FOR LRB ISOLATOR

4.2.1 Available results and selection of representative data

The available results of simulation with the LRB isolation system are identified in Table 16 with Y letters. The case numbers in this table and in the following correspond to those defined in Section 3.4.5. The first column of this table (P0) refers to the available results from the hybrid simulation tests described in Section 5.7.

TABLE 16. AVAILABLE RESULTS FOR LRB ISOLATION SYSTEM

		P0	P1	P2	P3	P4	P5	P6	P7	P8
LRB Isolator	Case 1	Y	Y	Y	Y	Y	Y	Y	Y	Y
	Case 2		Y	Y	Y		Y	Y	Y	Y
	Case 3	Y		Y	Y		Y	Y	Y	Y
	Case 4			Y	Y		Y		Y	
	Case 5	Y	Y	Y	Y		Y		Y	
	Case 6		Y	Y	Y		Y		Y	
	Case 7		Y	Y	Y		Y		Y	
	Case 8		Y	Y	Y		Y		Y	
	Case 9			Y	Y		Y		Y	
	Case 10			Y	Y		Y		Y	
	Case 11		Y	Y	Y		Y		Y	
	Case 12		Y	Y	Y		Y		Y	

For each case, the available time history results consist in absolute or relative displacements, absolute or relative accelerations and forces in the central isolator. These raw results were post-processed so as to produce:

- Displacement of the upper basemat relative to the ground at central node (N24718) and corner nodes (N25270, N24189, N24275, N25235);
- Floor response spectra at the upper basemat central node (N24718);
- Floor response spectra at the three buildings uppermost altitudes: node INM13 for the internal structure of the reactor building, node N6715 for the containment structure of the reactor building and node AM8 for the auxiliary complex building;
- Hysteresis curves for the central isolator connected to the upper basemat central node (node N24718).

All results provided by the participants were post processed. As it would not be practical to reproduce in this section all the comparisons, a selection is performed so as to highlight the main trends and set the basis for conclusions. The selected cases are:

- Case 1, corresponding to the design basis earthquake with RG 1.60 spectral shape and one single macro-isolator. It is the only case run by all participants and, as such, it provides the widest comparison basis. Together with case 7, it is also one of the simplest cases. Results of Case 1 are presented in Section 4.2.2.
- Case 2, corresponding to the beyond design basis earthquake with RG 1.60 spectral shape and one single macro-isolator. Results of Case 2 are presented in Section 4.2.3. The effect of increased seismic excitation is illustrated by comparison with Case 1.
- Case 6, corresponding to the beyond design basis earthquake with RG 1.60 spectral shape and 486 isolators. Results of Case 6 are presented in Section 4.2.4. The effect of correctly modelling the number and position of each isolators is assessed by comparison with results of Case 2.

- Case 12. Corresponding to the beyond design basis earthquake with EUR hard spectral shape. Results of Case 12 are presented in Section 4.2.5. The effect of the input spectral shape is assessed by comparison with Case 6.

For each of the selected cases, only the subset of figures relevant for the discussion is presented. The full set of figures corresponding to these cases can be found in Annex III. In addition to the benchmark cases, results of parametric study of participant P2 with further increase of the excitation level are presented in Section 4.2.6.

4.2.2 Results of Case 1 – LRB system – Comparison of computed responses

4.2.2.1 Case 1 – LRB system – Relative displacement of the centre of the upper basemat

The computed horizontal relative displacements at the upper basemat central node are given in Figure 43 for the horizontal X and Y directions.

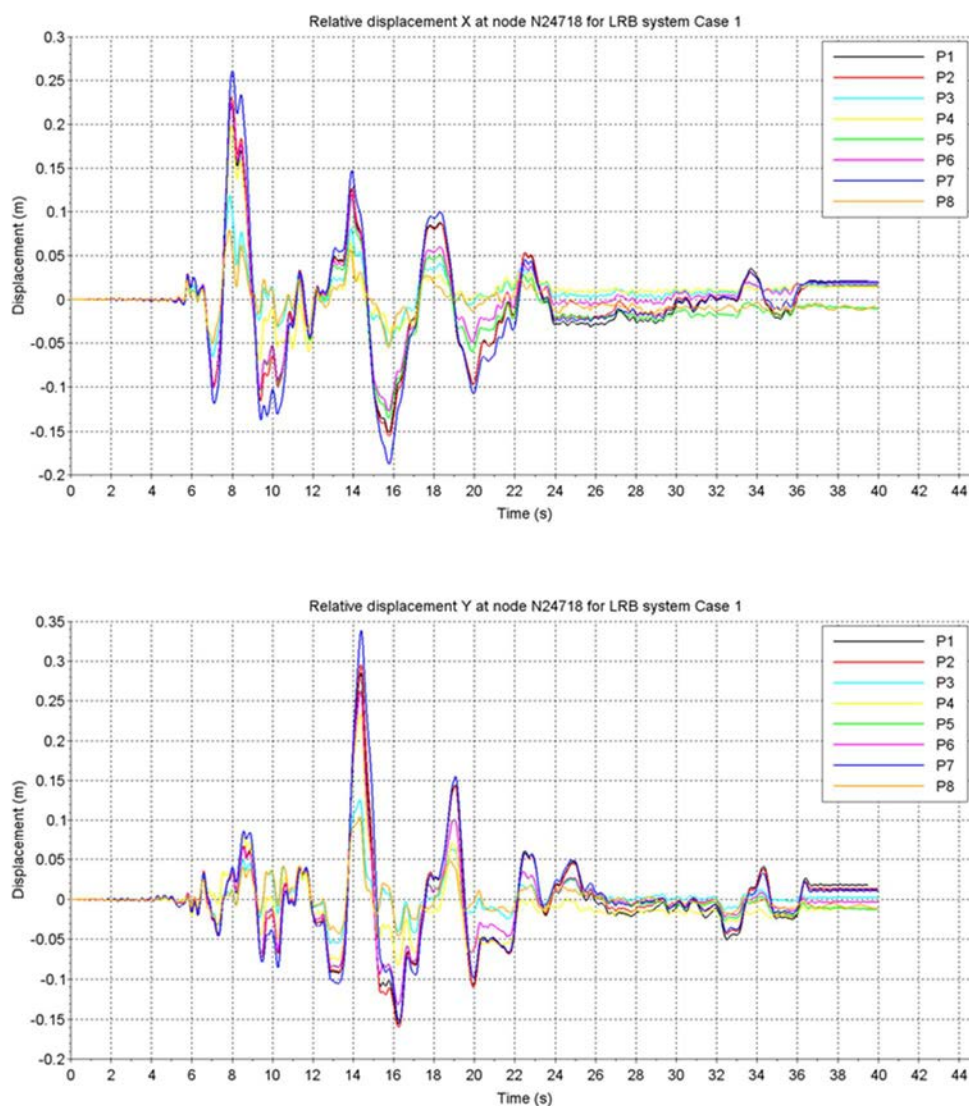


FIG. 43. LRB system - Case 1 – Relative horizontal displacement X and Y at centre of upper basemat.

For all participants, the differences between time periods where the lead does not yield, with oscillations of a few millimetres, and time periods where it does, with oscillations up to a few tens of centimetres, are clearly observable. These yielding and non-yielding periods are fully in phase for all participants, highlighting the fact that all models predict the onset of yielding and end of yielding at the same times.

The occurrence of displacement peaks, during the yielding periods, are also in phase for all participants. The amplitudes of these peaks vary from one participant to another with factors sometimes higher than two between peaks predicted by the apparently less damped model of participants P1, P2, P5, P6 and P7 (about 225 mm in X direction and 300 mm in Y direction) and those predicted by the apparently more damped models of participant P3, P4 and P8 (about 100 mm in X and Y directions).

The computed vertical relative displacements at the upper basemat central node are given in Figure 44, with a separation between the two participants that have updated their vertical isolators stiffness (P1 and P2), as detailed in Section 4.1.2, and other participants. Given the relatively high vertical response frequencies obtained, only the first 10 seconds of the results are shown. In this figure, a displacement drift is visible on results of participants P5 and P8. This drift is a signal processing issue, due to the determination of displacement based on acceleration values. It is not relevant for the comparison.

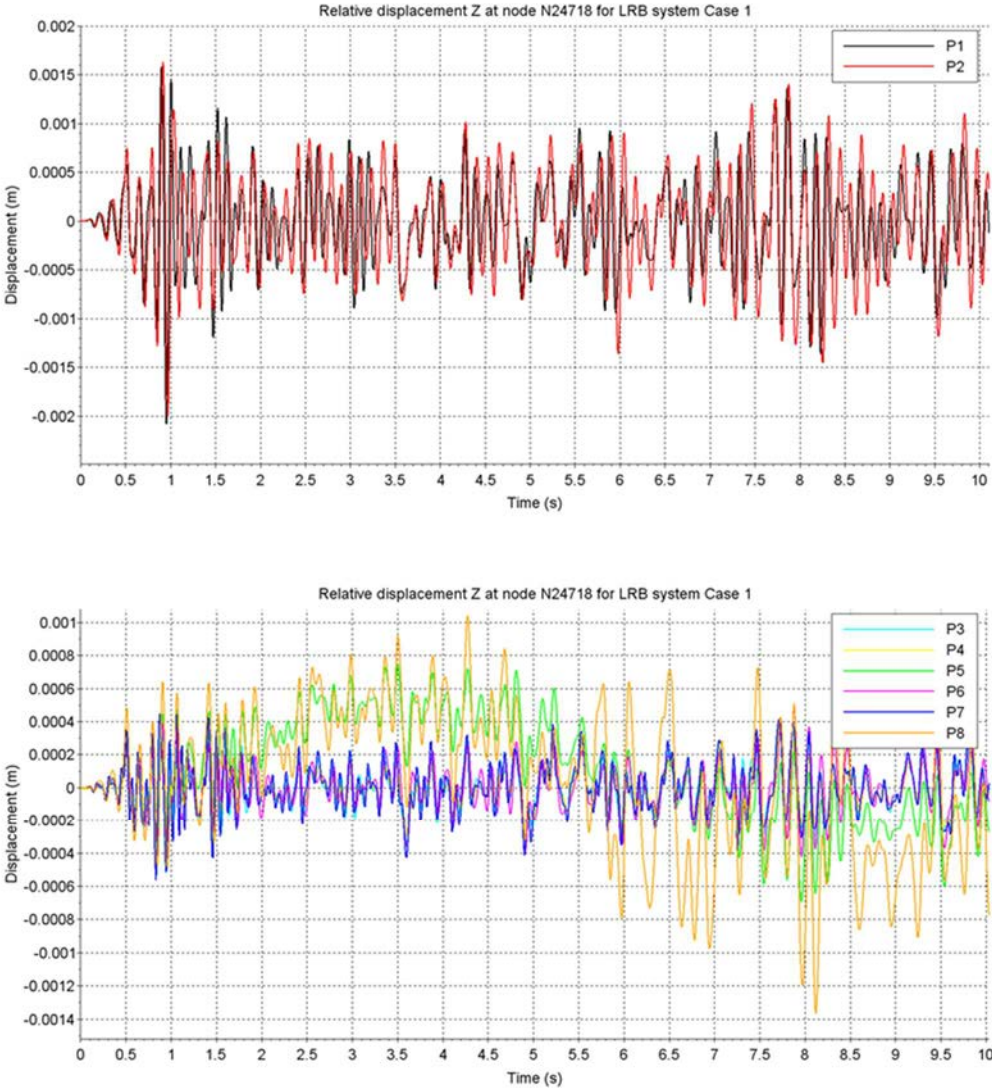


FIG. 44. LRB system - Case 1 – Relative vertical displacement Z at centre of upper basemat.

Models of participants P3, P4, P5, P6, P7 and P8 give results that are coherent in terms of phasing of the vertical displacement response. All but one of these results (P8) are also similar in terms of amplitude. Models of participants P1 and P2 give similar results in both phase and amplitude. The vertical stiffness update performed by participants P1 and P2 results in vertical relative displacements approximately 3 times higher than the ones obtained by other participants.

4.2.2.2 Case 1 – LRB system – Floor response spectra at the centre of upper basemat

Floor response spectra obtained at the upper basemat central node are given in Figure 45 for the three directions X, Y and Z.

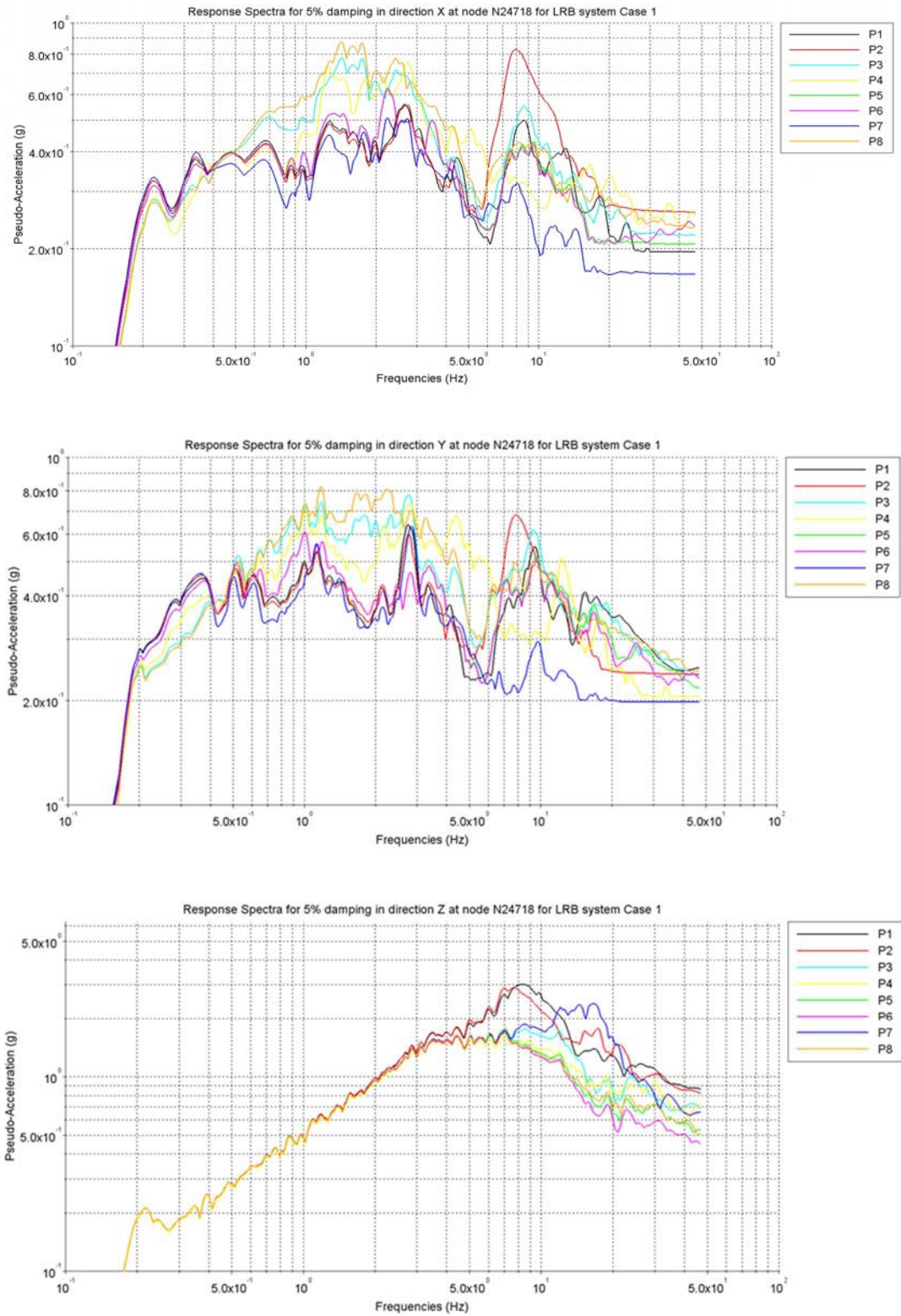


FIG. 45. LRB system - Case 1 – Floor response spectra at centre of upper basemat.

For all participant results, no significant peak appears on the horizontal spectra at the theoretical isolation frequency of the structure. At higher frequencies, structural modes are excited, and their response is felt

at the basemat level, where it generates peaks or plateaus. These higher frequency modes are excited by the vertical component of the seismic excitation and by the non-linear behaviour of the LRB isolators: steep changes of stiffness as illustrated in Figure 36.

In all three directions, results of participants P5 and P6 are the only ones to be practically identical, highlighting the use of a same model, a same code and a same set of hypotheses. All other results are different from these two and also different from one another, with difference varying from a few percent to factors higher than 2 for certain frequencies.

In the horizontal directions, spectra of all participants have approximately the same shape, differences in amplitudes are visible:

- In the 0 to 5 Hz range, where the response is dominated by the isolation system modelling, the difference between the two same groups of participants identified in the previous paragraphs, is clearly visible. Models of participants P3, P4 and P8 produce lower spectra in the 0.2 to 0.4 Hz range and significantly higher spectra in the 0.5 to 5 Hz range.
- In the 6 to 10 Hz range, where the response is dominated by the structural response modes, including the vertical ones, a different spread of participants results is observed, notably with the appearance of a peak in participant P2 and, to a lower extent, of participants P1 and P3 response spectra, and with the quasi absence of such peak in participant P4 and P7 response spectra.
- After 10 Hz, the spread is reduced, and all models converge to approximately the same zero period acceleration.

The standard deviation represents 15 to 30% of the mean value in the frequency range between 1 and 20 Hz for the X direction and 15 to 35% for the Y direction.

The mean ZPA value is 0.22 g in both horizontal direction, which represent a division by a factor two of the ground maximal acceleration (0.5 g) and demonstrates the extreme efficiency of the seismic isolation system in this case. The standard deviation of this value is about 14% in X and 8% in Y direction.

In the vertical direction, all response spectra are identical and follow the excitation response spectra up to the neighbourhood of the main global vertical mode frequency, when such mode appears.

- For participants P1 and P2, that have updated their vertical stiffness, a clear vertical mode appears around 8 Hz.
- For participant P7, and, to a lesser extent, for participant P3, such mode appears around 12 Hz.
- For other participants (P4, P5, P6 and P8), no vertical response is visible.

The standard deviation represents up to 50% of the mean value but this is fully due to the disparity between participants that have updated their vertical model and participants that have not. The mean ZPA value is around 0.7 g and the standard deviation on this value is about 20%.

4.2.2.3 Case 1 – LRB system – Floor response spectra at uppermost elevations

Floor response spectra are given for the three directions X, Y and Z in Figure 46 for the top of the reactor internal structures (node INM13), in Figure 47 for the top of the containment structure (node N6715) and in Figure 48 for the top of the auxiliary complex building (node AM8). The differences between participants results are significantly more pronounced at buildings top than at the upper basemat level.

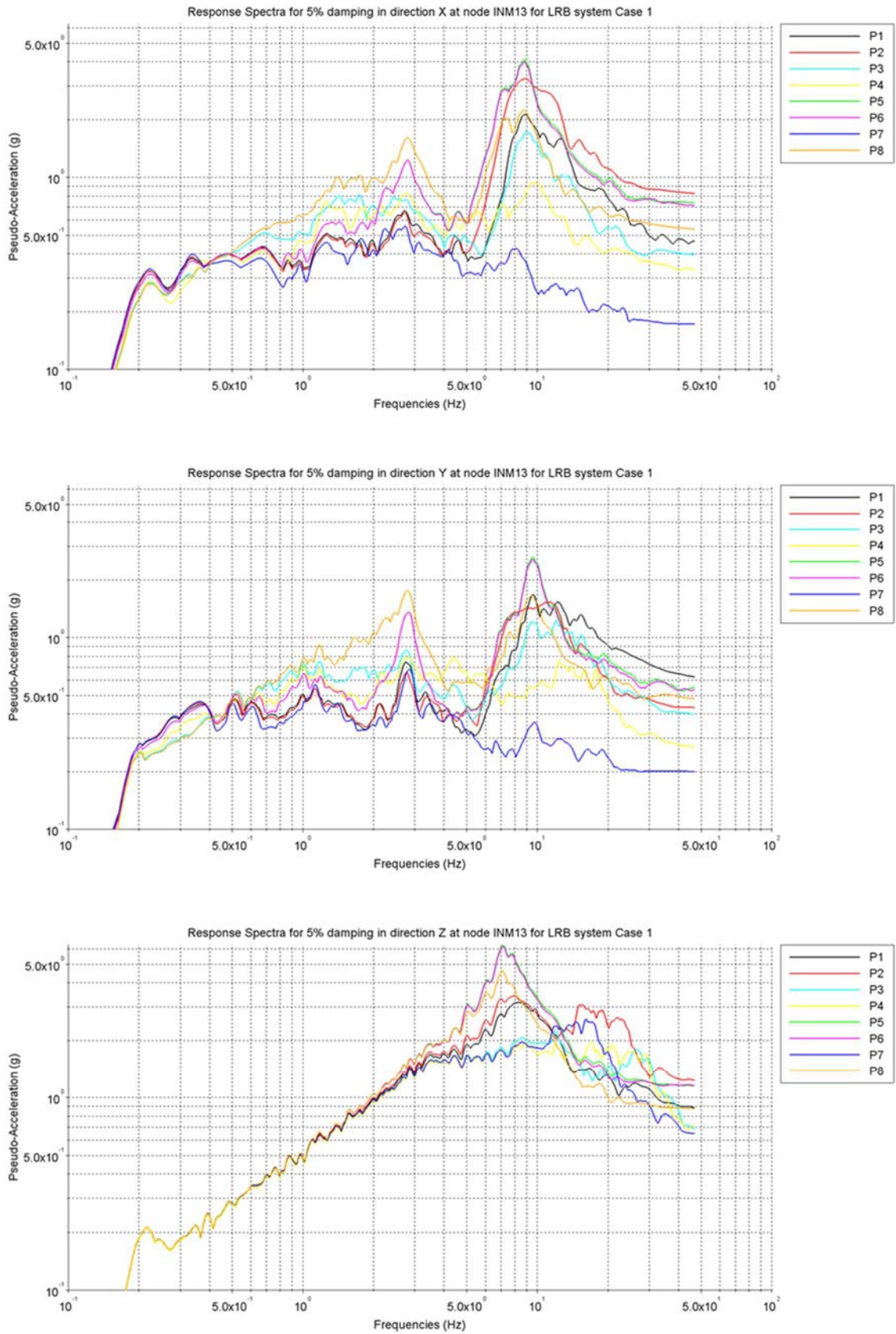


FIG. 46. LRB system - Case 1 – Floor response spectra at top of reactor building.

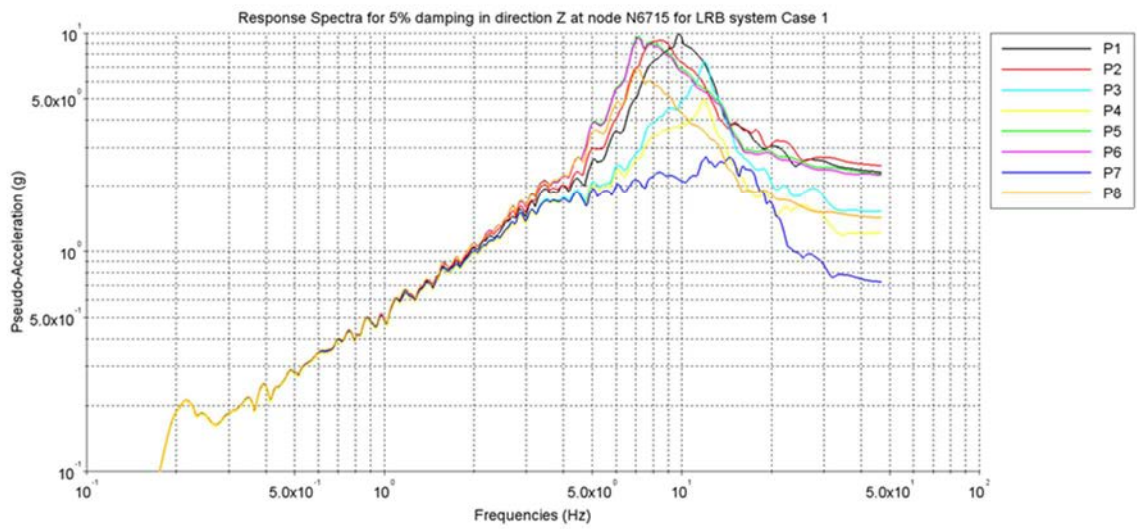
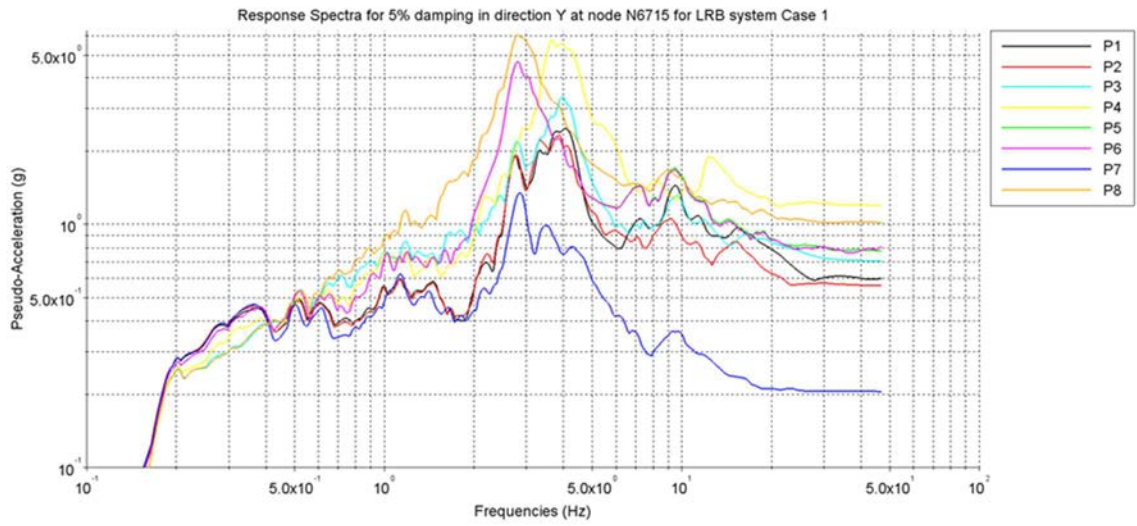
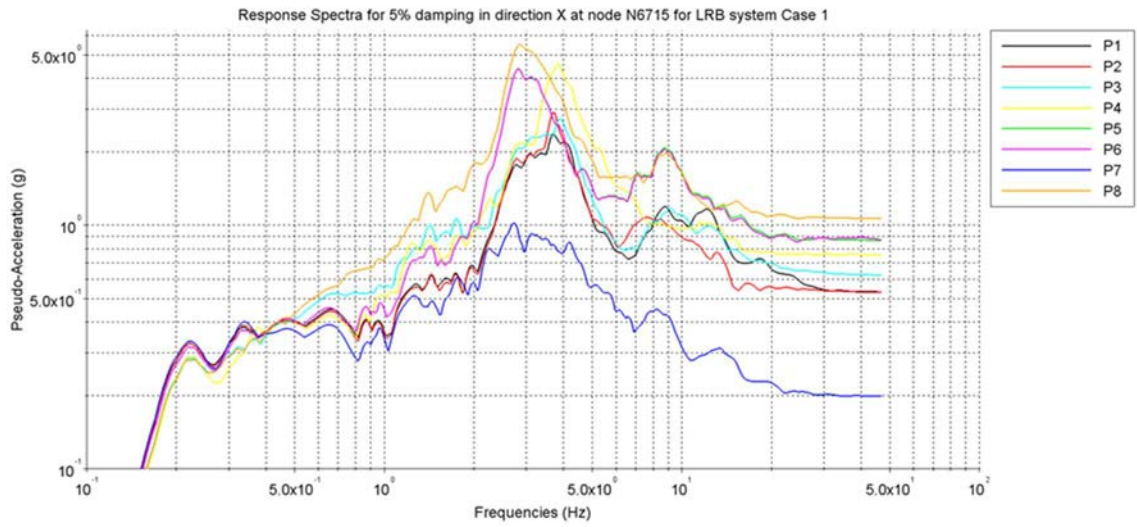


FIG. 47. LRB system - Case 1 – Floor response spectra at top of containment.

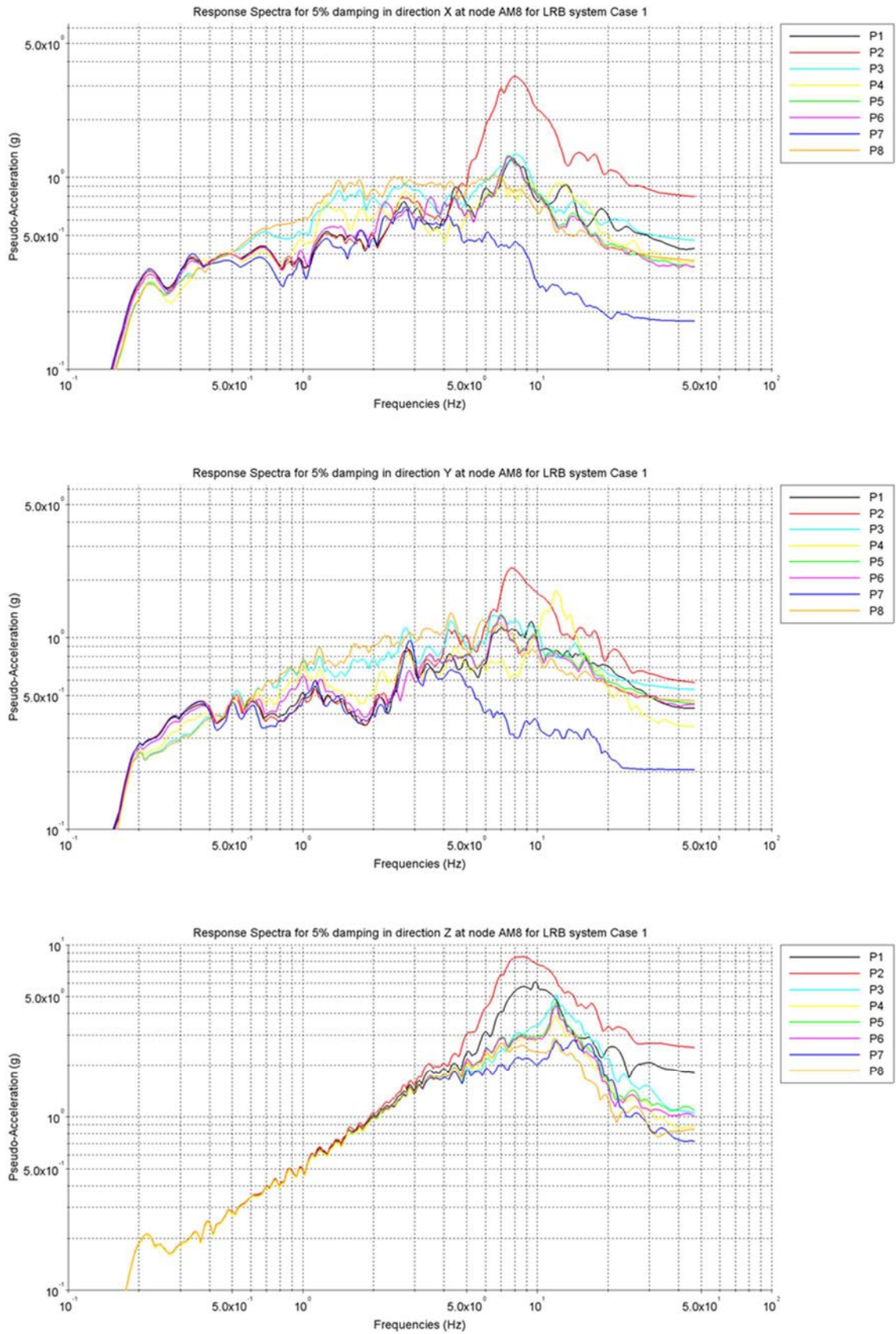


FIG. 48. LRB system - Case 1 – Floor response spectra at top of auxiliary complex building.

This is mainly because the peaks, corresponding to the buildings response on their first non-isolated modes do not coincide in frequencies. As an example, results at the top of the containment building (node N6715) indicate that:

- In both horizontal directions, the main response mode seems to be lower than 3 Hz for participants P5, P6 and P8, while remaining around 3.7 Hz for the others, which corresponds to value obtained by all participants with the fixed based modal analysis described in Section 4.1.1.
- In the vertical direction, the main response mode seems to be at 7 Hz for participant P5, P6 and P8, at 8 Hz for participant P2, at 10 Hz for participant P1 and at 12 Hz for participants P3, P4 and P7.

Since building models for all participant had the same fixed base frequencies, and since, in the vertical direction, the only isolation stiffness difference is between participant P1 and P2, with updated stiffness, and the others, the significant spread in the building response frequencies is attributed to the upper basemat modelling. As described in Section 4.1.1, participants P5, P6 and P8 did not increase the basemat stiffness of the original model provided as benchmark input. Consequently, their structural modes frequencies are affected in both horizontal and vertical directions compared to other participants.

Significant differences appear in the peak amplitudes obtained by the different participants. As an example, looking at results at the top of the internal structure building (node IM13), in all directions, participants P5 and P6 results exhibit the highest peaks, with values of 4 g, 2.5 g and 6g, respectively in the X, Y and Z direction. On the opposite, participant P7 results exhibit the lowest peaks with values lower than 1g in both horizontal directions and lower than 3g in the vertical direction. For the top of the containment structure (node N6715), the values of participant P8 tend to be higher than those of others. For the top of the auxiliary building (node AM8), it is those of participant P2 which are significantly higher, in this case driven by a higher vertical response coupled with the horizontal one. The results of participant P7 always fall below those of other participants at the structural response modes frequency, as if a much higher damping was applied to these modes.

4.2.2.4 Case 1 – LRB system – Hysteresis curves for the central isolator

Horizontal force versus distortion curves for the central isolator are given in Figure 49 and Figure 50, respectively, for the X and Y directions. In this case, values on the force scale are the ones calculated for the single macro-isolator divided by the total number of individual isolators. Participants' results are spread over several graphs to make comparisons clearer. The first graph comprises results of participants P1 and P2, which are very similar. The second graph comprises results of participants P5 and P6, which are exactly similar and those of participant P7, which are close to the two others. The third graph comprises results of participants P3, P4 and P8.

From these figures:

- It is confirmed that all participants models have the same yielding force and the same secondary stiffness during the yield phase. The initial yield force and the secondary slope value correspond to the ones prescribed by the manufacturer.
- For a first group comprising participants P1, P2, P5, P6 and P7, although the amplitude of motion is slightly different, the history of motions is relatively similar. Hysteresis curves all show the same shapes in both horizontal directions. For a second group comprising participants P3, P4 and P8, the distortion amplitude is smaller, and the history of motion is not clearly comparable to others.
- Forces of participant P8 are clearly higher than those of others and also higher than the manufacturer prescribed yield force. The shape of participant P8 hysteresis seems to indicate that both a yielding force and a viscous damping force were calculated and are added in the force values reported by participant P8.
- Participant P4 bilinear elastic-plastic model behaves independently in X and Y direction while all other participant models show a significant and mostly similar coupling of horizontal directions: distortion in X affects the hysteresis curve in Y and vice versa.

- A small effect of lead heating is observed on participants P1 and P2 curves, who included such effect in their models. The lead heating produces a decrease of the yielding force. Consequently, the energy dissipation within the isolator is diminished. As can be observed by comparison with results of participant P5, P6 and P7, this effect, although not negligible, is not predominant on the isolator response for this case.

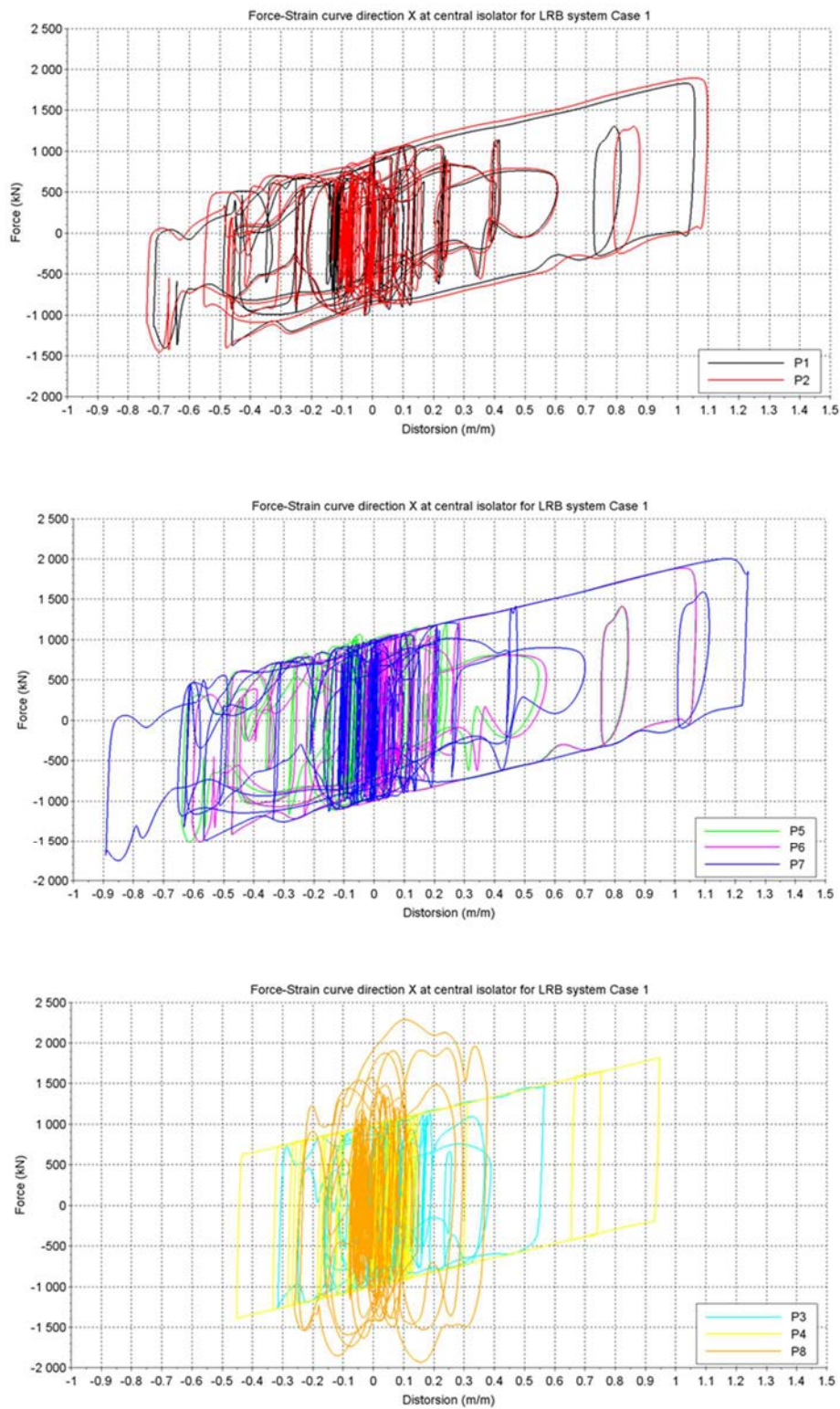


FIG. 49. LRB system - Case 1 – Force-displacement curves in X direction.

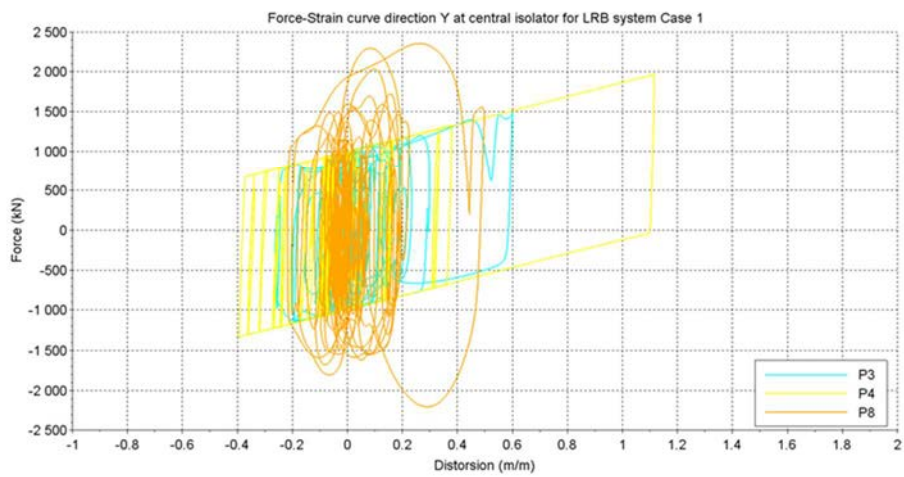
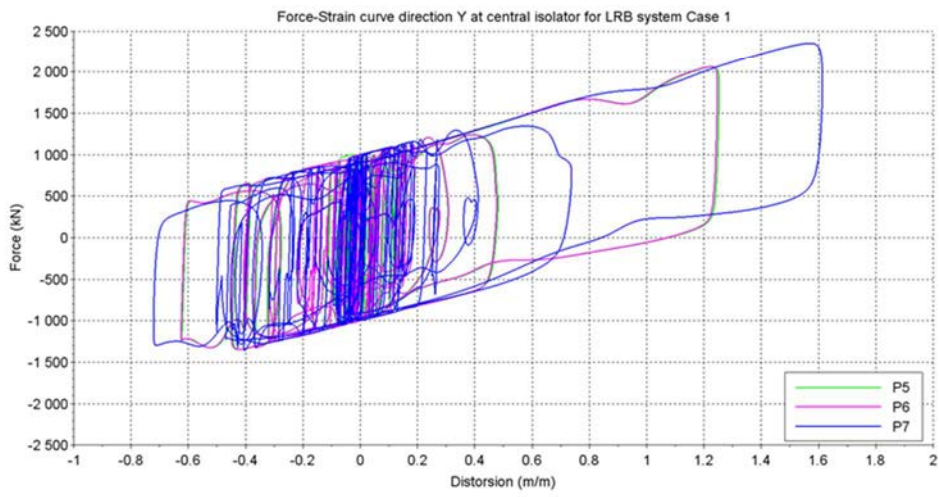
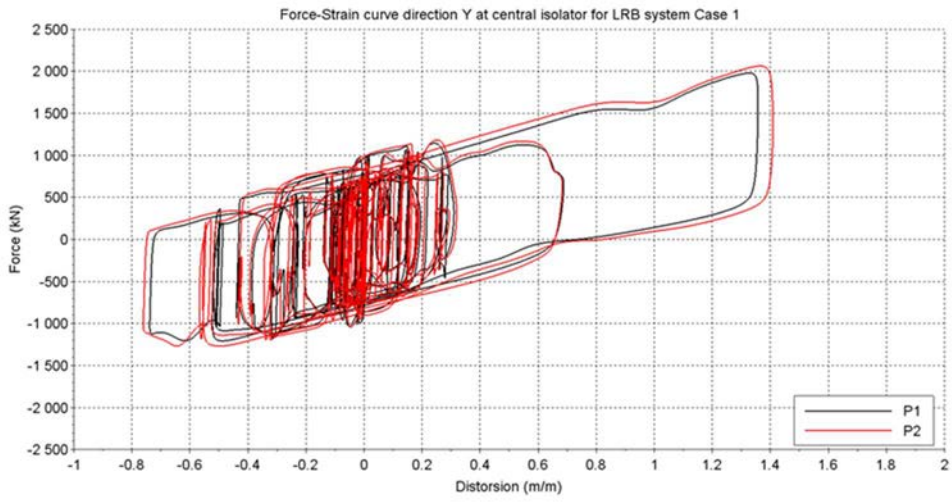


FIG. 50. LRB system - Case 1 – Force-displacement curves in Y direction.

Vertical force versus axial displacement curves are given in Figure 51. As for the horizontal direction, forces are expressed for one isolator by dividing the force obtained for the single macro-isolator. Participants results are also spread over several graphs to make comparisons clearer. The same grouping as for the horizontal direction is adopted. Results of participant P8 are not included because of a drift in the reported values.

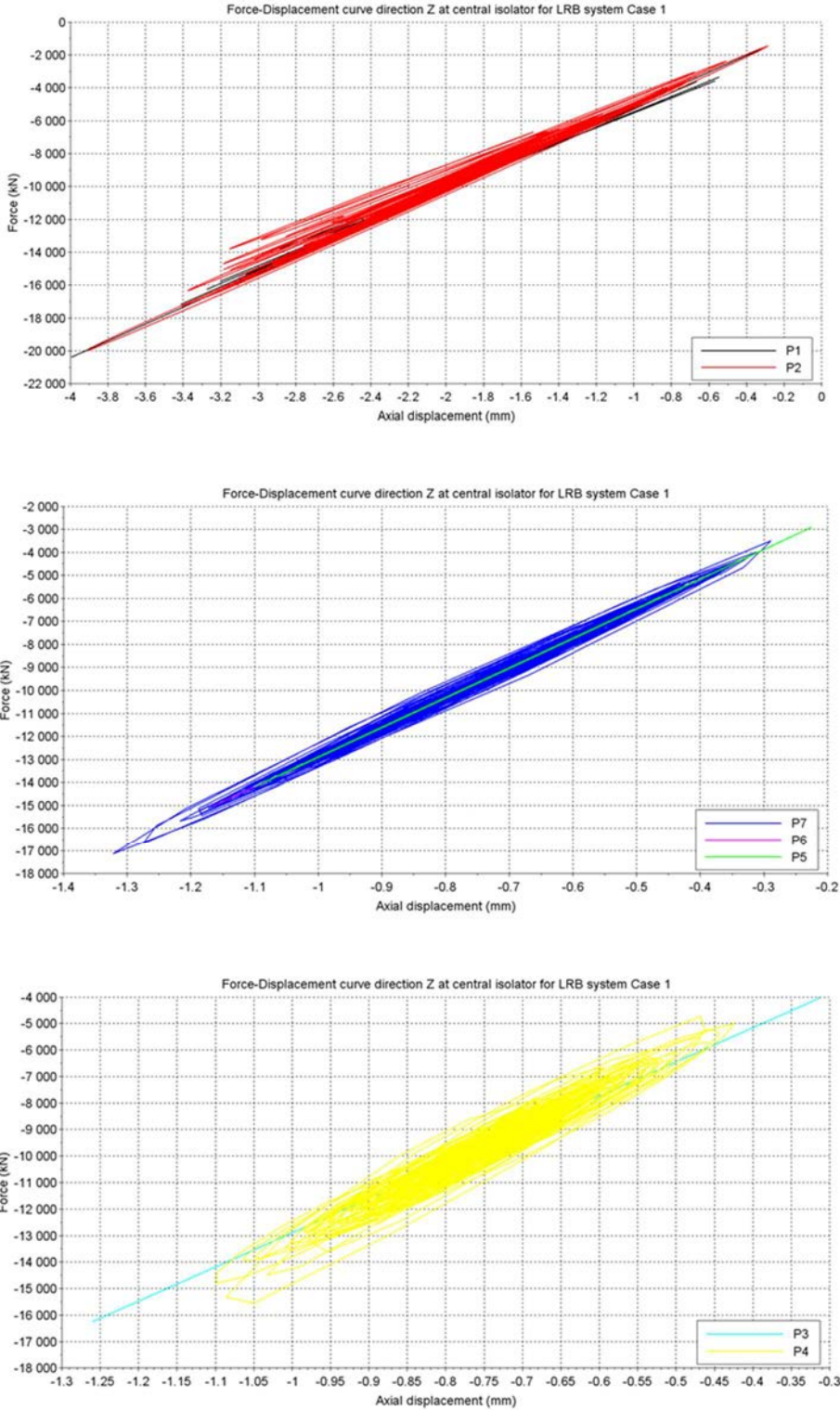


FIG. 51. LRB system - Case 1 – Force-displacement curves in Z direction.

From these figures:

- Differences in stiffness between participants who updated their vertical stiffness (P1 and P2, see Section 4.1.2) and others are obvious, leading to different equilibrium points under dead weight and to different force versus axial deformation slopes.
- Differences appear between participants that included the damping forces into their reported vertical forces and those who did not. Participant who included these damping forces have some visible energy dissipation into their curves while others have straight lines. This is only a reporting difference.
- The dependency of vertical stiffness to the horizontal distortion appears in results of participants P1 and P2, who included such effect in their models. This produces change of slope during the earthquake. For other participants, no such softening occurs, and the slope remains constant. In the present case, although noticeable, this change of vertical stiffness is not of primary importance.

Cavitation effects under tensile forces are not activated in this case and therefore produce no differences between participants results.

4.2.3 Results of Case 2 – LRB system – Effect of increased seismic excitation

4.2.3.1 Case 2 – LRB system – Relative displacement of the centre of the upper basemat

The computed horizontal relative displacements at the upper basemat central node are shown in Figure 52 for the X and Y directions. On the same figure, the displacements previously obtained for Case 1 are reproduced in dotted lines.

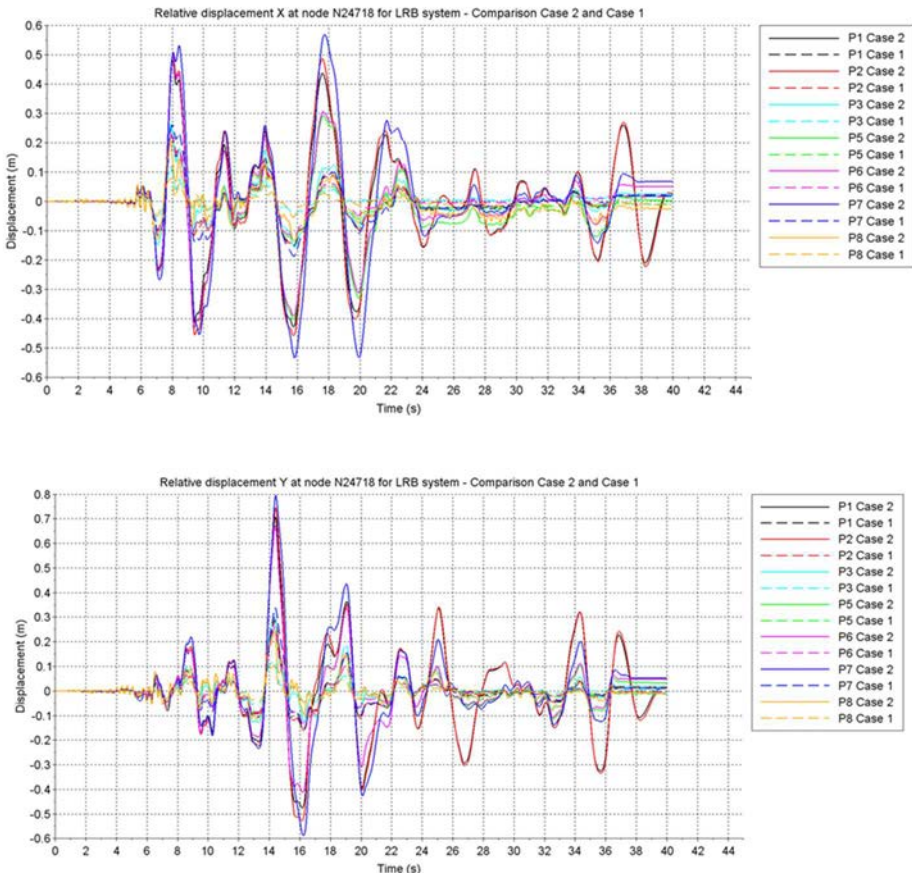


FIG. 52. LRB system – Comparison of horizontal relative displacement in Case 2 (1.67 DBE) and Case 1 (DBE).

As for Case 1, a clear difference is observed between results of participants P1, P2, P5, P6 and P7 on one side and results of participants P3 and P8 on the other side. The first group predicts significantly higher displacements (about 500 mm in X direction and 700 mm in Y direction) than the second (200 mm in X and 300 mm in Y).

Even though the excitation was multiplied by a factor 1.67 compared to Case 1, the resulting maximum displacements in both X and Y directions increase by a factor higher than 2 for all participants. This highlights the non-linearity of the LRB system response. For such isolation system, extended-design analysis, beyond-design analysis or seismic margin assessment cannot be performed based on extrapolation of design basis results.

In Case 2, and as opposed to Case 1, the lead plug heating is now found to have a significant effect on the displacement time histories of the two participants who implemented such effect in their model (P1 and P2). The apparent damping level for these participants, which appears to be slightly higher than the one of participant P7 at the beginning of the earthquake, becomes significantly lower toward the end of the excitation signal. A different excitation time history, with a longer duration, would further accentuate this effect.

The computed vertical relative displacements are compared to the ones obtained for Case 1 in Figure 53. This figure shows results only for a selected set of participants representative of three main groups.

The first group comprises the relatively similar results of participants P1 and P2, with updated vertical stiffness, the second comprises the relatively similar results of participants P3, P5, P6 and P7, without updated vertical stiffness, and the third group comprises the results of participant P8 alone, which are, in this case, ten times larger than those of other participants with theoretically similar vertical stiffness.

The model of participant P7 is representative of the linear models in vertical direction and the results for Case 2 are logically 1.67 times those obtained for Case 1. The model of participant P2 is representative of models whose vertical stiffness is altered by the horizontal distortion and in which rubber cavitation can occur. For example, it is seen in this figure that between 14 and 16 s, the vertical equivalent stiffness of the isolators decreases, which results in a static compaction of the whole isolation system. Finally, the results of participant P8 are outliers in this case.

4.2.3.2 Case 2 – LRB system – Floor response spectra at the centre of upper basemat

Floor response spectra obtained at the upper basemat central node are compared to those obtained for Case 1 in Figure 54 for the three directions X, Y and Z.

In this figure, the difference between two groups of participants that was already observed in Case 1, P1, P2, P5, P6 and P7 on one side and P3 and P8 on the other side, becomes even more acute.

For the first group of participants (P1, P2, P5, P6 and P7), and unlike for Case 1, a clear sharp peak appears at the apparent frequency of the isolation system around 0.35 Hz. This peak is similar for the 5 participants in this group. Such spectral shape is typically expected for a seismically isolated structure and is clearer in this case, where the lead yield is more important, than it was in Case 1. The acceleration spectra then drop to a level relatively similar to the one obtained for Case 1. At higher frequencies, and when the response is affected by the excited structural modes, a new separation occurs between results of Case 1 and Case 2.

For the second group of participants (P3 and P8), the horizontal spectra have a shape relatively similar to the one obtained in Case 1, with a wide peak located between 1 Hz and 2 Hz.

The dispersion between participants responses is higher for Case 2 than for Case 1 and is primarily driven by this fundamental difference of behaviour between two groups of participants. As for Case 1, the dispersion is reduced for the ZPA, representing the basemat acceleration. The standard deviation on ZPA is 14% of the mean in the X direction and 7% in the Y direction.

The mean ZPA value is 0.34 g in X direction and 0.38 g in Y direction, which represent a division by a factor two of the ground maximal acceleration (0.835 g) and demonstrates again the extreme efficiency of the seismic isolation system in this case.

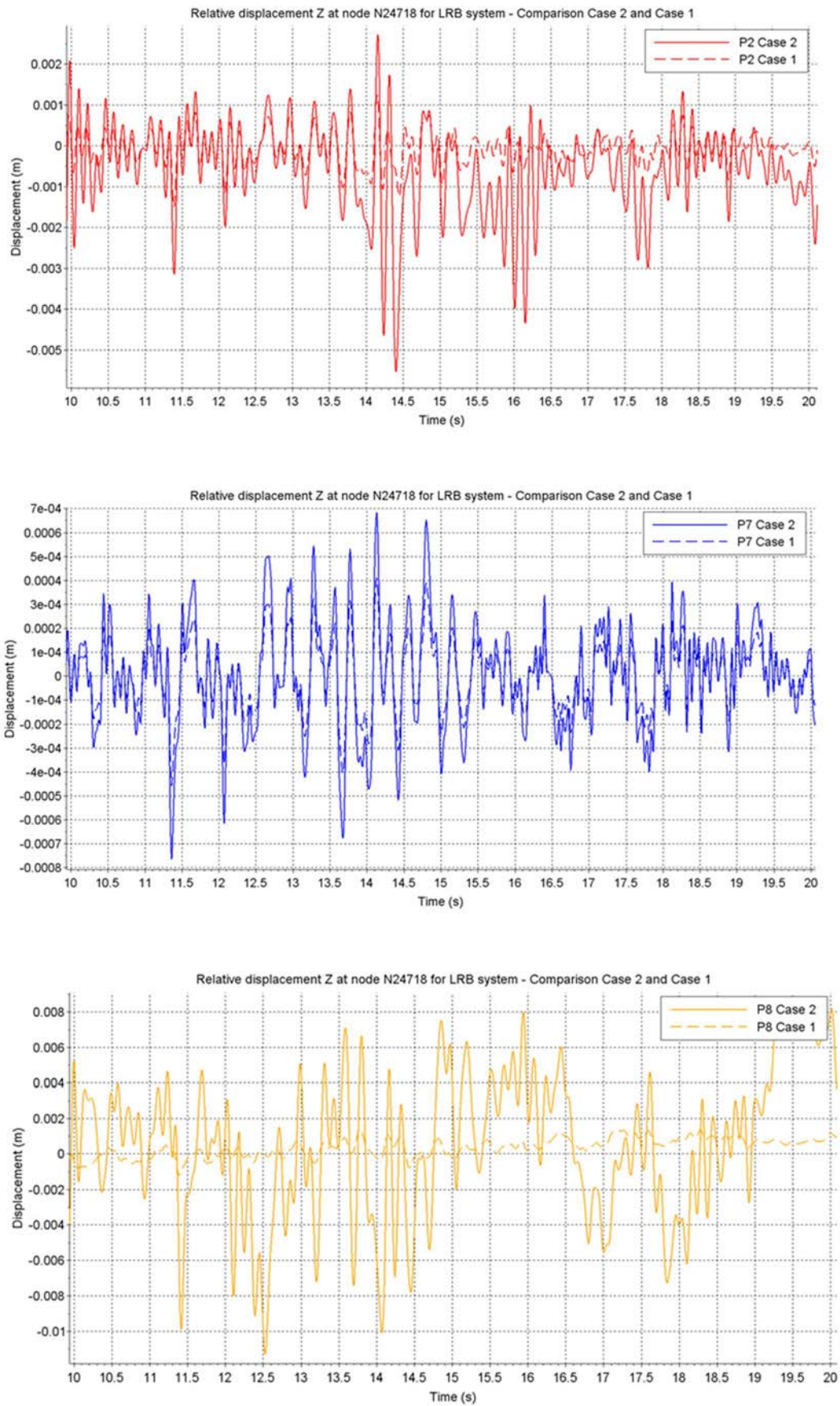


FIG. 53. LRB system – Comparison of vertical relative displacement in Case 2 (1.67 DBE) and Case 1 (DBE).

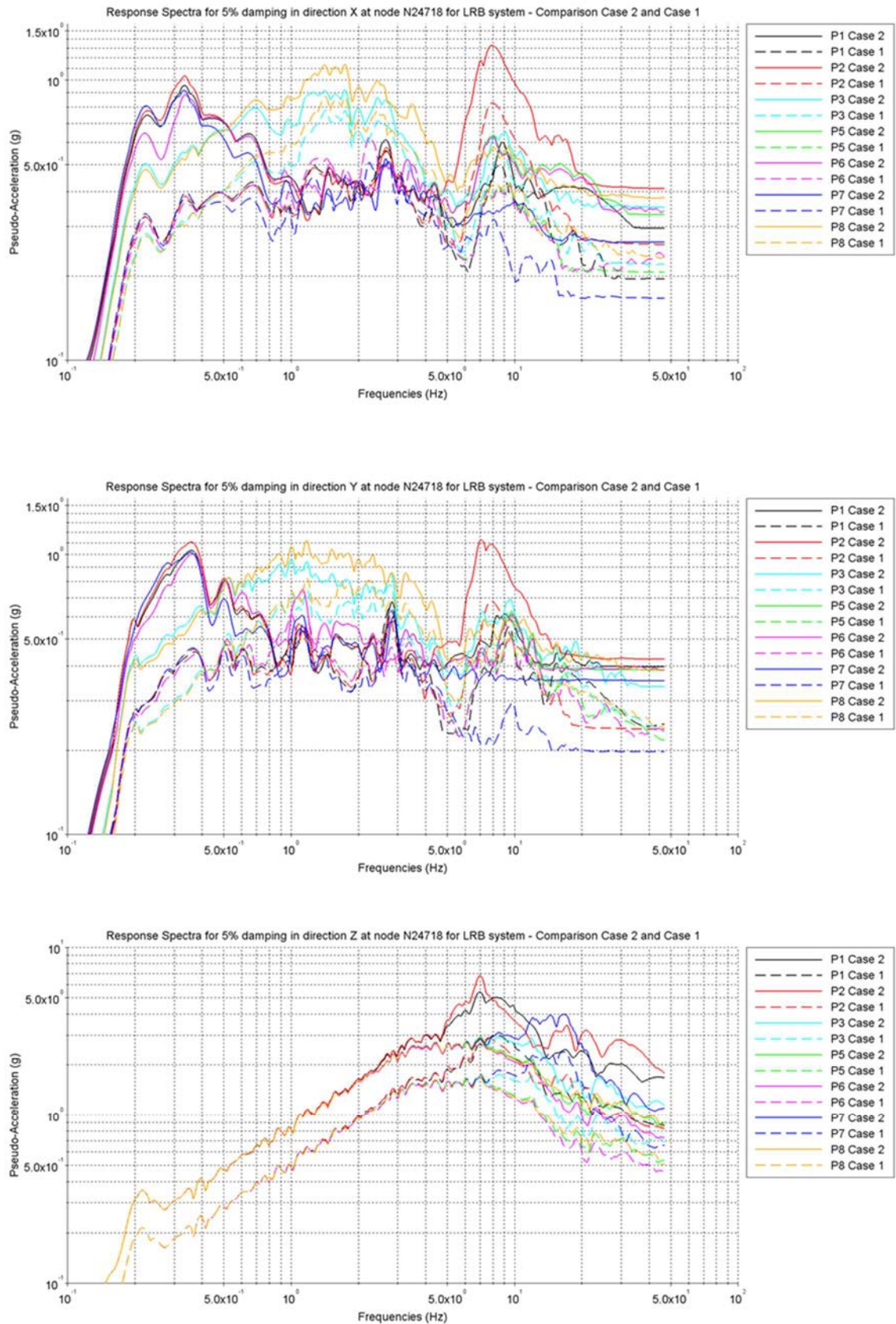


FIG. 54. LRB system – Comparison of Floor Response Spectra at centre of upper basemat in Case 2 (1.67 DBE) and Case 1 (DBE).

In the vertical direction, for participants P3, P5, P6, P7 and P8, as a logical consequence of the use of a linear vertical model, the spectral shapes are similar to those produced in Case 1 with a multiplication factor of 1.67.

For participants P1 and P2, the peak that appeared around 8 Hz in vertical spectra of Case 1 is moved to about 7 Hz in this case and its amplitude is more than doubled. This highlights the non-linear behaviour of participants P1 and P2 models in the vertical direction, with a decrease of the isolator apparent vertical stiffness due to horizontal distortion. An increase of the response spectra higher than 1.67 is also observed for participants P1 and P2 results between 10 and 50 Hz and is supposed to result from the onset of non-linear behaviour, such as cavitation, for the highest excitation level.

The dispersion on vertical spectra is higher for Case 2 than for Case 1. The mean ZPA value is around 1.17 g and the standard deviation on this value is about 30% of the mean.

4.2.3.3 Case 2 – LRB system – Floor response spectra at uppermost elevations

At buildings uppermost altitudes, the disparity of behaviour observed at basemat level is also observed and is combined to the disparity of structural model behaviours already observed for Case 1. As an example, floor response spectra at the top of the internal structure building are illustrated and compared to those of Case 1 in Figure 55. The combined conclusions of sections 4.2.5.2 and 4.2.3.3 adequately cover the present case and are therefore not repeated here.

4.2.3.4 Case 2 – LRB system – Hysteresis curves for the central isolator

Horizontal force versus distortion curves for the central isolator are given in Figure 56 and Figure 57 respectively for the X and Y direction. The participants results presentation on several graphs is similar to the one adopted for Case 1. From these figures:

- For five participants (P1, P2, P5, P6 and P7), the calculated maximal distortion is about 250% in the X direction and 350% in the Y direction. As for Case 1, the hysteresis curves of these five participants share some common characteristics. This gives confidence in the ability of different models, with different hypotheses and different tools to predict approximately the same distortion values.
- The curves of participants P1 and P2 clearly show a progressive decrease of the lead yield stress due to the lead heating effect, with the yielding force at the end of the earthquake being decreased to approximately the half of its original value. The hysteresis curves of these two participants are relatively close to each other.
- For two participants (P3 and P8), the calculated maximal distortion remains below 150% in both X and Y directions. Even though the bilinear behaviour for these participants is the same as for participants P5, P6 and P7. As identified for Case 1, there seems to be significantly more damping forces preventing the isolators distortion in participants P3 and P8 models and these forces are not reported in the hysteresis curves.

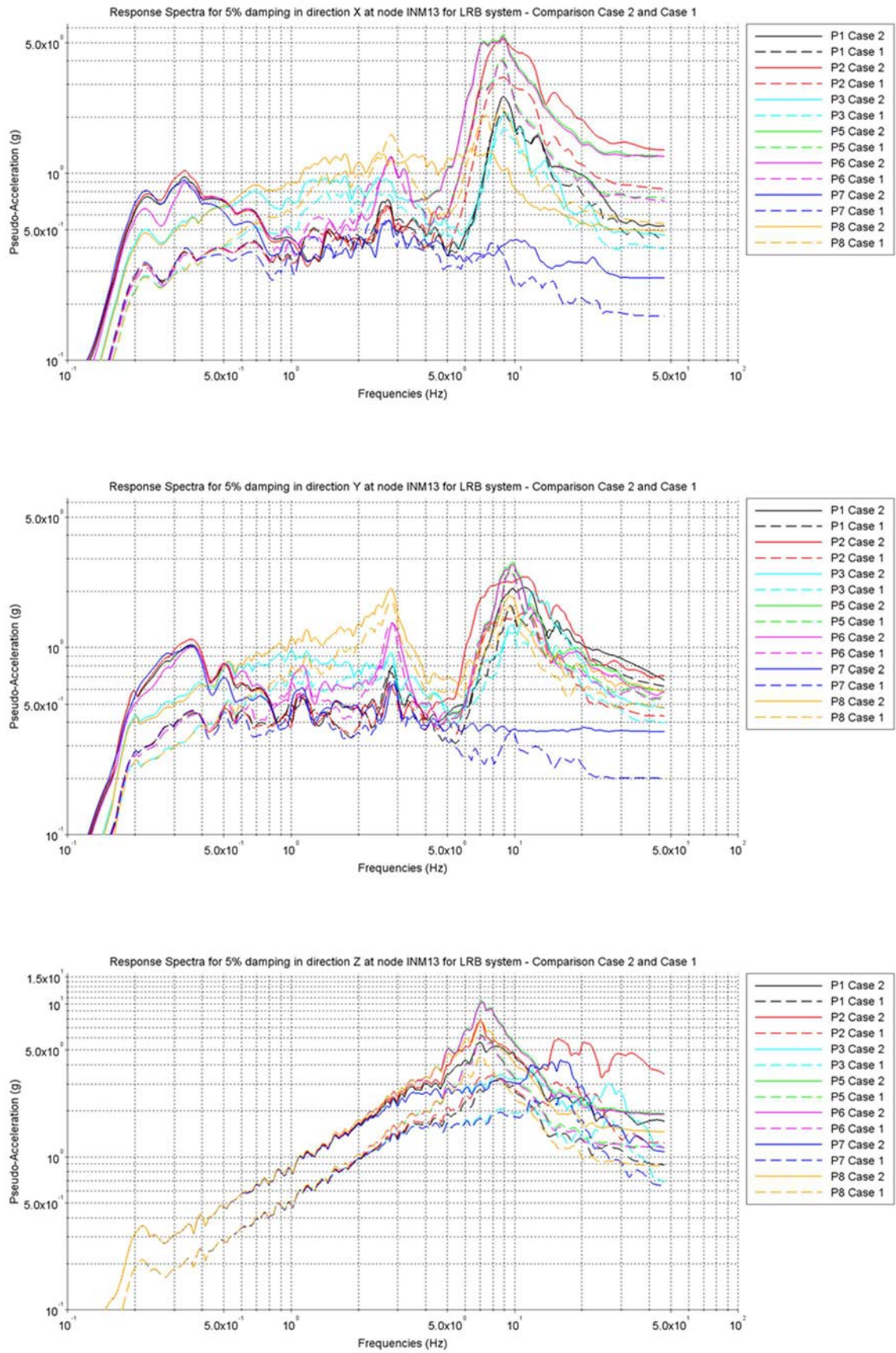


FIG. 55. LRB system – Comparison of Floor Response Spectra at top of the internal structure building in Case 2 (1.67 DBE) and Case 1 (DBE).

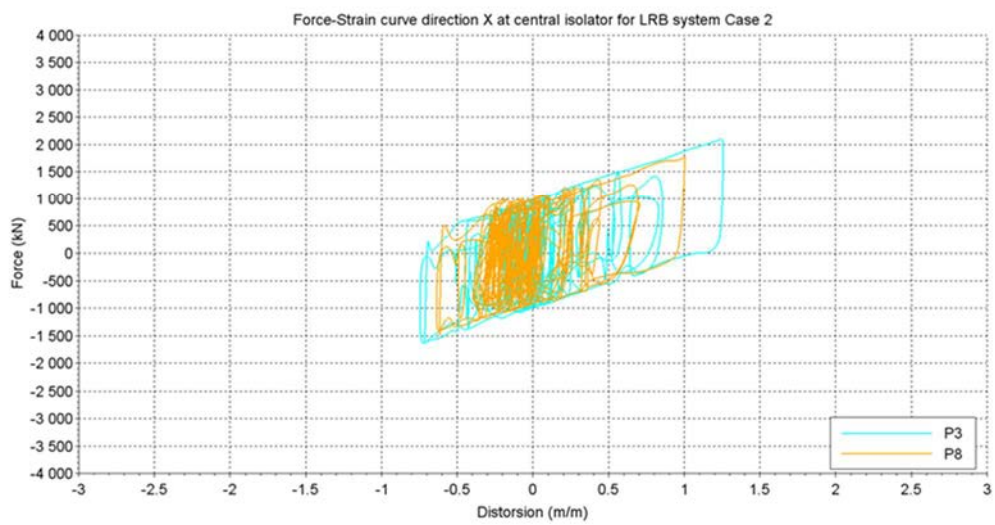
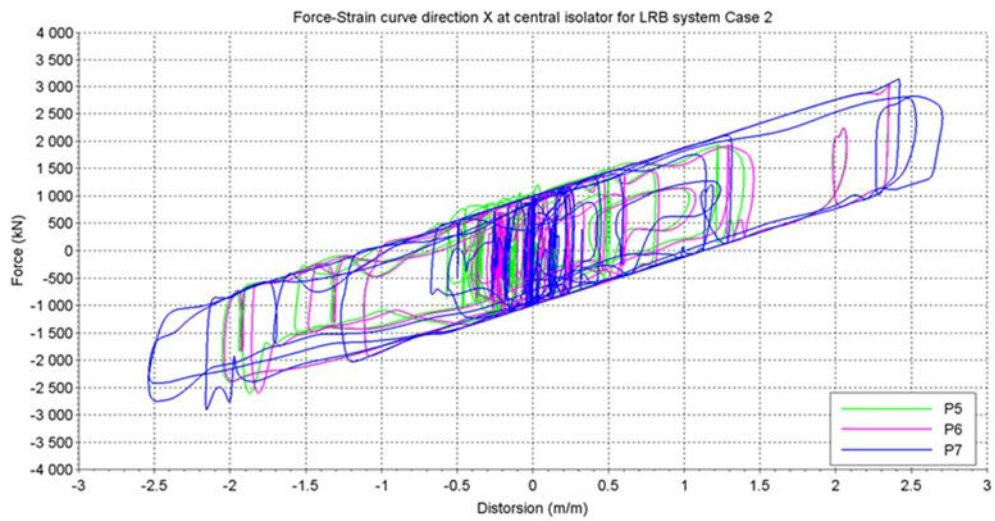


FIG. 56. LRB system - Case 2 – Force-displacement curves in X direction.

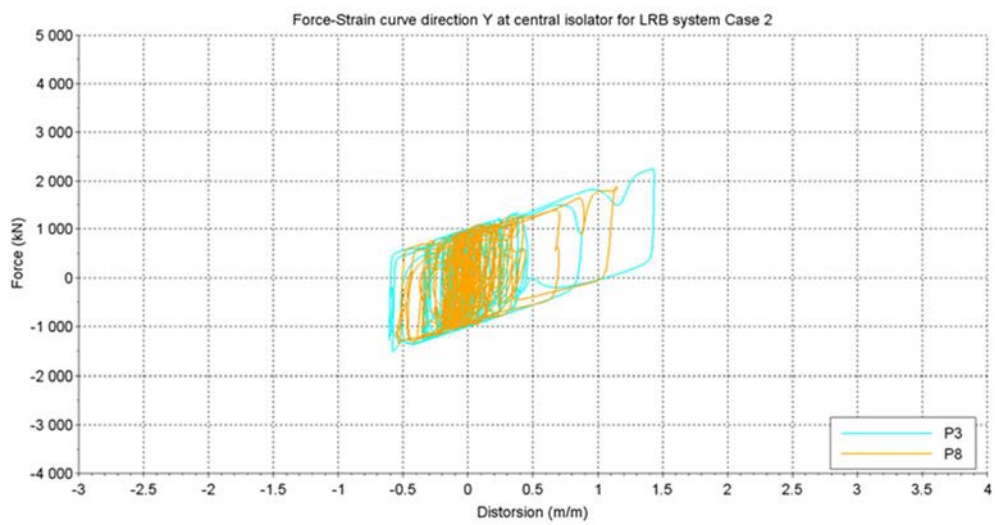
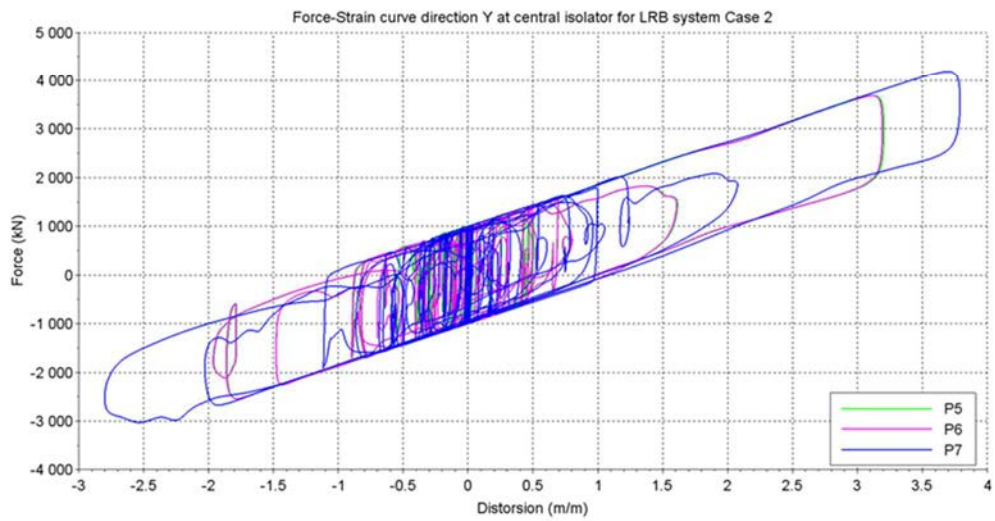
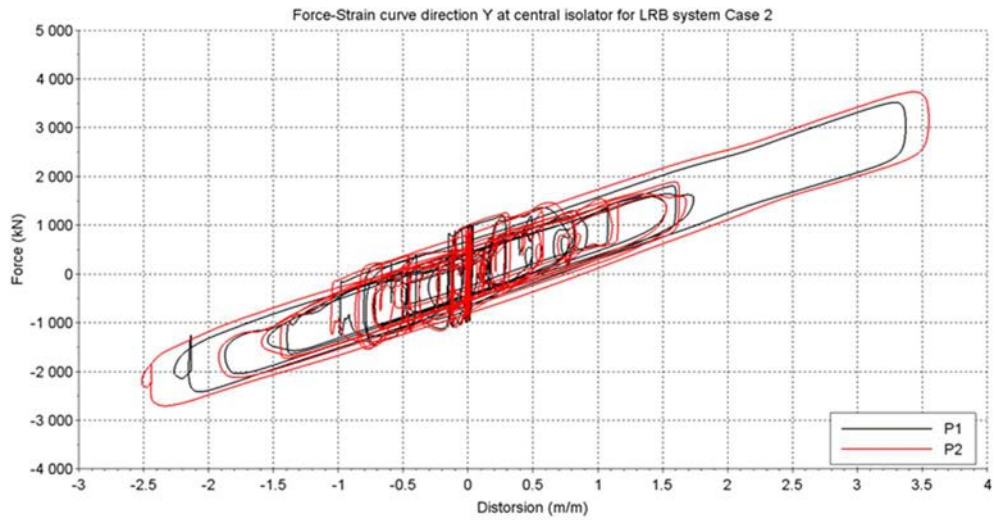


FIG. 57. LRB system - Case 2 – Force-displacement curves in Y direction.

Vertical force versus displacement curves are given in Figure 58. In addition to conclusions already stated for Case 1, it is observed that:

- The increase of seismic level produces no qualitative change in the force-displacement curves of participants P3, P5, P6, P7 and P8, which evolves linearly with the increase of excitation.

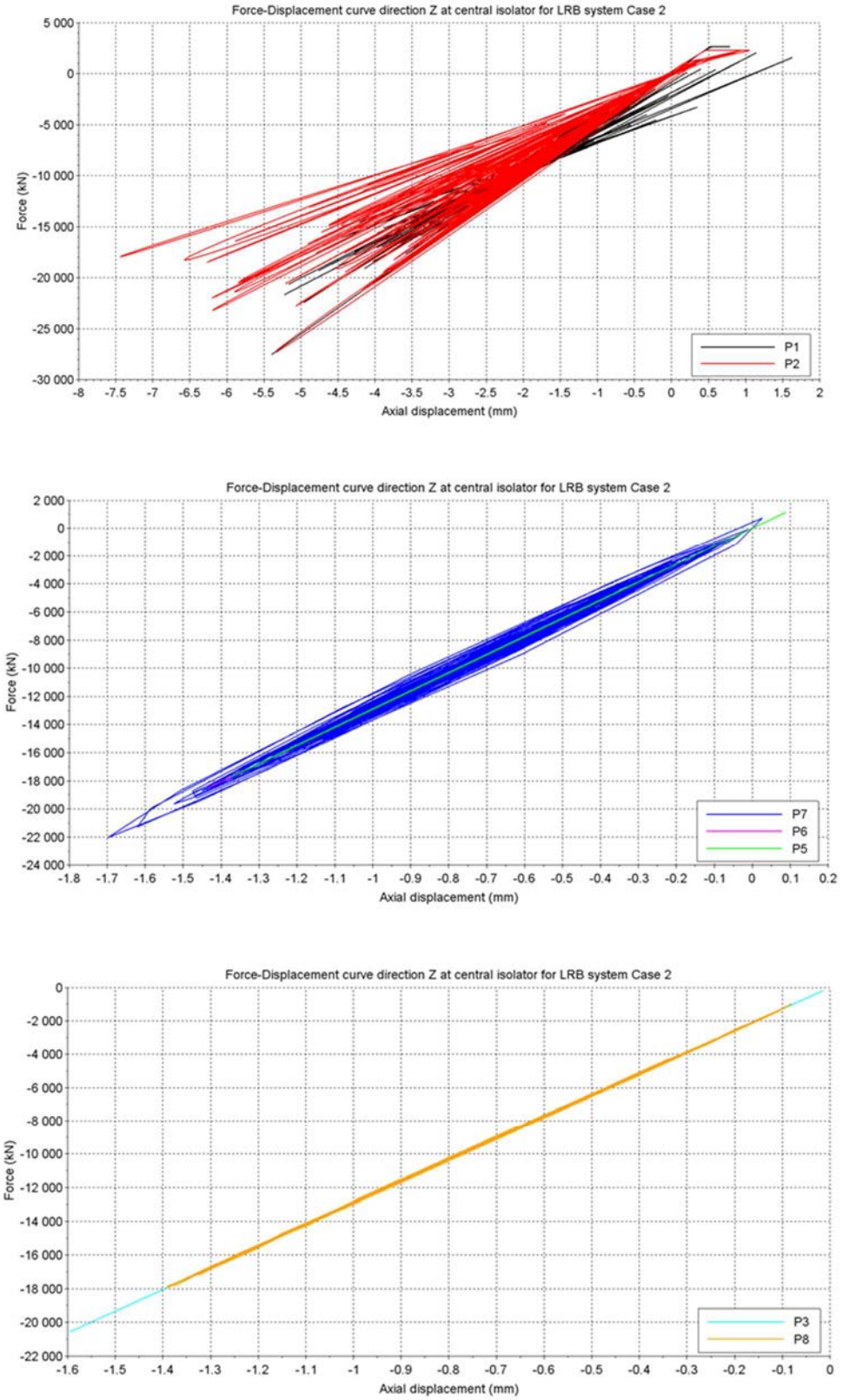


FIG. 58. LRB system - Case 2 – Force-displacement curves in Z direction.

- Horizontal distortion now produces a significant change of vertical stiffness in models of participants P1 and P2. As seen in Section 4.2.3.1, the change of vertical stiffness leads to an apparent lowering of the equilibrium point under dead weight during the earthquake. It also leads to a noticeable change of the isolated structure vertical response frequency, as identified in Section 4.2.3.2.
- A small amount of rubber cavitation is predicted by both participant P1 and participant P2 models. The predicted cavitation force is slightly lower for participant P2 than for participant P1. The unloading path also seems to be different between the two models. The occurrence of rubber cavitation induces some impact type loads in the vertical direction, due to the sudden change of vertical stiffness. This is the cause of the higher frequency content in response spectra at the basemat and building top elevations, as was observed in vertical response spectra of participant P2 between 10 and 50 Hz in Figure 54 and Figure 55.

4.2.4 Results of Case 6 – LRB system – Effect of representation of all isolators

4.2.4.1 Case 6 – LRB system – Relative displacement of the centre of the upper basemat

Figure 59 and Figure 60 compare the basemat relative displacements obtained by all participants for Case 6, with 486 isolators modelled independently, and for Case 2, with one macro isolator, respectively, for the upper basemat central node (N24718) and for one corner node (N25270). In the vertical direction, only a reduced time-interval, between 7 s and 10 s, is selected to make comparisons clearer.

From Figure 59, it is observed that the change of number of isolator modelling does not produce any significant change on the results at basemat central node.

From Figure 60, it is observed that the change of number of isolators modelling produces only negligible changes in horizontal direction at the corner of the basemat, but significant changes in vertical direction for participants P1, P2 and P5. No change at all is observed for participants P3 and P7.

Comparing both figures for the central and the corner node, the effect of torsional rotation is barely visible. The effect of rocking, on the other side, is clearly visible in the results of participant P1 and, even more, on those of participant P2. The occurrence of significant rocking for participants P1 and P2 is due to both to the updated vertical isolator stiffness value they used and to the possible softening of the isolators due to the modelling of cross direction effects and rubber cavitation effects.

4.2.4.2 Case 6 – LRB system – Floor response spectra at the centre of upper basemat

Figure 61 illustrates the comparison between response spectra obtained at basemat centre for Case 6 and Case 2.

In the horizontal directions, and except for participant P7 results, that appear not to be impacted at all, the modelling of 486 isolators has the effect of getting the different participants response closer to each other. Indeed, the higher peak on participant P2 response around 8 Hz is lowered while those of other participants in the same region are increased. The rest of the spectra is unaffected. The standard deviation represents approximately 20% of the mean value except between 1 and 2 Hz and around 8 Hz, where it is about 40 %. The mean ZPA value is 0.28 g in X and 0.31 g in Y. The standard deviation of this value is about 13 % in X and 10 % in Y direction.

In the vertical direction, no change is observed from Case 2 to Case 6.

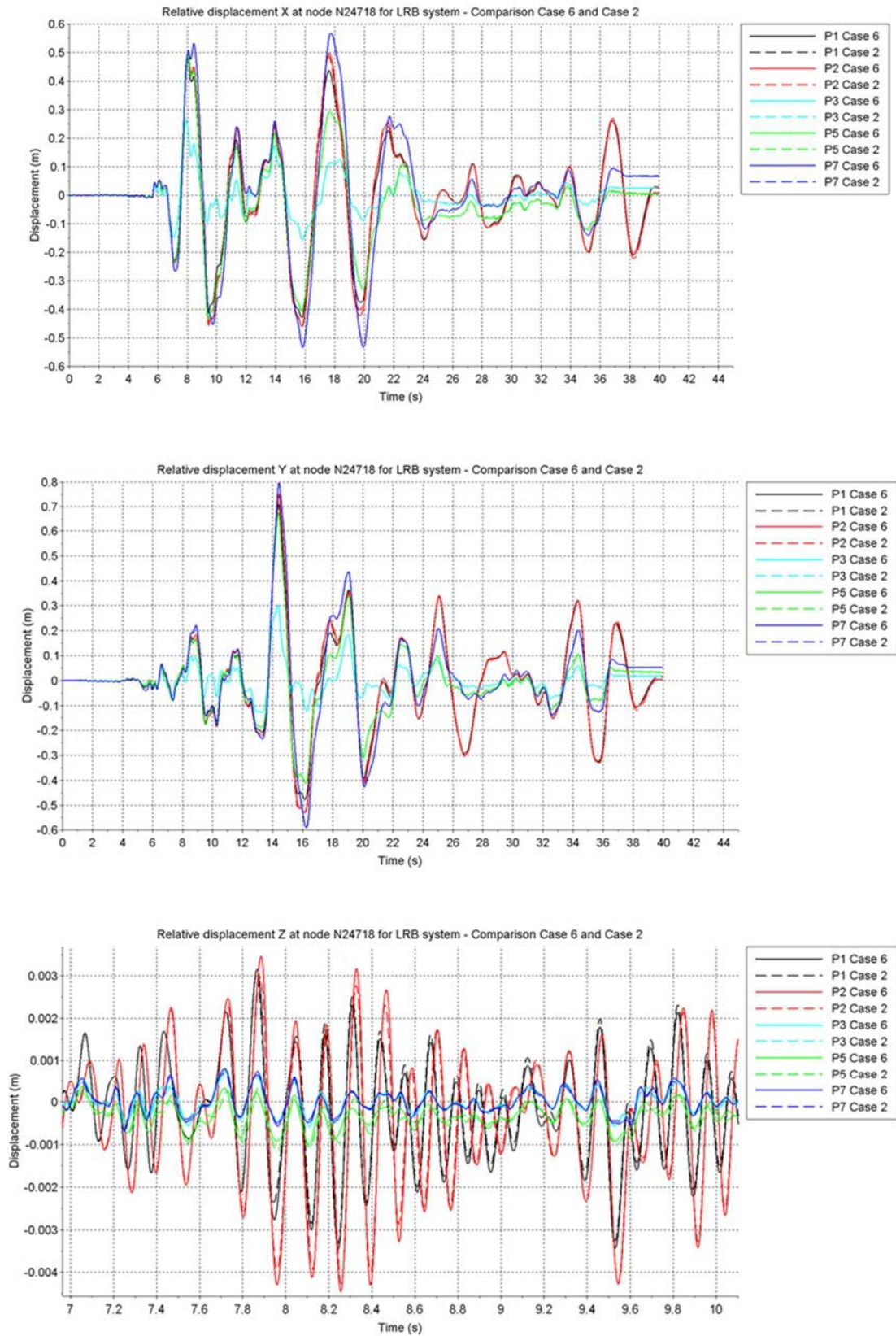


FIG. 59. LRB system - Comparison of relative displacement at upper basemat centre in Case 6 (486 isolators) and Case 2 (one macro-isolator).

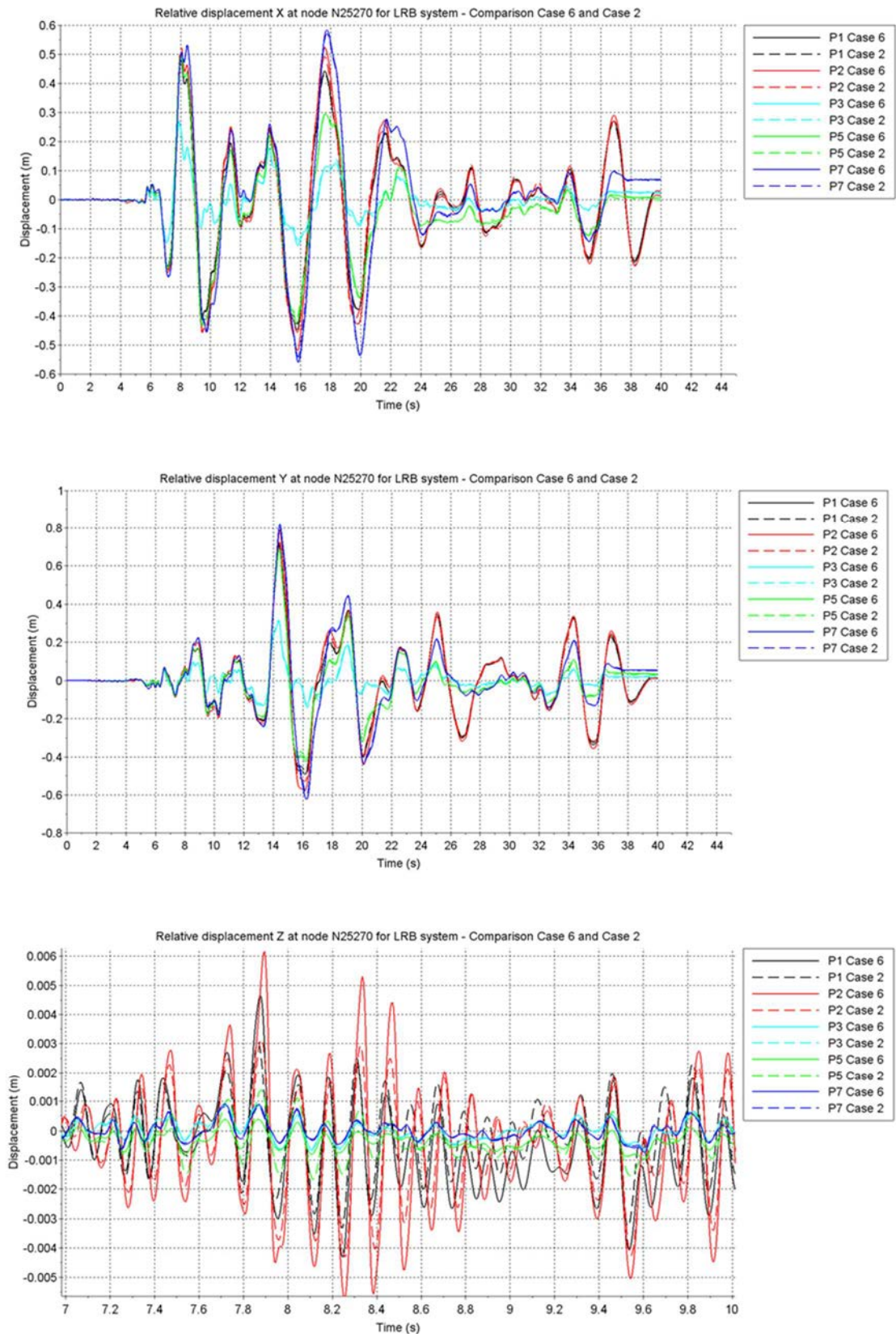


FIG. 60. LRB system - Comparison of relative displacement at upper basemat corner in Case 6 (486 isolators) and Case 2 (one macro-isolator).

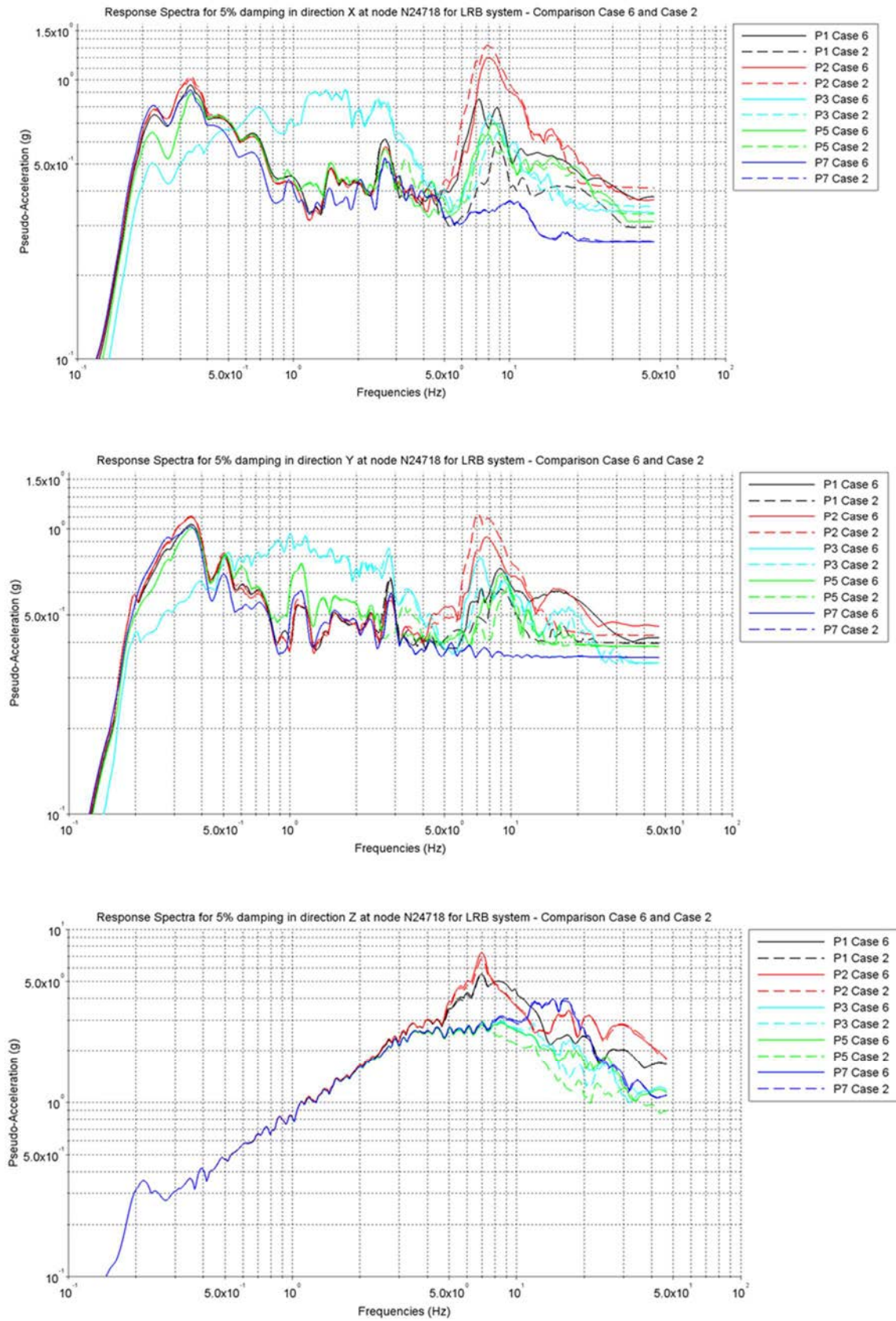


FIG. 61. LRB system - Comparison of upper basemat centre response spectra in Case 6 (486 isolators) and Case 2 (one macro-isolator).

4.2.4.3 Case 6 – LRB system – Floor response spectra at uppermost elevations

Floor response spectra are given for the three directions X, Y and Z in Figure 62 for the top of the reactor internal structures (node INM13), in Figure 63 for the top of the containment structure (node N6715) and in Figure 64 for the top of the auxiliary complex building (node AM8). In these figures, the same results obtained for Case 2, with one single macro-isolator, are plotted in dotted lines.

As it was observed on the response spectra at basemat level, the change of isolation system modelling does not affect the buildings top response spectra at low frequencies, but it affects them in the frequency ranges of the main structural modes. As observed for the spectra at basemat central node, the detailed modelling of the 486 isolators has the effect of bringing results of participants P1, P2, P3 and P5 closer to each other:

- The high peaks on participants P2 horizontal spectra around 8 Hz are decreased. This may indicate that the damping applied onto these modes without the complete modelling of the isolation system might have been under-estimated.
- On the opposite, and to a lesser extent, the peaks on participant P1 horizontal spectra are increased.
- The structural frequencies on participant P5 results, which were strongly affected by the basemat modelling, as described in Section 4.2.2.3, are now in line with those of participants who rigidified their basemat. This is especially visible at the top of the containment building in the horizontal directions and at top of all buildings in the vertical direction. The modelling of all 486 isolators seems to directly rigidify the basemat.

Results of participant P7 are unaffected by the change in isolation modelling, essentially because no influence of structural modes is observable on participant P7 response spectra.

On participants P1 and P2 horizontal and vertical response spectra, high values appear in the 10 to 30 Hz frequency range that are inexistent for other participants. These values indicate that the rubber cavitation effects, which were observed but still relatively small in Case 2, become more significant in Case 6, as the isolators located on the basemat periphery are more subject to tension than the central isolator.

4.2.4.4 Case 6 – LRB system – Hysteresis curves for the central isolator

Since the displacements at basemat centre are similar to those obtained in Case 2, no significant variation of the hysteresis curves is expected. These curves are therefore not analysed further.

Hysteresis curves at corner isolators, which could have been of interest, were not requested from participants and can therefore not be compared.

4.2.5 Results of Case 12 – LRB system – Effect of EUR ground motion spectra

4.2.5.1 Case 12 – LRB system – Relative displacement of the centre of the upper basemat

The computed relative displacements at the upper basemat central node are shown in Figure 65 for the three directions. As can be seen in this figure:

- Most of the displacement response occurs in the first 6 seconds of excitation.
- The LRB system undergoes only one significant cycle in the plastic domain. Afterwards, and for all participants, the system responds in its elastic domain.
- As it was observed in Cases 1, 2 and 6, with the RG 1.60 excitation, all participants predict the onset and end of lead yielding at the same instants.
- The maximum horizontal displacements predicted by all participants in Case 12 (EUR spectral shape) are 5 to 8 times lower than in Case 6 (RG 1.60 spectral shape), whereas the vertical displacements are of a same order of magnitude.

Other conclusions are similar to those of previous cases and are not repeated.

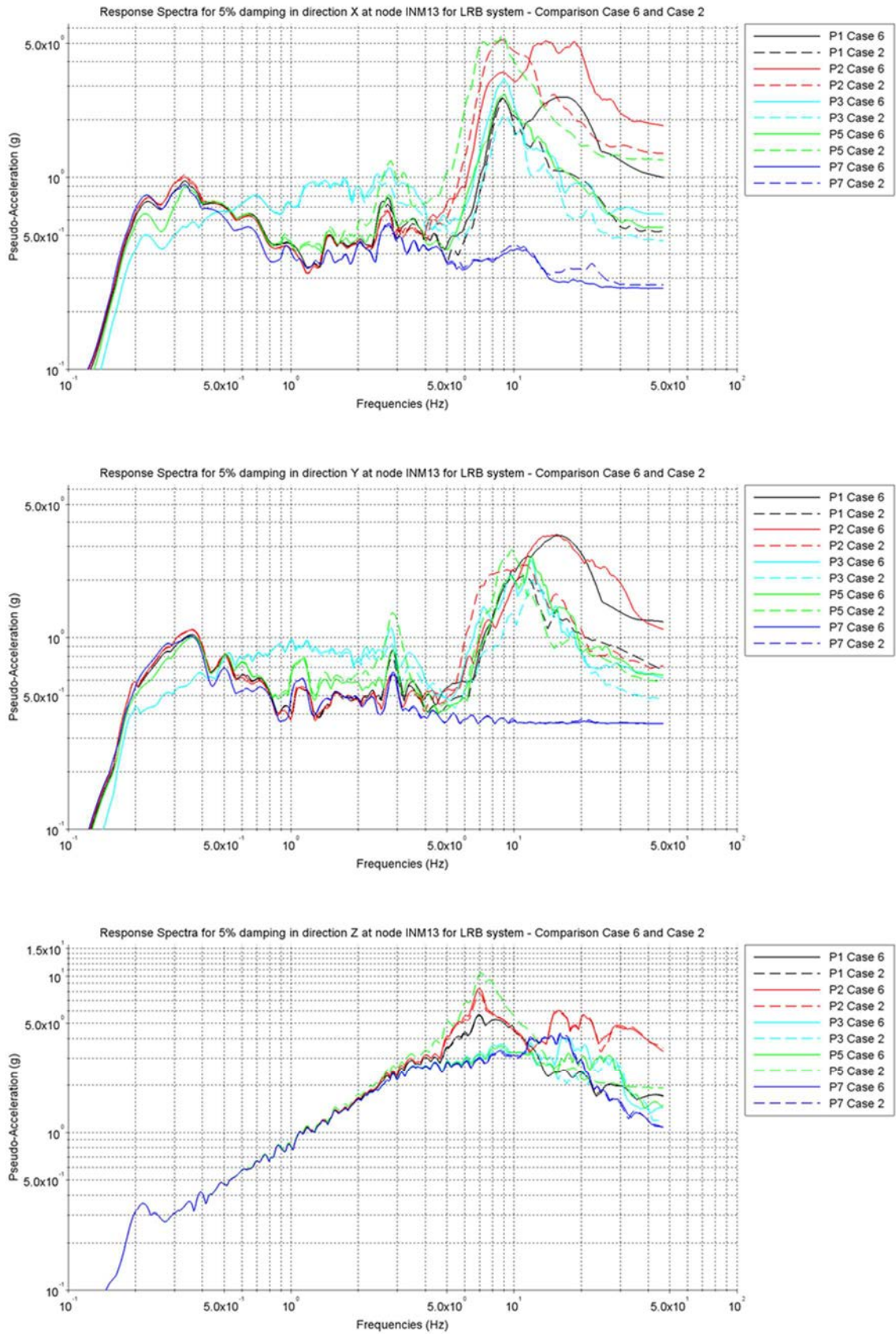


FIG. 62. LRB system - Comparison of response spectra at top of reactor internal structures building in Case 6 (486 isolators) and Case 2 (one macro-isolator).

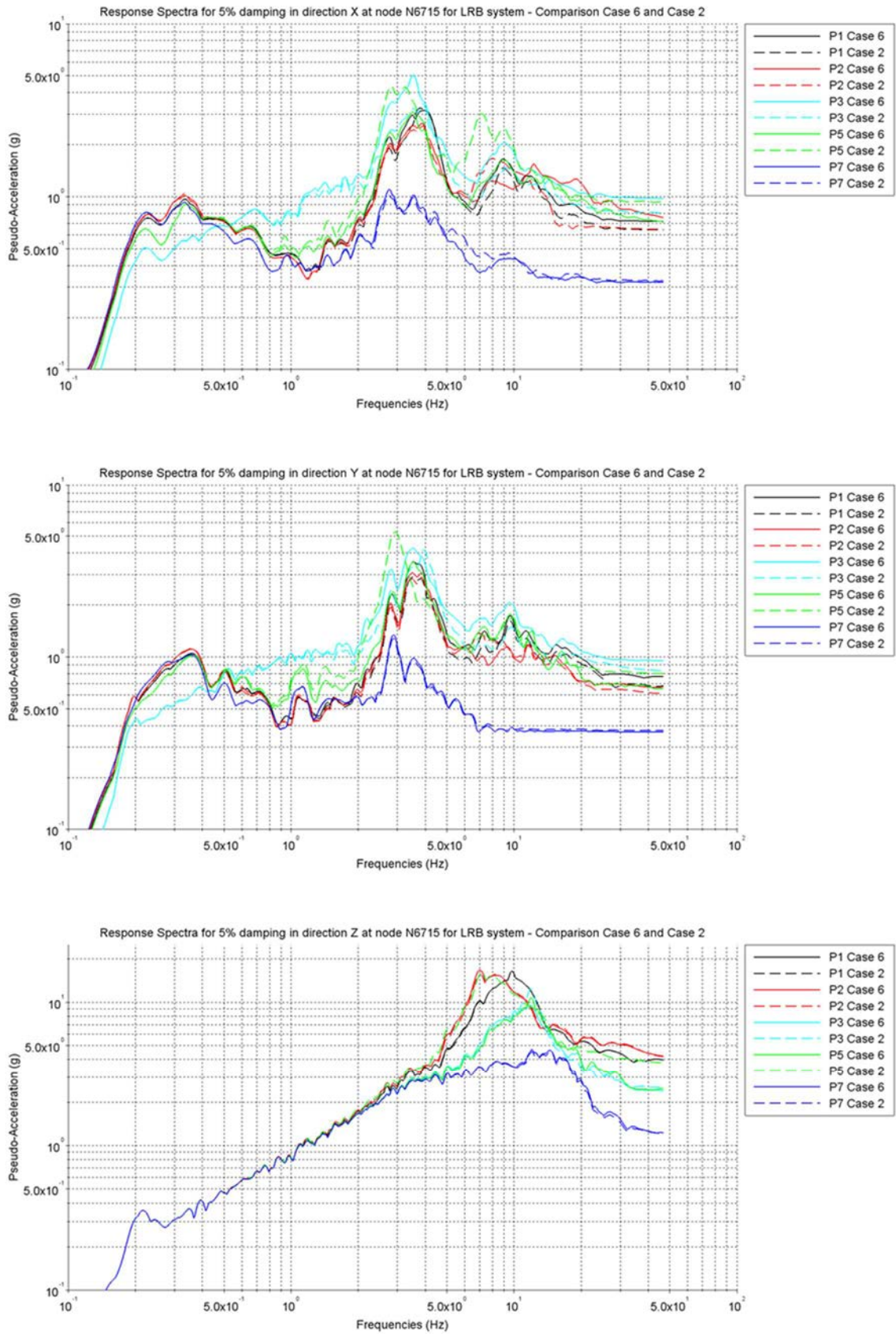


FIG. 63. LRB system - Comparison of response spectra at top of reactor containment building in Case 6 (486 isolators) and Case 2 (one macro-isolator).

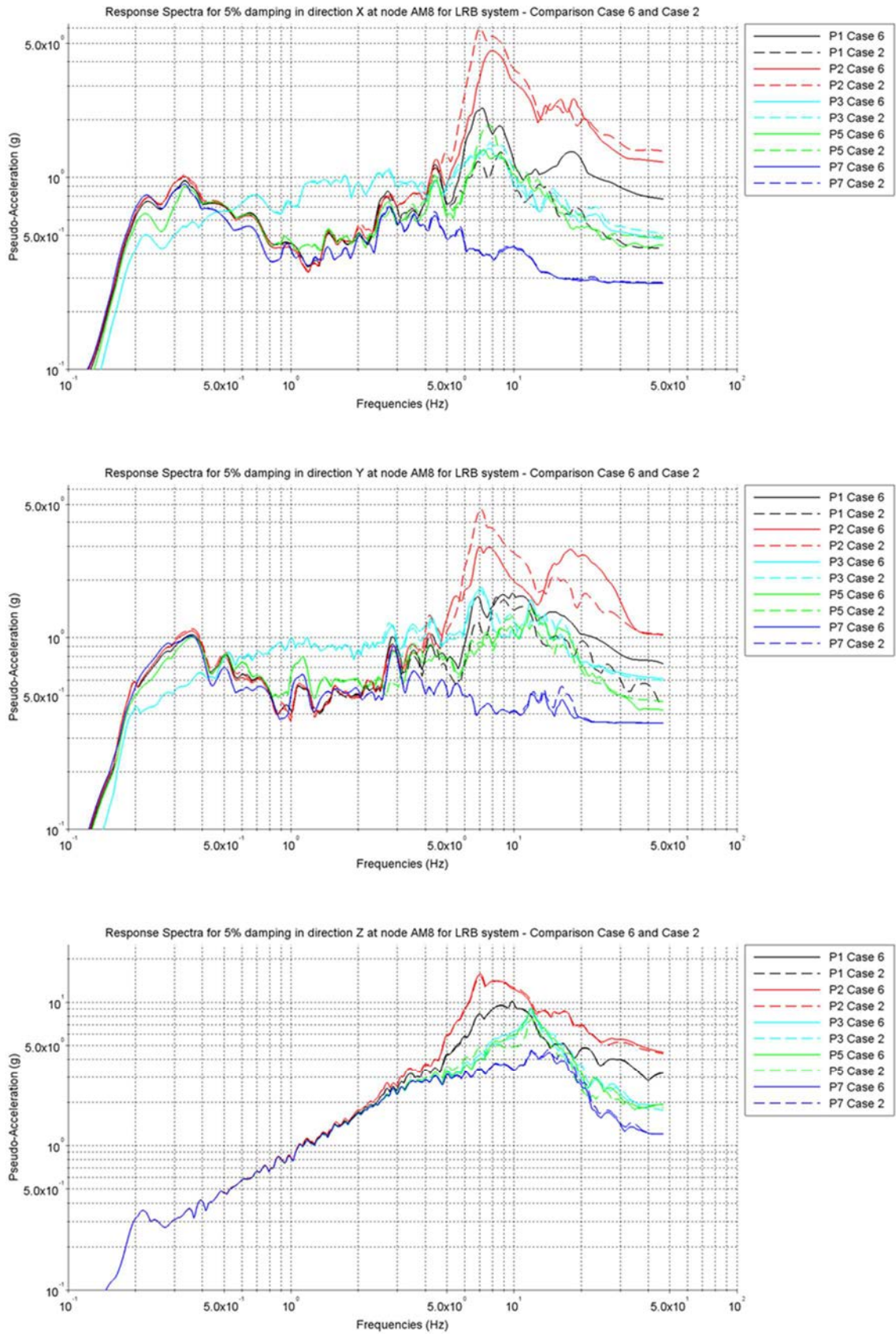


FIG. 64. LRB system - Comparison of response spectra at top of reactor auxiliary complex building in Case 6 (486 isolators) and Case 2 (one macro-isolator).

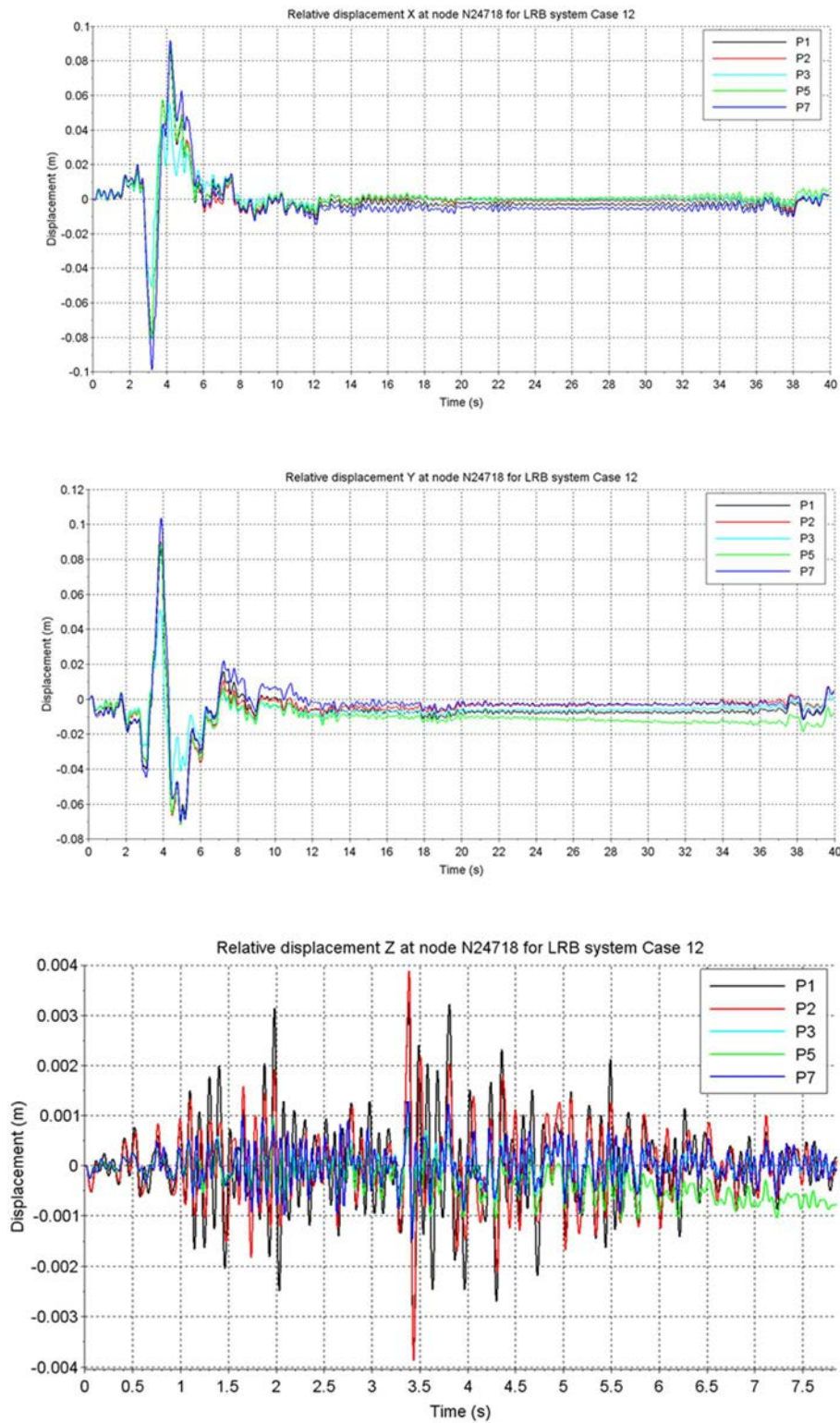


FIG. 65. Case 12 – LRB System – Relative displacement at basemat central node.

4.2.5.2 Case 12 – LRB system – Floor response spectra at the centre of upper basemat

Floor response spectra at the basemat central node for Case 12 are given in Figure 66.

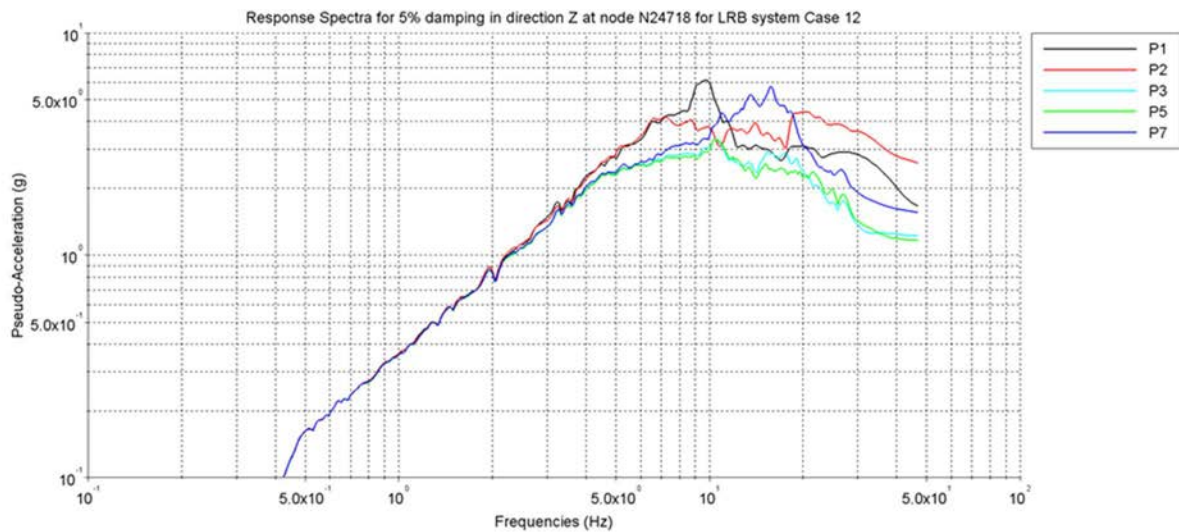
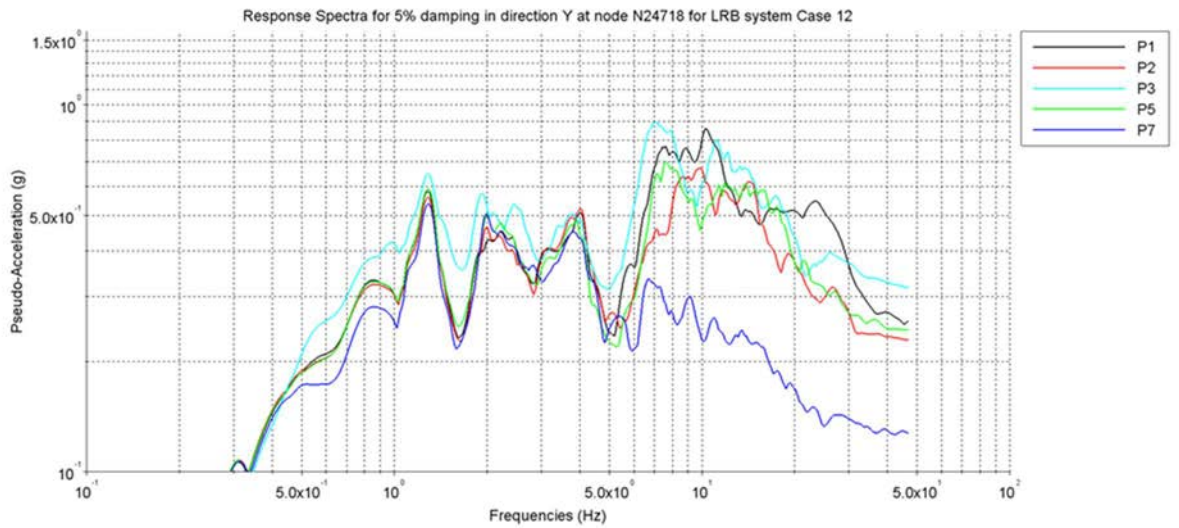
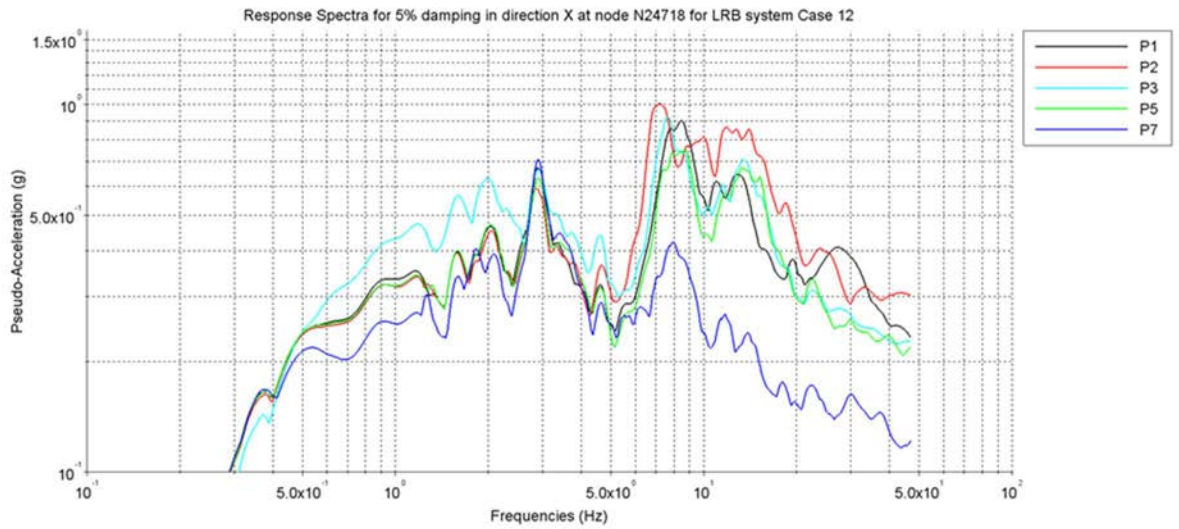


FIG. 66. Case 12 – LRB System – Floor response spectra at basemat central node.

Unlike for Case 6, none of the participant results exhibit a peak at the isolation frequency in the horizontal directions. The efficiency of the seismic isolation system is still excellent with average maximal acceleration of the basemat of 0.22 g in X direction and 0.23 g in Y direction for a peak ground maximal acceleration of 0.835 g.

The dispersion between participants results is significantly lower for this case, with only results of participant P7 separating from the four others at frequencies higher than 5 Hz.

In the vertical direction, the same conclusions as for previous cases apply and are not repeated.

4.2.5.3 Case 12 – LRB system – Floor response spectra at uppermost elevations

As a logical consequence of conclusions for Case 6 and in the previous paragraph, the dispersion observed between participant on the response spectra at buildings top is reduced in Case 12. As an example, Figure 67 gives the response spectra at top of the containment building in the three directions.

4.2.5.4 Case 12 – LRB system – Hysteresis curves for the central isolator

Forces versus distortion curves for the X and Y directions are given in Figure 68. The difference between two groups of participants, already identified in all previous cases is also visible here. Participants P1, P2, P5 and P7 predict about 45% of distortion while participant P3 predicts about 25%.

Hysteresis curves for the vertical direction are given in Figure 69. In this figure, the decrease of vertical stiffness under the effect of horizontal distortion, modelled by participants P1 and P2 seems to be negligible. This is explained by the much more limited distortion induced by the EUR spectral shape. As with the RG 1.60 spectral shape, the occurrence of rubber cavitation is predicted by participants P1 and P2.

4.3 COMPUTED RESPONSES FOR EQSB ISOLATOR

4.3.1 Available results and selection of representative data

For the EQSB isolators, hybrid tests were conducted for Case 1 and Case 3 only. Two participants (P3 and P4) performed all calculations and one participant (P7) performed calculations for all the cases with a DBE level of excitation. Even though reaching generic conclusions with such a reduced number of participant results is difficult, the available data are sufficient to illustrate the effects of different modelling of the EQSB isolator on the analysis outputs. Table 17 summarizes the available results for this type of isolator.

The type of results available are similar to those for the LRB isolator system and are post-processed the same way. The cases selected for detailed analysis are:

- Case 1, corresponding to the design basis earthquake with RG 1.60 spectral shape and one single macro-isolator. Results of Case 1 are presented in Section 4.3.2.
- Case 2, corresponding to the beyond design basis earthquake with RG 1.60 spectral shape and one single macro-isolator. Results of Case 2 are presented in Section 4.3.3. The effect of increased seismic excitation is illustrated by comparison with Case 1.

For each of the selected cases, only a meaningful subset of figures is presented.

No comparison is made between the representation of one macro-isolator and the representation of all individual isolators since the conclusions are strictly identical to those previously obtained for the LRB system. Especially, the stiffening effect of representing all isolators on the basemat of participants who did not rigidify it is also observed, reducing the spread between participants results.

No comparison is made between the response obtained with the EUR spectra and those obtained with the RG 1.60 spectra. Again, the same conclusions as for the LRB apply in this case. Among others, the isolation system undergoes only one significant cycle in the non-linear domain.

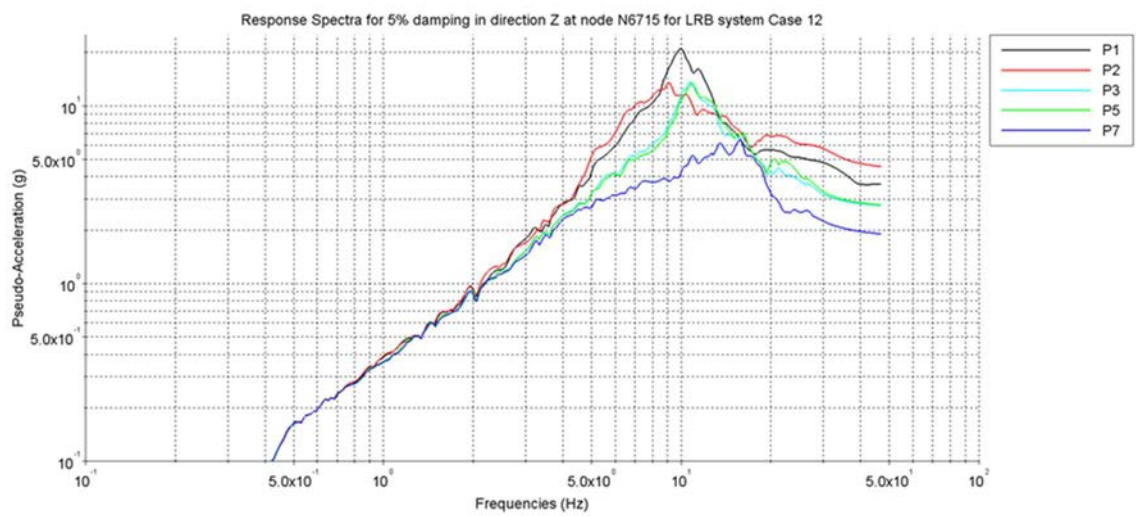
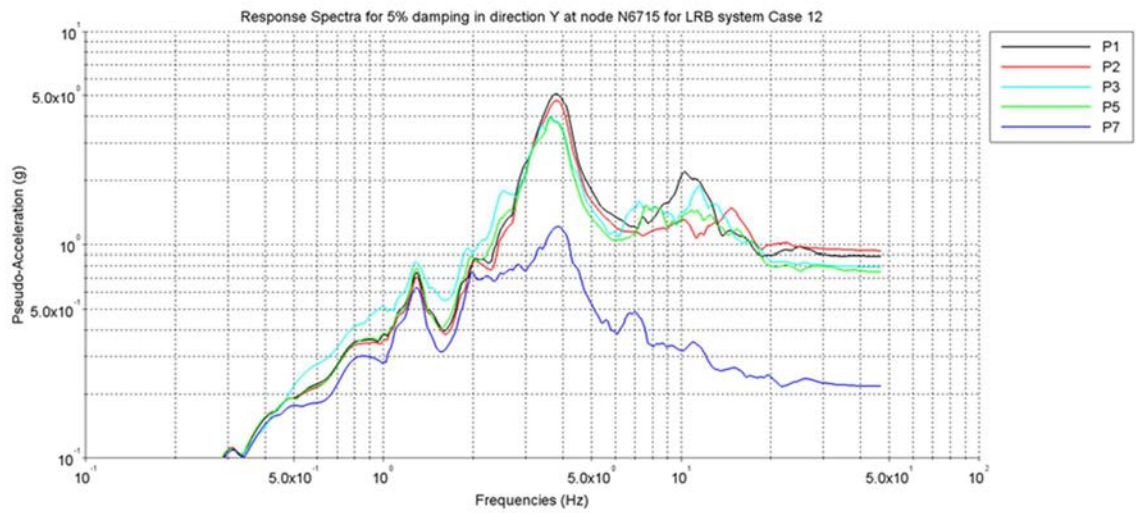
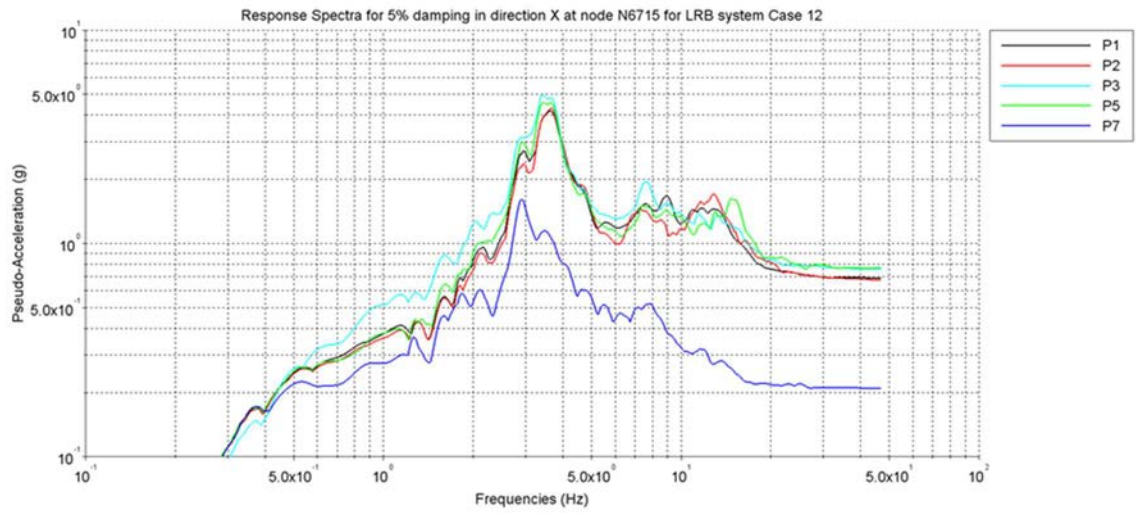


FIG. 67. Case 12 – LRB System – Floor response spectra at top of containment building.

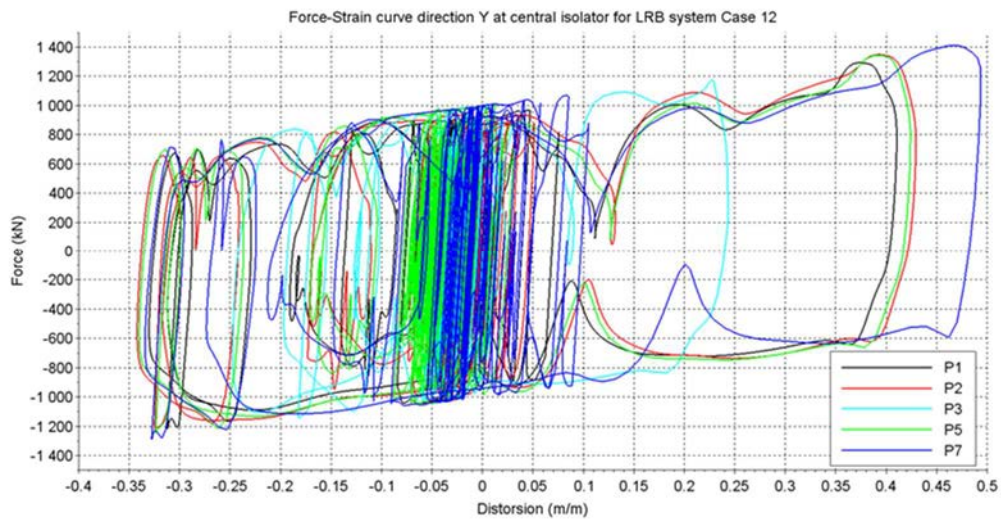
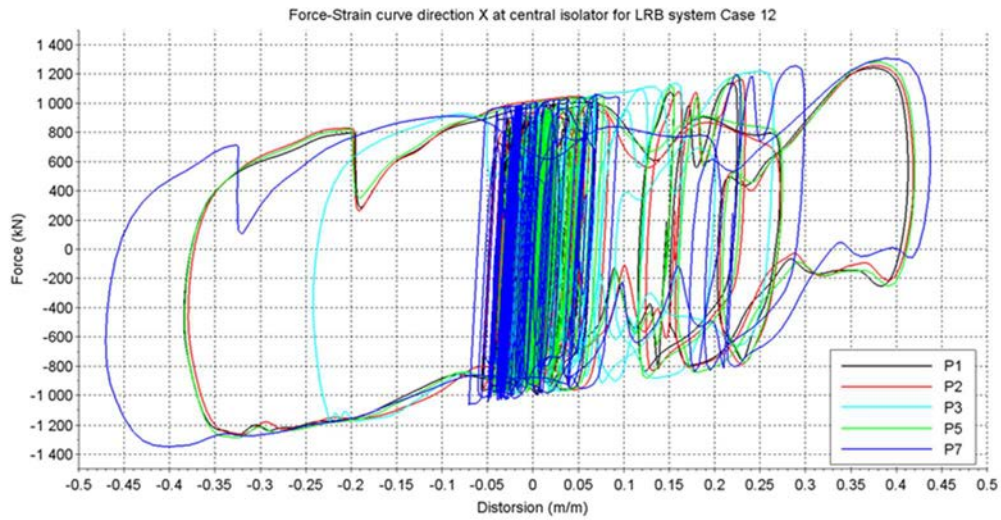


FIG. 68. Case 12 – LRB System - Case 12 – Force-distortion curves in X and Y direction.

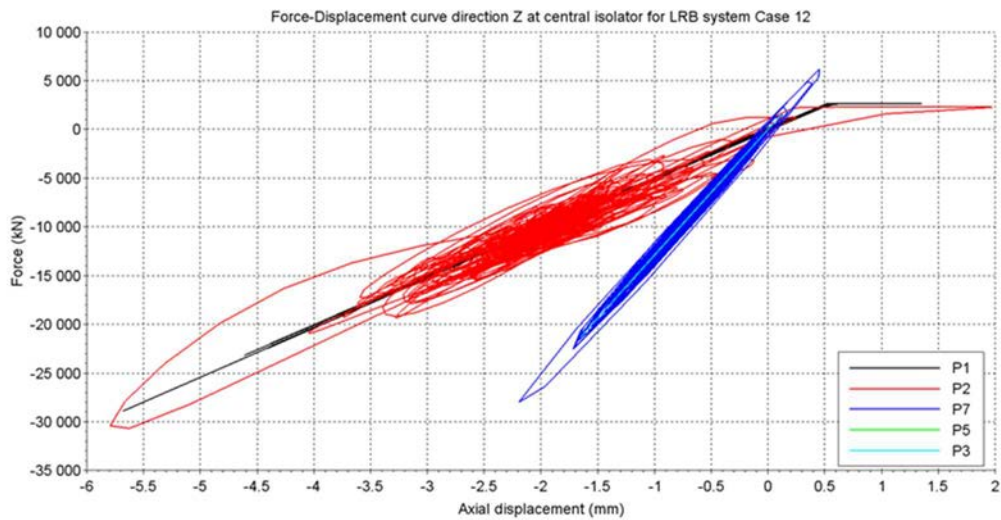


FIG. 69. Case 12 – LRB System – Case 12 – Force-displacement curves in Z direction.

TABLE 17. AVAILABLE RESULTS FOR EQSB ISOLATION SYSTEM

		P0	P1	P2	P3	P4	P5	P6	P7	P8
EQSB Isolator	Case 1	Y			Y		Y		Y	
	Case 2				Y		Y			
	Case 3	Y			Y		Y		Y	
	Case 4				Y		Y			
	Case 5				Y		Y		Y	
	Case 6				Y		Y			
	Case 7				Y		Y		Y	
	Case 8				Y		Y			
	Case 9				Y		Y		Y	
	Case 10				Y		Y			
	Case 11				Y		Y		Y	
	Case 12				Y		Y			

4.3.2 Results of Case 1 – EQSB system – Comparison of computed responses

4.3.2.1 Case 1 – EQSB system – Relative displacement of the centre of the upper basemat

Figure 70 gives the displacement at the central position of the upper basemat in the three directions X, Y and Z.

In the horizontal direction, one group of participants (P5 and P7) predicts significantly higher displacements than a second group of participants, comprising only P3. This grouping is similar to the one observed in all analyses with LRB isolation system. As previously, this division in two groups is not attributed to the modelling of the isolators themselves but to the apparent additional damping acting in parallel to the isolators in participant P3 model.

In the vertical direction, because of their rigid representation of the EQSB isolator, participants P3 and P5 have practically no displacement relative to the ground. The results of participant P7, who updated its vertical stiffness based on test results, shows a dynamic vertical response, even though of limited amplitude (0.5 mm at most).

4.3.2.2 Case 1 – EQSB system – Floor response spectra at the centre of upper basemat

Figure 71 shows the upper basemat response spectra at the central position of the upper basemat in the three directions X, Y and Z.

In the horizontal direction, the results of the two groups of participants identified earlier are again clearly different in the 0 to 5 Hz range. After 5 Hz, where the structural responses are dominant, participants P3 and P5 response spectra exhibit small peaks of approximately the same order of magnitude, whereas practically no peak appears on participant P7 response spectra. The absence of peak at structural frequencies on participant P7 response spectra is similar to the one observed for all cases with the LRB isolation system.

In the vertical direction, the spectra obtained by participants P3 and P5 are identical and correspond to the excitation spectra, once again because of a rigid representation of the EQSB isolator. For participant P7, a peak appears between 15 and 20 Hz.

4.3.2.3 Case 1 – EQSB system – Floor response spectra at uppermost elevations

Response spectra at the top of the internal structure building are selected as a representative example for all buildings and are given Figure 72. As observed for Case 1 with the LRB system, the effect of differences in participants structural responses are cumulated with the effect of different isolators representations, leading to an increased dispersion compared to the response spectra at the basemat level. The causes for the different structural responses were already identified previously: different basemat stiffness and different methods for application of damping.

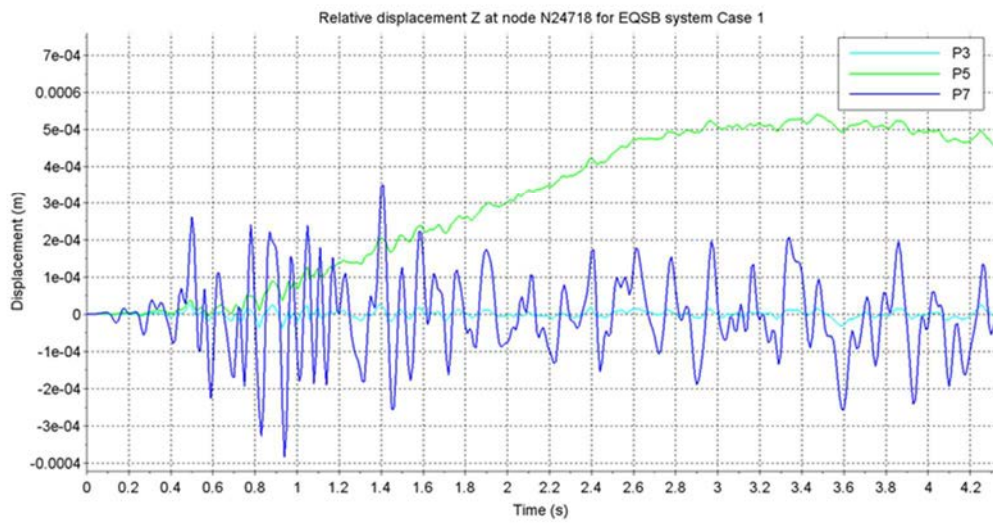
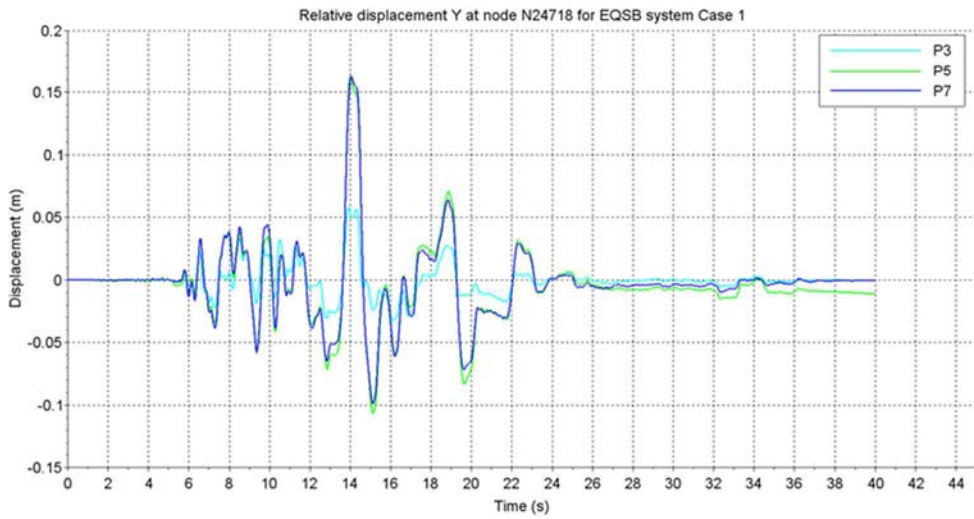
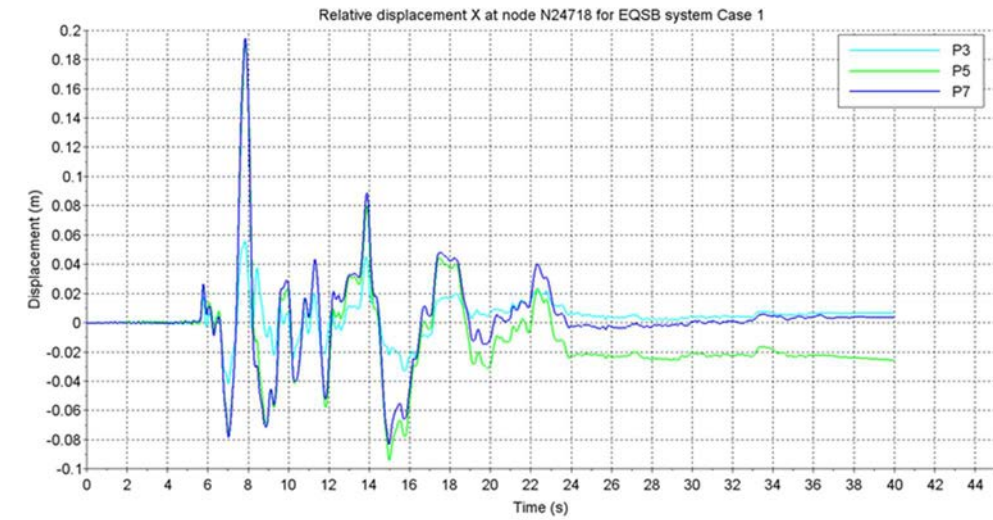


FIG. 70. EQSB system - Case 1 – Relative displacement at centre of upper basemat.

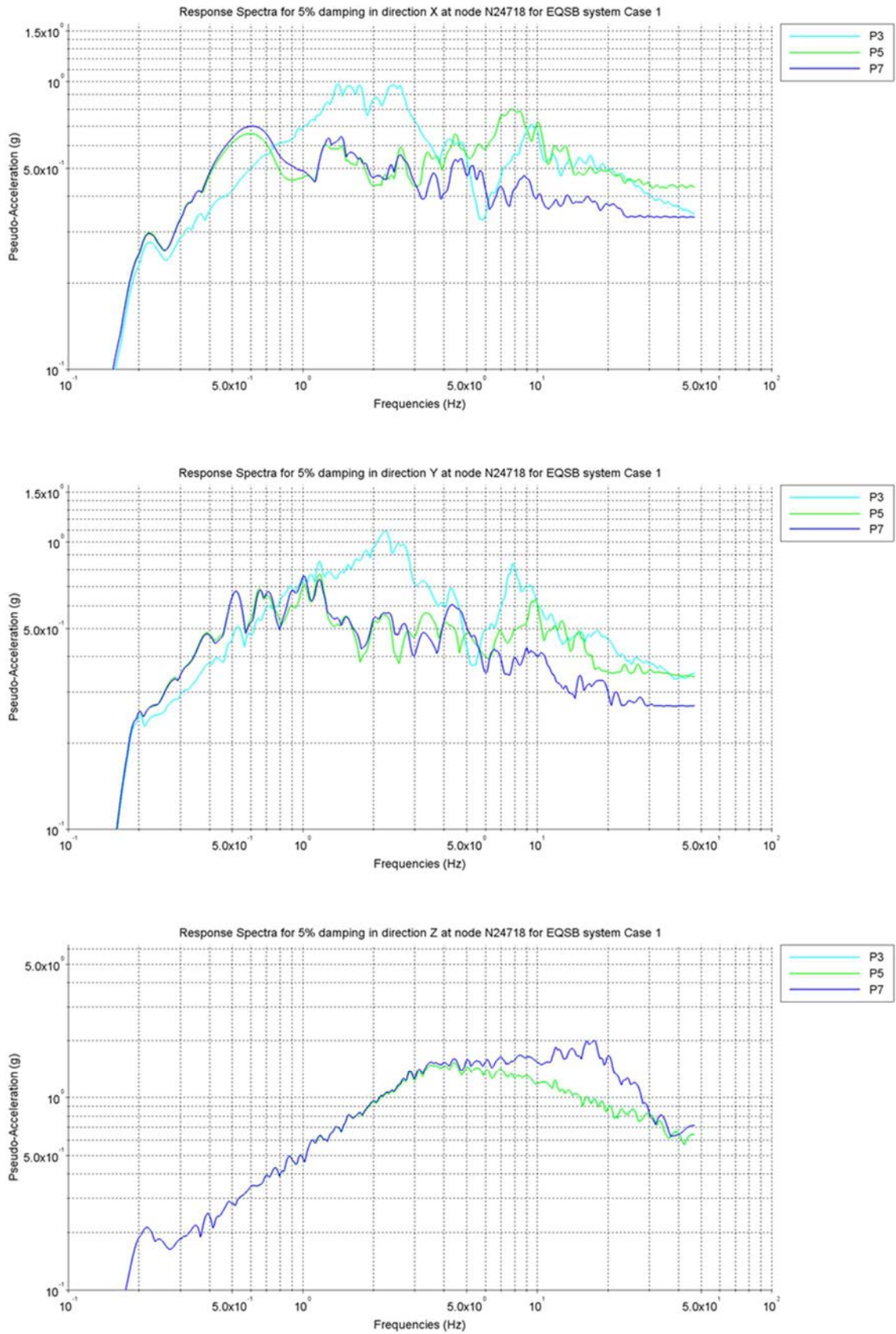


FIG. 71. EQSB system - Case 1 – Floor response spectra at centre of upper basemat.

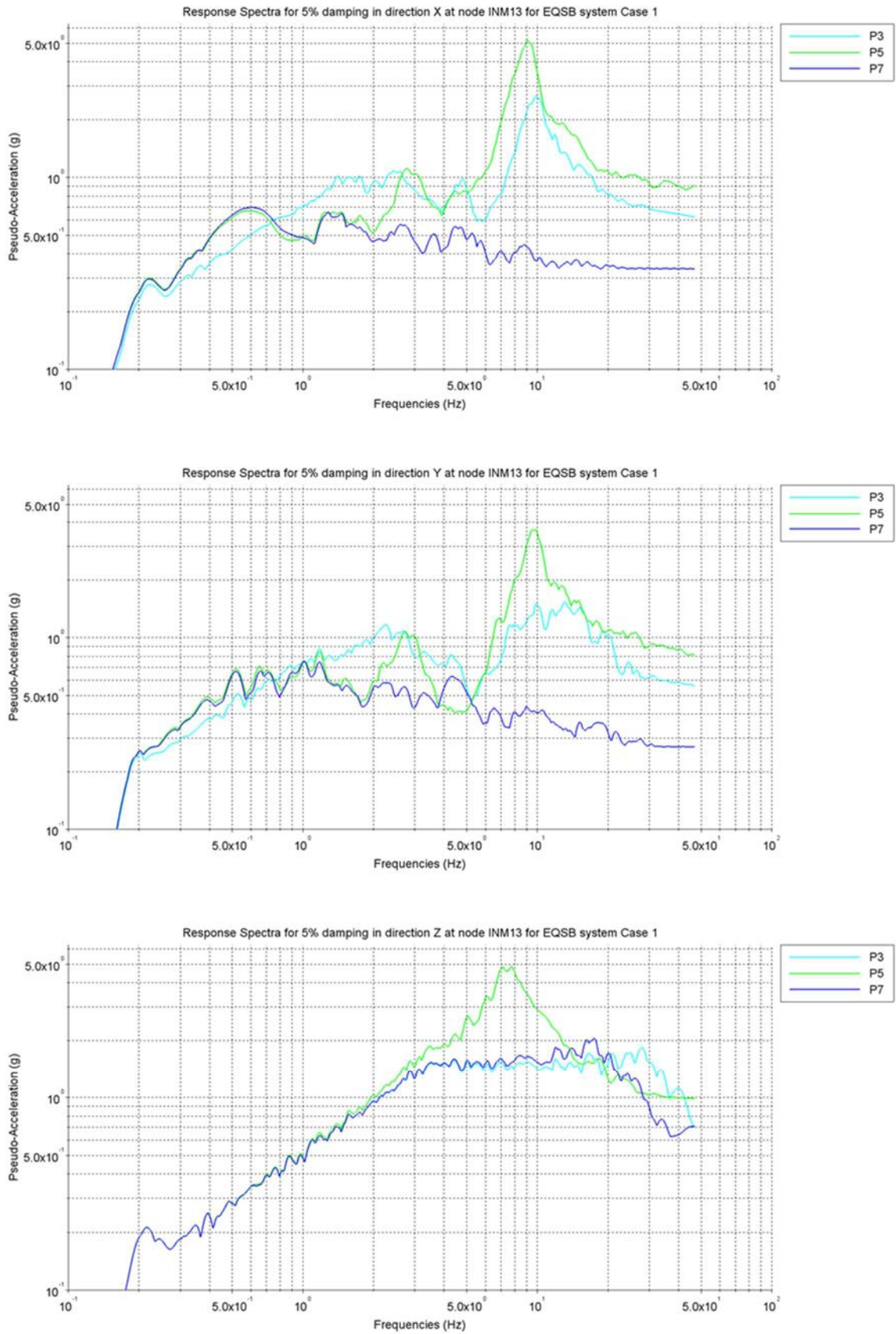


FIG. 72. EQSB system - Case 1 – Floor response spectra at top of internal structures building.

4.3.2.4 Case 1 – EQSB system – Hysteresis curves for the central isolator

Force-displacement curves for directions X and Y are given in Figure 73. In this figure, the horizontal model of participants P3 and P7 appears to have no dependency on the vertical load, with a constant second stiffness throughout the time history. On the opposite, participant P5 hysteresis curves show forces values that significantly overpass the limits defined by the perfect bilinear curves. This is clearly the effect of the vertical force variations on the friction forces within the EQSB.

In the vertical direction, force versus displacement curves are given in Figure 74. Curves for participants P3 and P5 are superposed and fully linear. No damping effect is visible in the forces reported by these participants. The much lower stiffness of participant P7 model is obvious.

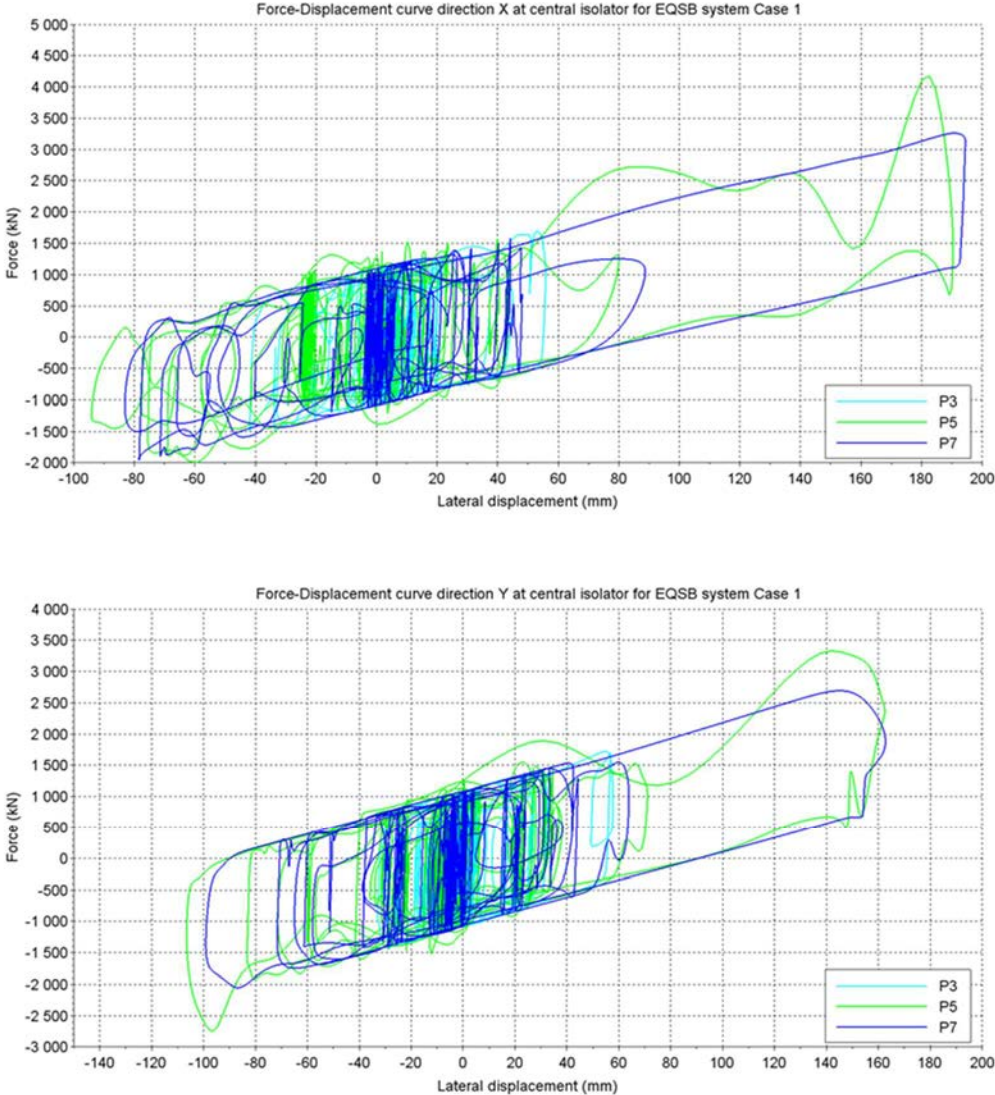


FIG. 73. EQSB system - Case 1 – Force-displacement curves in X and Y directions.

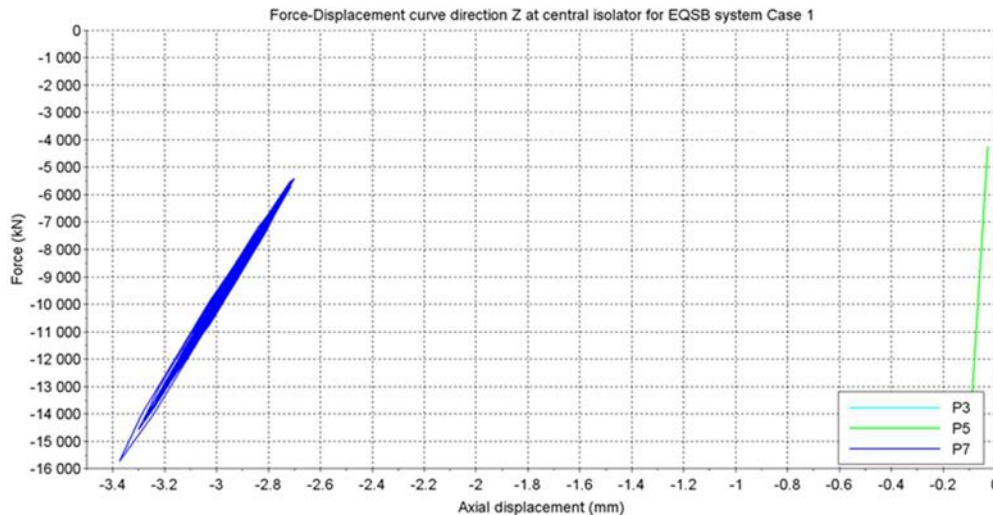


FIG. 74. EQSB system - Case 1 – Force-displacement curves in Z direction.

4.3.3 Results of Case 2 – EQSB system – Effect of increased seismic excitation

4.3.3.1 Case 2 – EQSB system – Relative displacement of the centre of the upper basemat

For the only two participants to have run Case 2 with EQSB isolators, resulting relative displacements are compared to those of Case 1 on Figure 75.

As it was observed with the LRB system, the increase of excitation by a factor 1.67 resulted in an increase of response horizontal displacement by a factor higher than 2. The difference of amplitude between the two participants, each belonging to one of the formerly identified two groups, is also observed in this case.

In the vertical direction, both participants having chosen a linear modelling of the isolator stiffness, the increase of vertical displacement response is linear.

4.3.3.2 Case 2 – EQSB system – Floor response spectra at the centre of the upper basemat

Figure 76 gives the comparison of floor response spectra at the basemat central node obtained in Case 1 and Case 2 and in the X, Y and Z directions.

The results of participant P5 show a clear change in response spectra shape, with a stark increase of both a peak at the isolation frequency and a peak in the range of the structural frequencies (mainly for the X direction). The results of participant P3, on the other side, exhibit a shape similar to the one observed in Case 1. This clear difference between the two participants is attributed to the effect of vertical response on horizontal friction forces within the EQSB. Indeed, as participant P5 modelled the coupling between vertical force and horizontal friction forces, this has the effect of increasing both the response at lower frequencies, when less friction and higher displacements occurs, and at high frequencies, when more friction and more excitation of the structural modes occurs. As a comparison, with the LRB system, it was essentially the peaks at low frequency showing a more than linear increase with excitation increase.

In the vertical direction, since both models are rigid, they produce the same response spectrum, which is equal to the excitation spectrum.

4.3.3.3 Case 2 – EQSB system – Floor response spectra at uppermost elevations

Figure 77 gives the comparison of floor response spectra at the top of one representative building in Case 1 and Case 2 and in the X, Y and Z directions.

The same conclusions as the ones reached for the floor response spectra at the basemat level apply. In the vertical direction, the appearance of a peak on participant P5 response is due to the non-rigid basemat modelled by this participant, as was already identified previously.

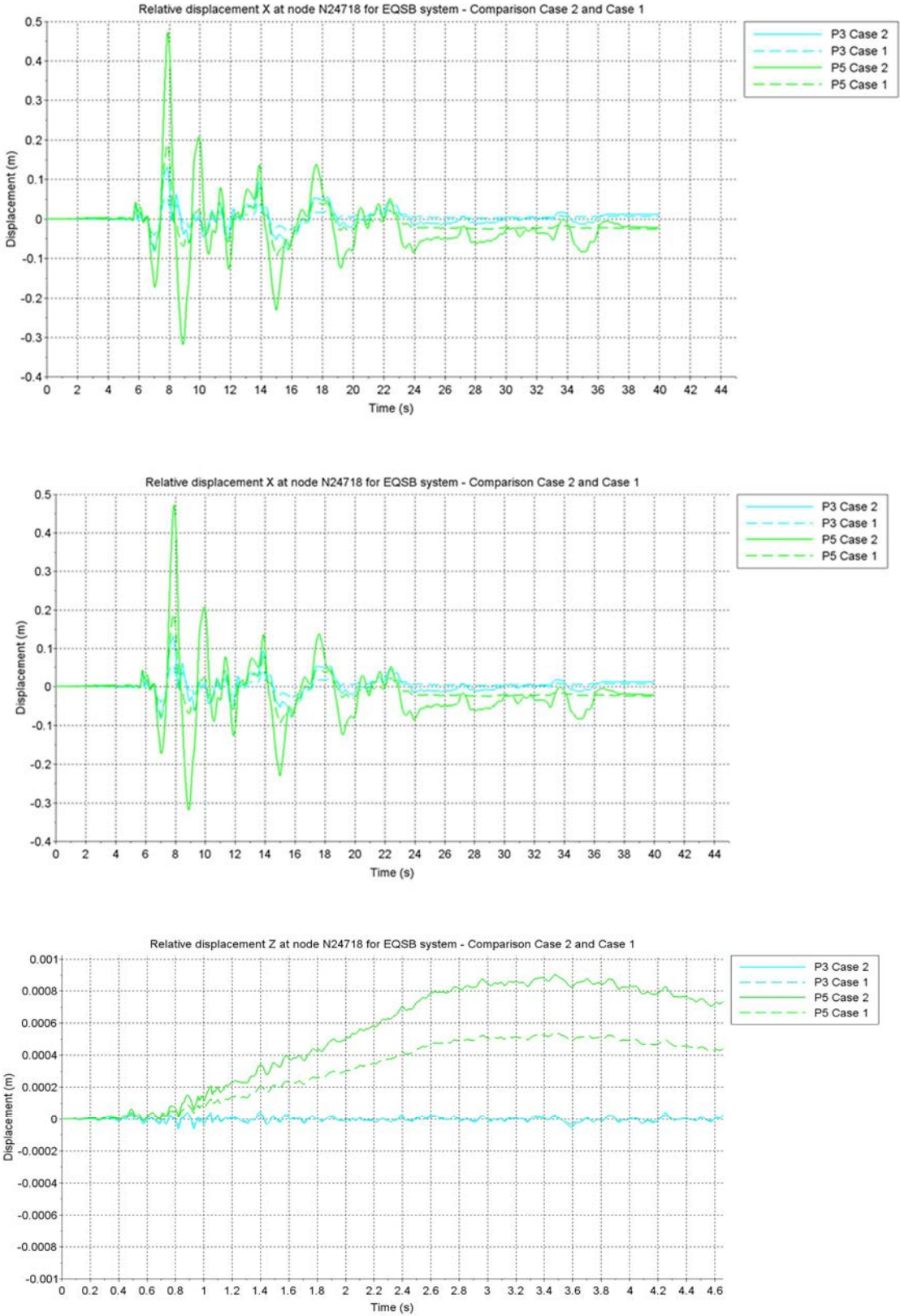


FIG. 75. EQSB system – Comparison of relative displacements in Case 2 (1.67 DBE) and Case 1 (DBE).

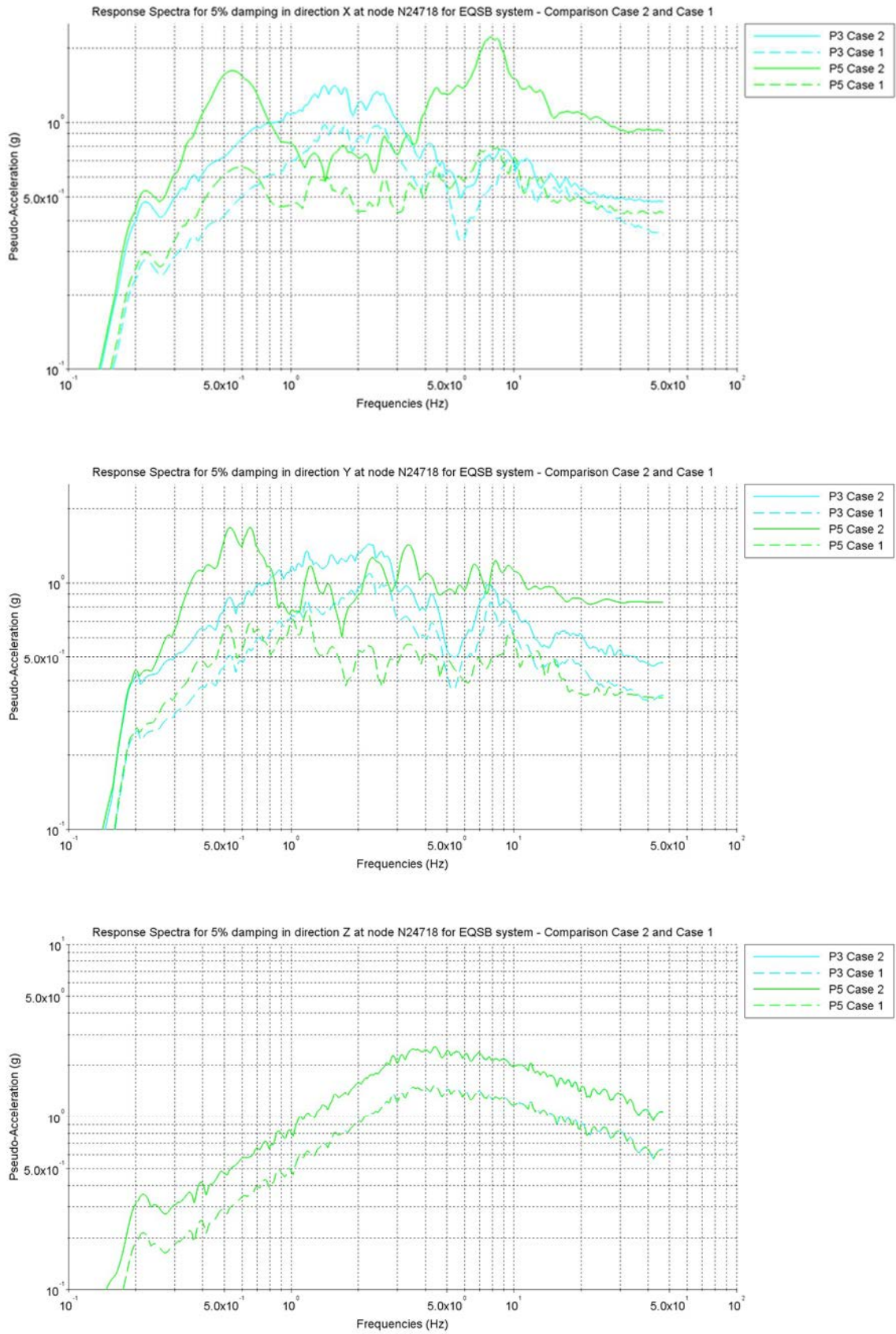


FIG. 76. EQSB system - Comparison of upper basemat floor response spectra in Case 2 (1.67 DBE) and Case 1 (DBE).

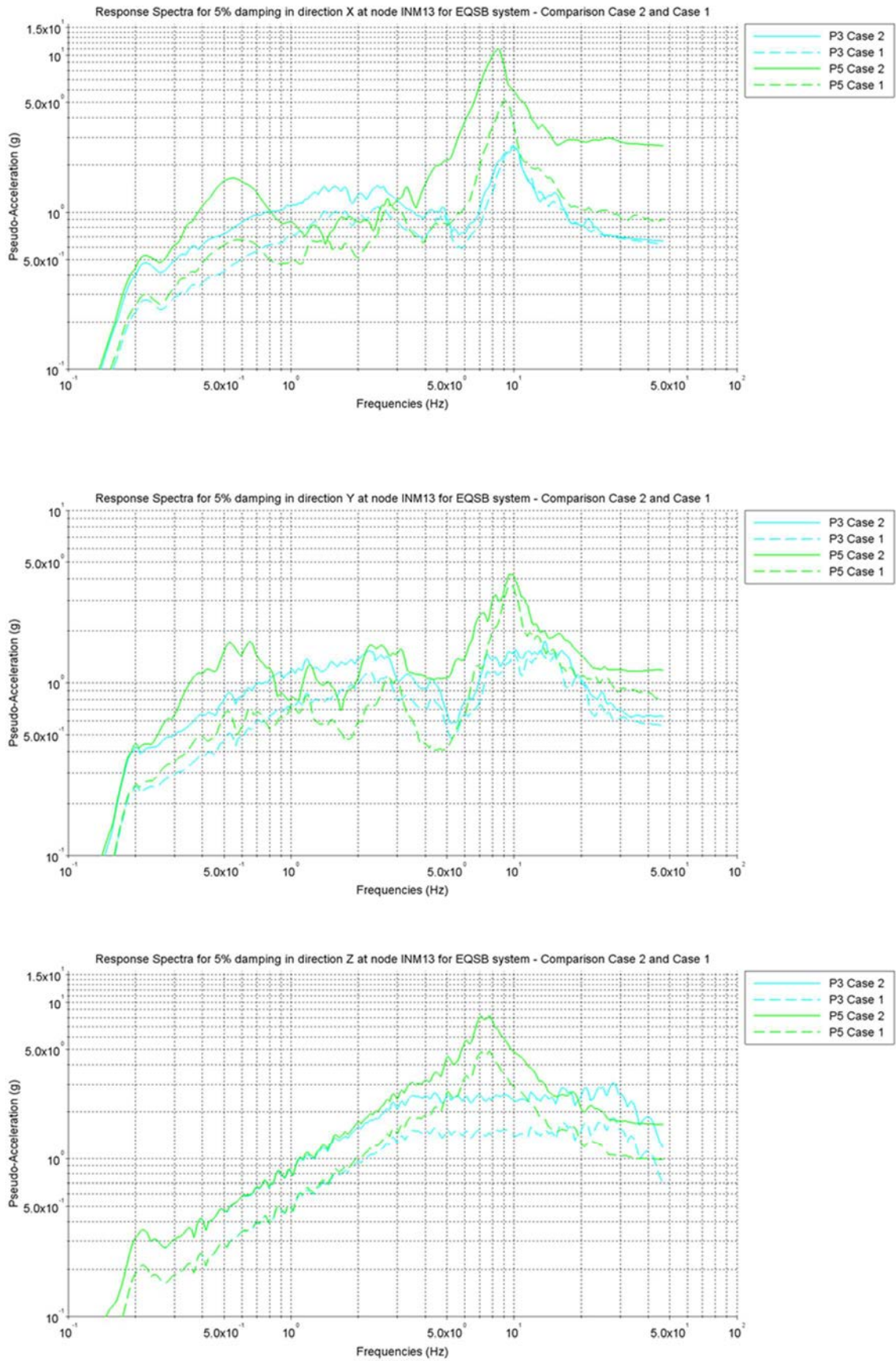


FIG. 77. EQSB system - Comparison of floor response spectra at top of internal structure building in Case 2 (1.67 DBE) and Case 1 (DBE).

4.3.3.4 Case 2 – EQSB system – Hysteresis curves for the central isolator

Figure 78 gives the forces versus displacement curves obtained in directions X and Y. The conclusions reached for Case 1 are even more strikingly observed for Case 2, with the horizontal hysteresis curves of participant P5 showing a strong dependency to the vertical loads whereas the ones of participant P3 exhibit no such dependency.

In the vertical direction, the behaviour for both participants is linear. The curves are showed on Figure 79 only to illustrate that no uplift is predicted to occur in this case, with the vertical stiffness selected by the participants.

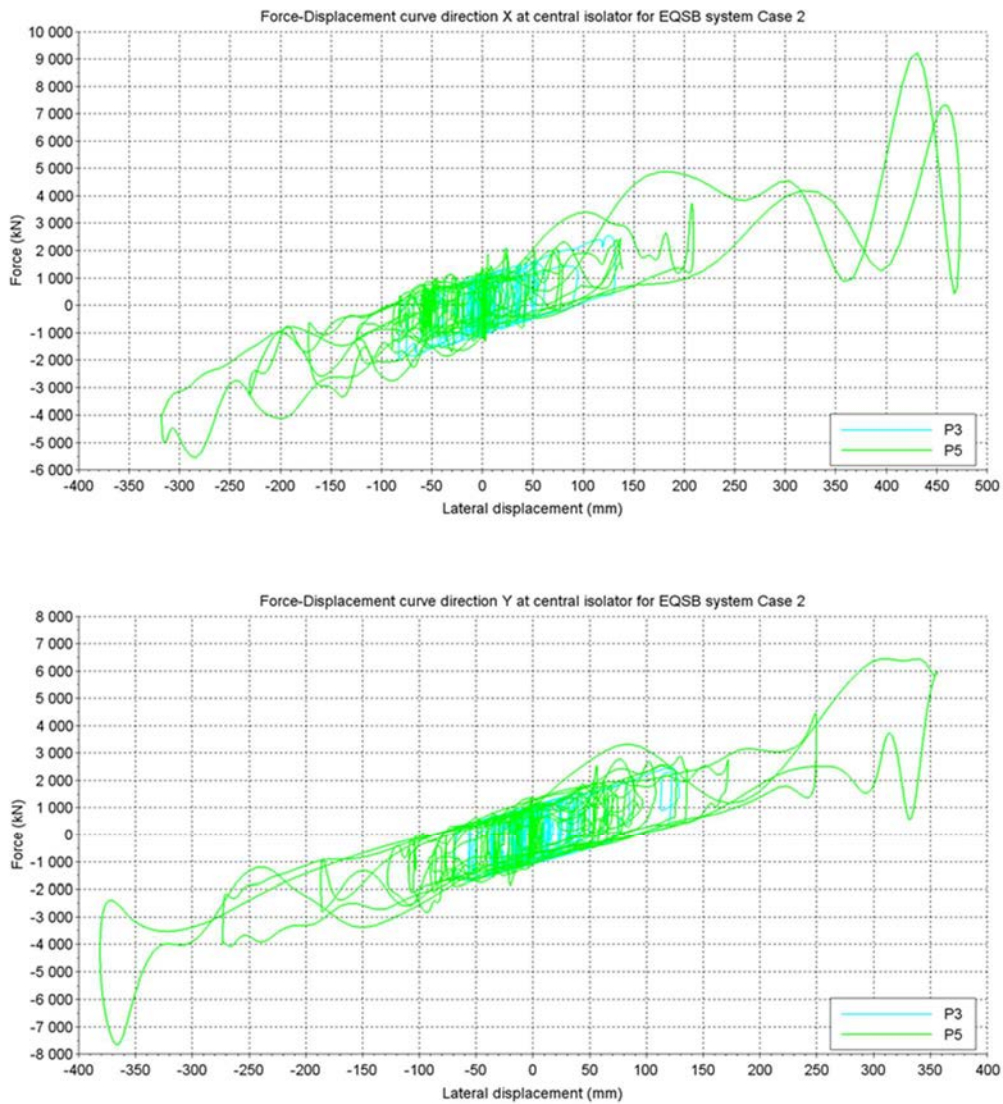


FIG. 78. EQSB system - Case 2 – Force-displacement curves in horizontal X and Y directions.

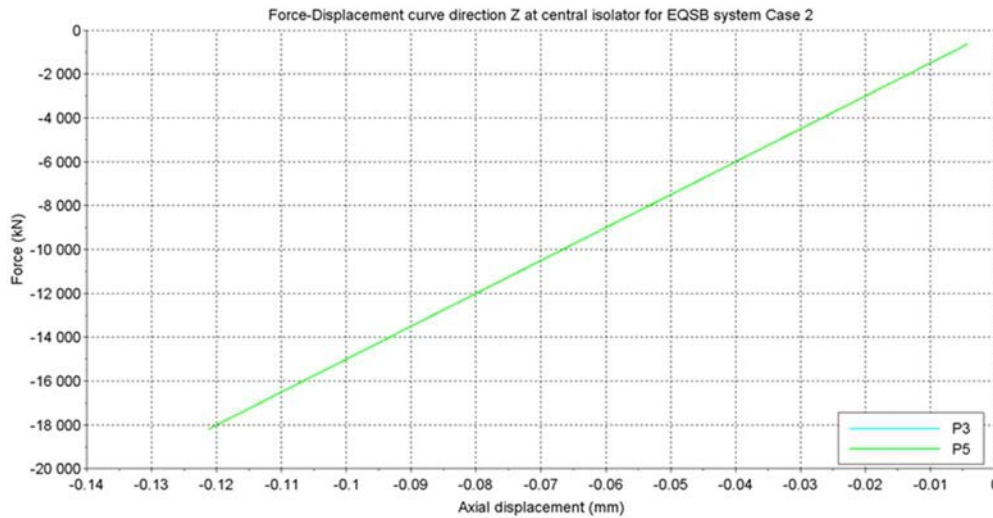


FIG. 79. EQSB system - Case 2 – Force-displacement curves in vertical Z direction.

4.4 COMPUTED RESPONSES FOR TPFB ISOLATOR

The TPFB isolation system was modelled only by participant P5. All cases were run by this participant but no comparison between several participants results is possible. Hybrid tests for the TPFB isolator were performed only for Case 1 (see Section 5).

4.5 CONCLUSIONS FROM THE ANALYSIS OF THE RESULTS BY PARTICIPANTS

4.5.1 Maximum global acceleration of the isolated superstructure

All participants, for all calculations cases, predicted a high efficiency of the seismic isolation system and a significant reduction of the horizontal response spectra in the superstructure, in comparison to what they would have been without isolation. The maximum basemat acceleration is always predicted to be significantly lower than the maximum ground acceleration (0.5 g for DBE and 0.837 g for BDBE) and amplification for higher elevations in the superstructure are low. In this qualitative aspect, results from all participants are fully consistent.

In a more quantitative way, Table 18 and Table 19 summarize the calculated maximum basemat accelerations for all participants and all cases analysed in the present Section. The mean value is also presented in these tables as well as the ‘coefficient of variation’ (COV), which is the ratio of the standard deviation to the mean. The COV is directly comparable with the logarithmic standard deviation (β) used in Seismic Probabilistic Safety Assessments (S-PSA) to introduce uncertainties, as far as it is less than about 40%. To have some reference value, note that in S-PSAs uncertainty in the seismic response results due to variability in structural modelling and damping effects is introduced by a composite β the order of 0.20 (Ref. [30]).

For all cases where the vertical excitation does not too significantly affect the horizontal response (case 1, 2 and 6 with LRB isolation system and case 1 with EQSB isolation system), the COV remains below 0.15, highlighting a rather good convergence of the different participants models, despite strong structural modelling differences for both the superstructure and the isolation system. These differences appear more stringently in other cases with COV values reaching, for example, 0.29 in case 12 with LRB isolation system.

4.5.2 Maximum displacements and hysteresis curves

Analysing the displacement curves and the force-distortion curves in the horizontal directions for all cases, it was observed that yielding and non-yielding time intervals, or sliding and non-sliding time

intervals, are always fully in phase in all participants' results. All models predict the onset of yielding or sliding and the end of yielding or sliding at the same time.

TABLE 18. SUMMARY OF CALCULATED BASEMAT MAXIMUM ACCELERATION IN THE X DIRECTION

Maximum basemat acceleration along X (g)						
	LRB isolation system				EQSB isolation system	
	Case 1 (DBE RG1.60)	Case 2 (BDBE RG1.60)	Case 6 (BDBE RG1.60)	Case 12 (BDBE EUR)	Case 1 (DBE RG1.60)	Case 2 (BDBE RG1.60)
P1	0.195	0.296	0.381	0.233		
P2	0.259	0.410	0.372	0.303		
P3	0.220	0.352	0.336	0.226	0.350	0.478
P4	0.252					
P5	0.206	0.331	0.311	0.218	0.430	0.926
P6	0.234	0.343				
P7	0.167	0.264	0.262	0.122	0.338	
P8	0.233	0.380				
Mean	0.221	0.339	0.332	0.220	0.373	0.702
COV	14%	14%	15%	29%	13%	45%

TABLE 19. SUMMARY OF CALCULATED BASEMAT MAXIMUM ACCELERATION IN THE Y DIRECTION

Maximum basemat acceleration along Y (g)						
	LRB isolation system				EQSB isolation system	
	Case 1 (DBE RG1.60)	Case 2 (BDBE RG1.60)	Case 6 (BDBE RG1.60)	Case 12 (BDBE EUR)	Case 1 (DBE RG1.60)	Case 2 (BDBE RG1.60)
P1	0.248	0.397	0.414	0.258		
P2	0.238	0.423	0.455	0.229		
P3	0.233	0.338	0.340	0.317	0.348	0.473
P4	0.205					
P5	0.218	0.387	0.387	0.244	0.340	0.833
P6	0.230	0.387				
P7	0.198	0.354	0.354	0.127	0.269	
P8	0.243	0.388				
Mean	0.227	0.382	0.390	0.235	0.319	0.653
COV	8%	7%	12%	29%	14%	39%

With the LRB system, the overall shape of the horizontal force-displacement curves is also the same for all participants. Significant differences are only observed when the excitation level is increased, and a separation occurs between the results of participants who modelled the lead heating phenomenon (P1 and P2) and the others.

With the EQSB system, significant differences in hysteresis curves are obtained between the participant who did include a dependency of the friction force on the vertical load (P5) and those who did not (P3 and P7). This difference is observed in all benchmark cases and is further amplified when the excitation level is increased. Even though it did not occur in the present simulations, it is expected to have an even more important effect if uplift occurs within the EQSB isolators.

The displacement amplitude in the yielding or sliding phases is predicted differently by the different participants, with one group (P1, P2, P5, P6 and P7) predicting significantly larger isolators distortions

and upper basemat displacements than the other (P3, P4 and P8). This difference is mainly explained by different modelling of damping forces. The group of participants predicting lower displacement has either implemented some equivalent viscous dampers acting in parallel to the lead cores or has used a mass proportional damping matrix on the superstructure, which is known to have the effect of artificially damping its rigid body motions.

Selecting only the results of the first group of participants, considered to be more representative, Table 20 and Table 21 summarize the computed basemat relative displacements respectively in X and Y directions. The mean value is also presented in these tables as well as the COV, as defined in the previous paragraph. In all cases, the COV is found to be lower than 0.12, most of the time significantly. This highlights the fact that, even with different tools, different models and different hypotheses, provided that no undue damping is added in the analysis, there is very limited scatter in the prediction of the maximum displacement values. When results of all participants are considered, the overall COV is in excess of 0.40.

TABLE 20. SUMMARY OF CALCULATED BASEMAT MAXIMUM DISPLACEMENT IN THE X DIRECTION, FOR A SELECTED GROUP OF PARTICIPANTS

Maximum displacement along X (m)							
		LRB isolation system				EQSB isolation system	
		Case 1	Case 2	Case 6	Case 12	Case 1	Case 2
Selected 1st group of participants	P1	0.221	0.480	0.479	0.087		
	P2	0.231	0.501	0.499	0.088		
	P5	0.225	0.494	0.496	0.088	0.190	0.473
	P6	0.225	0.494				
	P7	0.261	0.566	0.567	0.099	0.194	
	Mean	0.233	0.507	0.510	0.091	0.192	0.473
	COV	7%	7%	8%	6%	1%	

TABLE 21. SUMMARY OF CALCULATED BASEMAT MAXIMUM DISPLACEMENT IN THE Y DIRECTION, FOR A SELECTED GROUP OF PARTICIPANTS

Maximum displacement along Y (m)							
		LRB isolation system				EQSB isolation system	
		Case 1	Case 2	Case 6	Case 12	Case 1	Case 2
Selected 1st group of participants	P1	0.285	0.708	0.710	0.086		
	P2	0.296	0.746	0.752	0.090		
	P5	0.263	0.670	0.676	0.089	0.162	0.381
	P6	0.262	0.670				
	P7	0.339	0.796	0.797	0.104	0.163	
	Mean	0.289	0.718	0.734	0.092	0.163	0.381
	COV	11%	7%	7%	9%	0%	

4.5.3 Floor response spectra at higher elevations

The difference between the two above mentioned groups is also observed on response spectra in the 0 to 3 Hz frequency range. Particularly, for higher excitations, a peak appears at the isolation frequency for the first group while it does not appear for the second group. Instead, the second group always predict a higher peak between 1 and 2 Hz, with the LRB as well as with the EQSB system. For frequencies higher than 3 Hz, in all directions, the influence of structural modes is predominant and the differences between participants results are not anymore due to their different isolation system modelling but to different superstructure modelling and to the use of different simplifying hypotheses.

Among others, the structural responses were found to be significantly affected by different basemat representations: from fully stiff to significantly flexible, and by different ways to merge 486 non-linear isolators into one or several macro isolators. For cases where all 486 isolators were represented, a distinctly reduced scattering of participants response spectra is observed. Besides removing the simplifying hypothesis for macro isolators, the representation of all individual isolators effectively stiffens the basemat of those participants who represented it as unrealistically flexible.

The influence of the structural modes response on the horizontal and vertical response spectra is highly dependent on the modelling of damping forces that has been adopted by different participants. Among others, it was observed that one participant (P7) significantly overdamped its structural responses, leading to a quasi-absence of peaks at the structural modes frequencies on its response spectra. At the opposite, participant P2 seemed to have a low damping on its structural modes and possibly also on its isolators model in the vertical direction and in rocking, leading to high peaks on its response spectra.

As a consequence, a relatively high dispersion of floor response spectra was observed in the benchmark results, with COVs for ZPA in the top elevations of the different buildings sometimes exceeding 0.40.

4.5.4 Effect of seismic isolation system models

For the LRB isolation system at design basis earthquake level, the effect of introducing lead heating, reduction of vertical stiffness due to horizontal distortion and rubber cavitation into the isolators numerical models, as was done by participants P1 and P2, was not observed to be predominant.

On the other side, these effects were found to significantly affect all displacements, response spectra and hysteresis curves at beyond design basis earthquake level. The structural mode frequencies were also shifted in a noticeable manner when considering such effects. New peaks appear in the high frequency range of the response spectra due to the occurrence of cavitation, which produces impact like loads on the basemat.

Representing the dependency of the rubber horizontal stiffness to the vertical compressive force was not found to have any significant effect in this benchmark.

For the EQSB isolation system, the effect of coupling the friction force to the vertical pressure exerted on the bearing was found to be predominant on all results for both design and beyond design basis excitation levels.

4.5.5 Remarks on the dispersion of results

Only a few benchmark cases corresponding to the LRB isolator have enough contributions from participants to provide some statistically significant metrics of dispersion. Relevant statistics are those which refer to magnitudes important for a designer, such as, the maximum distortion computed at the isolators or the ZPA and peaks at floor spectra.

After reviewing dispersion between the results reported by the participants, the following points are noted:

- Maximum horizontal accelerations of the upper basemat are predicted with a relatively low dispersion. Computed COVs are between 0.07 and 0.15.
- Isolator distortion and upper basemat maximum displacements are predicted with a large scatter, for the reasons explained in the previous sections. When considering all participants, COVs are in excess of 0.40. When taking only the results of one group of participants, the COV of the predicted maximum displacement values is no greater than 0.11. This shows that if engineers follow carefully the same modelling assumptions, small dispersion of results can be obtained, thus highlighting the need for a design code sharing common practice, especially about modelling damping effects.
- For frequencies higher than 3 Hz, the influence of structural modes is predominant, and the differences are due to different superstructure modelling and to the use of different simplifying hypotheses. COVs for ZPA in the top elevations of the different buildings exceed 0.40. The

benchmark organization tried to avoid this source of dispersion by supplying all participants with the same structural model. However, it has proven to be very difficult that analysts use a given model without “correcting” it according to their own understanding.

When differences due to (a) different modelling of the basemat stiffness, (b) different representation of damping outside the isolators themselves, and (c) different hypotheses to merge 486 isolators into one or 5 macro-isolators are set aside, it is found that participants that have adopted the same hypotheses obtain globally similar results. This is illustrated in Figure 80 for participants P1, P2 and P5 in Case 6 with the LRB isolation system. The remaining differences on these curves, are explained by the consideration of lead plug heating and non-linear vertical isolators behaviour by participant P1 and P2 and not by participant P5.

Hence, it seems that, given the nature of this type of analyses, the role of a carefully implemented Peer Review of the modelling assumptions and results by experienced engineers, can be key to assure an acceptable reliability.

4.6 PARAMETRIC STUDIES WITH LARGER SEISMIC INPUT

As a supplement to the benchmark cases, and using the model with 486 individually represented isolators, one participant (P2) conducted a parametric analysis increasing the seismic level to 2.25 times and 3 times the DBE for the LRB case. The results of this study are presented here to further illustrate the effect of an increasing seismic level on the superstructure displacements and floor response spectra.

Figure 81 gives the evolution of displacement time histories in one horizontal direction with the RG 1.60 spectral shape. Figure 82 illustrates the same evolution with the EUR spectral shape. With the RG 1.60 spectral shape, the response non-linearity with increasing excitation level is obvious. The lead heating effect, already present for 1.67 times the DBE becomes predominant with 2.25 times the DBE, leading to calculated displacements that are above the LRB shear ultimate capacity (1 m of displacement is approximately 500 % of distortion). Curves for three times the DBE are not plotted in this case since the isolator model reaches its instability limits and produces unreasonable results. For the EUR spectral shape, on the other side, the LRB isolator distortion remains very limited, even with 3 times the DBE. With such ground motion spectral shape, the isolator failure is not expected to be caused by excessive shear alone.

Figure 83 and Figure 84 illustrate the vertical displacement time histories evolution, respectively, for the RG 1.60 and for the EUR spectral shapes. With the RG 1.60 spectral shape, the predominant effect is the strong reduction of vertical stiffness induced by the isolator’s distortion. A clear correlation is identified between the large yielding phases in Figure 81 and the resulting stiffness reduction in Figure 83. With the EUR spectral shape, this vertical stiffness reduction effect is not observed. Instead, the onset of significant cavitation phases, comparable to uplifts of the upper basemat relative to its foundation, is visible on Figure 84. The phenomenon is especially amplified with the excitation of 3 times the DBE level. Therefore, with an excitation signal fitting the EUR spectra, the isolator failure is expected to be caused by a combination of shear and tension within the rubber.

The evolution of floor response spectra is given in Figure 85 through Figure 88, for the RG 1.60 and the EUR spectral shape and for both the top of containment building and the top of internal structures building. In the horizontal directions, it is observed that:

- Between 0 and 1 Hz, the further the excitation level is increased, the higher and clearer is the peak at the isolation frequency. As for the displacement time histories, this peak amplitude increases in a very non-linear manner with the excitation level.
- Between 1 and 5 Hz, where the main containment building structural modes are, there is no significant increase of the response spectra with the excitation level. Modes in this domain are mostly excited by the elastic horizontal forces developing into the LRB system previous or after the yielding phases, which are intrinsically limited.
- Between 5 Hz and 10 Hz, where structural modes of other buildings as well as the superstructure vertical mode are located, there is a new increase of response spectra as a

function of the excitation. This increase is associated to the coupling between vertical excitation and horizontal structural response.

- After 10 Hz and at higher frequency, a new spectral content appears for the higher excitation levels. This is due to the onset of cavitation in the rubber layers, which produces impact like loads in the vertical direction that are also found to affect the horizontal modes.

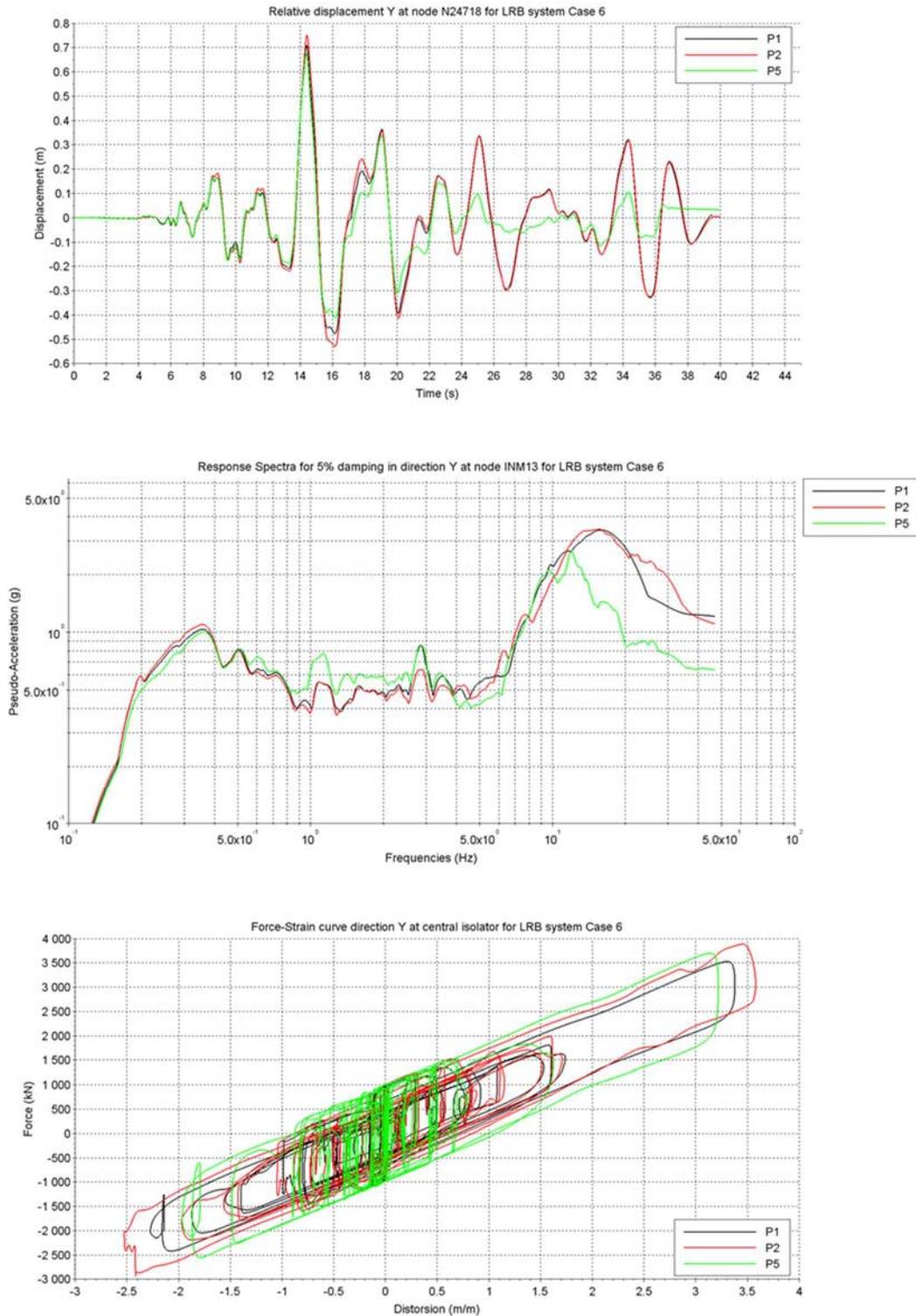


FIG. 80. Comparison of some participants' results for a case where no structural modelling differences or simplification hypotheses plays a significant role.

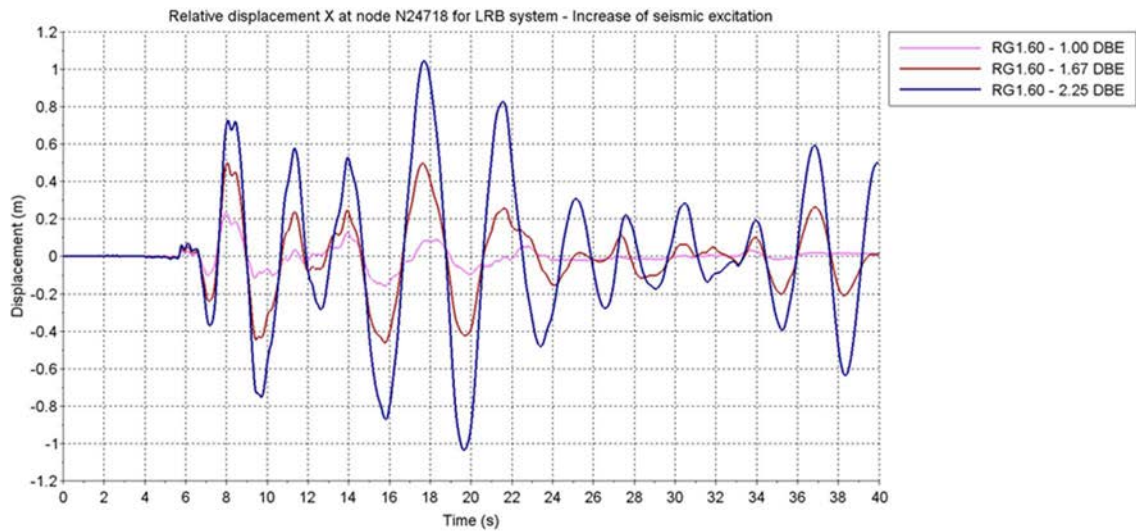


FIG. 81. LRB system – Parametric study – Upper basemat horizontal displacement with progressive increase of the excitation – RG 1.60 spectral shape.

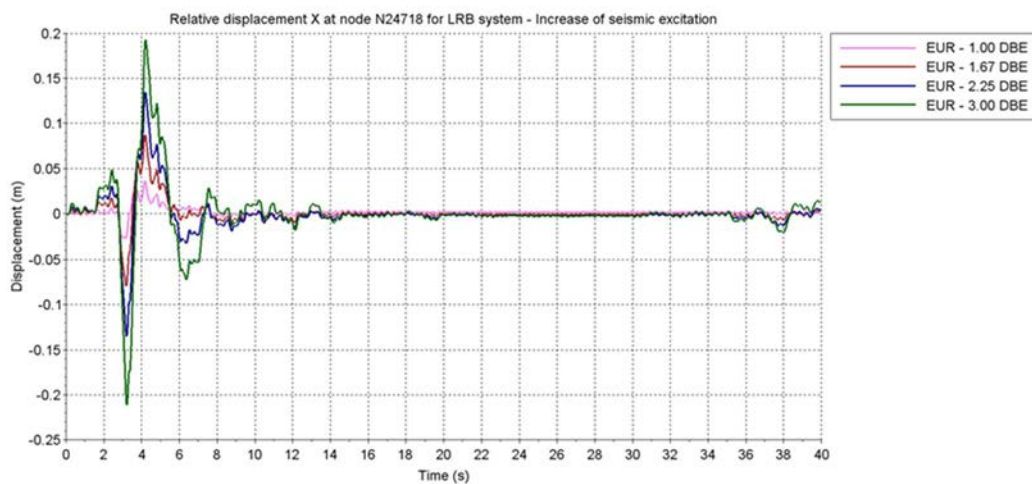


FIG. 82. LRB system – Parametric study – Upper basemat horizontal displacement with progressive increase of the excitation – EUR spectral shape.

In the vertical direction, with the RG 1.60 spectral shape excitation, the main observable phenomenon is a flattening of the peak with 2.25 times the DBE. In this case, the peaks become lower than the one observed with 1.67 times the DBE. This behaviour is associated to the isolators softening in the vertical direction, due to the large distortion. No such effect is observed with the EUR spectral shape. Instead, a stark non-linear increase of the response spectra at high frequency highlights the occurrence and the importance of the cavitation effects.

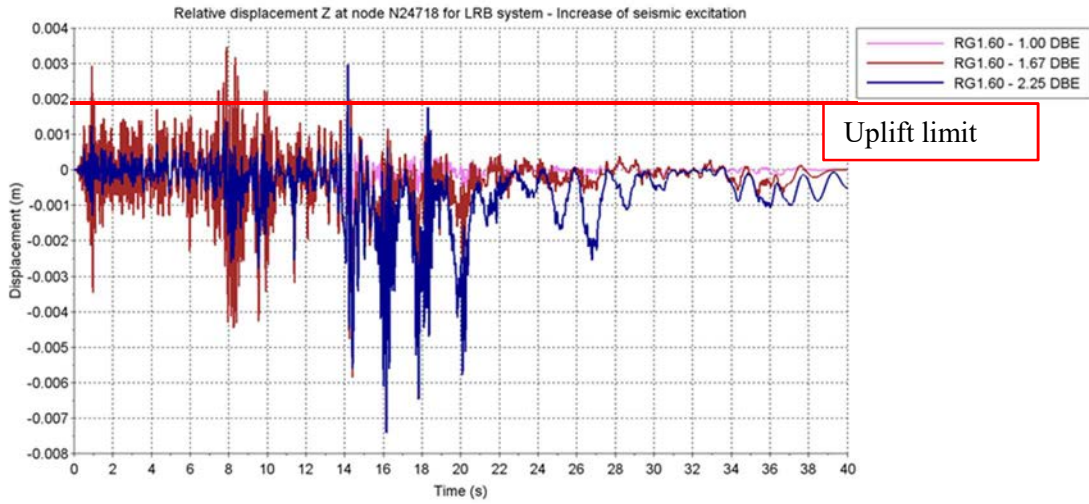


FIG. 83. LRB system – Parametric study – Upper basemat vertical displacement with progressive increase of the excitation – RG1.60 spectral shape.

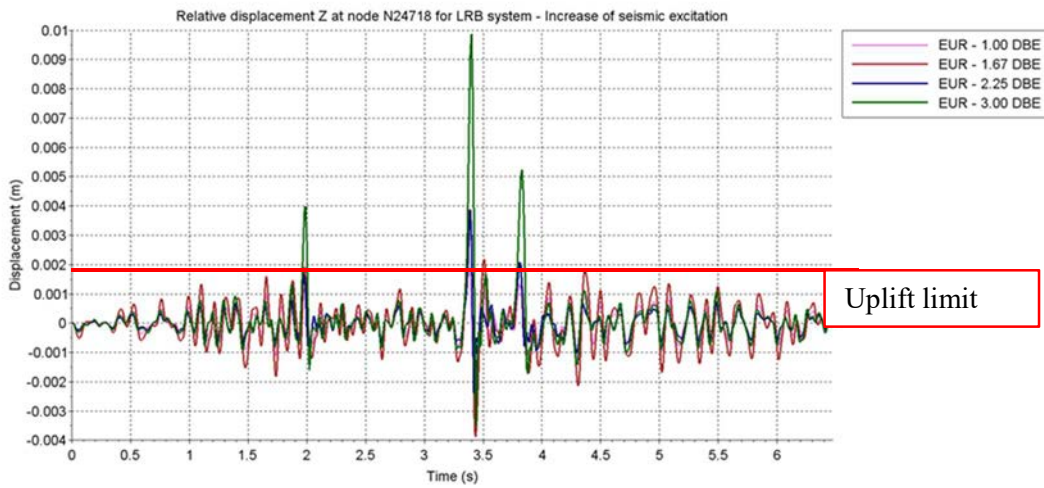


FIG. 84. LRB system – Parametric study – Upper basemat vertical displacement with progressive increase of the excitation – EUR spectral shape.

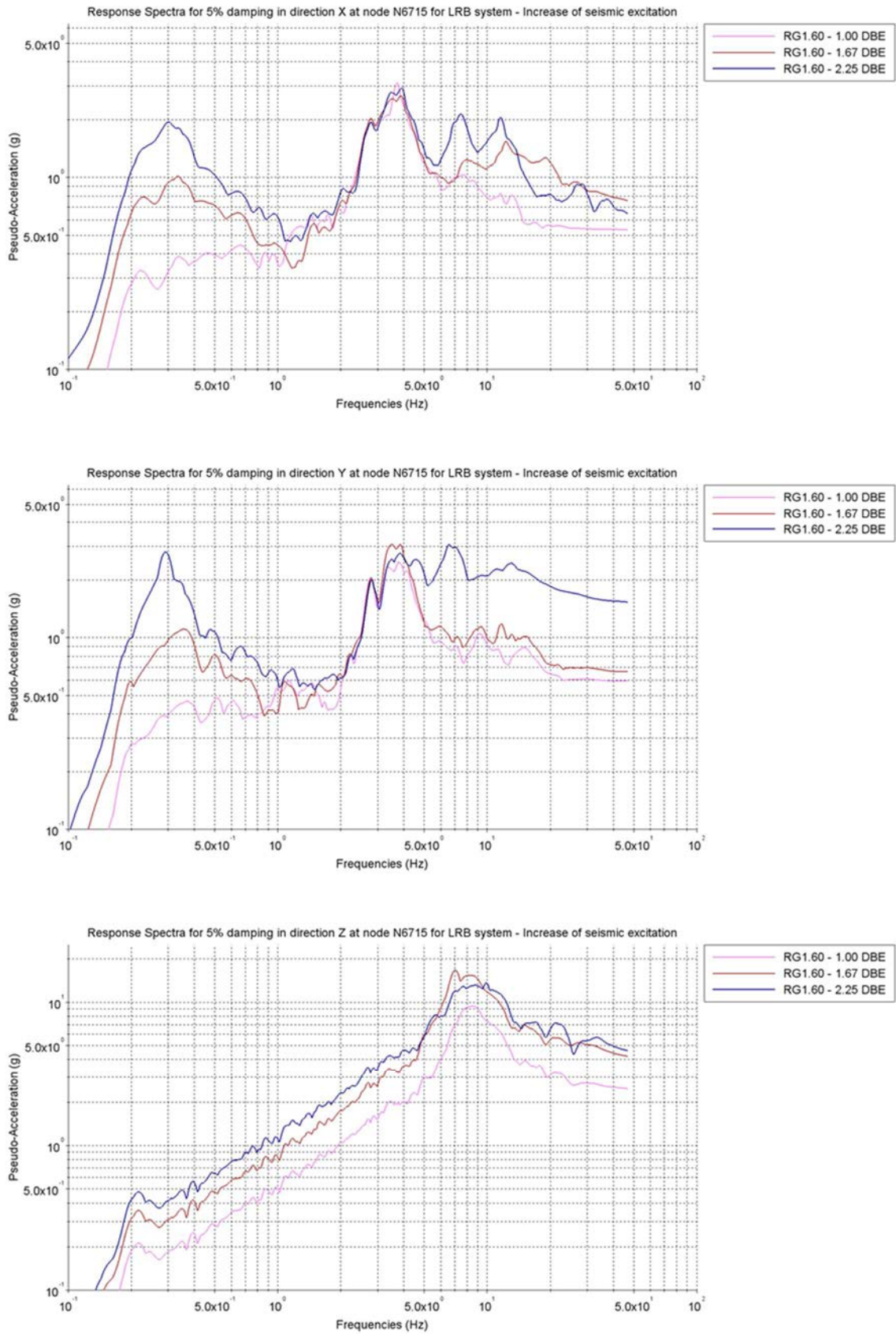


FIG. 85. LRB system – Parametric study – Response spectra at top of containment building with progressive increase of the excitation – RG 1.60 spectral shape.

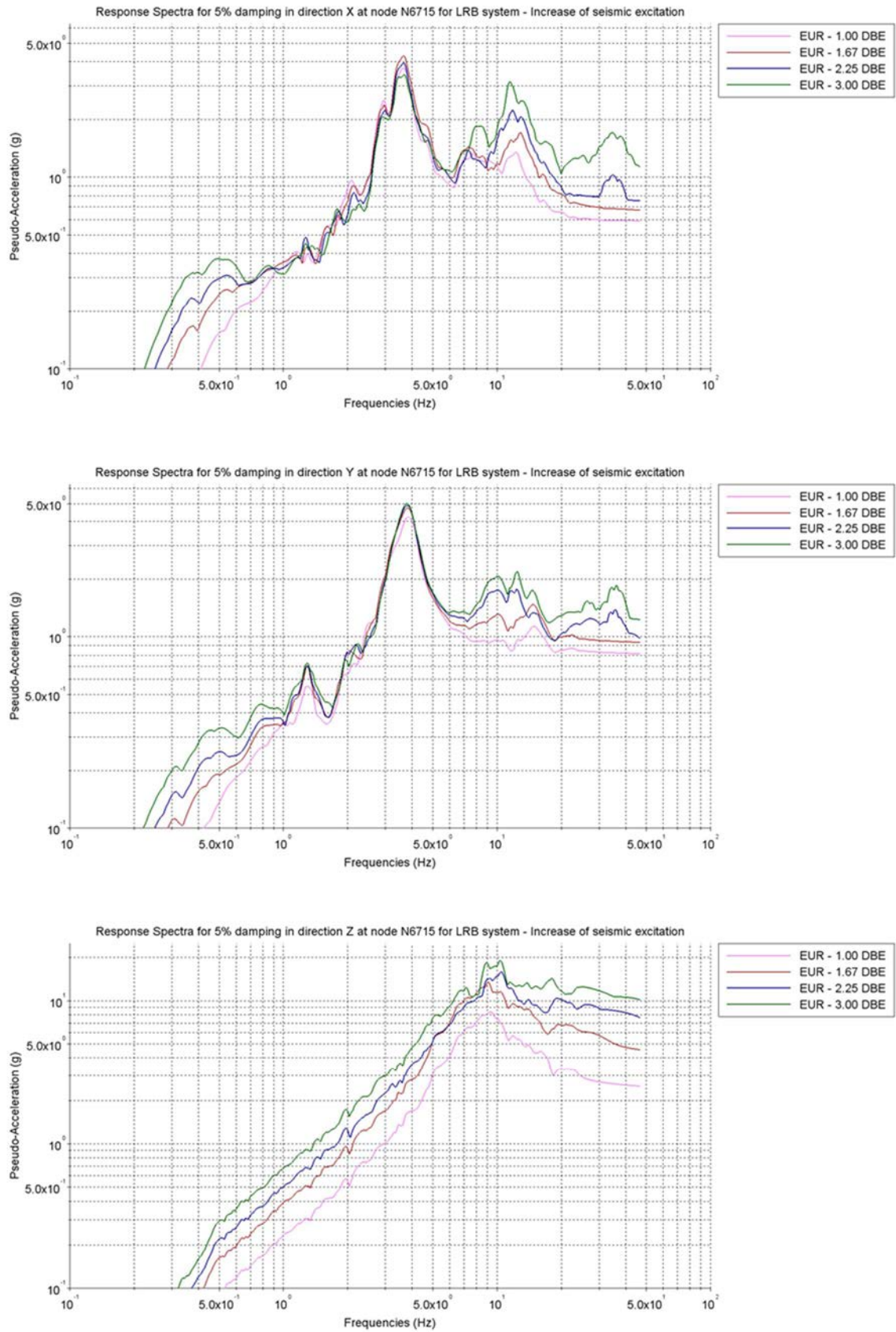


FIG. 86. LRB system – Parametric study – Response spectra at top of containment building with progressive increase of the excitation – EUR spectral shape.

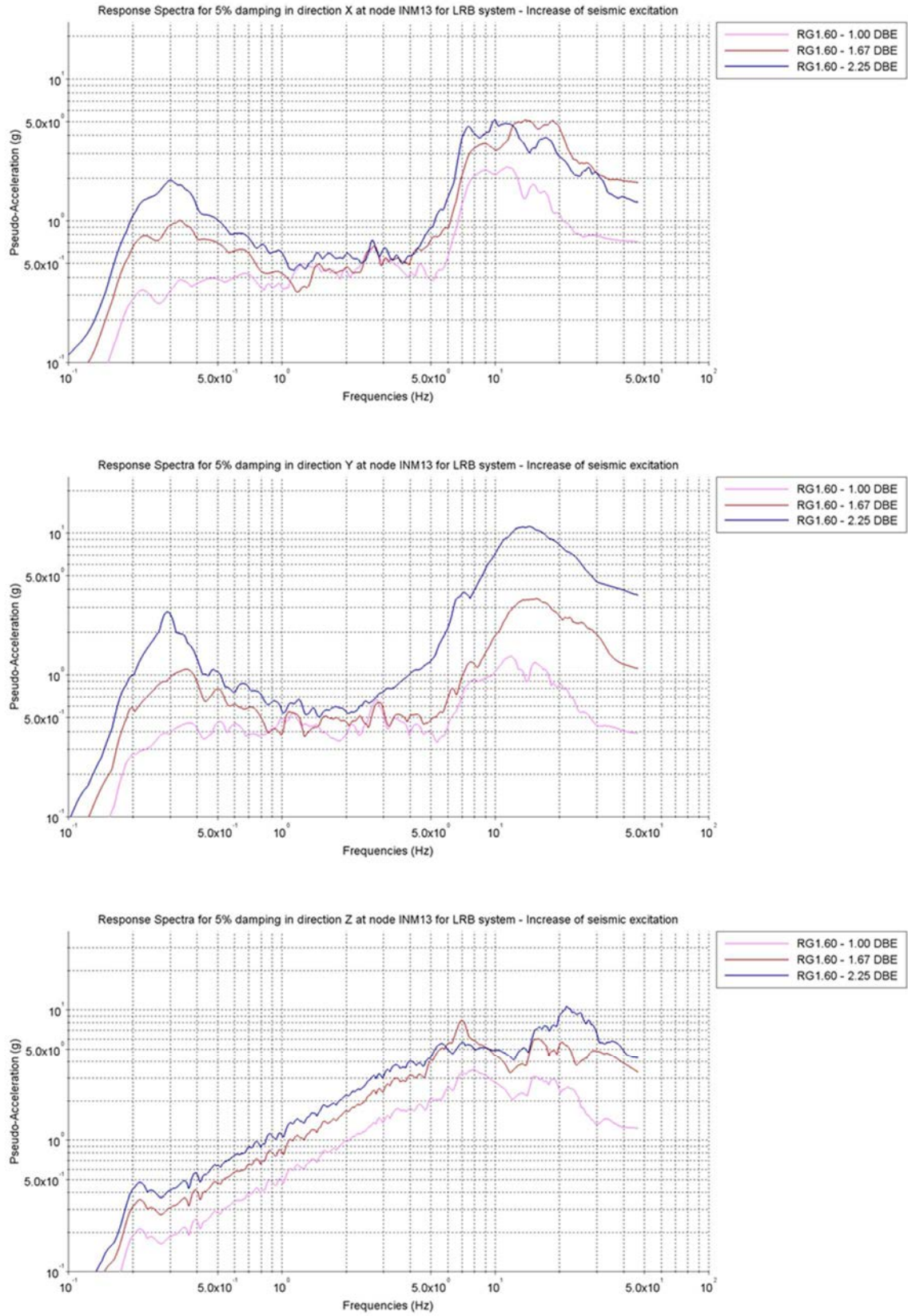


FIG. 87. LRB system – Parametric study – Response spectra at top of internal structures building with progressive increase of the excitation – RG1.60 spectral shape.

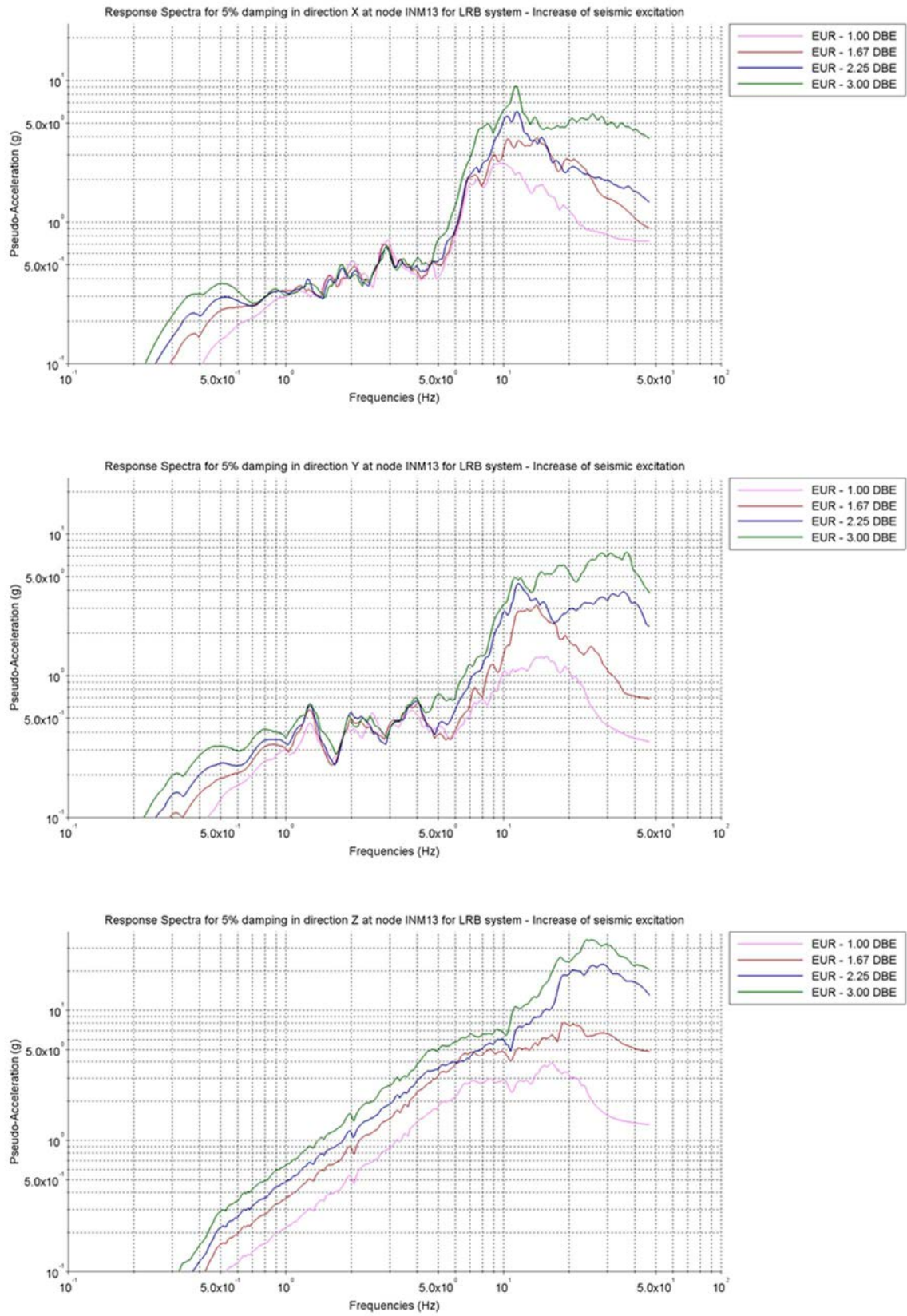


FIG. 88. LRB system – Parametric study – Response spectra at top of internal structures building with progressive increase of the excitation – EUR spectral shape.

5 EXPERIMENTAL RESULTS

5.1 SRMD-UCSD TESTING FACILITY

The experimental test program for the full-scale seismic isolation bearings was carried out at the Seismic Response Modification Device (SRMD) testing facility at the University of California, San Diego (UCSD). The capabilities of the machine, which enable dynamic testing of isolators at full scale, are described first, followed by recent upgrades of the control system that were necessary to achieve real-time hybrid simulation. An overview of additional algorithms that were required for delay compensation and the correction of friction during the real-time hybrid simulations are also discussed.

The Seismic Response Modification Device (SRMD) testing facility at the University of California, San Diego shown in Figure 89 was designed and built for real-time 6-DOF dynamic characterization of very large bearing devices and dampers using predefined loading protocols [31]. The capabilities of the SRMD testing facility are listed in Table 22. Longitudinal displacement capacity of 1220 mm and lateral displacement capacity of 610 mm facilitate testing of bearings to large displacements while imposing axial loads of up to 53.4 MN. This range of loading is generally applicable to anticipated demands on individual bearings for large buildings, bridges, and industrial structures designed based on current codes.



FIG. 89. SRMD testing facility at UC San Diego.

TABLE 22. SRMD TECHNICAL SPECIFICATIONS [32]

Component	Capacity	Accuracy of application	Accuracy of readout
Vertical force	53,400 kN	±5%	0.5% full range
Longitudinal force	8,900 kN		1.0% full range
Lateral force	4,450 kN		1.0% full range
Vertical displacement	±0.127 m	±2%	1.0% full range
Longitudinal displacement	±1.22 m	±2%	1.0% full range
Lateral displacement	±0.61 m	±2%	1.0% full range
Vertical velocity	±254 mm/sec	±10%	
Longitudinal velocity	±1,778 mm/sec	±10%	
Lateral velocity	±762 mm/sec	±10%	
Rotation (roll, pitch, and yaw)	±2 degrees		

The testing system consists of a prestressed concrete reaction frame box surrounding a moving platen. Four horizontal actuators control the lateral and longitudinal displacements of the platen. The platen is

3658 mm wide by 4750 mm long and slides over four hydrostatic low friction bearings, which are attached to the floor of the concrete structure and control the vertical movement of the platen. In addition, the platen is connected to four steel outrigger arms that are supported by four pairs (i.e., upper and lower) of low friction sliding bearing actuators. These actuators are used to control the vertical and rotational motions of the platen (Figure 90).

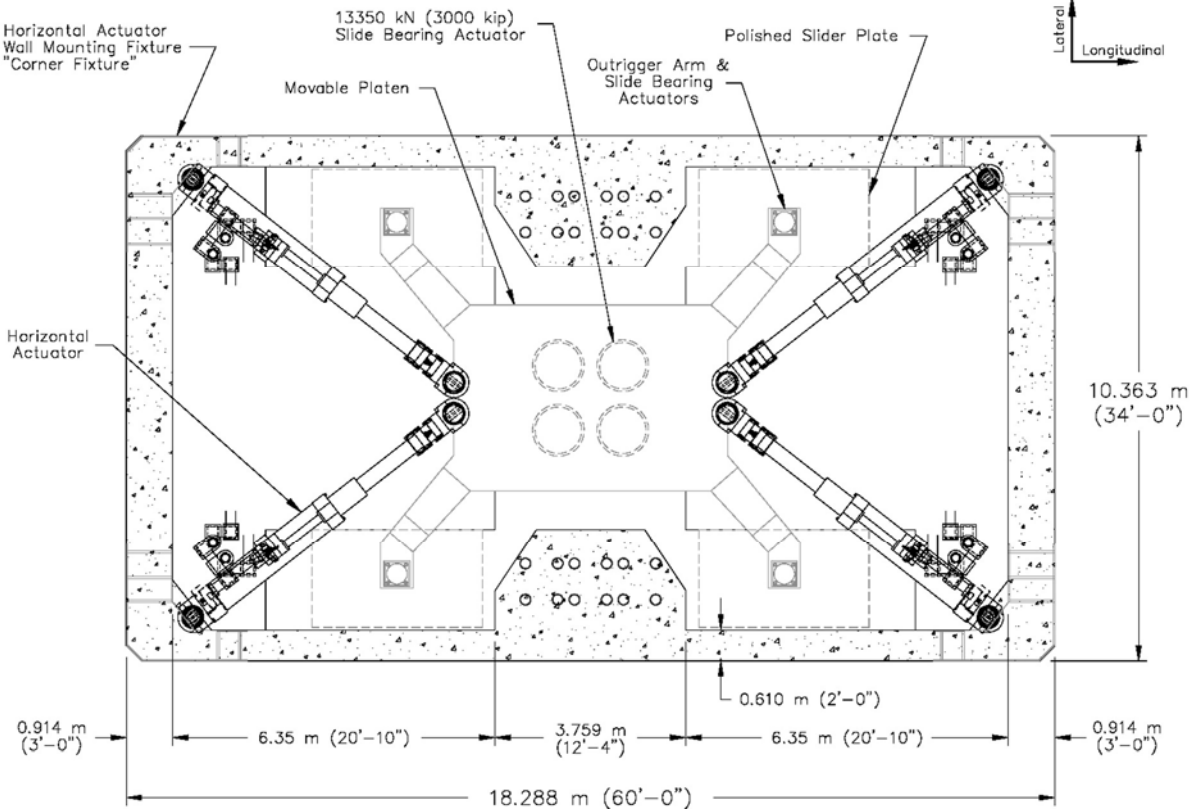


FIG. 90. SRMD plan view [31].

The testing system is completed by two additional reaction structures: a removable steel cross beam and a prestressed reaction wall on the west end of the machine. The removable cross beam and the configuration of the platen make the system flexible to perform different types of tests. The facility was updated in 2003 with a MTS digital three-variable controller and a digital off-line simulation for performance prediction. These upgrades enable the machine to operate as a shake table.

In 2014, the testing facility was adapted for quasi-static hybrid simulation for the purposes of a test program described in [32]. More recently, an upgrade to provide digital communication was implemented in an effort to enable real-time hybrid simulations that are discussed in this publication. The SRMD was used to conduct real-time and near-real-time hybrid simulations on three different types of large full-scale seismic isolation devices that represented the physical portion of a hybrid model of the seismically isolated NPP subject of the international benchmark.

5.2 ISOLATOR TEST SPECIMENS

Isolator test specimens are described in Section 3.4. Figures 91 thru 93 show the specimens as received by the testing facility.



FIG. 91. LRB specimen provided by the manufacturer.

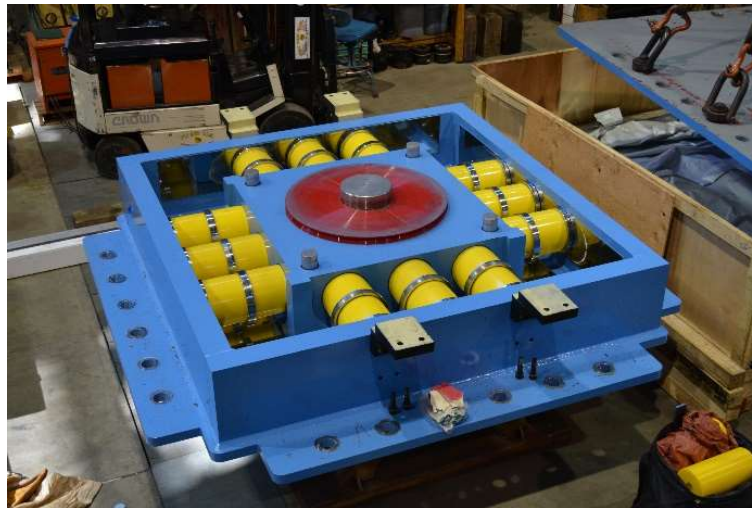


FIG. 92. EQSB specimen provided by the manufacturer.



FIG. 93. TPFB specimen provided by the manufacturer.

5.3 ISOLATOR CHARACTERIZATION TESTS

Characterization tests were conducted prior to the hybrid simulations in order to evaluate and better understand the behaviour of the three types of isolators under different loading conditions. Based on selected characterization test results, numerical isolator element parameters were calibrated and then used in the subsequent hybrid simulations. As stated above, three types of seismic isolation bearings were considered in this test program and a large number of characterization tests were conducted considering different combinations of loading conditions. A systematic parametric evaluation was carried out to investigate the effect of the different loading conditions on the hysteretic behaviour of each bearing type in both, the vertical and horizontal directions.

The loading condition parameters considered for the characterization tests and the associated standard reference design values for the three bearing types are summarized in Table 23. The standard reference design values are based on specifications provided by the three bearing manufacturers. In this section, characterization test results considering variations of these parameters are compared and discussed for each isolator type. Results of the characterization tests are provided in Annex II.

TABLE 23. SUMMARY OF KEY CHARACTERIZATION TEST LOADING CONDITION PARAMETERS

	Axial Force [kN/US tons]	Peak Disp. [mm/in]	Loading Freq. [Hz]	Temperatur e [°C/°F]	Horizontal offset for axial compression test [mm/in]
LRB	10900 / 1094	210.8 / 8.3	0.33	Ambient	0.0 / 0.0
EQSB	10900 / 1094	152.4 / 6.0	0.51	Ambient	0.0 / 0.0
TPFB	10900 / 1094	584.2 / 23.0	0.20	Ambient	0.0 / 0.0

5.3.1 LRB isolator

The two LRB specimens (UET1 and UET2) were used for both the characterization and hybrid simulation tests. The properties and behaviour of UET1 and UET2 were nearly identical. Therefore, no distinction between the two specimens is made in the following discussions. The horizontal characterization tests were conducted in longitudinal direction of the SRMD, meaning that horizontal force-displacement relations shown are all for the longitudinal direction.

5.3.1.1 Vertical

The axial behaviour of the LRB was evaluated by conducting axial compression tests where the load was slowly increased, and after the design axial load was reached, slow unloading-reloading cycles were performed. The same axial loading protocol was executed for three different horizontal deformation states of the isolator: (1) initial configuration without horizontal deformation, (2) horizontally deformed to 25% of the design displacement of the bearing, and (3) horizontally deformed to 150% of the design displacement of the bearing.

The comparison of axial force-deformation relations for the three cases is shown in Figure 94. In general, the axial stiffness gradually increases when the compression load is small. Once the design axial load of 10900 kN is reached, the axial behaviour becomes nearly linear. Under cyclic axial compression loads the LRB clearly dissipates energy as is obvious from the hysteresis loops. Comparing the isolator axial behaviour for the three different horizontal deformation states, the overall axial behaviour within each case is similar as the three loading curves are parallel to each other. This indicates that the axial compression stiffness is not much affected by the horizontal deformation state of the LRB for axial forces at and above the design level where the response becomes linear. However, for larger horizontal displacements, the initial axial deformation needed to reach the stable linear compression behaviour is larger as indicated by the horizontal shift in the plots.

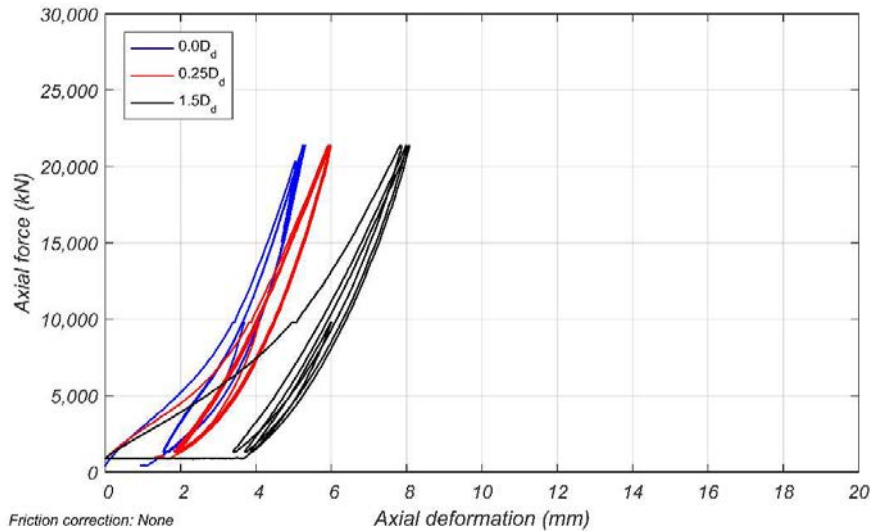


FIG. 94. Comparison of axial force-deformation behaviour of LRB for axial compression tests with three different levels of horizontal offset.

Based on the axial characterization test results, a multi-linear model with equivalent viscous damping ratio derived from the hysteresis loops was used for modelling the compression behaviour of LRB in the subsequent hybrid simulations. The data points used to define the multi-linear behaviour were derived from the axial hysteresis at zero horizontal deformation. The calibrated parameters for the experimental element in OpenFresco are discussed later.

5.3.2 Horizontal (effect of axial load)

The effect of different axial compression loads on the horizontal hysteretic behaviour of the LRB are investigated by comparing horizontal hysteresis loops from horizontal displacement controlled characterization tests with compression levels equal to 50%, 100%, and 200% of the design compression force. Results are shown in Figure 95. Within each plot, all other loading parameters are the same except for the compression force acting on the bearing. The comparison is conducted at different loading rates: (a) standard loading rate and (b) slow loading rate. The horizontal hysteresis loops are almost identical considering the different axial compression loads in each plot. It can be concluded that for the specific LRB specimens tested here, the compression force acting on the isolator has a negligible effect on the horizontal shear behaviour of the bearing.

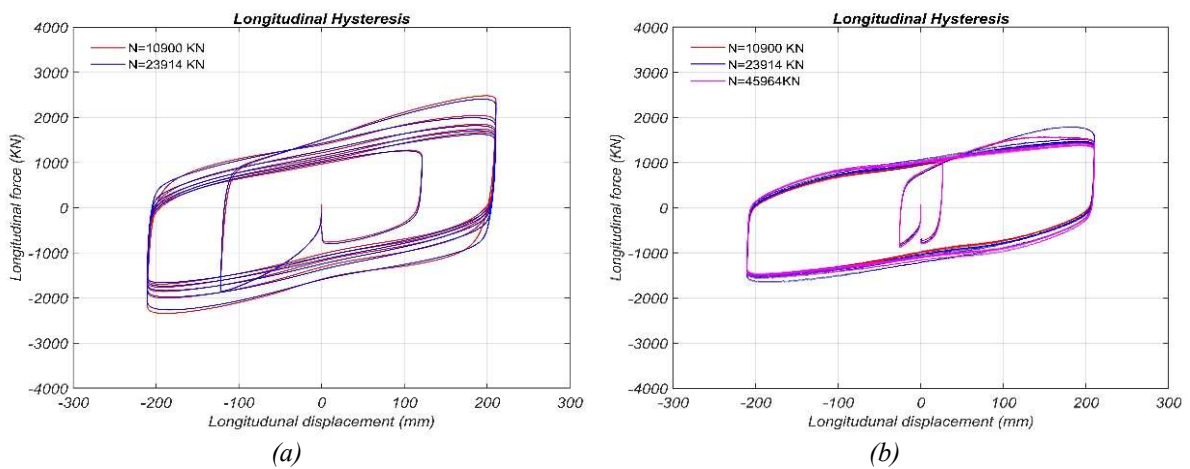


FIG. 95. Comparison of horizontal force-deformation behaviour of LRB for different levels of axial compression. (a) Results from characterization tests conducted at normal test rate (0.33 Hz). (b) Results from characterization tests conducted at low test rate (0.005 Hz).

5.3.2.1 Horizontal (effect of loading rate)

The effect of loading rates was investigated by comparing horizontal force-deformation hysteresis loops for a range of different loading speeds. Given the same sinusoidal shape and design displacement amplitude of the loading histories, horizontal displacement-controlled characterization tests were conducted with three different loading rates of 0.005 Hz (quasi-static), 0.33 Hz and 1.15 Hz.

From the comparison of the horizontal hysteresis loops shown in Figure 96, it can be observed that the loading cases with 0.33 Hz and 1.15 Hz are almost identical. For the quasi-static case (0.005 Hz), the hysteresis loop is thinner and the isolator force from cycle to cycle does not change much. While for the other two faster loading cases (0.33 Hz and 1.15 Hz), the isolator forces become smaller with each subsequent cycle. This behaviour is mainly caused by the heating of the lead core when loading speeds are large. For the very slow test the heat developed in the lead cores is negligible. The larger characteristic strength at the faster loading rates and the increased post-yield stiffness in the first half-cycle is caused by the strain-rate dependent behaviour of the lead core. Scragging effects in the rubber also contribute to the decrease of the post-yield stiffness after the first half-cycle, but it is believed that the stiffness contribution from the lead core is the main cause of this phenomenon. Almost identical observations were reported by Kasalanati [33].

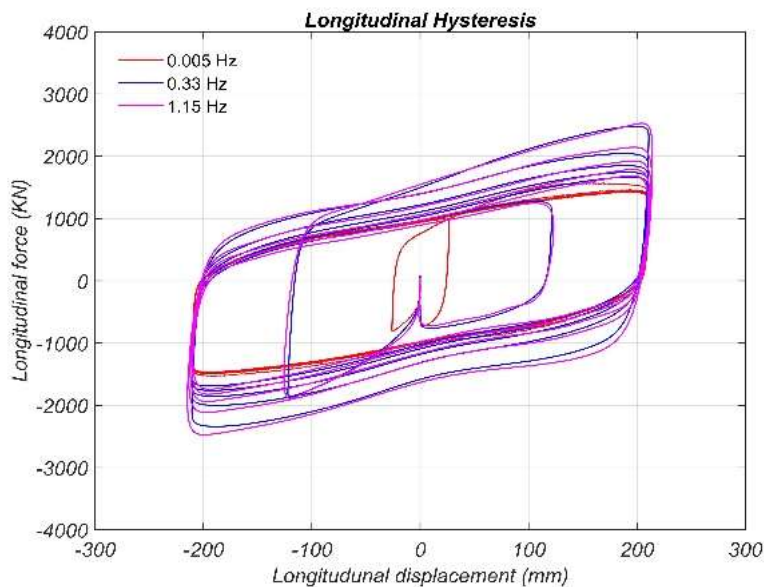


FIG. 96. Comparison of horizontal force-deformation behaviour of LRB for different loading rates.

5.3.2.2 Horizontal (effect of temperature)

The effect of temperature was investigated by conducting characterization tests at ambient temperature and hot temperature (after a previous characterization run). However, due to the time required between each run to recharge the accumulators back to the required oil pressure, the difference between the starting temperatures of the two cases was quite small (28.4°C versus 30.7°C); therefore, as shown in Figure 97, the hysteresis loops of the two runs are nearly identical, with the hysteresis loop for the hot condition being slightly thinner as expected.

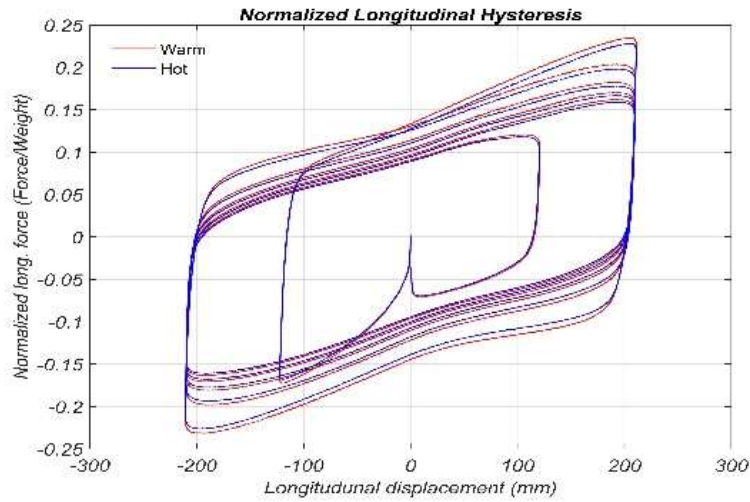


FIG. 97. Comparison of horizontal force-deformation behaviour of LRB for different bearing temperatures (warm: 28.4°C, hot: 30.7°C).

However, within each characterization test, the temperature increase was significant (as much as 10°C). Therefore, if the isolator shear force history during the test is investigated as shown in Figure 98, the degradation of the isolator shear strength with each loading cycle can clearly be observed. This indicates that the horizontal shear strength, meaning the yield strength of the four lead cores, decreases with the increase of the temperature in the bearing. A numerical model which can capture the strength reduction due to heating of the lead cores in these types of bearings will be useful for future evaluations of this phenomenon.

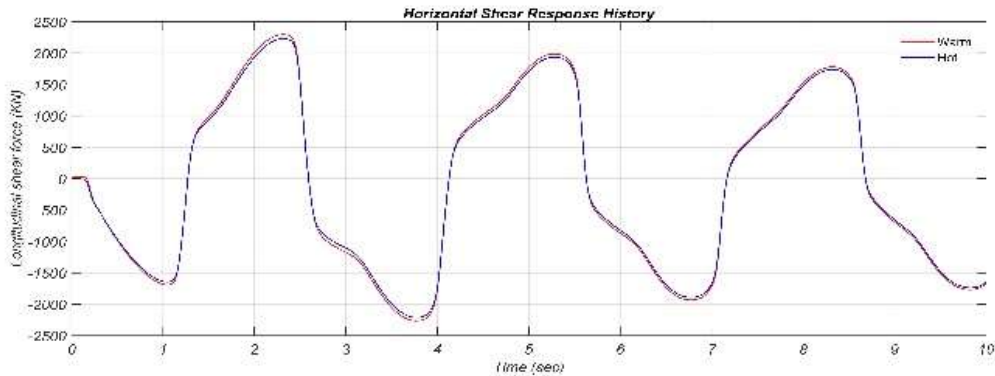


FIG. 98. Comparison of horizontal shear force histories of LRB for different loading temperatures (warm: 28.4°C, hot: 30.7°C).

5.3.2.3 Horizontal (effect of displacement amplitude)

The isolator behaviour under different horizontal displacement amplitudes was investigated by comparing results of experimental runs for a range of loading amplitudes. As indicated in Table 23, the design displacement for the LRB is around 210 mm, which corresponds to 100% shear strain of the rubber. In a series of displacement-controlled characterization tests, loading displacement amplitudes were increased to 200%, 300% and 350% of the design level shear strain. The corresponding horizontal hysteresis loops of the isolator are shown in Figure 99. As indicated in the figure, when bearing deformations are larger, a significant hardening behaviour is observed starting at about 400 mm horizontal deformation (200% of the design displacement). The shear behaviour of the bearing before the hardening commences is almost identical for all cases. It is also interesting to notice that for the first half cycle of the hysteresis loops the shear forces in the LRB are generally larger than for the successive cycles. This phenomenon was already explained in Section 5.3.2.1.

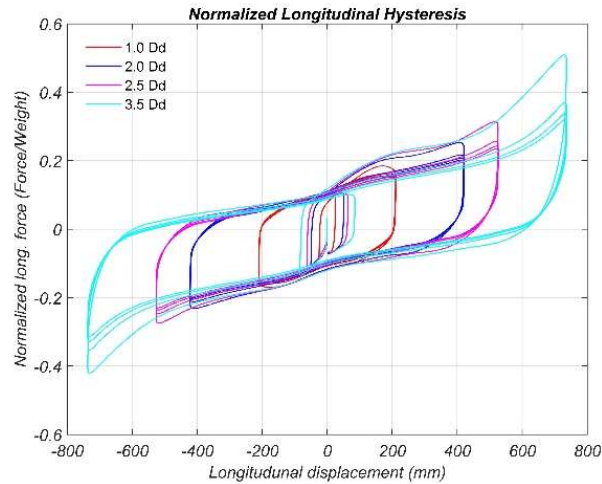


FIG. 99. Comparison of horizontal shear force-deformation behaviour of LRB for different displ. amplitudes.

The nonlinear hardening behaviour at large deformations indicates the need for a numerical isolator model which incorporates this unique behaviour. This becomes especially important when simulating the response of nuclear power plants for beyond design basis events. In the hybrid simulations conducted in this phase of the test program, the ground motion records were developed to match the design level target spectrum. Therefore, the isolator displacement demand was not expected to be significantly larger than the original design displacement of 210 mm. A model which can accurately capture the hardening behaviour will not be necessary for the purpose of these hybrid simulation tests. However, it will be important when isolator safety under extreme events is studied and evaluated.

5.3.2.4 Horizontal (failure test)

Finally, a test was conducted to characterize the horizontal failure behaviour of the LRB at extremely large shear strains. The characterization test was executed using an elliptical input motion targeting 580% shear strain. Failure of the bearing was observed at approximately 899 mm longitudinal displacement amplitude as indicated in Figure 100, this corresponds to 428% shear strain, a factor of 4.3 times the design shear strain. The failure mechanism of the bearing specimen is shown in Figure 101, which indicates that the failure was due to delamination between rubber and steel shim.

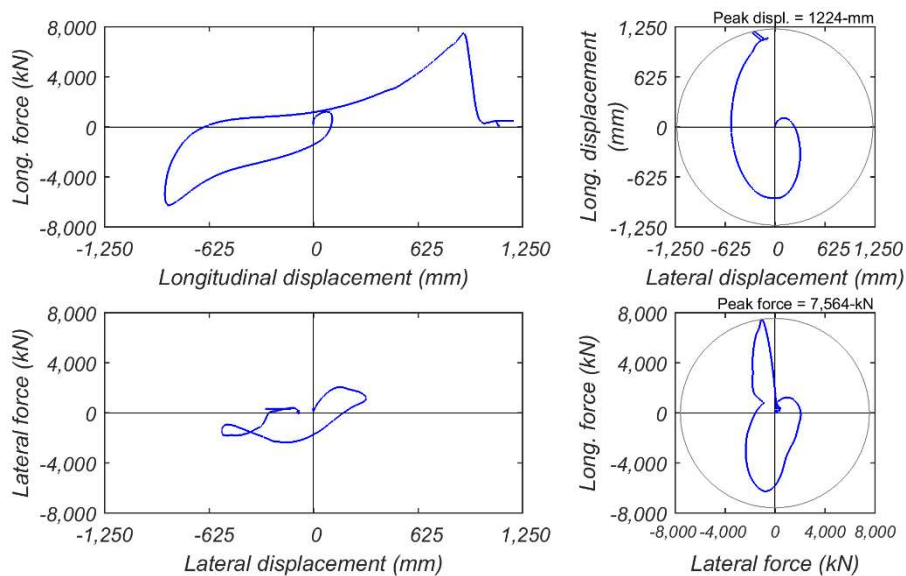


FIG. 100. Responses for horizontal failure test of LRB specimen (UET2). Upper left: Longitudinal shear force-deformation hysteresis loop. Upper right: Horizontal displacement orbit. Lower left: Lateral shear force-deformation hysteresis loop. Lower right: Shear force orbit.



FIG. 101. Failure mechanism of LRB specimen (UET2). (a) Large horizontal shear strain before failure. (b) Failure observed between rubber and steel shim and extreme deformation of lead cores.

5.3.2.5 Summary

The LRB characterization test results were discussed in this section while focusing on the effect of different loading conditions. The results indicated that the horizontal shear behaviour of the tested LRB was quite stable and was not much affected by axial compression force and horizontal loading rate. However, at faster loading rates an increase of the post-yield stiffness in the first half-cycle was observed. It was concluded that this stiffness increase was caused by the strain-rate dependent behaviour of the lead core. Temperature changes in the bearing had a moderate effect on the strength of the isolator. Increasing core temperatures reduced the yield strength of the four lead cores which led to an overall bearing strength reduction from cycle to cycle. At larger shear deformations, the LRB isolator exhibited a gradual hardening behaviour commencing at about 200% horizontal shear strain. Horizontal shear failure occurred at approximately 430% shear strain, which was more than 4 times the design deformation of the LRB.

5.3.3 EQSB isolator

5.3.3.1 Vertical

Similar to the LRB the axial behaviour of the EQSB was evaluated by conducting axial compression tests where the load was slowly increased, and after the design axial load was reached, slow unloading-reloading cycles were performed. However, this axial loading protocol was only executed for the initial configuration without a horizontal deformation offset.

The axial force-deformation behaviour for the EQSB is shown in Figure 102 94. At small compression loads the axial stiffness of the EQSB is very low due to the large flexibility of the low shape factor

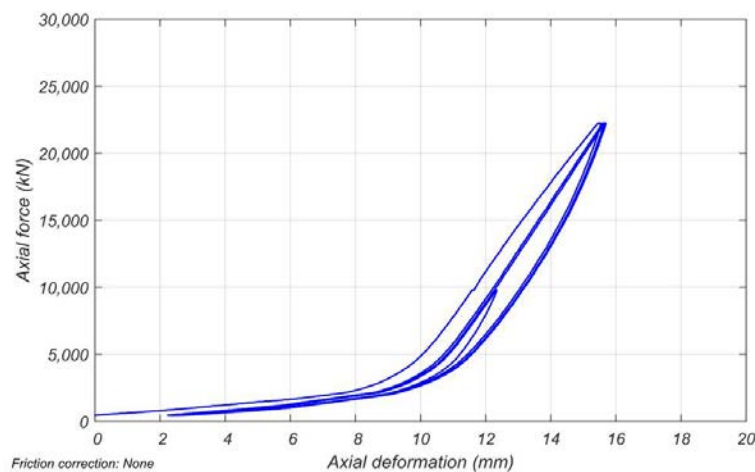


FIG. 102. Axial force-deformation behaviour of EQSB for cyclic axial compression test.

Polytron disk. The stiffness then rapidly increases for compression loads above 5000 kN and becomes nearly linear for compression loads above 7500 kN, which is well below the design axial compression load of 10900 kN. Under cyclic axial compression loads the EQSB dissipates a fair amount of energy as is obvious from the pronounced hysteresis loops.

5.3.3.2 Horizontal (effect of axial load)

The horizontal restoring force of the EQSB is a combination of sliding friction forces and nonlinear MER spring resisting forces. The friction force is a function of the axial compression load acting on the sliding surface but also depends on the sliding velocity as will be seen later. The MER spring exhibits a mostly nonlinear-elastic behaviour that is independent of axial load and the bearing horizontal restoring forces are therefore expected to not only depend on the instantaneous axial load but also on the displacement amplitude. Characterization test results considering three different levels of axial load are shown in Figure 103.

Generally, with larger axial load, the horizontal restoring force increases as evident by the wider hysteresis loops. However, the horizontal stiffness of the bearing is independent of the axial load and remains the same. All the post-sliding (post-yield) stiffness ratios have the same slope. This is the case because the horizontal stiffness is only controlled by the MER springs, while the bearing’s characteristic strength at zero deformation is controlled by the friction force which depends on the axial load. Two compression load series conducted at different loading rates are shown in plot (a) and (b) in Figure 103. When the loading is slow as shown in plot (b), the effect of axial loads on the shear resistance is more pronounced because the horizontal hysteresis loops are more stable. Compared to the horizontal behaviour of the LRB, which was not much affected by axial compression loads for the same displacement-controlled loading history, the horizontal restoring force of the EQSB increases significantly if larger compression loads are acting on the bearing.

Looking more closely at the horizontal force-displacement behaviour in in Figure 103, spikes in the hysteresis loops (indicated by the red circles in the plots) can be identified at initiation of sliding and at some of the load reversal points. This behaviour is likely due to breakaway or static friction when movement is commencing, which is larger than the dynamic friction force when sliding is well underway. From the size of the spikes it can be concluded that breakaway and static friction effects are considerably more pronounced for larger axial loads. The very obvious change in the characteristic strength of the EQSB for the fast tests shown in plot (a) are discussed in the next section.

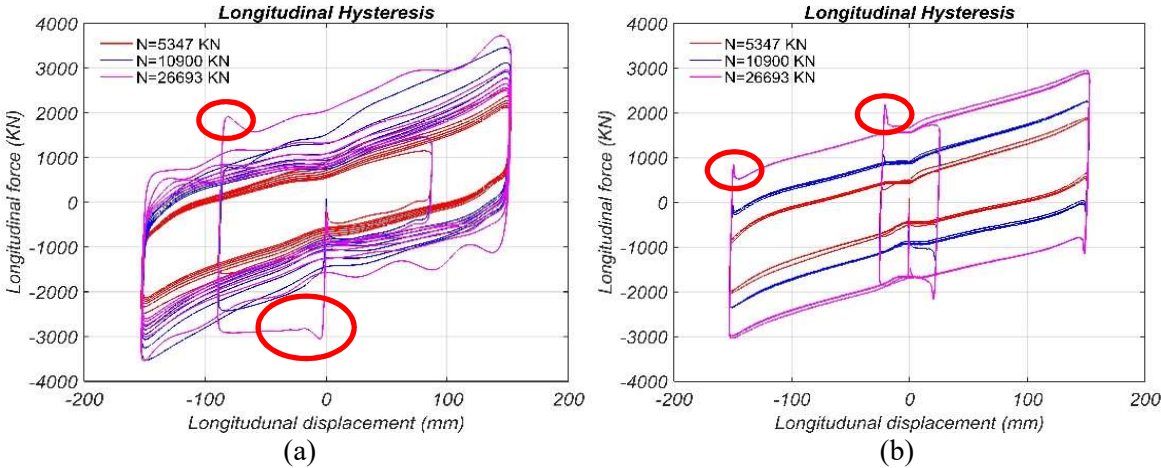


FIG. 103. Comparison of horizontal force-deformation behaviour of EQSB for different levels of axial compression. (a) Characterization tests conducted at normal test rate (0.51 Hz). (b) Characterization tests conducted at slow test rate (0.02 Hz).

5.3.3.3 Horizontal (effect of loading rate)

Test results for an EQSB isolator loaded at different loading rates are shown and compared in Figure 105 below. Slow loading rates result in more stable hysteretic behaviour. When loading speeds are

increased, the bearing tends to exhibit a larger horizontal shear force in the first cycle as compared to the slow loading rate of 0.25 Hz. However, after the first cycle the shear force amplitude rapidly degrades from cycle to cycle.

The degradation of the characteristic strength can also be observed in Figure 1043 where bearing horizontal shear force histories are compared for the three loading rates. The degradation of the EQSB isolator’s characteristic strength is caused by temperature effects at the sliding interface, where more heat is produced more rapidly for the faster loading rates. It can be concluded that the coefficient of friction for the PTFE material used in the EQSB is fairly temperature dependent. Only at slow loading rates the coefficient of friction is stable as obvious from the constant width of the hysteresis loops. The other effect observed from the horizontal shear behaviour is the “pinching effect” of the hysteresis loops when the bearing deformation crosses the zero-displacement point, especially when the loading is dynamic (larger loading rate) as indicated by the red circles in Figure 1054. The pinching effect can be attributed to the kinematic behaviour (backlash) of the MER springs when resistance is transferred from the three springs on one side of the slider to the three springs on the other side.

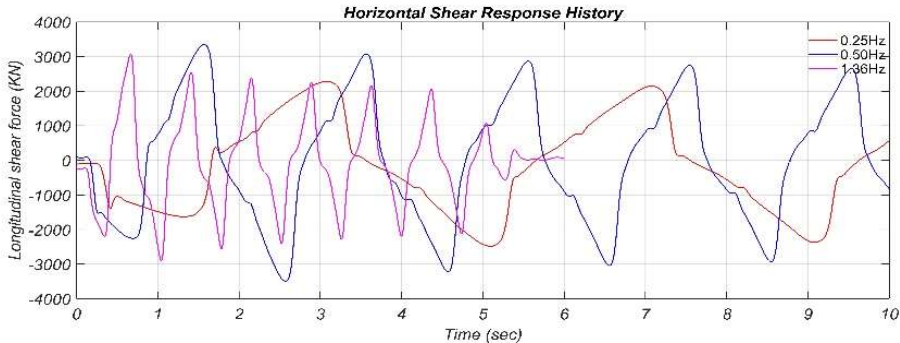


FIG. 1043. Comparison of horizontal shear force histories of EQSB for different loading rates. Characterization tests shown are conducted at 10900 kN axial compression load.

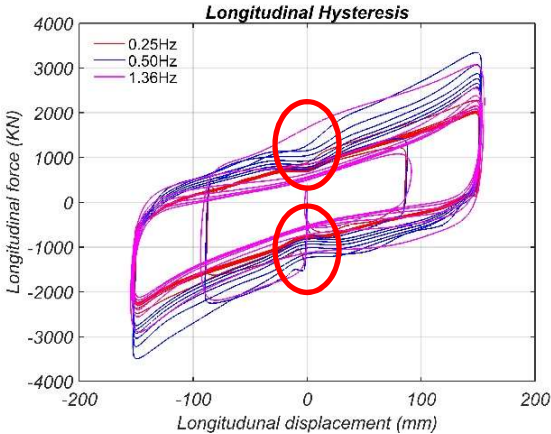


FIG. 105. Comparison of horizontal force-deformation behaviour of EQSB for different loading rates. Characterization tests shown are conducted at 10900 kN axial compression load.

5.3.3.4 Horizontal (effect of temperature)

The effect of temperature on the shear behaviour of the EQSB is evaluated by comparing two characterization runs conducted at different starting temperatures. However, due to the recharging time required at the SRMD between successive tests, temperatures at the start of two characterization runs are not that different (only approximately 3°C difference), although the intention was to test at “ambient/cold” (≈25°C) and “hot” conditions. This explains the only minor differences that can be observed in the horizontal shear behaviour shown in Figure 106. However, if the behaviour within each run is evaluated as shown in Figure 107 for the shear force response histories, one can observe the decay

of shear strength with time. This is mainly due to the increase of temperature induced by work done by the isolator at the sliding interface but also in the MER springs. It can be concluded that the increase of the temperature at the sliding interface and in the MER springs considerably affect the strength of the EQSB isolator.

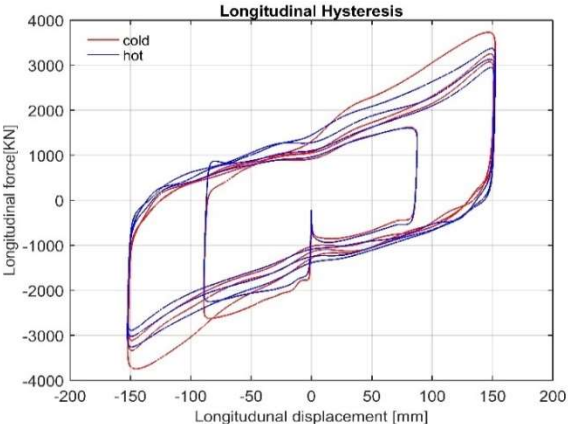


FIG. 106. Comparison of horizontal force-deformation behaviour of EQSB for different bearing temperatures (The actual starting temperatures are very similar for the two runs).

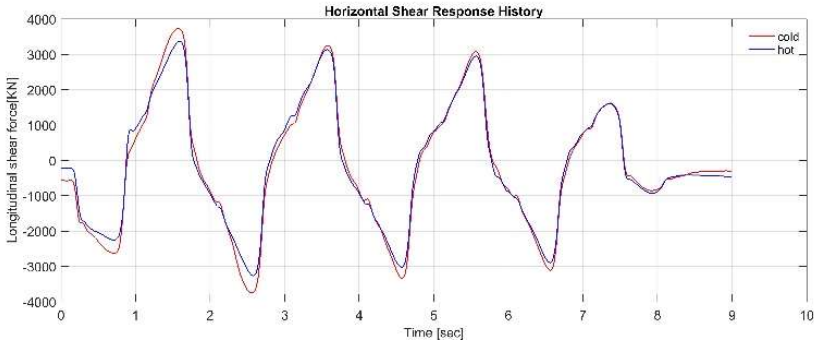


FIG. 107. Comparison of horizontal shear force histories of EQSB for different bearing temperatures.

5.3.3.5 Horizontal (ultimate displacement test)

Finally, the behaviour of the EQSB at extreme deformation states was investigated by conducting an ultimate displacement characterization test. The large lateral force capacity of the bearing exceeded the adapting hardware’s capacity inducing slip between the bearing and adapter plate. Slip occurred at 4681 kN and the maximum shear force that could be achieved was 6475 kN, which corresponds to 73% of the machine’s longitudinal force capacity. The ultimate displacement in this test was 275 mm (approximately 180% of the design displacement) and the hysteresis loop of the isolator is shown in Figure 108. One can clearly observe a significant stiffening behaviour that starts around the design displacement of 150 mm. Figure 109 shows the progression and squeezing of the MER springs, the cause of the nonlinear stiffening behaviour, as the horizontal bearing deformation gets larger.

5.3.3.6 Summary

The EQSB characterization test results were discussed in this section while focusing on the effect of different loading conditions. In axial direction the isolator showed low compression stiffness at small axial loads due to the flexible Polytron disk. The lateral results indicated that the shear behaviour of the EQSB significantly depends on the axial compression force. Larger axial compression loads on the bearing resulted in higher horizontal shear forces (larger characteristic strengths) but did not affect the horizontal force-deformation stiffness. Temperatures had a fairly significant effect on the strength of the isolator. As the temperature increased the coefficient of friction of the PTFE material was reduced which

led to a reduction in the characteristic shear strength of the EQSB from cycle to cycle. The temperature effect was more pronounced when the loading was fast, and more heat was generated more rapidly. At larger shear deformation, the isolator exhibited a gradual stiffening behaviour commencing around the

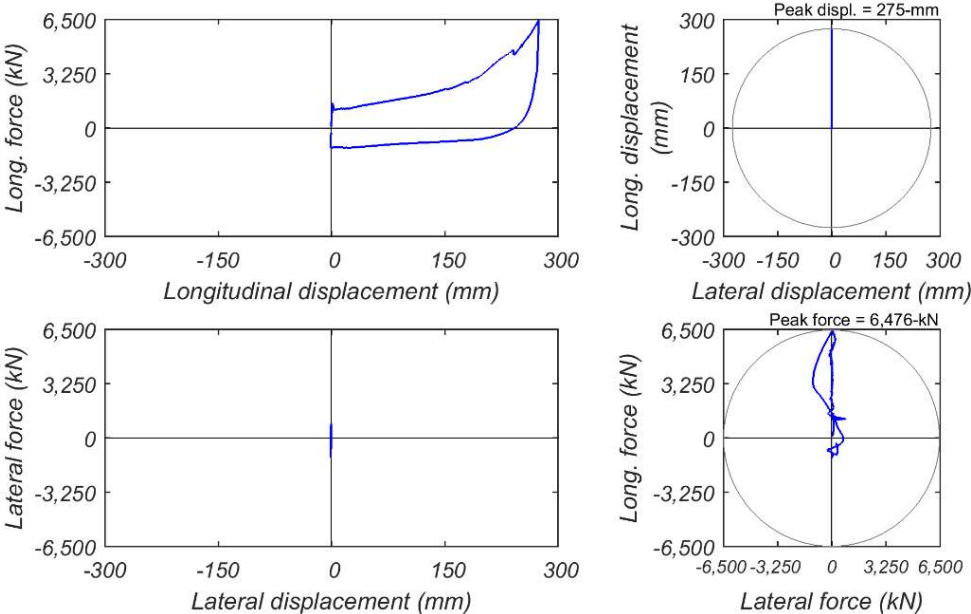


FIG. 108. Responses for ultimate horizontal displacement test of EQSB specimen. Upper left: Longitudinal shear force-displacement hysteresis loop. Upper right: Horizontal displacement orbit. Lower left: Lateral shear force-displacement hysteresis loop. Lower right: Shear force orbit.

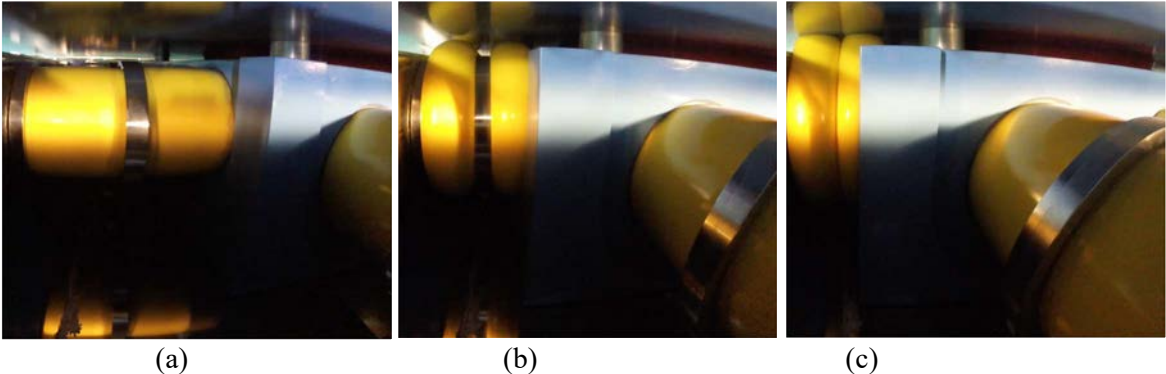


FIG. 109. Sequence of the MER spring deformation for the EQSB for the ultimate horizontal displacement test (a) 0 mm, (b) 192 mm, (c) 275 mm (ultimate).

design displacement of 150 mm. Due to the capacity of the SRMD test facility and the occurrence of slip, the ultimate displacement the EQSB isolator was tested to, was 275 mm.

5.3.4 TPFB isolator

5.3.4.1 Vertical

Similar to the vertical tests performed on the LRB, the same axial loading protocol was executed for three different horizontal deformation states of the isolator: (1) initial configuration without horizontal deformation, (2) horizontally deformed to 50% of the design displacement of the bearing, and (3) horizontally deformed to 100% of the design displacement of the bearing.

The axial force-deformation test results shown in Figure 110 indicate that the axial compression behaviour of the TPFB isolator does not depend on horizontal deformation. The compression behaviour demonstrates a nonlinear nature, especially at low axial force levels before the design axial load of 10900 kN is reached. The compression stiffness starts with a low value and gradually increases until it reaches a larger value that nearly stays constant beyond the design axial load. The highly nonlinear behaviour occurs all within the first 5 mm of compression deformation. The initial nonlinear axial shortening of the TPFB can be attributed to three mechanical effects: (1) the settling of all the different internal pieces of the multi-stage sliding mechanism until full contact is achieved, (2) the deformation of the fairly flexible PTFE liners (4 of them in series), and (3) the bending deformations of the outer concave sliding dishes as they get pushed into the reaction blocks. The third effect would be even more pronounced in a real-world installation of the TPFB on a concrete pedestal. All these effects lead to an axial stiffness of the TPFB isolator that is on the order of 10-15% (10% for larger isolators and 15% for smaller isolators) of the theoretically calculated stiffness of all the steel pieces in the bearing.

Based on the axial characterization test results, a multi-linear force-deformation model with associated damping ratio was calibrated. This numerical model was then subsequently used to perform the hybrid simulation tests. The data points used to define the multi-linear behaviour were derived from the axial hysteresis loop at the zero horizontal displacement state shown in Figure 110.

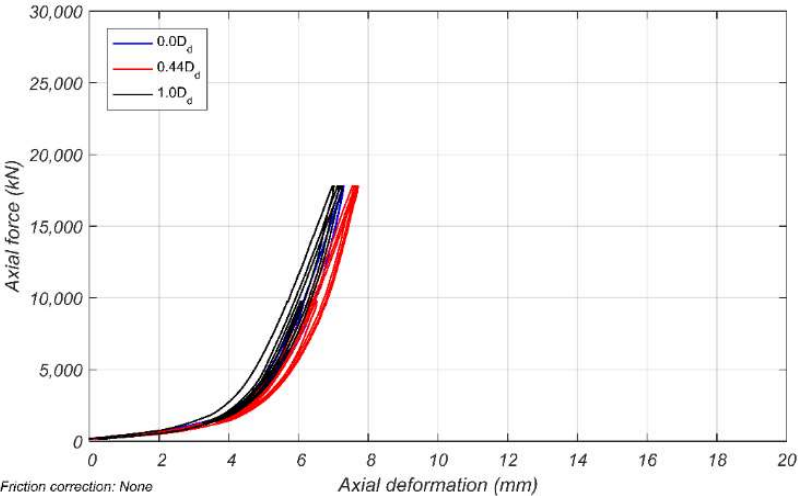


FIG. 110. Comparison of axial force-deformation behaviour of TPFB for axial compression tests with three different levels of horizontal offset.

To compare the axial compression behaviour for the three different types of isolators, axial characterization test results are plotted together as shown in Figure 111. All three bearing types

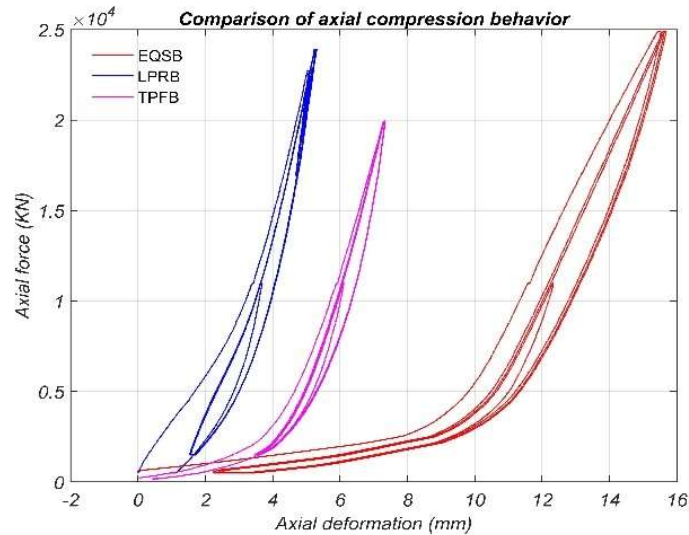


FIG. 111. Comparison of axial force-deformation behaviour of different bearing types (LRB, EQSB, TPFB) for axial compression tests with no horizontal deformation.

demonstrate increasing compression stiffnesses at low axial force levels and constant compression stiffnesses when the axial load is ramped up to larger values exceeding the design level axial load. The LRB and the TPFB isolators exhibit similar compression stiffness at and beyond design level axial compression forces. The EQSB is axially more flexible due to the low vertical stiffness of the Polytron disk. Due to the more flexible initial nonlinear behaviour, overall larger axial deformation is expected for the EQSB and TPFB isolators.

5.3.4.2 Horizontal (effect of axial load)

The horizontal force-displacement relations for the TPFB at different levels of compression load are shown in Figure 112. The horizontal restoring force for the TPFB isolator comes from multiple pendulum systems in series and is controlled by the friction forces at each sliding surface. Because the absolute amplitude of the friction force depends on the axial force at the sliding surface, the horizontal shear forces are also largely dependent on axial compression as shown in Figure 112. In addition, the post yield (post sliding) stiffness ratios are proportional to the instantaneous axial force and inverse-proportional to the effective pendulum length. Hence, the post yield stiffnesses are also different for the three axial load levels. To better illustrate the horizontal behaviour of friction bearings, such as the TPFB, the horizontal restoring force is often normalized by the instantaneous axial compression force. This results in a preferred representation of the horizontal hysteresis loops as shown in Figure 113.

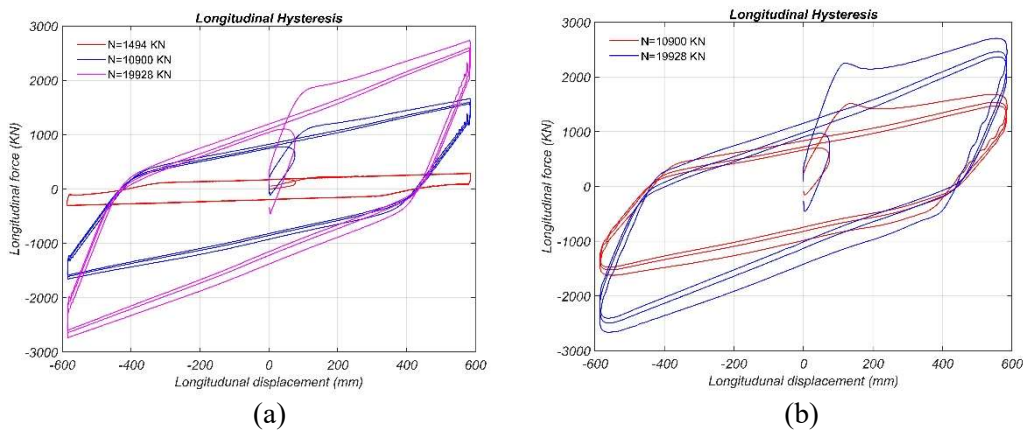


FIG. 112. Comparison of horizontal force-deformation behaviour of TPFB for different levels of axial compression. (a) Results from characterization tests conducted at 0.02 Hz. (b) Results from characterization tests conducted at 0.1 Hz.

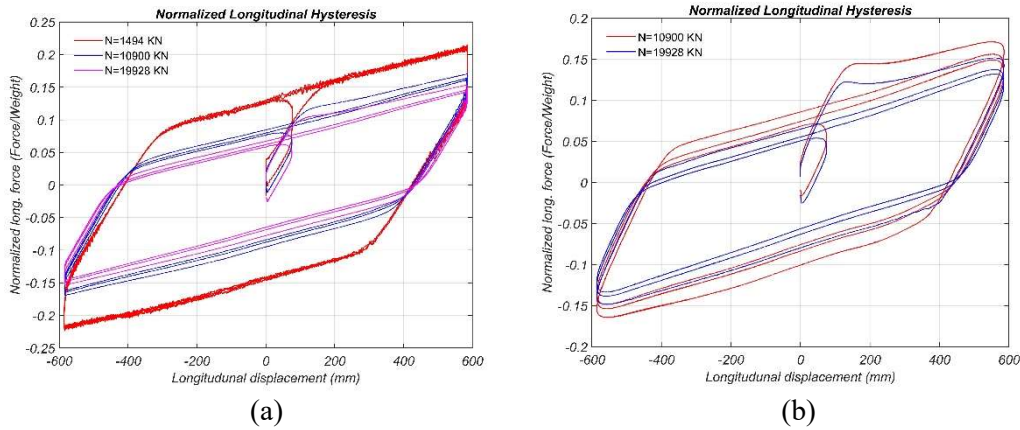


FIG. 113. Comparison of normalized horizontal force-deformation behaviour of TPFB for different levels of axial compression. (a) Results from characterization tests conducted at 0.02 Hz. (b) Results from characterization tests conducted at 0.1 Hz.

When plotting hysteresis loops where shear forces are normalized by axial compression, the horizontal behaviour of the TPFB isolator is quite similar for different levels of axial load. This is particularly the case when axial load levels are equal or larger than the design level axial load of 10900 kN.

Because of pressure dependency of the coefficient of friction, normalized shear amplitudes are larger for small axial compression loads. This clearly indicates that the coefficient of friction for PTFE to stainless steel sliding interfaces increases as the pressure on the contact surface decreases. This effect becomes fairly pronounced for small axial loads well below the design level axial load and demonstrates that it is important to design TPFB systems with adequate contact surface pressures on all the sliding surfaces of the multi-stage bearing. Considering the working axial compression loads for the TPFB isolator design discussed here, it can be concluded that the horizontal shear behaviour is quite stable for the expected range of axial load fluctuation.

The axial compression force histories for the two characterization tests at the faster loading rate of 0.1 Hz are shown in Figure 114. As evident from the graph, there was a moderate amount of axial force fluctuation observed in both tests, indicating that the SRMD machine was having difficulties maintaining the prescribed constant axial load for these tests at the faster loading rate. This problem was caused by the inherent kinematic behaviour of the TPFB isolator which gets taller as it deforms horizontally in shear due to the pendulum mechanisms. The change in height is nonlinear as well as path dependent complicating the control of the axial load applied by the SRMD. The faster the bearing deforms horizontally, the faster the SRMD platen has to move down to be able to maintain the constant axial compression load. Although kinematic vertical-horizontal coupling is also seen in the LRB (they get shorter as they deform horizontally in shear), the effect is much more pronounced in the TPFB and hence the tracking of the vertical load was less accurate.

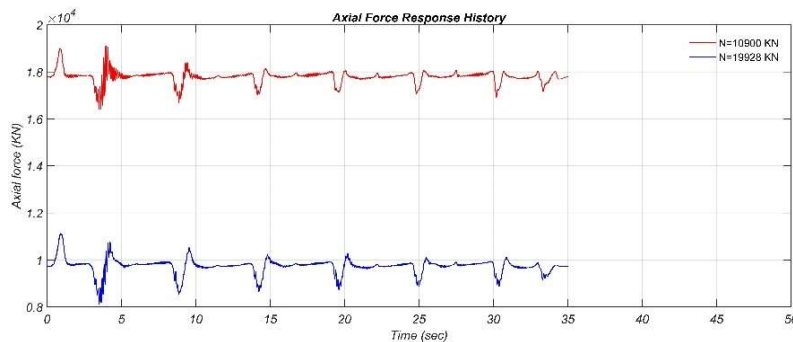


FIG. 114. Axial compression force histories for two characterization tests conducted at 0.1 Hz.

5.3.4.3 Horizontal (effect of loading rate)

The effect of the rate of loading on the horizontal shear behaviour is investigated by comparing hysteresis loops from four tests conducted at different loading frequencies (0.02 Hz, 0.1 Hz, 0.2 Hz and 0.4 Hz). Two sets of results for different levels of axial compression are shown in Figure 115. It can be concluded that the behaviours at different loading rates are very similar, except for the first half-cycle when the isolator starts to move, as indicated by the red circles in Figure 115. For higher testing speeds, the shear force spike at the initiation of movement is increasing.

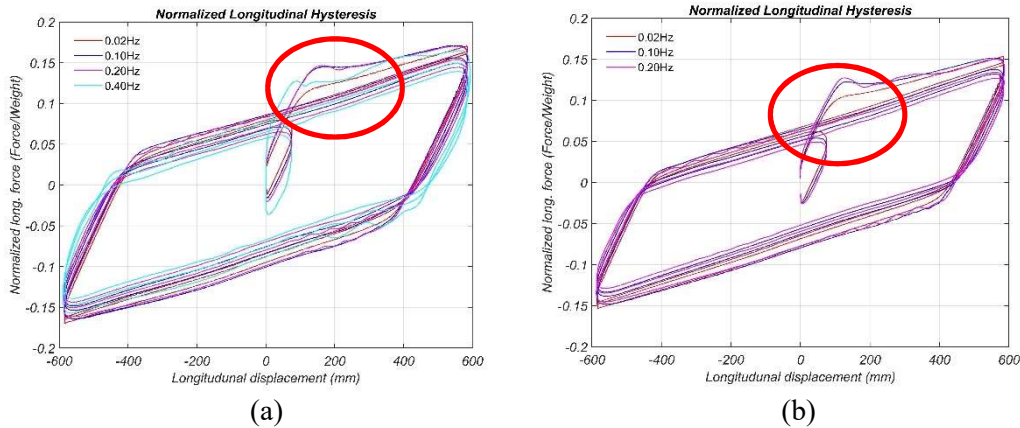


FIG. 115. Comparison of normalized horizontal force-deformation behaviour of TPFB for different loading rates. (a) Characterization tests with different loading rates are conducted at 10900 kN axial compression load (b) Characterization tests with different loading rates are conducted at 19928 kN axial compression load.

This spike was also observed for the EQSB characterization test results as discussed previously. This increase in the horizontal resisting force is caused by the bonding force (due to adhesion) between the stainless-steel sliding surface and the PTFE slider. When the two surfaces suddenly start to move against each other, the adhesion that developed during the static stage tends to resist the relative movement from commencing. Hence, a break-away force which is larger than the dynamic friction force determined based on nominal friction coefficients is needed to start the sliding stage. This break-away force results in an abnormal behaviour for the first half-cycle because the shear force needs to return to a stable hysteretic behaviour. The shear force overshoot at the beginning causes a nearly negative horizontal post-yield stiffness in the first half-cycle of movement. The magnitude of the break-away force due to adhesion is dependent on velocity and jerk (derivative of acceleration) of the movement. Therefore, if the initiation of movement is gentle, or the test is conducted very slowly, the adhesion effect is small and the spike in the shear force nearly disappears. Studies on the frictional response of PTFE sliding surfaces similar to the ones used in the TPFB and EQSB isolators, have found very similar behaviour [34].

As long as the isolator starts moving and transitions into a stable hysteresis after the first half-cycle, this spike will not appear in further loading cycles. The horizontal behaviour under different loading speeds is almost identical thereafter. It is suggested that this break-away friction effect is included in any future numerical model developments of friction type isolators. Under seismic loading conditions, depending on the nature of the ground motion, a friction isolator might experience the maximum shear force due to the break-away friction effect.

5.3.4.4 Horizontal (effect of temperature)

Temperature effects are investigated by performing characterization tests for ambient temperature conditions and for elevated temperature conditions resulting from a previous characterization test. However, due to the recharging time required between successive tests, temperatures at the start of two characterization runs are not that different. The temperature (28.5 °C) of the concave sliding surface for the second test (elevated temperature condition) was only a few degrees above the ambient temperature

condition (25 °C). Therefore, the hysteresis loops shown in Figure 116 are nearly identical for the ambient and elevated temperature conditions.

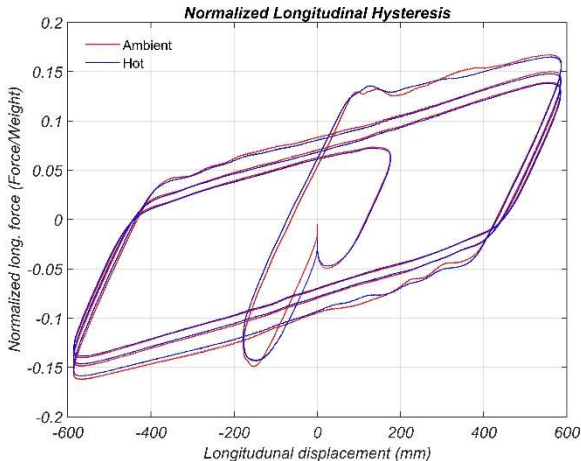


FIG. 116. Comparison of horizontal force-deformation behaviour of TPFB for different bearing temperatures (The actual starting temperatures are very similar for the two runs).

Nonetheless, after a characterization run, the temperature of the concave sliding surface increases to 42 °C. By investigating the horizontal shear force time history as shown in Figure 117, it can be observed that the shear force amplitude is decreasing significantly with each loading cycle. This indicates that the friction coefficient is reducing because of the increase in temperature at the sliding surface.

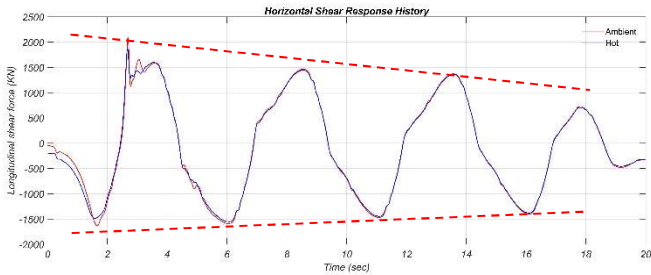


FIG. 117. Comparison of horizontal shear force histories of TPFB for different initial temperature conditions.

5.3.4.5 Horizontal (effect of displacement amplitude)

To investigate the behaviour of TPFB under different horizontal displacement amplitudes, several characterization tests were performed with increasing peak displacements corresponding to 45%, 100%, and 165% of the design displacement. Results in terms of horizontal hysteresis loops are compared in Figure 118.

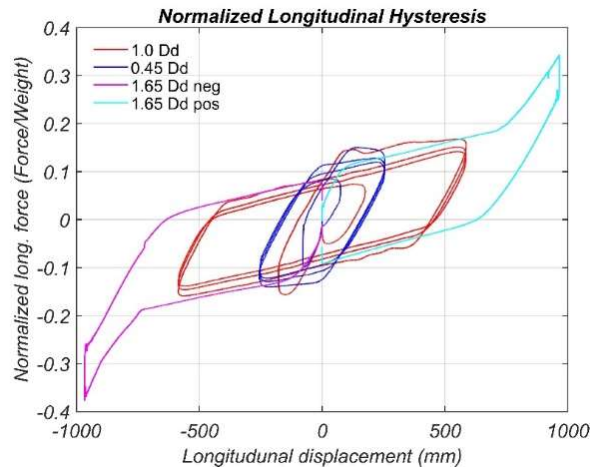


FIG. 118. Comparison of normalized horizontal shear force-deformation behaviour of TPFB for different displacement amplitudes.

When displacement amplitudes are small, such that the stiffening stage of the TPFB is not activated, the bearing tends to produce hysteresis loops that are similar to the loops at the design displacement amplitude (red line) and the 45% design displacement amplitude (blue line). When the isolator displacement amplitude is very small, the TPFB exhibits slightly larger shear restoring forces as can be observed from the wider hysteresis loops. A possible cause for this behaviour is the fact that the heating of the sliding surface is significantly smaller when the isolator travels shorter distances. This leads to smaller reductions in the coefficients of friction and thus the shear force amplitudes.

In contrast, when the isolator deformation exceeds 120% of the design displacement (710 mm), the stiffening behaviour of the TPFB is triggered. As indicated in Figure 118, the isolator shows an almost constant increase of the stiffness after passing through a gradual transition zone. This transition into the hardening stage of the isolator is achieved by two mechanisms including the intentional yielding and permanent damage of certain parts of the isolator as shown in Figure 119. The unique design of the tested TPFB consists of the main sliding surfaces for the top and bottom concave dishes, which both have constant curvature, and a specially designed retaining rim with gradually increasing curvature that is surrounding the main sliding surfaces (also see Figure 26). When the movement of the outer slider reaches the edge of the main sliding area (stainless steel area shown in Figure 119b), the slider starts to dig into and move up on the outer rim area (white area shown in Figure 119b). This results in an increase of the isolator stiffness because of the change in curvature. Simultaneously, the upper and lower edges of the slider, which are specially designed to have yielding lips, are gauging into the outer rim, resulting in permanent plastic deformations. The lips at the upper and lower edges of the slider start to deform and close. This yielding mechanism contributes to the gradual hardening behaviour but also protects the PTFE sliding material.

The built-in mechanical hardening behaviour of the TPFB is expected to provide additional horizontal displacement and shear force capacity and is important for safety considerations under extreme loading conditions. Due to the limited vertical stroke of the SRMD testing machine, the maximum horizontal displacement achieved during the ultimate displacement characterization test was 899 mm. Although stiffening and yielding already occurred at this displacement amplitude, it was still far from the ultimate horizontal displacement capacity of the TPFB.

5.3.4.6 Summary

The TPFB characterization test results were discussed in this section while focusing on the effect of different loading conditions. The results indicated that the absolute horizontal shear force amplitude depended on axial compression because both the characteristic strength and the post-sliding stiffness of the TPFB depended on the instantaneous axial compression force. It was found that friction coefficients at the sliding interfaces were slightly larger if the axial compression was small. Loading speeds did not affect the general horizontal behaviour of the TPFB. However, it was observed that for greater loading speeds, a larger break-away force was needed in the first half-cycle to initialize the movement of the

bearing. It was concluded that the break-away force was most likely caused by adhesion at the sliding interface. Temperature had a moderate effect on the strength of isolator which was decreasing from cycle to cycle as temperature was increasing due to the work done at the sliding interface. At larger shear deformations, the TPFB exhibited a gradual hardening behaviour that commenced around 710 mm. The gradual hardening was achieved by a yielding mechanism that caused intentional damage to specially designed parts of the bearing.

5.3.5 Numerical bearing model parameters calibrated from characterization tests

Based on selected characterization test results, numerical isolator element parameters were calibrated for OpenSees and then subsequently used to perform the hybrid simulation tests. The calibrated numerical isolator element parameters are summarized in this section.



FIG. 119. Behaviour of TPFB when hardening stage initiates. (a) Large displacement of the bearing into the hardening stage. (b) Yielding mechanism and damage of rim and slider edge after the run.

Firstly, as concluded from the characterization tests discussed above, the axial compression behaviour for all three bearing types is highly nonlinear. Before starting the hybrid simulation tests, it was decided that using a single constant compression stiffness to represent the vertical behaviour of the bearings would not be accurate enough. Therefore, based on the axial force-deformation hysteresis loops obtained from the characterization tests, a multilinear material model was used to represent the axial compression behaviour for each type of bearing. The data points used to define the backbone curve of the material model are summarized in Table 24. The vertical effective damping value was calculated based on the energy dissipation inside the axial hysteresis loops. The single valued effective compression stiffness was only used to calculate the rotational resistance of the isolator in the 1-bearing and 5-bearing equivalent hybrid models.

The horizontal key parameters were calibrated based on a combination of characterization and hybrid simulation test results. An optimization approach was used to determine optimal key that correspond to the element parameters of the OpenSees numerical isolator models. For the LRB element the parameters that were optimized are the yielding strength, f_y , the linear hardening ratio, α_1 , and the nonlinear hardening parameters α_2 and μ . For the EQSB element the parameters that were optimized are the coefficients of friction at slow and fast sliding velocities, and the linear hardening ratio. For the TPFB element the parameters that were optimized are only the coefficients of friction at slow and fast sliding velocities for the second sliding surface which are identical to the coefficients of friction of the third sliding surface. Other parameters for the TPFB are based on the bearing geometry which is fixed and hence does not require optimization. For the optimization based on the characterization tests the first negative cycle was typically used and for the calibration based on the hybrid simulation results the largest displacement cycle was used. The key parameters needed to define the LRB, EQSB and TPFB models and their values are summarized in Tables 25 thru 27. For the subsequent hybrid simulation experimental work, element parameters for the numerically modelled isolators are based on the values given in Tables 24 thru 27.

TABLE 24. DATA POINTS USED TO DEFINE MULTI-LINEAR AXIAL COMPRESSION BEHAVIOR OF BEARINGS

LRB		EQSB		TPFB	
Deformation (mm)	Force (kN)	Deformation (mm)	Force (kN)	Deformation (mm)	Force (kN)
-4.85	-21351.46	-15.61	-22241.11	-6.83	17792.89
-4.45	-17472.61	-13.96	-15337.47	-6.34	13513.70
-3.81	-12615.16	-12.71	-10960.42	-5.73	-9296.78
-3.17	-8776.34	-11.43	-6983.71	-5.09	-6263.10
-2.53	-6138.55	-10.15	-4021.19	-4.45	-3896.64
-1.89	-4248.05	-8.90	-2482.11	-3.81	-2348.66
-1.28	-2882.45	-7.62	-1823.77	-2.54	-1036.44
0.00	0.00	0.00	0.00	-1.27	-453.72
0.88	845.16			0.00	0.00
Kvertical_eff (kN/mm)	5099.69	Kvertical_eff (kN/mm)	3662.78	Kvertical_eff (kN/mm)	6567.26
Damping_eff	3.25%	Damping_eff	3.00%	Damping_eff	1.80%

TABLE 25. KEY PARAMETERS NEEDED TO DEFINE LRB ELEMENT

Kinitial (kN/mm)	fy (kN)	Linear hardening ratio	Nonlinear hardening ratio	Nonlinear hardening exponent	Keff (kN/mm)
263.61	1387.85	1.76%	0.028%	4.8	12.67

TABLE 26. KEY PARAMETERS NEEDED TO DEFINE EQSB ELEMENT

Kinitial (kN/mm)	μ_{Fast}	μ_{Slow}	Linear hardening ratio	Keff (kN/mm)
470.70	0.15	0.10	2.15%	19.83

TABLE 27. KEY PARAMETERS NEEDED TO DEFINE TPFB ELEMENT

μ_{1Fast}	μ_{1Slow}	μ_{2Fast}	μ_{2Slow}	μ_{3Fast}	μ_{3Slow}	L1 (mm)	L2 (mm)	L3 (mm)	Keff (kN/mm)
0.025	0.025	0.115	0.077	0.115	0.077	533.4	3670.2	3670.2	2.76

5.4 HYBRID MODELS OF ARCHETYPE PLANT

The finite element analysis models used in the hybrid simulation tests described in this publication were developed in the Open System for Earthquake Engineering Simulation (OpenSees) software. Three different analysis models of varying complexity were developed for this purpose. All of the models are based on the information supplied within the international benchmark specification (Section 3).

5.4.1 Material and damping properties

The strength, stiffness and weight density of the reinforced concrete, which was used to model the reactor containment building, internal structure, auxiliary complex building, and the common base mat, were defined with the following properties:

RCB & INS reinforced concrete material:

- Strength: 41.4 MPa
- Elastic Modulus: 30452 MPa
- Shear Modulus: 13014 MPa
- Poisson's Ratio: 0.17
- Weight Density: 23.56 kN/m³

ACB & MAT reinforced concrete material:

- Strength: 27.6 MPa
- Elastic Modulus: 27771 MPa
- Shear Modulus: 11868 MPa
- Poisson's Ratio: 0.17
- Weight Density: 23.56 kN/m³

Rigid material:

- Strength: 27.6 MPa
- Elastic Modulus: 2777100 GPa
- Shear Modulus: 1388550 GPa
- Poisson's Ratio: 0.0
- Weight Density: 0.0 kN/m³

Damping was assigned as stiffness proportional damping with the following value:

- 5% anchored at 3.7 Hz

For simplicity the same amount of damping anchored at the fundamental frequency of the RCB was assigned to all structural components.

5.4.2 Development of ANT 3D model in OpenSees

The benchmark specification (Section 3) provided three variations of the ANT model in the SAP2000 structural analysis software format. The three models consist of the same plant superstructure as it was described in the previous section but use three different approaches to model the seismic isolation plane. The first and simplest model utilizes one equivalent bearing element to represent the entire isolation plane. The second model consists of five bearings where each one of them represents a group of bearings under the four sections of the auxiliary building and the one reactor containment building section. The third and most complex model includes all 486 bearings in the isolation plane and is used to best represent the behaviour of the seismic isolation plane in terms of overturning, vertical, and torsional response. The stick model properties (nodal coordinates, nodal mass and mass moment of inertia assignments, and frame section properties) of the power plant superstructure are described in detail in Section 3 of this publication.

All three models were being used for the hybrid simulations. For the one-bearing equivalent model, the experimental bearing specimen represented all of the isolators beneath the power plant. For the hybrid simulations with the five-bearing equivalent model, the experimental element was assigned to represent either the group of bearings under the RCB or the group of bearings under ACB1 (the north-east quadrant of the ACB). In the hybrid tests with the 486-bearing model the experimental element was assigned to the isolator in the northeast corner of the nuclear island mat. In terms of numerical isolator models, for the five-bearing equivalent model and the 486-bearing model, three bearing types were considered: Lead Plug Rubber Bearings (LRB), EradiQuake System Bearings (EQSB) and Triple Pendulum Friction Bearing (TPFB). For the lead plug rubber bearings, two different numerical models

were employed. One is the LRB_BW based on the Bouc-Wen hysteretic model and the other is the LRB_X. The latter model contains the effect of strength reduction due to temperature increase during a seismic event.

The OpenSees models for the hybrid simulations were created by converting the SAP2000 models provided by the benchmark specification. Typically, a three-step procedure was employed to convert the models. First, the translation tool that is available in the OpenSees Navigator graphical user interface (GUI) was used to convert the SAP2000 models into OpenSees Navigator models. Second, the converted model was checked, and model properties were graphically adjusted in the OpenSees Navigator GUI wherever the translation process had difficulties finding an appropriate match. Third, the OpenSees Navigator model was exported as TCL scripts and those scripts were manually parameterized, to be run in OpenSees and OpenSeesSP.

After the SAP2000 model had successfully been converted to OpenSees, a gravity analysis was performed to check the weights (dead loads) of the different components of the converted model. It was confirmed that the dead load analysis produced the same gravity forces in the structure as for the original SAP2000 model. The weights for the individual components of the model are in Table 28.

TABLE 28. ANT MODEL WEIGHTS

Component	Weight [kN]	Weight [kip]
NI-Buildings	3699150	831602
NI-Mat	1031142	231810
Total NI	4730292	1063412
Pedestals	150697	33878
Total Plant	4880989	1097290

It is important to note that some changes were introduced in the SAP2000 models once converted to OpenSees. Knowledge about those changes is important when interpreting hybrid simulation results. The changes mainly affect the discretization of the upper basemat. They are summarized in the following subsections. Note that not all prescriptions in the benchmark specification were followed. Particularly, the upper basemat was not considered to be a rigid body.

The axial force distribution under the gravity load case for the three different isolator types is shown in Figure 120. Generally, the axial forces in the bearings are fairly consistent and do not vary too much from the average axial load of 9733 kN. However, it is also clear from the plots that the isolators on the west side of the ANT model see axial loads that are larger than the average and conversely the isolators on the east side see axial loads that are smaller than the average. The isolators under the RCB experience axial loads that are very close to the average axial load.

The differences in the axial load distribution for the three different isolator types are minor, as can be seen from Figure 120. The plant isolated with the EQSB sees the smallest axial force variation, followed by the plant isolated with LRB, and the plant isolated with the TPFb experiences the largest axial force variation.

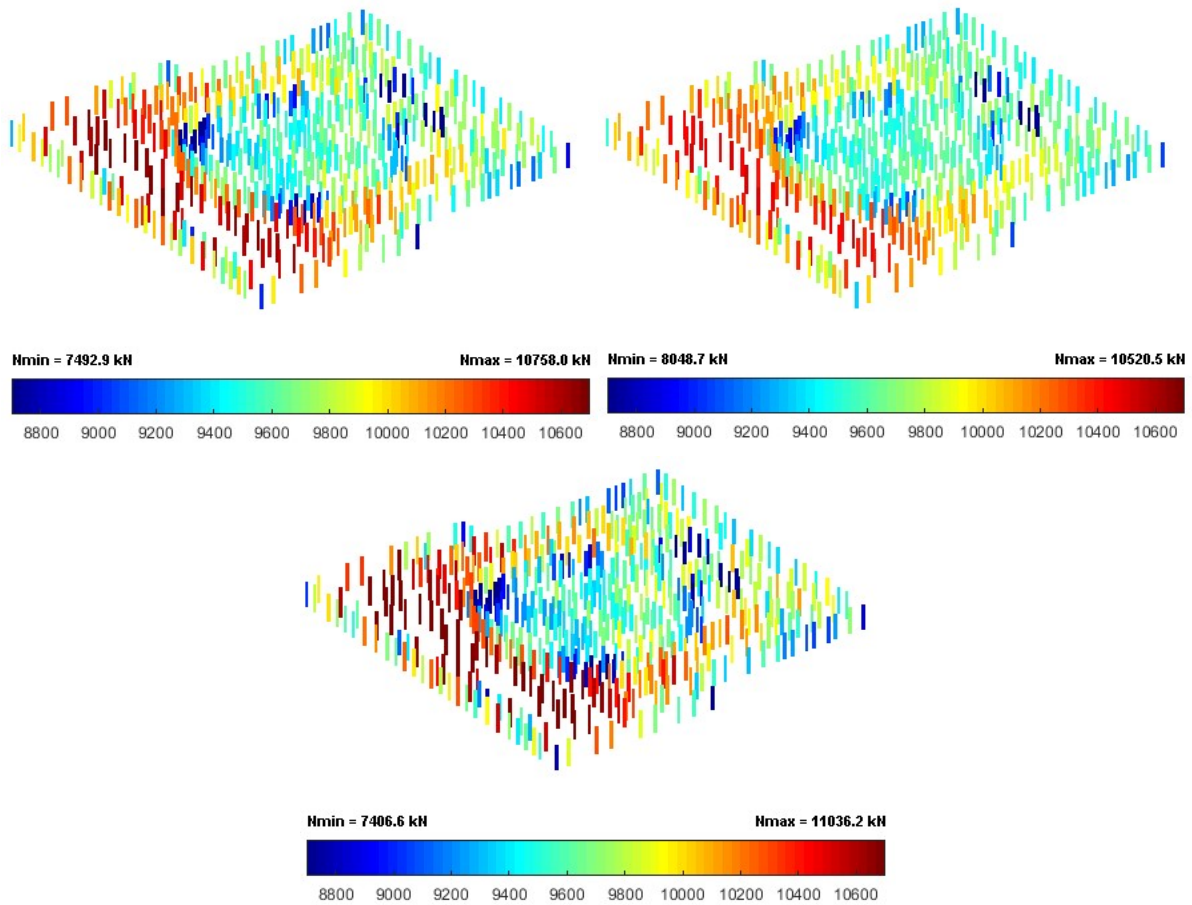


FIG. 120. Comparison of isolator axial force distribution for gravity load case. LRB (top left), EQSB (top right), and TPFB (bottom centre).

5.4.2.1 486-bearing model with coarse mesh in the basemat

In an effort to reduce the number of free degrees of freedom and thus speed up the analyses, especially for the hybrid simulations, the nuclear island basemat was manually re-meshed. The new discretization of the mesh tried to create fewer subdivisions between the locations of the isolators. Furthermore, it used only one solid element over the 3 m thickness of the basemat under the ACB and one solid element for the 7 m thick portion of the basemat under the RCB.

Given this new coarser mesh the total number of free degrees of freedom was reduced from 18597 down to 10752. As desired, this change significantly reduced computation times for the 486-bearing model. The modal information comparing frequencies between the original SAP2000 model and the converted OpenSees model showed a good agreement, which confirms that the coarse mesh model was a valid simplification.

5.4.2.2 Five-bearing equivalent model

The five-bearing model, as it was included in the benchmark specification, included the whole basemat and had some problems with the way the basemat was supported on the five equivalent isolators included in the model. To reduce computation times and correct the vertical support of the power plant superstructure, a new five-bearing equivalent model was developed, which used frame elements combined with rigid elements to model the ACB and RCB mats.

The nuclear island was first divided into the five parts shown in Figure 14 and then equivalent cross section properties, masses, and mass moments of inertia were calculated for each part, so that they could be assigned to the equivalent frame elements and nodes shown in Figure 121. For simplicity, sections

ACB1 and ACB4 were assumed to have the same properties and sections ACB2 and ACB3 were made identical. The properties are summarized in Table 29.

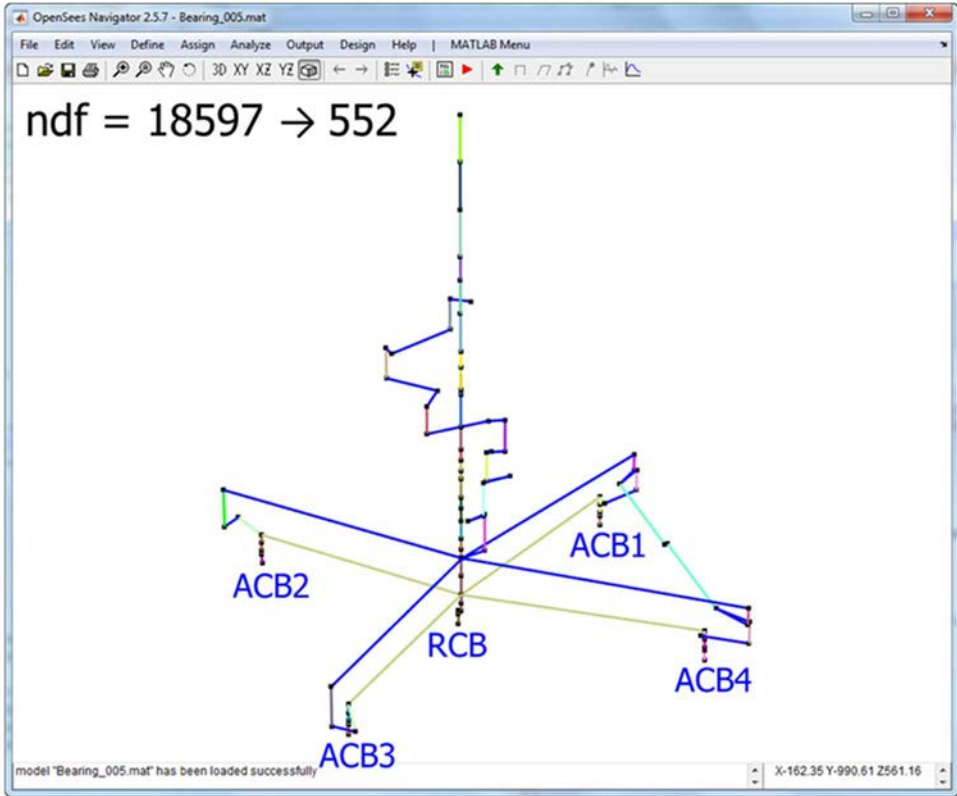


FIG. 121. Five-bearing model in OpenSees.

TABLE 29. PROPERTIES FOR BEAM CROSS SECTIONS MODELLING THE UPPER BASEMAT FOR THE FIVE-BEARING MODEL IN OPENSEES

Prop.	ACB1 & ACB4	ACB2 & ACB3	RCB	Units
xCG	104.51	-92.57	0.0	ft
yCG	78.70	96.33	0.0	ft
A	19023	21675	22165	ft ²
h	10	10	10	ft
V	190230	216750	221650	ft ³
ρ	0.15	0.15	0.15	kip/ft ³
W	28535	32513	33248	kip
M	886.88	1010.52	1033.32	kip-s ² /ft
Mxx	1327577	2108876	1838733	kip-s ² -ft
Myy	1956408	1990553	1838773	kip-s ² -ft
Mzz	3269203	4082588	3660324	kip-s ² -ft
Ix	28308908	45045709	39420233	ft ⁴
Iy	41800282	42507051	39420233	ft ⁴
Ixy	11903087	-14423529	0	ft ⁴
J	42473839	56906441	78840467	ft ⁴
Avx	16175	18659	20010	ft ²
Avy	15942	18,776	20010	ft ²

The calculated cross section properties for the five different nuclear island parts were assigned to vertical frame elements located at each sections center of gravity. Additional nodes were created at mid-height of the basemat (elevation 15.24 m, 50 ft) and the calculated masses and mass moments of inertia were assigned to these nodes. Similarly, for the upper part of the RCB mat two frame elements were used to define the cross section and an additional node was created at elevation 20.27 m (66.5 ft) to assign masses and mass moments of inertia. The properties for the upper part of the RCB mat are listed in Table 29. The five different parts of the upper basemat were connected together using rigid frame elements as can be seen in Figure 121. Given this approach of using equivalent frame sections to represent the nuclear island mat and tying them together with rigid elements, the total number of free degrees of freedom was reduced from 18597 down to 552. This significant reduction of degrees of freedom made it possible to conduct real-time hybrid simulations without any timing issues from the numerical analysis.

Next, it was necessary to determine equivalent bearing properties for the five isolators. For this the 486 isolators were divided into sections as shown in Figure 14. The number of isolators in the four quadrants of the ACB was balanced as well as possible, leading to 86 isolators supporting ACB1 and 87 isolators supporting each of the other three quadrants. There were 139 isolators under the RCB section of the mat. The equivalent properties for the five isolators are shown in Table 30. As can be seen from the table, the rotational properties of the equivalent bearings were calculated based on horizontal and vertical effective stiffness and effective damping properties that were obtained according to the procedure described in Section 5.3.5. Minor adjustments of the rotational stiffness on the order of 3% to 5% (as can be seen from the factors in Table 30) were necessary to obtain a better match of the modal periods between the 486-bearing model and the five-bearing equivalent model.

Comparison of frequencies in the original 5-bearing SAP2000 model and the converted OpenSees model showed a good agreement of the first three frequencies, which corresponded to the isolation modes. However, higher mode frequencies, especially the ones that included vertical and overturning effects, did not match well, due to an interpreted vertical support problem in the SAP2000 model. Since the matching of frequencies with the original 486-bearing SAP2000 model was much better, it was concluded that the newly developed 5-bearing equivalent model in OpenSees could be used for the experimental hybrid simulations.

5.4.2.3 *One-bearing equivalent model*

To further simplify the analysis model, a one-bearing equivalent model was developed next. The one-bearing model can represent the global behaviour of the power plant quite well but cannot capture torsional and overturning effects on the behaviour of the individual isolator. The main advantages of this most simplified model are much faster computation times and less convergence issues, which are both very important for conducting real-time hybrid simulations.

Similar to the five-bearing model, the lower part of the upper basemat was approximated by two equivalent frame elements and the upper part of the basemat beneath the RCB was also modelled with two equivalent frame elements. Nodes for assigning masses and mass moments of inertia are again placed at mid-height through the mat thickness. Figure 122 shows the model in OpenSees. The total number of free degrees of freedom was reduced from 18597 down to 456. Table 31 and Table 32 summarize the properties of the cross sections and the equivalent isolator properties, respectively. It is important to note that for the ACB cross section the moments of inertia from the RCB cross-section were used instead of the actual calculated ones. This was necessary to approximate the bending stiffness of the ACB mat. Similar to the five-bearing equivalent model it was necessary to slightly adjust the rotational properties of the equivalent bearing to obtain a better match of the modal periods between the 486-bearing model and the one-bearing equivalent model. In this case the R_{yy} properties had to be reduced by 10% as is evident from the factors in Table 32.

Finally, the modal information for the converted OpenSees models is shown in Table 33, where the natural frequencies of the original 486-bearing SAP2000 model are included for comparison.

TABLE 30. EQUIVALENT ISOLATOR PROPERTIES FOR THE FIVE-BEARING MODEL IN OPENSEES

Section	Direction	Linear		Nonlinear		
		Stiffness	Damping	Stiffness	Yield Strength	Post Yield Stiffness Ratio
RCB	X	$139 \cdot k_{v_{eff}}$	$139 \cdot c_{v_{eff}}$	-	-	-
	Y	$139 \cdot k_{h_{eff}}$	$139 \cdot c_{h_{eff}}$	$139 \cdot k_{h_{init}}$	$139 \cdot q_d$	7.82E-03
	Z	$139 \cdot k_{h_{eff}}$	$139 \cdot c_{h_{eff}}$	$139 \cdot k_{h_{init}}$	$139 \cdot q_d$	7.82E-03
	XX	$1.03 \cdot 588120 \cdot k_{h_{eff}}$	$1.03 \cdot 588120 \cdot c_{h_{eff}}$	-	-	-
	YY	$0.95 \cdot 299216 \cdot k_{v_{eff}}$	$0.95 \cdot 299216 \cdot c_{v_{eff}}$	-	-	-
	ZZ	$0.95 \cdot 288904 \cdot k_{v_{eff}}$	$0.95 \cdot 288904 \cdot c_{v_{eff}}$	-	-	-
ACB1	X	$86 \cdot k_{v_{eff}}$	$86 \cdot c_{v_{eff}}$	-	-	-
	Y	$86 \cdot k_{h_{eff}}$	$86 \cdot c_{h_{eff}}$	$86 \cdot k_{h_{init}}$	$86 \cdot q_d$	7.82E-03
	Z	$86 \cdot k_{h_{eff}}$	$86 \cdot c_{h_{eff}}$	$86 \cdot k_{h_{init}}$	$86 \cdot q_d$	7.82E-03
	XX	$1.03 \cdot 289905 \cdot k_{h_{eff}}$	$1.03 \cdot 289905 \cdot c_{h_{eff}}$	-	-	-
	YY	$108770 \cdot k_{v_{eff}}$	$108770 \cdot c_{v_{eff}}$	-	-	-
	ZZ	$181135 \cdot k_{v_{eff}}$	$181135 \cdot c_{v_{eff}}$	-	-	-
ACB2	X	$87 \cdot k_{v_{eff}}$	$87 \cdot c_{v_{eff}}$	-	-	-
	Y	$87 \cdot k_{h_{eff}}$	$87 \cdot c_{h_{eff}}$	$87 \cdot k_{h_{init}}$	$87 \cdot q_d$	7.82E-03
	Z	$87 \cdot k_{h_{eff}}$	$87 \cdot c_{h_{eff}}$	$87 \cdot k_{h_{init}}$	$87 \cdot q_d$	7.82E-03
	XX	$1.03 \cdot 425040 \cdot k_{h_{eff}}$	$1.03 \cdot 425040 \cdot c_{h_{eff}}$	-	-	-
	YY	$190550 \cdot k_{v_{eff}}$	$190550 \cdot c_{v_{eff}}$	-	-	-
	ZZ	$234490 \cdot k_{v_{eff}}$	$234490 \cdot c_{v_{eff}}$	-	-	-
ACB3	X	$87 \cdot k_{v_{eff}}$	$87 \cdot c_{v_{eff}}$	-	-	-
	Y	$87 \cdot k_{h_{eff}}$	$87 \cdot c_{h_{eff}}$	$87 \cdot k_{h_{init}}$	$87 \cdot q_d$	7.82E-03
	Z	$87 \cdot k_{h_{eff}}$	$87 \cdot c_{h_{eff}}$	$87 \cdot k_{h_{init}}$	$87 \cdot q_d$	7.82E-03
	XX	$1.03 \cdot 422533 \cdot k_{h_{eff}}$	$1.03 \cdot 422533 \cdot c_{h_{eff}}$	-	-	-
	YY	$185840 \cdot k_{v_{eff}}$	$185840 \cdot c_{v_{eff}}$	-	-	-
	ZZ	$236693 \cdot k_{v_{eff}}$	$236693 \cdot c_{v_{eff}}$	-	-	-
ACB4	X	$87 \cdot k_{v_{eff}}$	$87 \cdot c_{v_{eff}}$	-	-	-
	Y	$87 \cdot k_{h_{eff}}$	$87 \cdot c_{h_{eff}}$	$87 \cdot k_{h_{init}}$	$87 \cdot q_d$	7.82E-03
	Z	$87 \cdot k_{h_{eff}}$	$87 \cdot c_{h_{eff}}$	$87 \cdot k_{h_{init}}$	$87 \cdot q_d$	7.82E-03
	XX	$1.03 \cdot 356944 \cdot k_{h_{eff}}$	$1.03 \cdot 356944 \cdot c_{h_{eff}}$	-	-	-
	YY	$182203 \cdot k_{v_{eff}}$	$182203 \cdot c_{v_{eff}}$	-	-	-
	ZZ	$174741 \cdot k_{v_{eff}}$	$174741 \cdot c_{v_{eff}}$	-	-	-

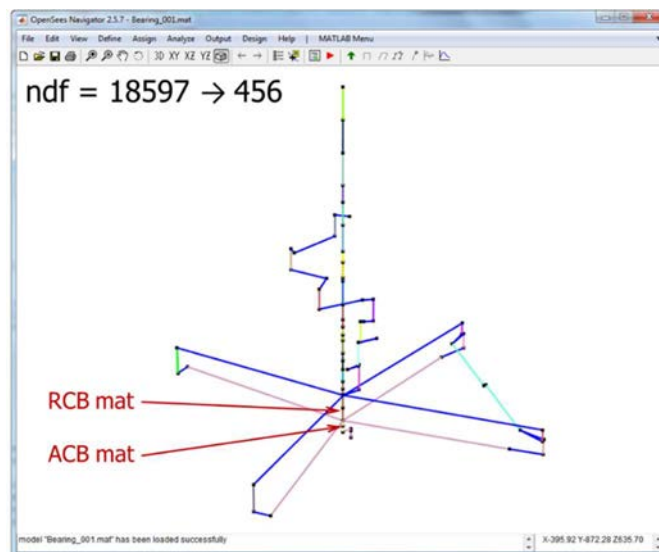


FIG. 122. One-bearing model in OpenSees.

TABLE 31. PROPERTIES FOR BEAM CROSS SECTIONS MODELLING THE UPPER BASEMAT FOR THE ONE-BEARING MODEL IN OPENSEES

Prop.	ACB	RCB	Units
A	103,560	22,165	ft ²
h	10	23	ft
V	1,035,600	509,800	ft ³
ρ	0.15	0.15	kip/ft ³
W	155,340	76,470	kip
M	4,828.12	2,376.76	kip-s ² /ft
M _{xx}	38,454,519	4,314,374	kip-s ² -ft
M _{yy}	46,429,943	4,314,374	kip-s ² -ft
M _{zz}	84,803,993	8,419,197	kip-s ² -ft
I _x	823,960,800	39,420,233	ft ⁴
I _y	995,015,385	39,420,233	ft ⁴
J	1,428,154,743	78,840,467	ft ⁴
A _{vx}	85,906	20,010	ft ²
A _{vy}	89,031	20,010	ft ²

TABLE 32. EQUIVALENT ISOLATOR PROPERTIES FOR THE ONE-BEARING MODEL IN OPENSEES

Direction	Linear		Nonlinear		
	Stiffness	Damping	Stiffness	Yield Strength	Post Yield Stiffness Ratio
X	486*k _{v,eff}	486*c _{v,eff}	-	-	-
Y	486*k _{h,eff}	486*c _{h,eff}	486*k _{h,init}	486*q _d	7.82E-03
Z	486*k _{h,eff}	486*c _{h,eff}	486*k _{h,init}	486*q _d	7.82E-03
XX	8394366*k _{h,eff}	8394366*c _{h,eff}	-	-	-
YY	0.9*3826953*k _{v,eff}	0.9*3826953*c _{v,eff}	-	-	-
ZZ	4567413*k _{v,eff}	4567413*c _{v,eff}	-	-	-

TABLE 33. COMPARISON OF MODAL INFORMATION FOR ALL OPENSEES MODELS

Mode	f [Hz] 486 iso SAP2000	f [Hz] 486 iso	f [Hz] 5 iso	f [Hz] 1 iso	Bldg. Comp.	Direction
1	0.477	0.477	0.477	0.477	INS	H2 translation
2	0.477	0.477	0.477	0.477	INS	H1 translation
3	0.710	0.711	0.710	0.711	INS	V rotation
4	3.546	3.539	3.509	3.822	RCB	H2 translation
5	3.572	3.547	3.514	3.831	RCB	H1 translation
6	6.998	7.023	7.104	6.989	ACB	H2 translation
7	7.484	7.523	7.670	7.544	ACB	H1 translation
8	7.947	7.971	8.213	8.191	INS	H1 translation
9	8.753	8.763	8.874	8.922	ACB	V rotation
10	9.881	9.817	9.795	10.122	INS	H1 translation
11	10.644	10.451	10.632	10.951	RCB	V translation
12	11.070	11.114	11.185	11.669	RCB	H2 translation
13	11.545	11.586	11.451	11.730	RCB	H1 translation
14	11.651	11.633	11.735	12.001	INS	H2 translation
15	11.673	11.724	11.765	12.542		
16	14.640	14.631	14.790	14.933		
17	15.159	15.220	15.741	15.728		
18	17.633	17.660	17.893	17.669		
19	18.951	18.986	18.806	18.654		
20	19.121	19.072	20.197	19.251		

5.5 GROUND MOTIONS

For the hybrid simulation tests, only the US-NRC RG 1.60 motions at the DBE level (0.50 g) were eventually used (see Section 3.4.3).

5.6 IMPLEMENTATION OF HYBRID SIMULATION

The SRMD testing facility was originally designed to conduct dynamic characterization tests of full scale bearing devices and dampers. This facility hosts required infrastructure (hardware and software components) that can be used to adapt the facility to conduct hybrid simulation. Hybrid simulation requires that customizable hardware components communicate with the computational driver, which solves the equations of motion for the hybrid model composed of numerical and experimental subassemblies, and the controller in the laboratory loading the experimental subassembly. For the large scale bearing tests presented here, the hybrid model needs to communicate with the SRMD control system in each integration time step to send command signals and receive measured feedback signals. For real-time testing, communications need to be very fast and reliable among the various components. Performance limitations such as actuator tracking, actuator delays, and communication speeds determine the rate of testing that can be achieved.

5.6.1 Hardware configuration

The three-loop architecture shown in Figure 123 was implemented at the SRMD to achieve continuous communication of commands and feedbacks between different components. This architecture includes OpenSees as the computational driver, the SRMD control system, and a real-time digital signal processor (DSP) all communicating through SCRAMNet+ (Shared Common Random Access Memory Network [35]).

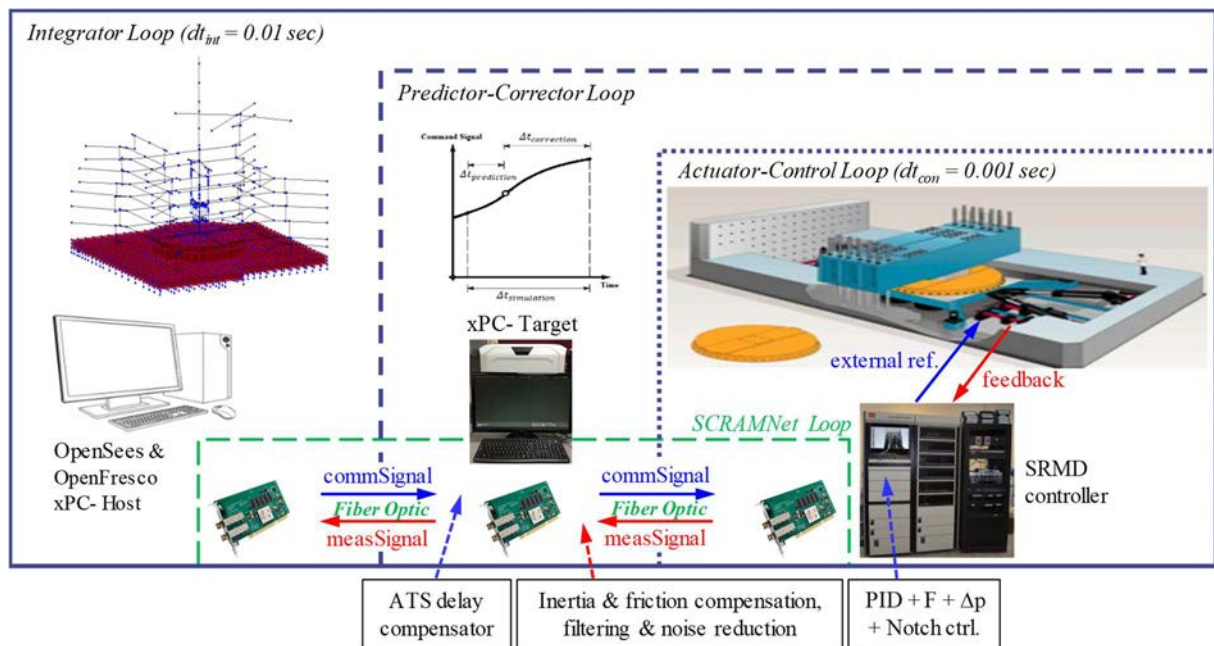


FIG. 123. Hybrid simulation hardware configuration at SRMD.

In its original configuration, the SRMD control system could only receive and send signals through analogue input/output channels and this was the approach used in previous tests (Schellenberg et al. [32]). To enable real-time testing and eliminate previously encountered problems with synchronization, delays, and noise caused by D/A and A/D conversions, the SRMD control system was upgraded with a SCRAMNet+ interface that provides complete digital communication, thus eliminating any D/A and A/D conversions.

5.6.2 Software configuration

The complex models utilized in the hybrid simulation presented in this publication require integrated software components. Fast solver operated under multi-processor computing system communicates with the hydraulic controller through a middleware, OpenFresco.

OpenSeesSP is used as the computational driver in the hybrid simulation. It provides advanced capabilities for modelling and analysing the nonlinear response of structural systems using a wide range of material models, elements, and solution algorithms.

The OpenFresco (Open-source Framework for Experimental Setup and Control) software framework [14] is the middleware that was deployed to connect the finite element model with the SRMD control and data acquisition systems. A new experimental bearing element was developed in OpenFresco that is able to transfer three translational and three rotational degrees of freedom to the experimental substructure. Furthermore, this new experimental bearing element provides the user-selectable option to either transfer deformation or force in the axial direction. Due to the high axial stiffness of the bearings investigated here, force control is preferred in the vertical direction. This enables 3D testing that can capture the vertical-horizontal coupling of large-scale seismic isolation bearings.

The SRMD control system operates at a rate of 1000 Hz, updating the actuator commands and getting feedback signals from sensors measuring the current displacement and force state of the machine. For smooth control and movement of the platen, the external commands to the actuators need to be updated and synchronized at the same rate. However, the numerical analyses of the hybrid simulation don't complete in the given time step size of 1 ms. The real-time predictor-corrector algorithm applied in the hybrid simulation enables to make smooth command signals by synchronizing the rate of the control system base clock frequency.

5.6.3 Special Settings for Testing Triple Friction Pendulum Bearings

Testing pendulum bearings in horizontal direction requires significant movement of the table platen in the vertical direction due to the geometry of these bearings. In other words, once the slider inside the bearing starts to move up as it slides sideways on the concave surfaces, the table platen needs to move down to accommodate the increase in height of the bearing. In case of poor tracking of the vertical displacement of the system (which is controlled by the inner loop in the cascade control loop), the axial force on the bearing (controlled by the outer loop in the cascade control loop) will likely have poor tracking as well. This may result in a different horizontal response of the bearing due to the coupling between the vertical and horizontal bearing response.

The horizontal response of friction pendulum bearings strongly depends on the axial force of the bearing. During 1D and 2D hybrid simulations with a constant axial force on the bearing, it was observed that the SRMD controller could not maintain that constant axial force very accurately. Significant axial force fluctuations occurred mostly at horizontal displacement turnaround points during fast and real-time hybrid simulations. To compensate for these erroneous fluctuations of the axial force, the Simulink model was modified such that the horizontal shear forces of the bearing were first normalized by the instantaneous measured axial force on the bearing and then multiplied by the constant design axial force on the bearing.

5.6.4 Test Setup

5.6.4.1 Hybrid Infrastructure

Several hardware and software components as well as correction and compensation procedures are necessary to conduct hybrid simulations with the SRMD, especially when performing rapid or real-time hybrid simulations. Figure 124 shows the relationship and flow of several hardware and software components. OpenSeesSP, the equation of motion solver, calculates new target displacements at time $t+\Delta t$ and sends these to all numerical elements as well as the experimental element in OpenFresco which generates the desired horizontal deformations and vertical load on the isolator test specimen. OpenFresco transforms the target signals from global degrees of freedom to basic element degrees of

freedom and then communicates with the xPC-Target machine running the Simulink predictor-corrector model. The command signals generated by the predictor-corrector algorithm are sent as external reference values to the SRMD real-time controller which ultimately moves the machine platen accordingly.

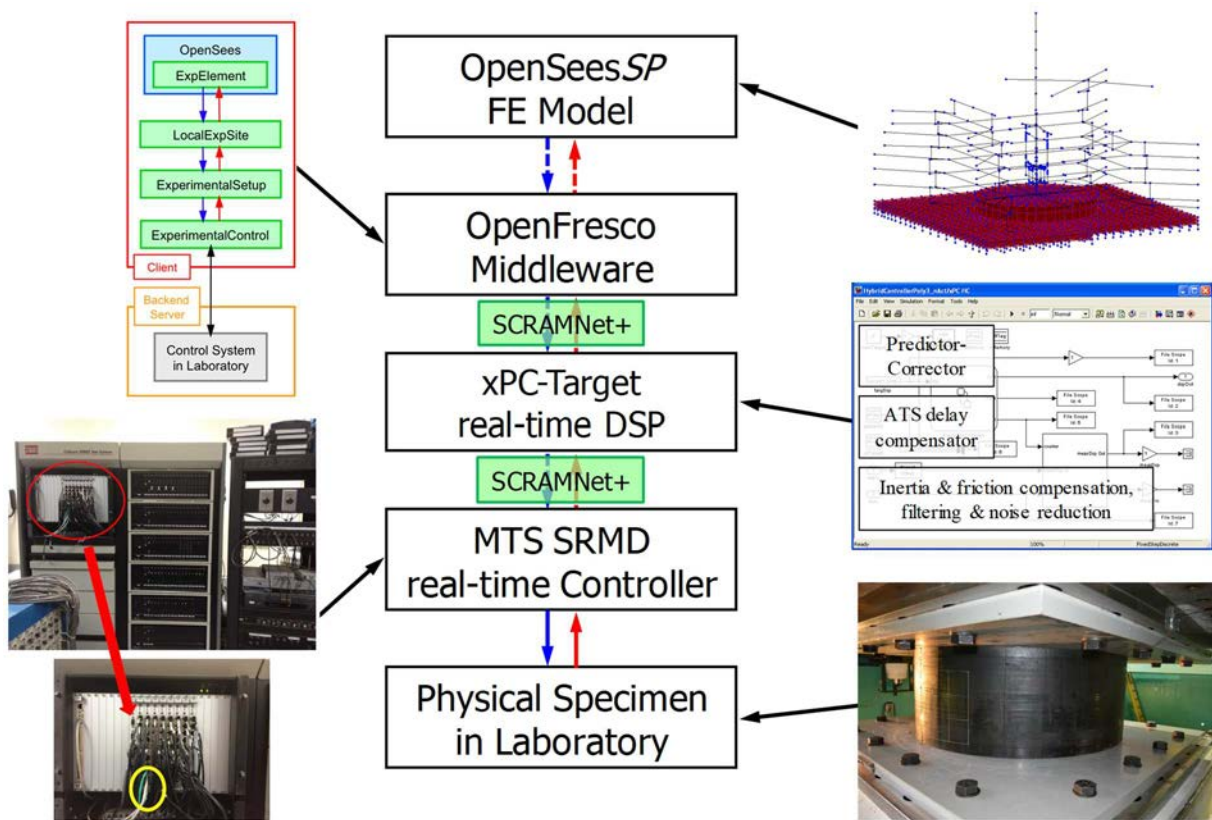


FIG. 124. Schematic of the test setup.

Two horizontal displacements and their corresponding horizontal shear forces are measured in 2D hybrid simulation tests. For a 3D hybrid simulation, the measurements also include the vertical displacement and force. However, the vertical force measurement in the 3D tests is not sent back to the hybrid model and the analytically estimated vertical bearing force (which is identical to the vertical force command sent to the SRMD) is being used instead. Once the numerical simulation receives the restoring forces from the numerical and experimental elements, the analysis proceeds to the next integration time step.

5.6.4.2 Delay Compensation

Delay is one of the most critical parameters in real-time hybrid simulation that needs proper compensation. In general, delay is the time difference between the command signal and its measured response. The rate of testing for hybrid simulation is primarily governed by the computation time of the numerical model and the delay in the actuator system. For these tests, the numerical portion of the response was computed using a high-performance computer with parallel processing capabilities achieving computation times that were sufficient fast to enable real-time testing.

In order to assess system delays in the SRMD for the different platen degrees of freedom during a hybrid simulation, cross correlation functions and minimization of RMS (root mean square) errors were used for system identification. The SRMD was estimated to have about 60 msec of delay in the measured displacement response compared to a command from its internal control system. This delay is mainly due to a lag in the response of the hydraulic actuators driven by the four-stage poppet valve assembly. To enable real time testing, the adaptive time series (ATS) delay compensator developed by [21] was utilized and implemented in the xPC-Target machine and feed-forward control was turned on and tuned

on the SRMD controller. It important to note that since SCRAMNet+ shared memory was used for communication; negligible communicational delays were added in terms of signal transmission.

5.6.4.3 *Inertia and Friction Correction*

A model based on system identification techniques was developed and implemented in the xPC-Target machine to correct for friction and inertia on the fly during a hybrid simulation test.

5.6.4.4 *Experimental Setup*

Concrete spacer blocks, steel spaces and upper and lower adapter plates were utilized to locate the isolators for tests. An overview of the basis experimental setup is shown in Figure 125.

5.6.4.5 *Instrumentation*

Four uniaxial load cells recorded horizontal forces. Pressure cells on vertical actuators and outrigger actuators read the signals of vertical forces. Accelerometers on the platen, within the top surface plate, measured acceleration signals in x, y and z directions.

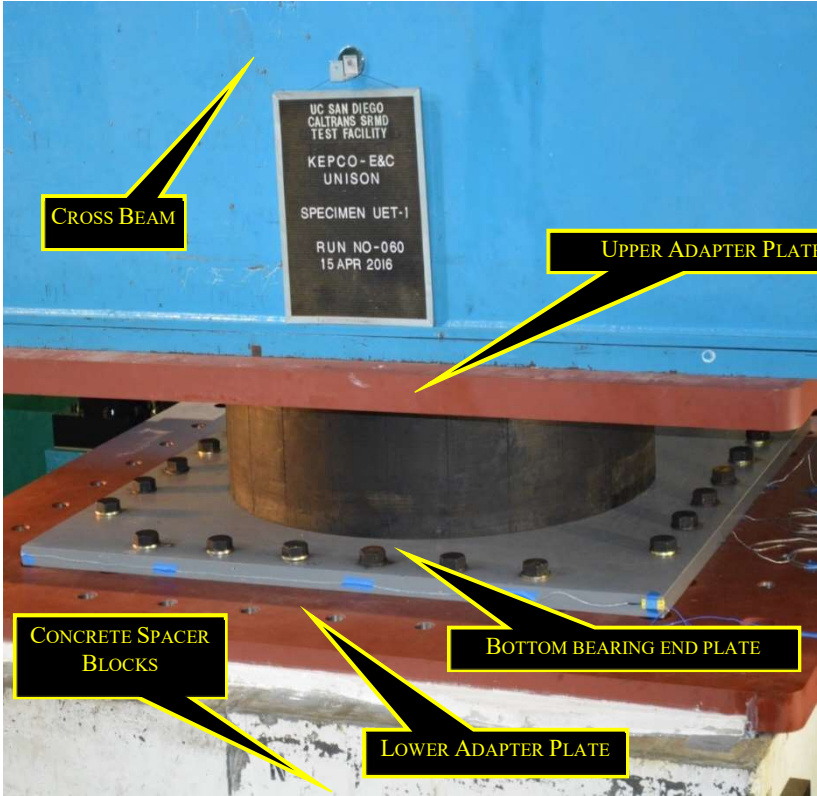


FIG. 125. Overview of the typical experimental setup.

Linear voltage displacement transducers (LVDTs) were used to obtain more accurate vertical displacement measurements for the bearings (Figure 126).

Video and audio recordings were obtained of all the tests via three colour cameras. Three additional cameras were installed inside the EQSB and TPFB bearings. Video captured from these cameras helped to understand the behaviour of the bearing and in the case of failure helped identify the failure mechanism.

A total of 10 thermocouples (five on the top and five on the bottom) were installed in the LRB bearings and monitored by a separate data acquisition system. Four of the five thermocouples on each side were monitoring lead temperature on each core while the fifth one was placed in the centre of the bearing.

Thermocouples on the top side were placed 20 to 25 mm into the lead cores while the bottom ones were placed on the end caps. Synchronization of this system with the primary data acquisition system was achieved by comparison of a common signal recorded on both systems.

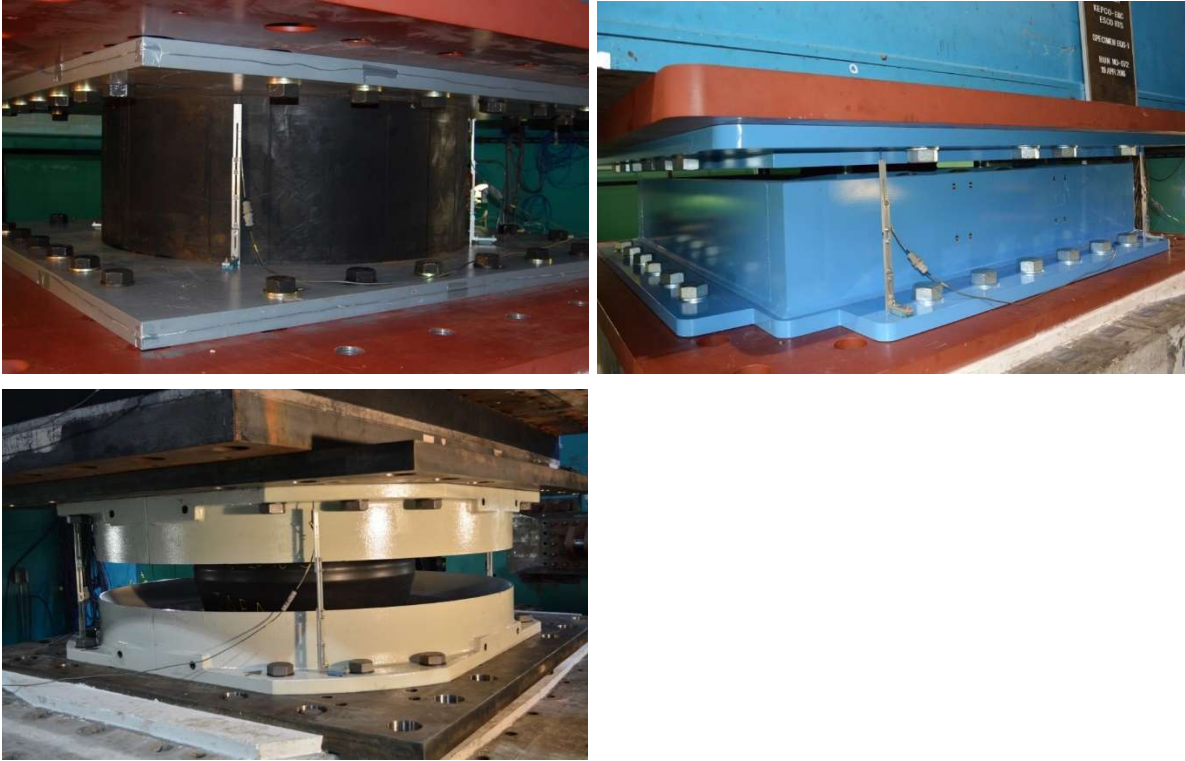


FIG. 126. LVDTs to measure average vertical displacement of a bearing.

5.7 TEST RESULTS

For the hybrid simulations, data are stored at different locations of the overall test system. Based on the test setup shown in Figure 124, different response quantities as well as hybrid testing calibration data are recorded on four machines, as summarized in Table 34. Each test point where data is recorded has its own data acquisition frequency.

TABLE 34. DATA RECORDING LOCATION FOR THE OVERALL HYBRID TESTING SYSTEM

Device	Frequency	Measured responses quantity
High Performance Computing machine	50 Hz	Quantities of in-structure Responses both numerical element and response experimental element
XPC Target machine	1000 Hz	All data passing through predictor-corrector
MTS SRMD real-time digital controller	50 Hz	Command and measure signals for six platen degrees-of-freedom of controller
Thermocouples	1 Hz	Temperature of lead core (Only used for LRB)

The hybrid test results presented and discussed in this section focus on the in-structure response of the upper plant as well as the seismic isolator response recorded by OpenSees and OpenFresco on the high-performance computing machine. For the upper plant response, pseudo-acceleration elastic floor response spectra (with 5% damping) are provided at three different elevations in the reactor containment building (RCB), the internal structure (INS) and the auxiliary complex building (ACB) as shown in Figure 127. The corresponding elastic response spectrum for the ground motion input is included for comparison. The elastic response spectra were generated by analysing 2-DOF linear-elastic systems with 5% damping and the values shown in the plots are vector norms of the two horizontal directions. For the isolator response, horizontal force-deformation hysteresis loops in both longitudinal and lateral directions are provided. In addition, the horizontal displacement orbit and the shear force interaction surface are plotted.

For the evaluation of the isolated plant behaviour, special attention is paid to the effect of various loading and modelling conditions on the results. The primary parameters of interest include (a) hybrid simulation testing rate, (b) distinct bearing behaviour of different isolator types, (c) number of excitation components, and (d) discretization at the isolation plane. The cases that are compared and discussed are summarized in Table 35.

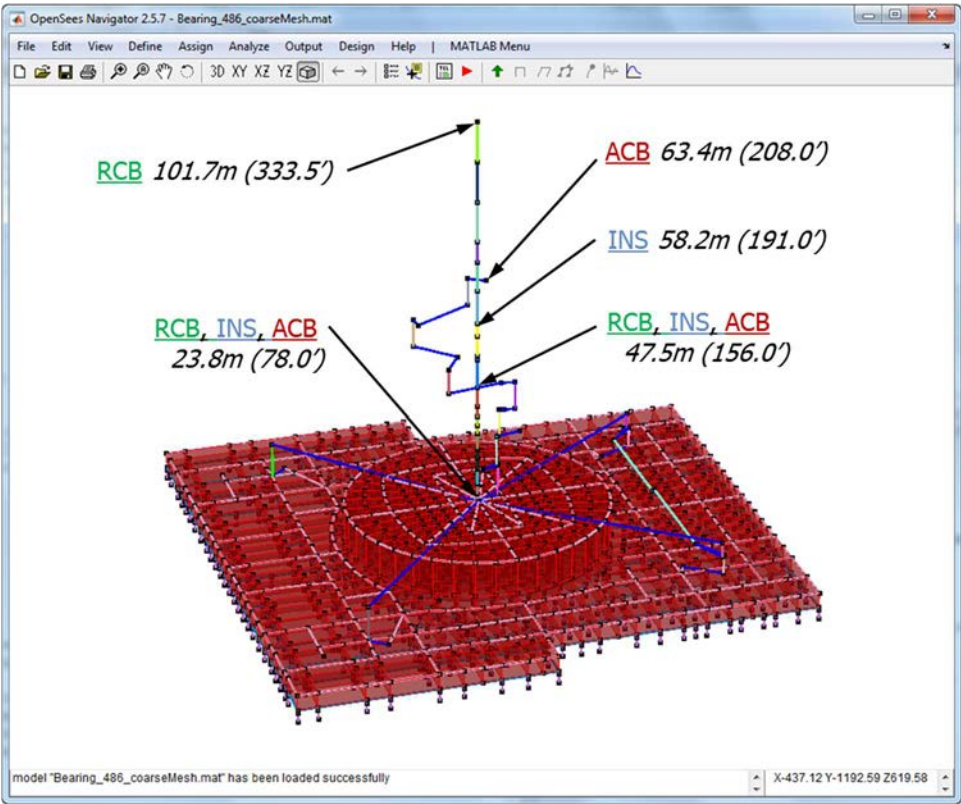


FIG. 127. Result output locations for upper plant structure.

TABLE 35. RUN NUMBERS FOR HYBRID SIMULATION COMPARISONS

	LRB	EQSB	TPFB
1D vs. 2D	38 vs. 42 (real time) 55 vs. 56 (2× slower)	98 vs. 96 (real time) 103 vs. 104 (2× slower)	216 vs. 217 (2× slower)
Test Rate	38 vs. 55 (1D) 42 vs. 56 (2D) 46 vs. 57 (3D)	98 vs. 103 (1D) 96 vs. 104 (2D)	216 vs. 218 vs. 220 (1D) 217 vs. 219 (2D)
Vertical Excitation	56 vs. 57 (2× vs. 10×)	104 vs. 121 (2× vs. 10×)	197 vs. 198 (DBE, 10×) 230 vs. 231 (OBE, 10×)
Model Discretization	56 vs. 166 vs. 172 (2D)	98 vs. 108 (1D, real-time) 104 vs. 110 (2D, 2× slower)	n/a

5.7.1 LRB isolator

5.7.1.1 Comparison of 1D and 2D horizontal input

a. Run 38 vs. 42 (real time, 1-bearing model)

The effect of the number of excitation components is investigated considering unidirectional and bidirectional horizontal ground motion inputs. Results from a 1D longitudinal hybrid simulation (Run 38) and a 2D bidirectional hybrid simulation (Run 42) are compared. Both tests were conducted in real time using the 1-bearing equivalent structural model.

Isolator responses are compared in Figure 128. Due to the bidirectional loading, the horizontal movement of the bearing in the 2D test forms a displacement orbit rather than moving in longitudinal direction only as in the 1D test. This results in a larger bearing horizontal displacement demand for the 2D case (191 mm) as compared to the 1D case (167 mm). For the 2D test, the horizontal force-displacement hysteresis loop for a specific direction (e.g. longitudinal) is less smooth with more shear

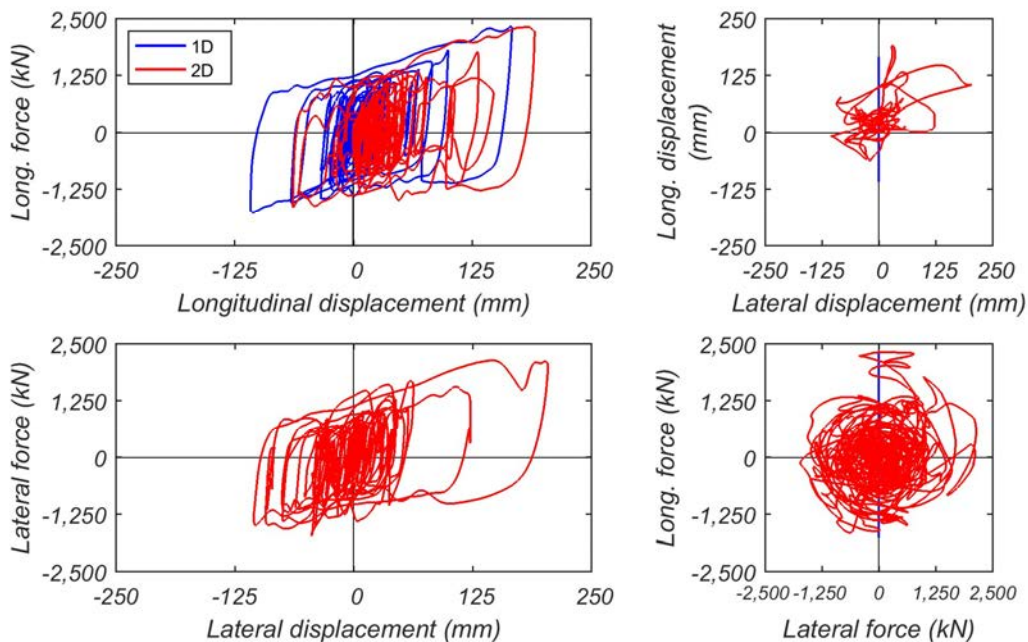


FIG. 128. Comparison of LRB isolator response for 1D vs. 2D ground motion inputs. (Both hybrid simulations were conducted in real time using the 1-bearing equivalent model).

force fluctuations as compared to the 1D test. The shear force fluctuations in one direction are caused by the movement of the bearing in the perpendicular direction.

It is also observed that for the 2D test, after only few seismic loading cycles the isolator hysteresis loops become thinner more quickly than in the 1D test. This behaviour indicates that the reduction of the LRB yield strength due to heating of the four lead cores is more pronounced in the 2D case as compared to the 1D case. This conclusion is further confirmed when comparing the work done by the isolator for the two loading conditions as shown in Figure 129. Because of the bidirectional horizontal movement, the

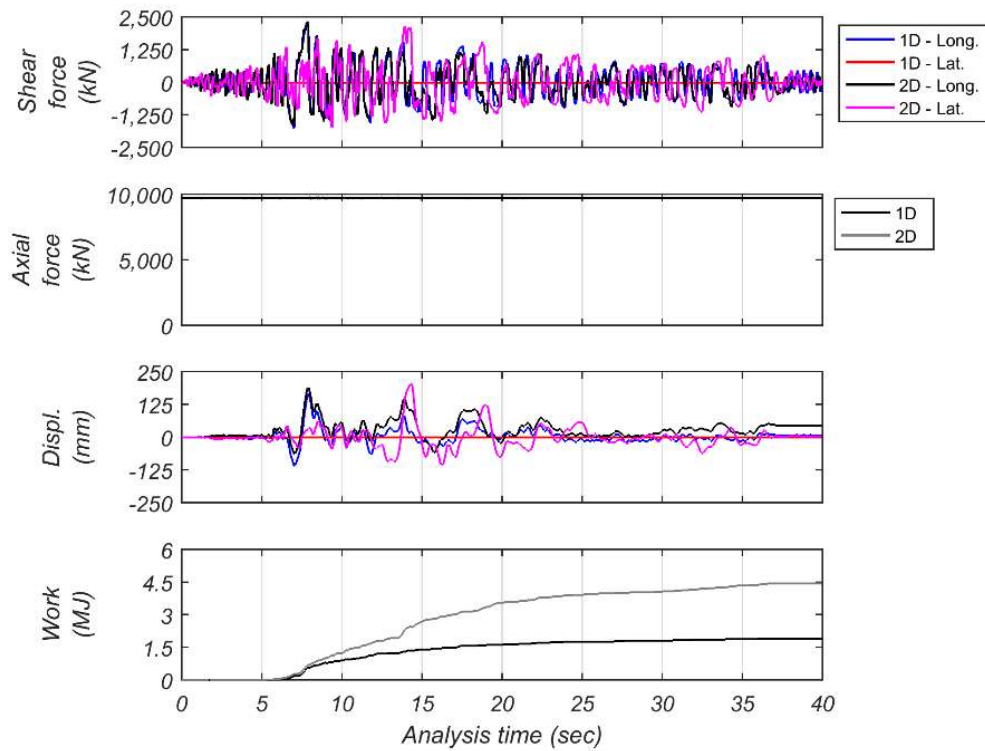


FIG. 129. Comparison of LRB isolator response histories for 1D vs. 2D ground motion inputs. (Both hybrid simulations were conducted in real time using the 1-bearing equivalent model).

bearing travels further and therefore more work is done in the 2D test as compared to the 1D test. Hence, the strength reduction effect of the LRB due to the temperature increase is more pronounced in the bidirectional hybrid simulation.

Floor spectra are shown in Figure 130 for three power plant superstructures. Responses at different heights within each building component are plotted together. Firstly, for the response spectrum amplitudes within each building, a significant amplification effect is observed from lower level locations to higher elevations, especially around the pseudo acceleration peaks in the response spectra. The peaks of these horizontal floor response spectra are primarily located around the horizontal fundamental frequencies of the different plant superstructures.

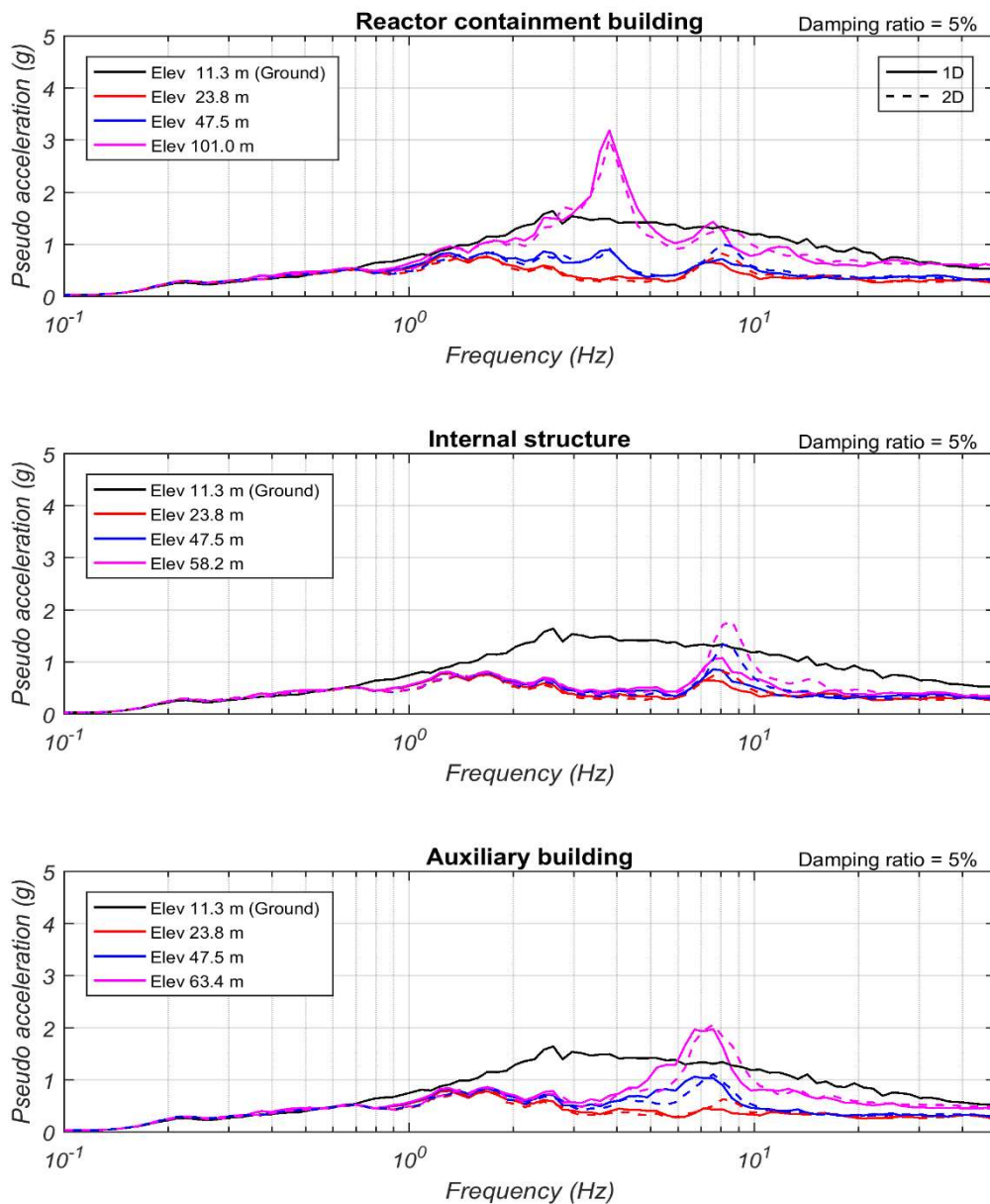


FIG. 130. Comparison of floor response spectra for 1D vs. 2D ground motion inputs. (Both hybrid simulations were conducted in real time using the LRB 1-bearing equivalent model).

For the reactor containment building (RCB), the peak occurs around a frequency of 3.8 Hz, which corresponds to the first horizontal vibration mode of the RCB. The spectral acceleration peak at the roof is as high as 3.2 g. The main peaks in the floor spectra for the internal structure (INS) and the auxiliary building (ACB) are located around 8 Hz and 7.5 Hz and reach amplitudes of 1.9 g and 2.1 g at their highest elevation. The frequencies again correspond to the horizontal fundamental frequencies of the two building structures.

For the low frequency range of the floor spectra, small peaks are observed between 1.2-1.7 Hz and also, at 2.5 Hz. These smaller peaks correspond to the frequency of the equivalent isolator. Responses obtained from 1D and 2D hybrid simulation tests are almost identical except for the high frequency response of the INS where 2D tests resulted in slightly larger floor spectrum peaks around 8-9 Hz.

As discussed above, in the 2D hybrid test, the yield strength of the LRB lead cores decreased faster from cycle to cycle due to the larger and faster temperature increase as compared to the 1D test. In addition, due to the bidirectional interaction of the bearing deformations, hysteresis loops for each horizontal direction are more rounded in the 2D test. Therefore, one would expect the floor response spectra to be lower in the 2D test results than in the 1D test results. However, this is not evident from the floor response spectra shown in Figure 130. On the contrary, for the INS floor response spectrum amplitudes

for the 2D case are larger in the frequency range between 8-9 Hz. This counterintuitive behaviour is caused by experimental errors which were fairly large for the real-time hybrid simulations. Not all of the system delay could be compensated for and an average delay of approximately 8.5 ms remained for the 1D test and a delay of 5 ms remained for the 2D test. Please see [7], [8], and [9] for a detailed explanation on the effects of lead and lag experimental errors on hybrid simulation test results. Comparing Fourier amplitude plots of the displacement errors, one can identify amplitude spikes around 8 Hz for the 2D test which are not present in the 1D test. We can conclude that even though average delays were a bit smaller in the 2D test, the displacement errors, especially at higher frequencies were worse than in the 1D test. This behaviour, which was caused by the tracking error of the SRMD, is likely the reason for the counterintuitive results observed in the floor response spectra.

b. Run 55 vs. 56 (2x-slower than real time, 1-bearing model)

To further assess the behaviour of 1D versus 2D hybrid simulations, results from tests conducted at a slower rate (2x-slower than real time) are compared. Isolator responses are summarized in Figure 131. Isolator horizontal deformations are slightly larger for the 2D case because of the bidirectional movement. However, in longitudinal direction the differences are much smaller in comparison to the real-time case. Especially for peak isolator displacement, 1D and 2D tests generated identical longitudinal displacement demands of 149 mm.

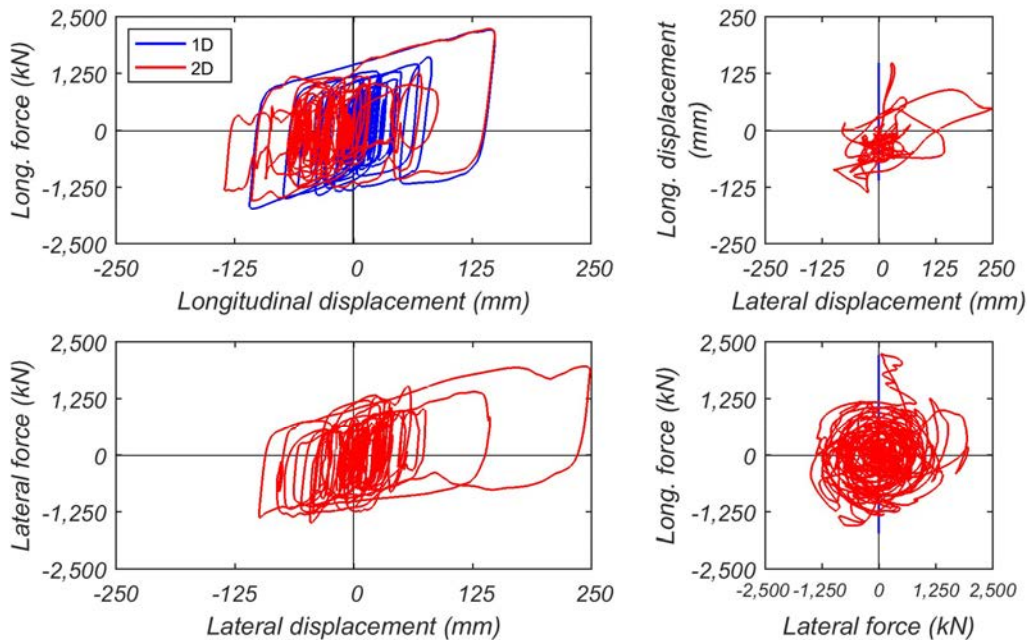


FIG. 131. Comparison of LRB isolator response for 1D vs. 2D ground motion inputs. (Both hybrid simulations were conducted 2x-slower than real time using the 1-bearing equivalent model).

Shear forces fluctuate again more for the 2D case as compared to the 1D case, which is due to the response interaction between the two perpendicular horizontal directions. Similar to the results for the real-time tests discussed above, an increased reduction of horizontal shear forces occurs for the 2D test, because more work is done by the bidirectional movement of the isolator.

Comparisons of floor response spectra for the 2x-slower tests are shown in Figure 132. Slightly smaller responses are observed for the 2D case in comparison to the 1D case. For example, the main floor spectrum peaks which correspond to the fundamental frequencies of the RCB, INS and ACB are 2.8 g, 0.8 g and 1.3 g for the 1D hybrid simulation. While the response amplitudes for the 2D test case are slightly reduced to 2.6 g, 0.7 g and 0.9 g, respectively. As discussed above, the first reason for this reduction of floor spectrum peaks in the 2D case is the greater and faster temperature increase in the lead cores, which in turn results in a greater reduction of the isolator characteristic strength. Hence, less shear force is transmitted into the superstructures and floor spectral accelerations are smaller. The second reason is the more rounded hysteresis loops that are produced by the bidirectional movement.

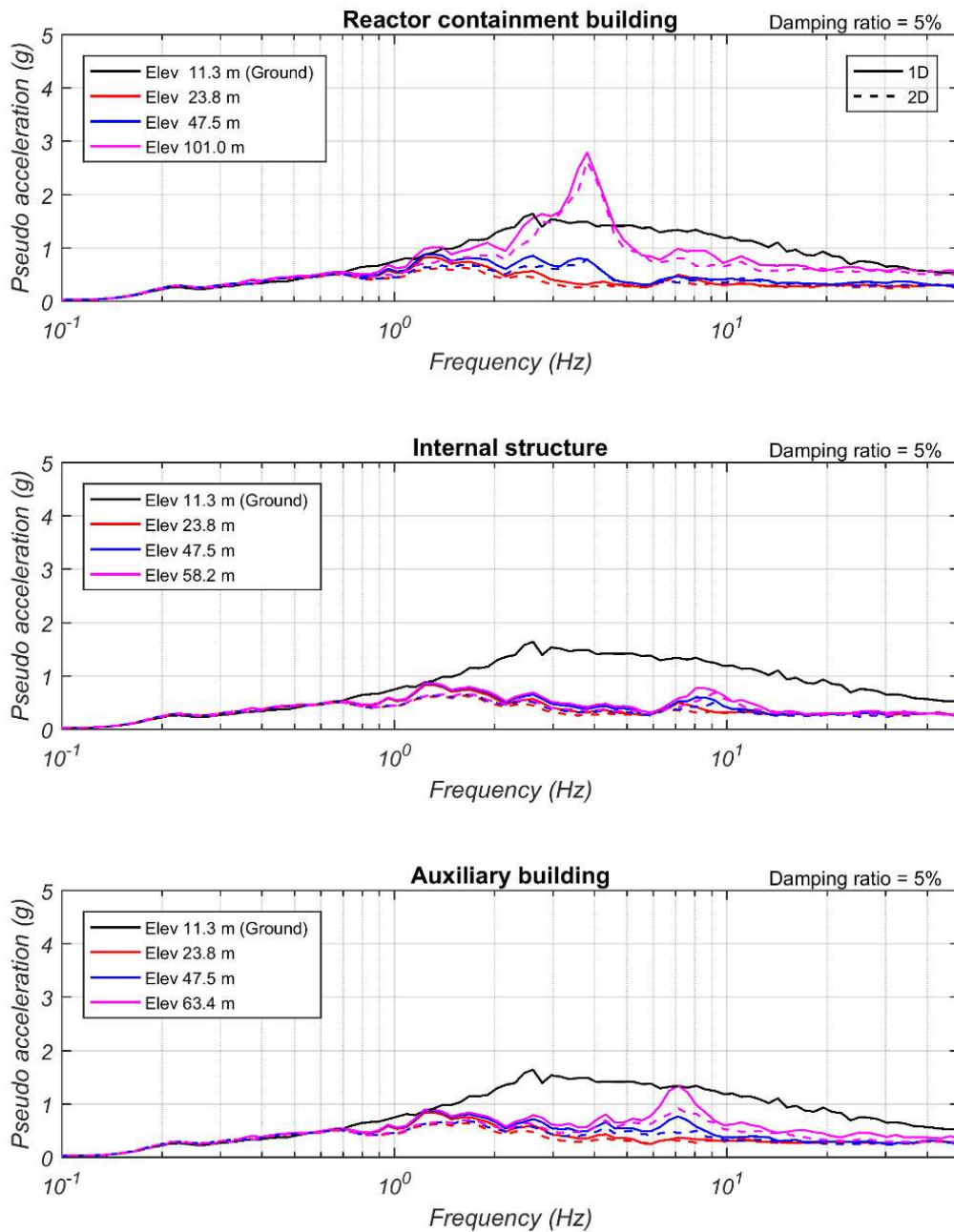


FIG. 132. Comparison of floor response spectra for 1D vs. 2D ground motion inputs. (Both hybrid simulations were conducted 2x-slower than real time using the LRB 1-bearing equivalent model).

This causes fewer sudden stiffness and shear force changes in the bearing. Therefore, somewhat smaller upper plant floor response spectrum amplitudes are observed. Unlike in the real-time hybrid simulations discussed before, experimental errors are very small for the 2x-slower tests and the floor response spectrum results are not affected.

5.7.1.2 Comparison of different test rates

a. Run 38 vs. 55 (1D input, 1-bearing model)

In order to investigate the effect of different test rates, results from a real-time hybrid simulation and from a hybrid simulation conducted at a rate 2x-slower than real time are compared. For both cases, 1D hybrid simulations considering only longitudinal input are conducted using the 1-bearing equivalent model. Isolator responses are shown in Figure 133.

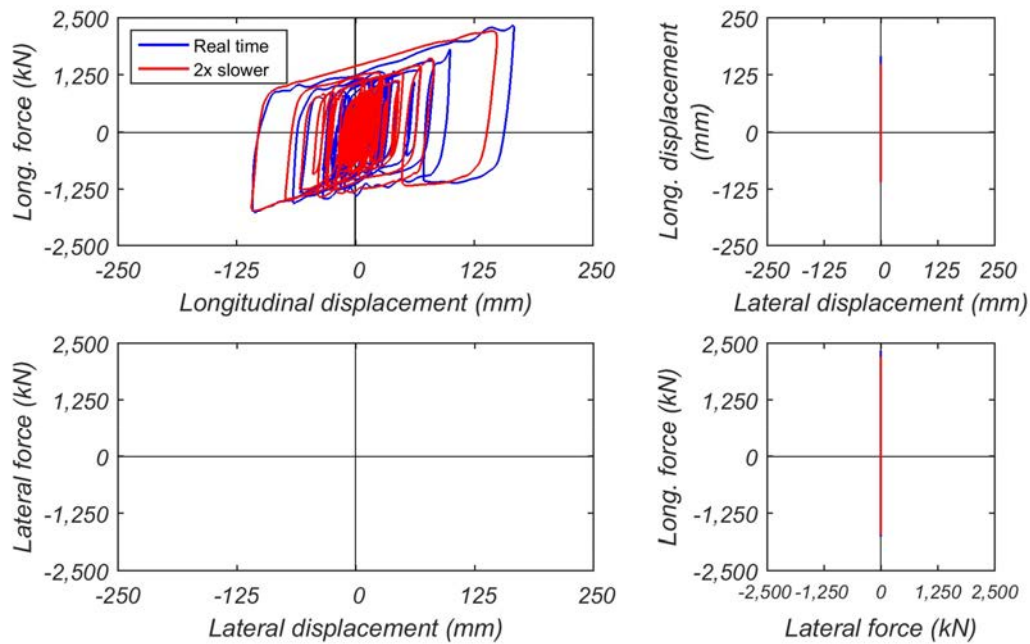


FIG. 133. Comparison of LRB isolator response for real-time hybrid test and hybrid test executed 2x-slower than real time. (Both hybrid simulations were conducted with 1D longitudinal input using the 1-bearing equivalent model).

It can be observed that the maximum isolator deformation for the real-time test is 167 mm, while the demand for the 2x-slower test is smaller, reaching 149 mm. Shear force fluctuations are more pronounced for the real-time case in relation to the 2x-slower case. This is due to the fact that dynamic effects in terms of inertia and friction forces in the test setup and specimen are more prominent in the real-time test. In addition, experimental errors were larger in the real-time hybrid simulation as compared to the 2x-slower test. The larger experimental errors also contributed to the increase of the shear force fluctuations. As discussed before a reduction of the characteristic strength is expected due to the temperature increase, and it seems this strength reduction effect is slightly larger for the real-time test than for the 2x-slower test. The small differences can be attributed to the slightly larger dynamic and inertia effects in the real-time case. However, overall, the differences in the isolator response are not significant and it can be concluded that a rapid hybrid simulation is accurate enough to capture the behaviour of LRB isolators.

Floor response spectra are shown in Figure 134. Generally, a smaller in-structure floor spectrum response can be observed for the slower test in relation to the real-time test case for frequencies above 3 Hz. The differences are most pronounced at the high frequency peaks of the floor spectra for the INS and ACB. More high frequency response content is transmitted into the plant superstructures when the hybrid simulation is executed in real time. This behaviour can be attributed to several reasons as discussed above, one is the more pronounced dynamic and inertia effects in the real-time test, the other is the larger experimental errors due to reduced tracking performance in the real-time hybrid simulation.

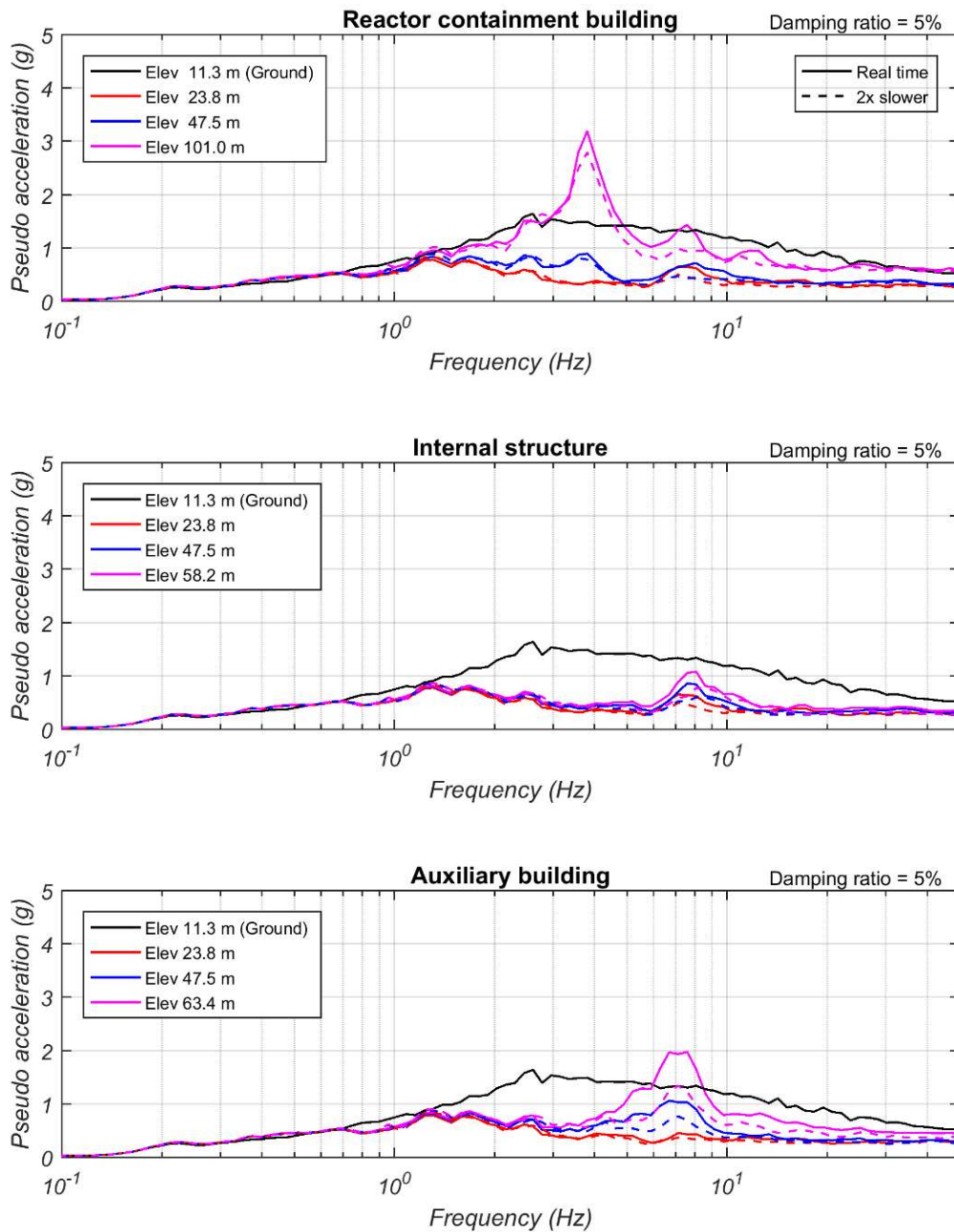


FIG. 134. Comparison of floor response spectra for real-time hybrid test and hybrid test executed 2x-slower than real time. (Both hybrid simulations were conducted with 1D longitudinal input using the LRB 1-bearing equivalent model).

The average delay for the real-time test was about 8.5 ms, whereas in the 2x-slower test the average delay was only 2.9 ms. It is difficult to uncouple dynamic effects on the floor response spectra from experimental error effects on the spectra for the hybrid simulations performed in real time. However, one can find from this comparison that the experimental error, which is possibly large in real-time hybrid simulations, can significantly affect the superstructure floor response spectra because they are sensitive to the response frequency content. Hence, under these circumstances, careful attention needs to be paid when evaluating the accuracy of in-structure response results from real-time hybrid simulations.

b. Run 42 vs. 56 (2D input, 1-bearing model)

To further investigate the effect of test rates on the response of the seismically isolated power plant, a bidirectional real-time hybrid simulation is compared with a rapid hybrid simulation executed 2x-slower than real time. The 1-bearing equivalent model was utilized for both hybrid tests. Isolator responses are depicted in Figure 135. The maximum horizontal displacement amplitude for the real-time test is

230 mm, which is smaller than the 254 mm demand from the 2x-slower test. However, in longitudinal direction, due to the horizontal shift of the hysteresis loops, a larger positive isolator displacement demand is expected for the real-time case. The shift was most likely caused by imperfect (non zero) shear force initial conditions in the real-time test. From the hysteresis loops, it can be observed that for both cases, significant shear force fluctuations exist. As discussed above, horizontal shear force fluctuations are expected for the real-time hybrid simulation due to the more prominent dynamic and inertia effects as well as the larger experimental tracking errors. In addition, due to the effect of bidirectional movement, the shear forces in two perpendicular directions interact with each other, causing additional fluctuations. Therefore, even for the rapid hybrid simulation conducted 2x-slower than real time, shear force fluctuations can be expected and are observed.

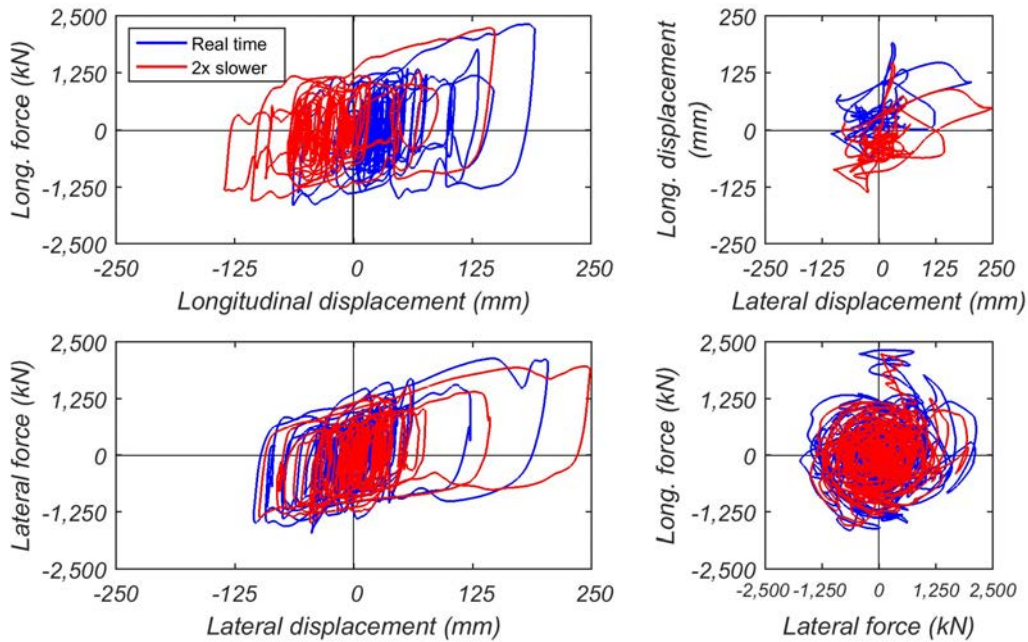


FIG. 135. Comparison of LRB isolator response for real-time hybrid test and hybrid test executed 2x-slower than real time. (Both hybrid simulations were conducted with 2D bidirectional input using the 1-bearing equivalent model).

From the isolator shear force interaction surface, larger shear force amplitudes are identified for the real-time hybrid simulation case. The maximum shear force is 2410 kN as compared to 2235 kN for the 2x-slower test. This difference in the isolator shear forces is again caused by dynamic and inertia force effects in the test setup and specimen. The same conclusion can be made for the 2D tests as for the 1D tests. Overall, the testing rate of the hybrid simulation has a moderate effect on the isolator behaviour and the response differences are mainly due to the inertia effect of the test setup and specimen. A rapid hybrid simulation executed 2x-slower than real time is accurate enough to assess the behaviour of LRB isolators and can substantially reduce problems due to experimental errors.

Floor spectra are summarized in Figure 136. Similar to the 1D cases discussed before, the floor spectrum amplitudes for the real-time hybrid simulation are larger than for the 2x-slower case, especially at spectral peaks in the high frequency range. For example, as shown in Figure 136, the peak response spectrum amplitudes at the fundamental frequencies of the RCB, INS and ACB are 4.1 g, 1.8 g and 2.7 g for the real-time hybrid simulation, while for the 2x-slower test the floor response spectrum peaks at the same frequency locations are reduced to 3.3 g, 0.7 g and 1.1 g, respectively.

As was discussed for the 1D input case the greater floor spectrum amplitudes at high frequencies in the real-time test case are caused by the increase of dynamic and inertia effects as well as larger experimental errors in the test system. However, by comparing the FFTs of displacement errors, FFTs of force feedbacks, and error monitors, it can be seen that the overall tracking performance was quite similar between real-time and 2x-slower tests. Average delays in longitudinal and lateral directions were fairly

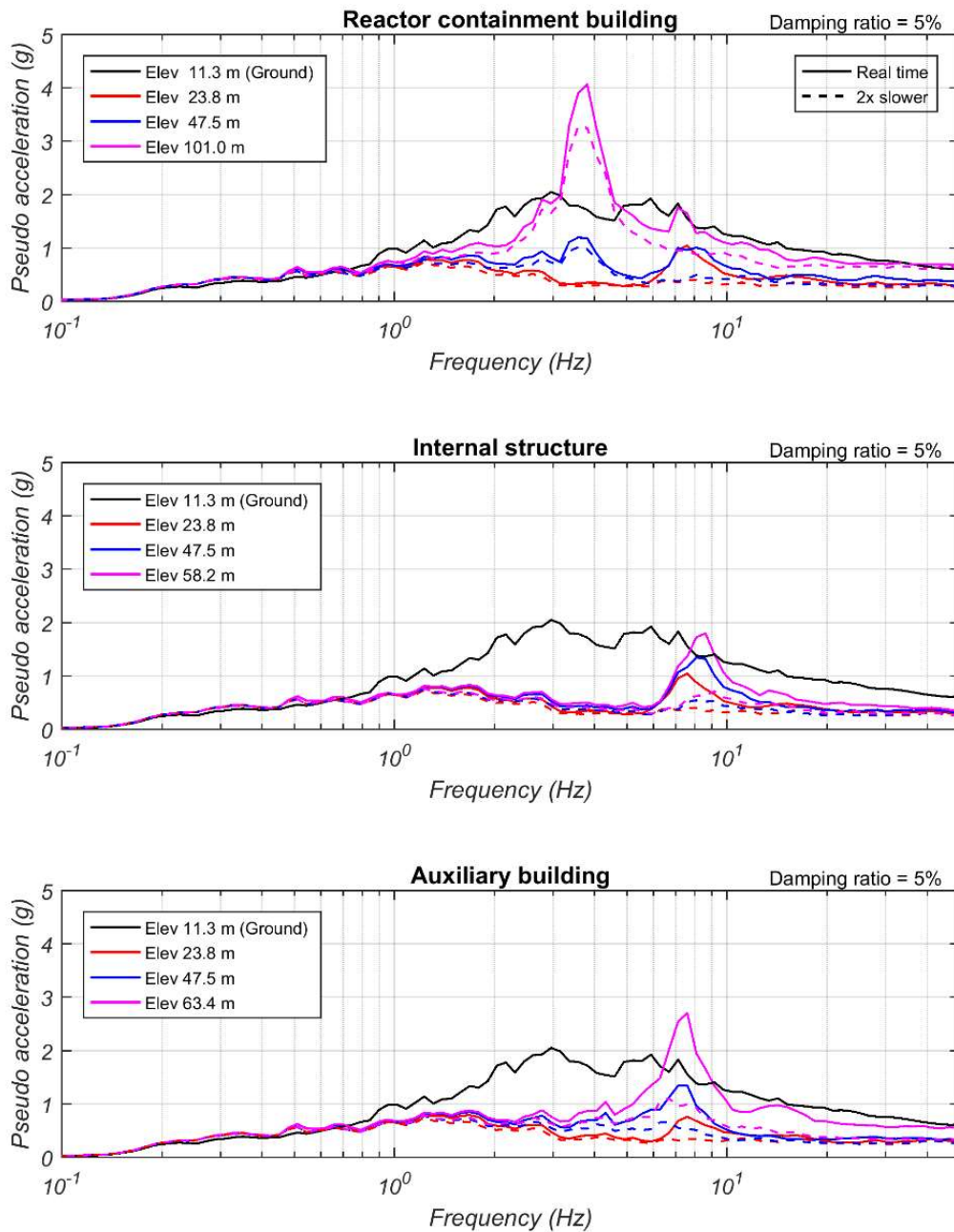


FIG. 136. Comparison of floor response spectra for real-time hybrid test and hybrid test executed 2x-slower than real time. (Both hybrid simulations were conducted with 2D bidirectional input using the LRB 1-bearing equivalent model).

similar for the two different test rates. However, for the real-time hybrid simulation a large peak is observed in the Fourier amplitude spectrum of the displacement errors. The peak is located between 7-9 Hz and does not appear in the FFT for the 2x-slower test. As shown in Figure 136, the largest differences in the floor spectrum amplitudes also occur around 7-9 Hz. It seems that the SRMD had more difficulties in maintaining the constant axial design load on the bearing during the real-time hybrid simulations, especially for the bidirectional ground motion input case as can be seen from Figure 137. Due to the vertical-horizontal coupling of the LRB isolator the axial load fluctuations contributed to the increase of the floor response spectrum peaks.

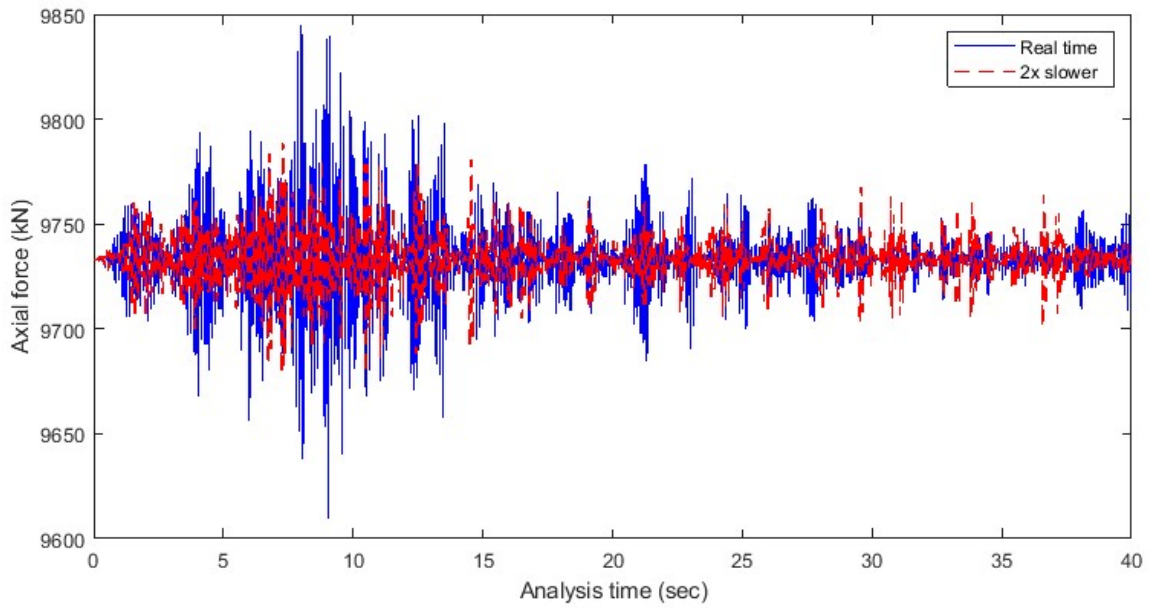


FIG. 137. Comparison of axial force history for real-time hybrid test and hybrid test executed 2x-slower than real time. (Both hybrid simulations were conducted with 2D bidirectional input using the LRB 1-bearing equivalent model).

c. Run 46 vs. 57 (3D input, 1-bearing model)

Finally, results from two hybrid simulation tests conducted under 3D ground motion input are compared to further investigate the difference between real-time and slower than real-time test results. The comparison is conducted between a 3D real-time hybrid simulation and a hybrid simulation executed 10x-slower than real time. Isolator responses are shown in Figure 138. The maximum isolator horizontal displacement amplitude for the real-time test is around 240 mm, which is smaller than the 254 mm displacement demand for the 10x-slower test. Similar to the 1D and 2D hybrid simulations discussed above, more fluctuations in the isolator shear force are seen for the real-time test. From the isolator shear force interaction surface, it can be observed that for the real-time case, larger shear forces are generated.

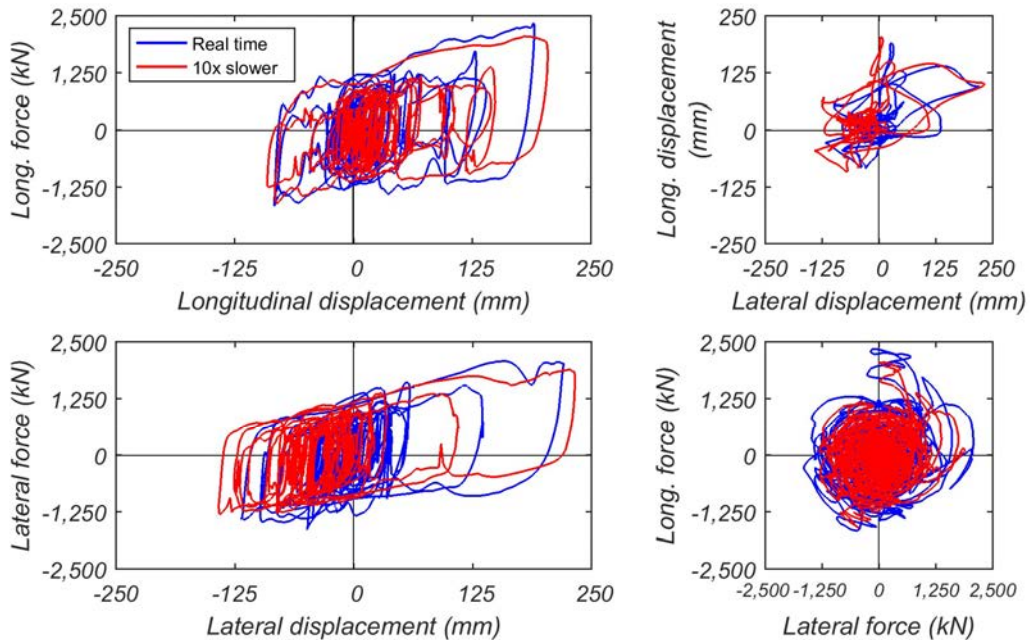


FIG. 138. Comparison of LRB isolator response for real-time hybrid test and hybrid test executed 10x-slower than real time. (Both hybrid simulations were conducted considering 3D ground motion inputs using the 1-bearing equivalent model).

The peak shear force is 2355 kN as compared to 2058 kN for the 10x-slower case. This is again caused by dynamic and inertial effects in the test setup and specimen which are basically non-existent in the 10x-slower test. Hence, the same conclusion can be drawn for the 3D tests as for the 1D and 2D tests. The real-time execution of a hybrid simulation has a moderate effect on the hysteresis loops of the LRB.

Floor spectra are depicted and compared in Figure 138. For the RCB in-structure response one can observe that the real-time hybrid simulation produced somewhat larger floor spectrum peaks as compared to the 10x-slower test. For the real-time test the spectral amplitude at the first-mode frequency of the RCB is 3.7 g, whereas the one for the 10x-slower test is only 3.0 g. However, for the INS and ACB, unlike the cases previously discussed for the 1D and 2D tests, the floor spectrum amplitudes are similar. In addition, a new high frequency peak in the floor spectra is identified for the ACB and INS between 15-16 Hz. Most likely this new peak in the floor spectra is caused by the vertical-horizontal coupling behaviour of the LRB isolator. The coupling is much more pronounced in the 3D hybrid simulation with vertical ground motion input in relation to the 1D and 2D tests without vertical input.

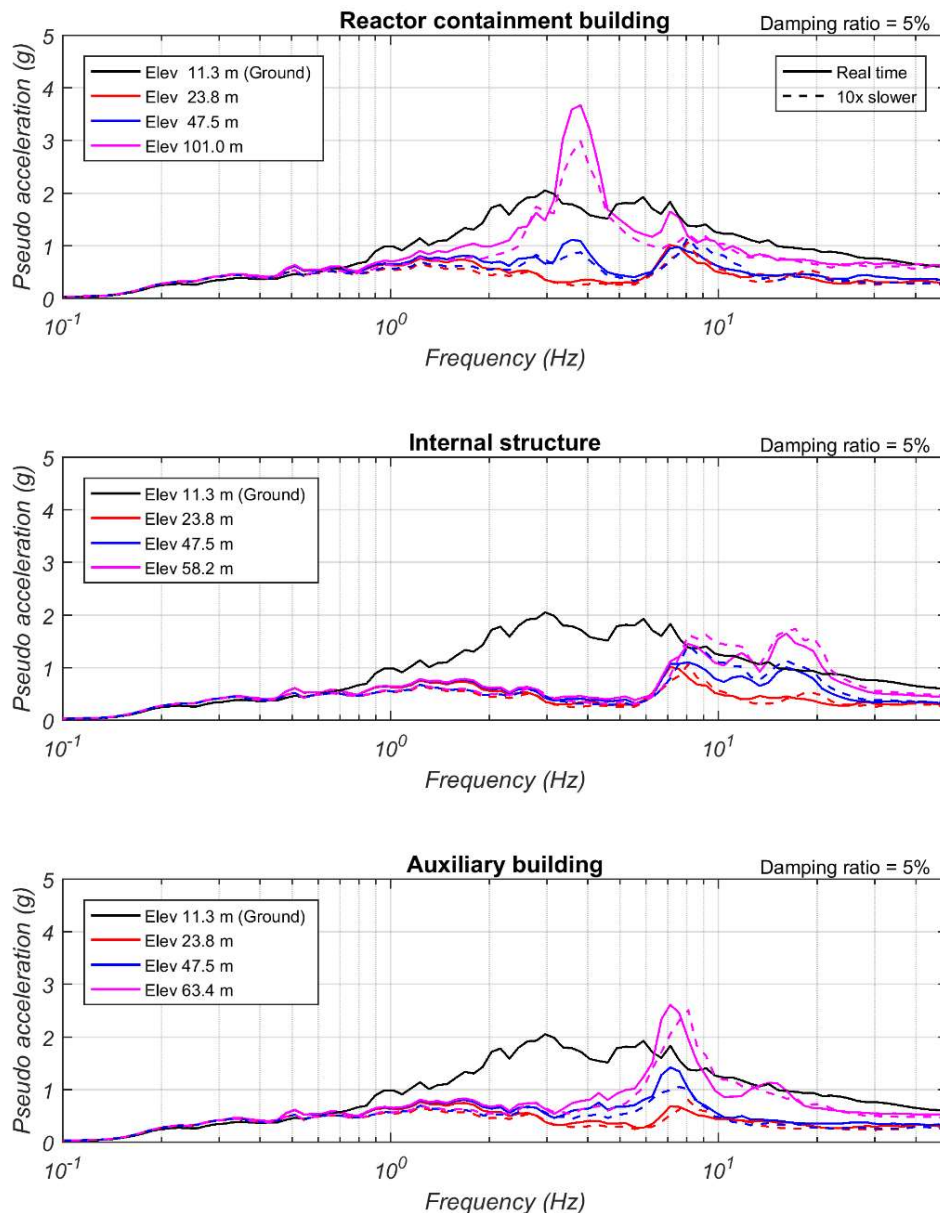


FIG. 139. Comparison of floor response spectra for real-time hybrid test and hybrid test executed 10x-slower than real time. (Both hybrid simulations were conducted considering 3D ground motion inputs using the LRB 1-bearing equivalent model).

Hence, the vertical behaviour of the isolator directly affects the horizontal floor response spectra.

For the 3D real-time hybrid simulation discussed here, tracking performance of the vertical degree of freedom, which is controlled in force, is very inaccurate. The large lag between command and feedback force signals in the vertical degree of freedom of the SRMD resulted in signals that were between 90-180 degrees out of phase. In addition, the force feedback was also overshooting by up to 50% in certain instances. This inaccurate response (especially at higher frequencies) of the SRMD during real-time hybrid simulations that include the vertical degree of freedom is caused by several issues. Firstly, the vertical actuators are hydrostatic actuators that are controlled by four-stage poppet valve assemblies. Because of this, the vertical actuators do not track as accurately and cannot respond as fast leading to amplitude overshoot and phase roll-off at higher frequencies. Secondly, the control of the vertical degree of freedom is using a cascade controller with the inner loop being in displacement control and the main outer loop being in force control. Force control of servo-hydraulic actuators is very challenging and tracking performance for force-controlled actuators is typically not as good as for actuators in displacement control. Given these difficulties it is not surprising that it is not possible to perform 3D real-time hybrid simulations with the SRMD. Nevertheless, it was very valuable to try to run a few 3D real-time hybrid simulations to determine machine performance and assess limitations for these kinds of tests.

Finally, it is also important to assess vertical tracking performance for the 3D 10x-slower hybrid simulation. Overall performance was much better in comparison with the 3D real-time test, but the average delay for the vertical DOF was still large. The average delay in the OpenSees analysis was 4.8 ms, which means that the actual delay in the control system was 48 ms (10x more). In addition, there was still a small amount of overshoot occurring. Thus, it can be concluded that it is currently not possible to conduct 3D real-time hybrid simulations with the SRMD due to insufficient vertical tracking performance. To achieve acceptable performance and accuracy in the force controlled vertical DOF, a hybrid simulation needs to be performed at a minimum 10x-slower than real time. Results from the 3D real-time hybrid simulation (Run 46) are not accurate and are not to be used in making any conclusions related to the isolated power plant behaviour. They are only valuable in terms of assessing machine performance and limitations.

5.7.1.3 Effect of vertical excitation

a. Run 56 vs. 57 (2x-slower for 2D input, 10x-slower for 3D input, 1-bearing model)

In order to investigate effects of including the vertical ground motion input in 3D hybrid simulations, results of hybrid tests with 3-component ground motion input (Run 57) and 2-component input (Run 56) are compared. The 1-bearing equivalent ANT model was used for both hybrid simulations and the test was executed 10x-slower than real time for the 3D case and 2x-slower than real time for the 2D case. Isolator responses are shown in Figure 140. Comparing 3D and 2D test results for the bearing, responses are generally quite similar except for a slight offset of the horizontal force-deformation hysteresis loops in both longitudinal and lateral direction. Isolator shear force fluctuations in the horizontal hysteresis loops are observed for both 2D and 3D cases for both longitudinal and lateral directions. However, for the 3D case, oscillations at a higher frequency (around 10 Hz) are identified. The higher frequency shear force oscillations are a result of the vertical-horizontal coupling behaviour of the LRB. As explained before, axial force fluctuations in the isolator caused by the vertical ground motion input affect the shear resistance of the LRB resulting in horizontal force fluctuations at the same frequency as the vertical force fluctuations.

Responses of upper plant floor spectra are compared in Figure 141 for the 2D and 3D hybrid simulation cases. It can be seen that the floor response spectrum amplitudes in the high frequency range are significantly larger for the 3D test as compared to the 2D test, especially for the INS and ACB floor spectra above 7 Hz. For example, for the top elevation of the INS, the peak spectral acceleration obtained from the hybrid simulation without vertical excitation is 0.7 g, whereas the spectral amplitude from the test including vertical ground motion input reaches 1.6 g. For the ACB, the spectral acceleration reaches a maximum of 1.1 g for the 2D test, but for 3D test, the amplitude is as high as 2.5 g. Note that the vertical fundamental frequency of the plant superstructure is around 10 Hz and the horizontal fundamental frequencies of the INS and ACB are 8 Hz and 7.5 Hz, respectively, These horizontal frequencies are much closer the vertical frequency of the plant superstructure in comparison with the

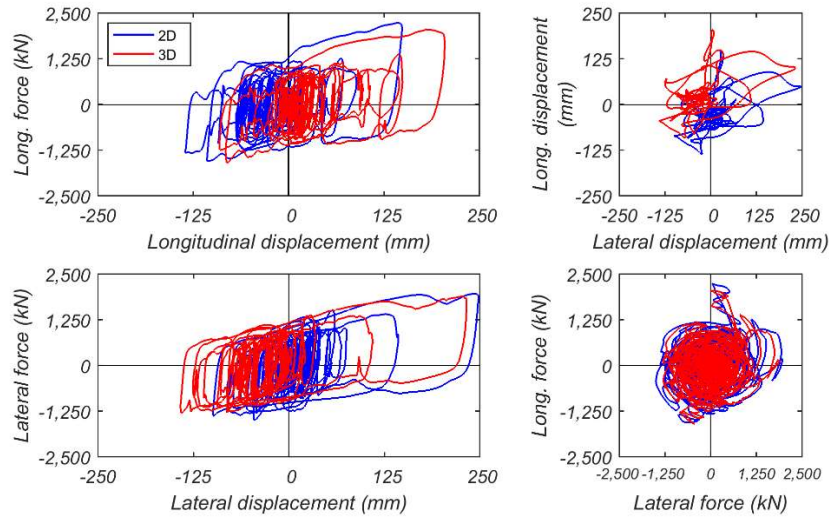


FIG. 140. Comparison of LRB isolator response for 2D vs. 3D ground motion inputs. (The 2D test is executed 2x-slower and the 3D test 10x-slower than real time. Both hybrid simulations are using the 1-bearing equivalent model).

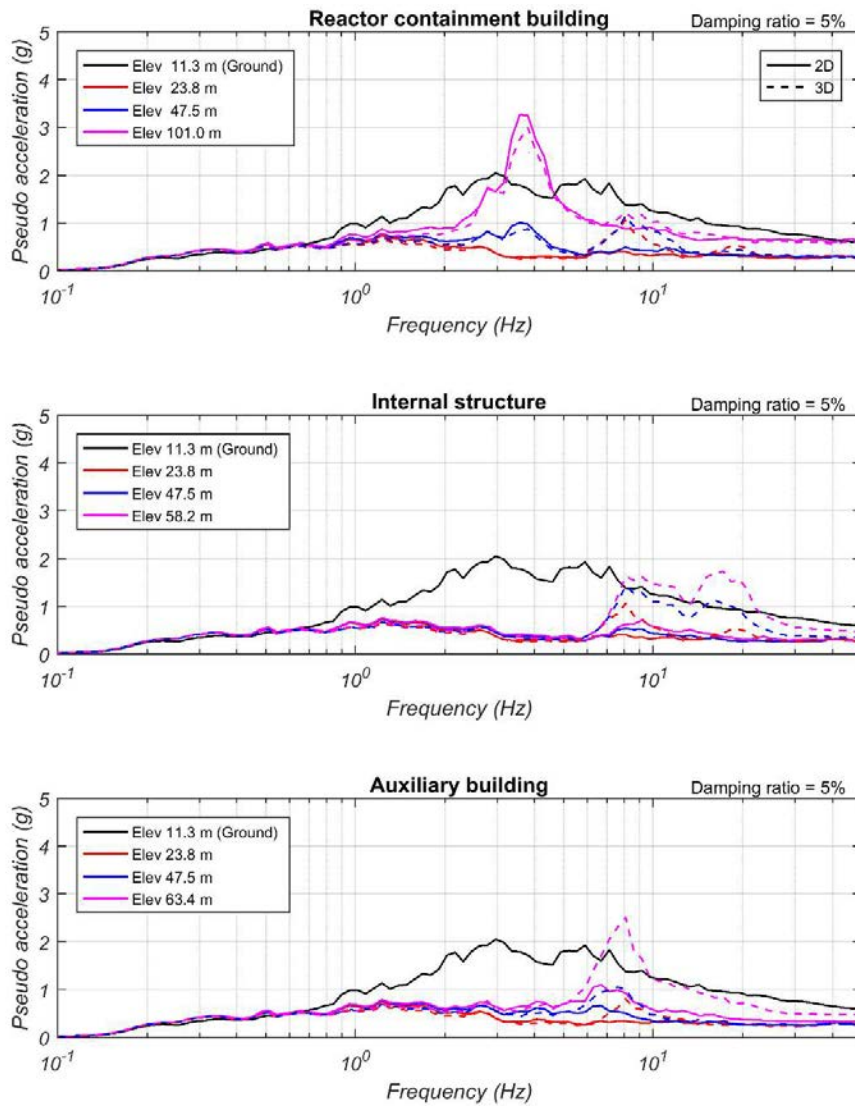


FIG. 141. Comparison of floor response spectra for 2D vs. 3D ground motion inputs. (The 2D test is executed 2x-slower and the 3D test 10x-slower than real time. Both hybrid simulations are using the LRB 1-bearing equivalent model).

RCB. Therefore, the isolator shear force oscillations caused by the vertical-horizontal coupling of LRB has a pronounced amplification effect on the horizontal floor response spectra of the INS and ACB. In contrast, the RCB has a horizontal fundamental frequency of 3.7 Hz which is well separated from the vertical frequency of the plant superstructure. Therefore, the horizontal floor spectra of the RCB are less affected by the inclusion of vertical excitation.

5.7.1.4 Variation due to bearing discretization models

a. Run 56 vs. 166 vs. 172 (2D input)

Finally, the effects of three different bearing discretization models are compared considering hybrid simulation results obtained using the 1-bearing equivalent model, the 5-bearing equivalent model, and the 486-bearing model. For the first test (Run 56), the 1-bearing equivalent ANT model was used and the test was executed at a rate 2x-slower than real time. For the second case (Run 166), the 5-bearing equivalent ANT model was used, with the experiment bearing located in the north-east quadrant of the ACB and the hybrid simulation was executed 2x-slower than real time. The third case (Run 172) used the 486-bearing ANT model with the experimental bearing located in the north-east corner of the ACB and the hybrid simulation was executed at a rate 15x-slower than real time. All three hybrid simulations were conducted considering 2D bidirectional ground motion input. It is important to note that in this series of comparisons, hybrid tests were conducted at different speeds and with different placement of the experimental bearing. Therefore, it is somewhat difficult to identify the effects of different bearing discretization models by simply comparing responses for the three cases.

The experimental bearing responses are shown and compared in Figure 142. It can be seen that the response from the 5-bearing equivalent model and the 486-bearing model are quite similar while the isolator response from the 1-bearing equivalent model is different. Peak isolator horizontal displacement amplitudes of 254 mm, 215 mm, and 204 mm were obtained from the test results of the 1-bearing, 5-bearing, and 486-bearing model, respectively. The main reason for the response difference of the 1-bearing equivalent model is that the isolator behaviour is 100% determined from the experimental test specimen, while for the other two models the response of the isolation level and thus the behaviour of the experimental isolator is dictated by the numerical isolators. In addition, overturning effects are taken into account when the experimental isolator is located in the corner of isolation plane which is the case for the 5-bearing and 486-bearing models, while in the 1-bearing equivalent model, no overturning effects are captured. The differences highlight the inaccuracy of the analytical isolator model that was used in the 5-bearing equivalent and 486-bearing models in relation to the actual behaviour of the test specimen. Hence increased computation speed for full-bearing model and development of more detailed equivalent isolator model are required to minimize those differences. Additionally, methods to further increase computation speeds for the 486-bearing model are needed to perform hybrid simulations at rates 2x-slower than real time rather than 15x-slower than real time.

Floor spectra are compared in Figure 143 for the three hybrid models considered. It can be seen that for the response spectra of the INS and ACB, the 5-bearing equivalent model and the 486-bearing model spectral amplitudes are quite similar, while the spectral amplitudes for the 1-bearing equivalent model are significantly smaller. In addition, for the floor response spectra of the RCB a frequency shift occurred of the main spectral acceleration peak around the fundamental period of the superstructure. For the 1-bearing equivalent model the main spectral acceleration peak occurred at a frequency of 3.7 Hz, but for the 5-bearing equivalent model and the 486-bearing model the peak shifted to a frequency of about 3 Hz. At this point it is unclear why this shift was so large. Based on modal analysis results the shift needed to be on the order of 0.3 Hz. Further investigation of this phenomenon is necessary to determine the cause.

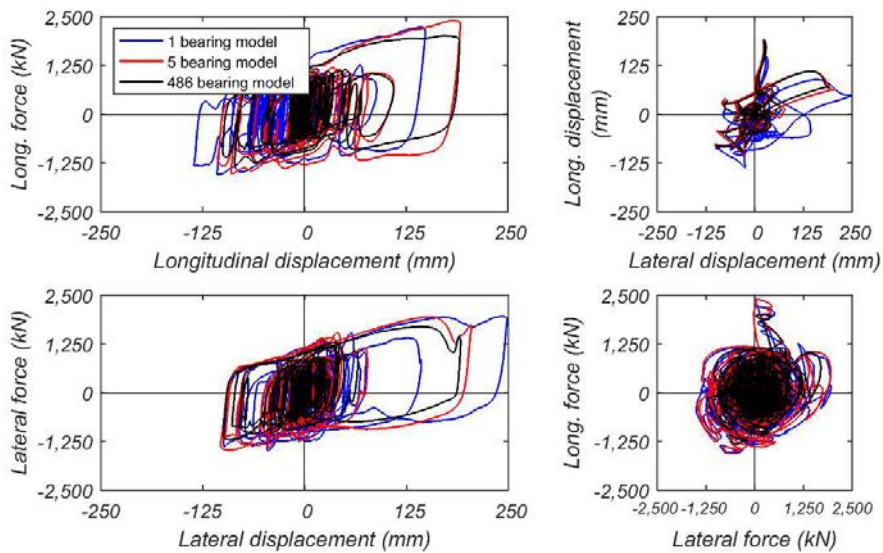


FIG. 142. Comparison of LRB isolator response for different bearing discretization models. (All hybrid simulations were conducted with 2D bidirectional ground motion input).

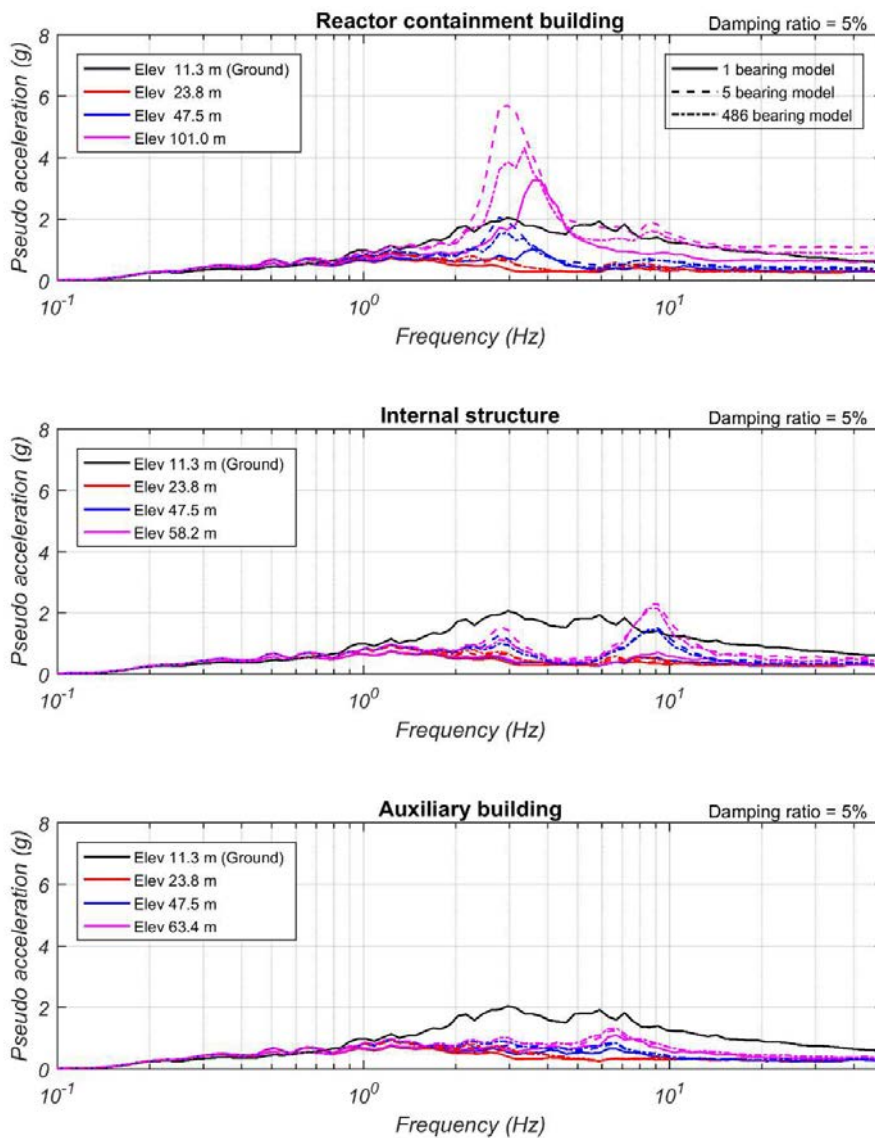


FIG. 143. Comparison of floor response spectra for different LRB bearing discretization models. (All hybrid simulations were conducted with 2D bidirectional ground motion input).

5.7.2 EQSB isolator

5.7.2.1 Comparison of 1D and 2D horizontal input

a. Run 98 vs. 96 (real time, 1-bearing model)

For the hybrid simulation tests with the EQSB experimental specimen, similar comparisons are made as for the LRB to investigate the effect of different loading and modelling conditions on hybrid test results. Firstly, to investigate the effect of the number of horizontal excitation components a comparison is conducted between a 1D longitudinal hybrid simulation (Run 98) and a 2D bidirectional hybrid simulation (Run 96). Both hybrid tests used the 1-bearing equivalent model and were executed in real time.

Isolator responses are compared in Figure 144. The maximum longitudinal displacement for the 1D test is slightly larger than for the 2D test, however, the overall displacement demand considering bidirectional motion is larger for the 2D case. For the lateral direction in the 2D test, hardening of the MER springs is observed which leads to larger horizontal shear forces as compared to the 1D case (3393 kN vs. 2978 kN). In longitudinal direction significant isolator shear force fluctuations can be observed in the 2D test in comparison to the 1D test. This is due to the simultaneous movement of the bearing in the perpendicular lateral direction in the 2D test which results in an increase of the shear force fluctuations in longitudinal direction. This behaviour is caused by two effects. Firstly, bidirectional sliding produces a circular yield surface which means that the horizontal friction forces in the longitudinal and lateral directions are coupled. Secondly, the longitudinal friction force at the ends of the lateral MER springs fluctuates as they are compressed and the normal force in that sliding interface fluctuates. So, the MER springs further increase the coupling behaviour between the longitudinal and lateral directions.

The horizontal floor response spectra for the RCB, INS and ACB are shown and compared in Figure 145. A moderate difference in peak spectral amplitudes at the fundamental frequencies of the plant superstructures can be observed. However, the peaks occur at identical frequencies for both the 1D and 2D hybrid simulation test. Generally speaking, for the two specific tests compared here, the introduction of perpendicular ground motion input does not significantly affect the plant superstructure response spectra in the original longitudinal direction. As was discussed for the LRB hybrid

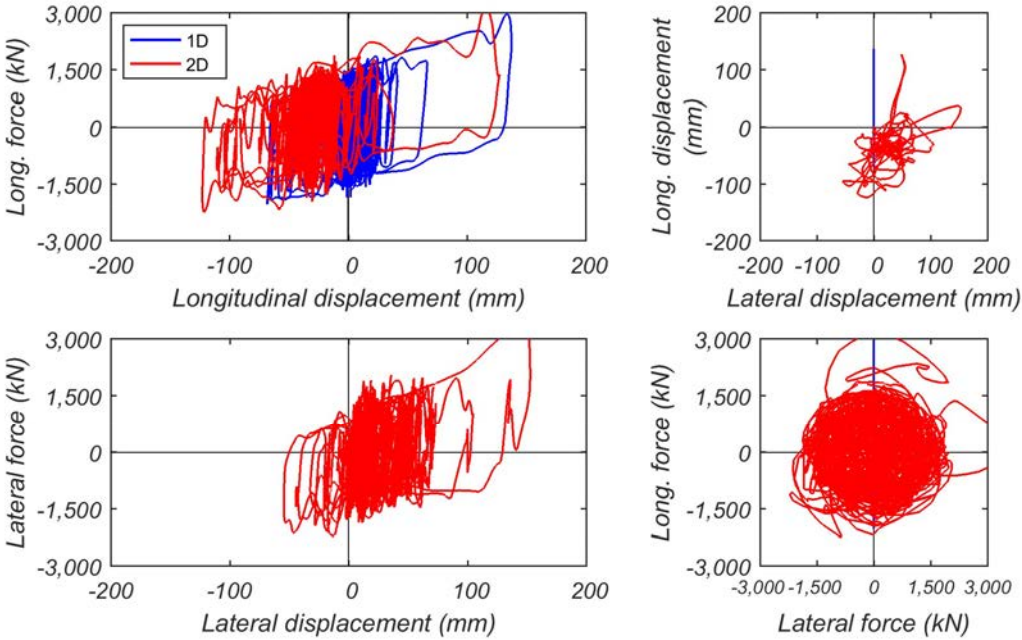


FIG. 144. Comparison of EQSB isolator response for 1D vs. 2D ground motion inputs. (Both hybrid simulations were conducted in real time using the 1-bearing equivalent model).

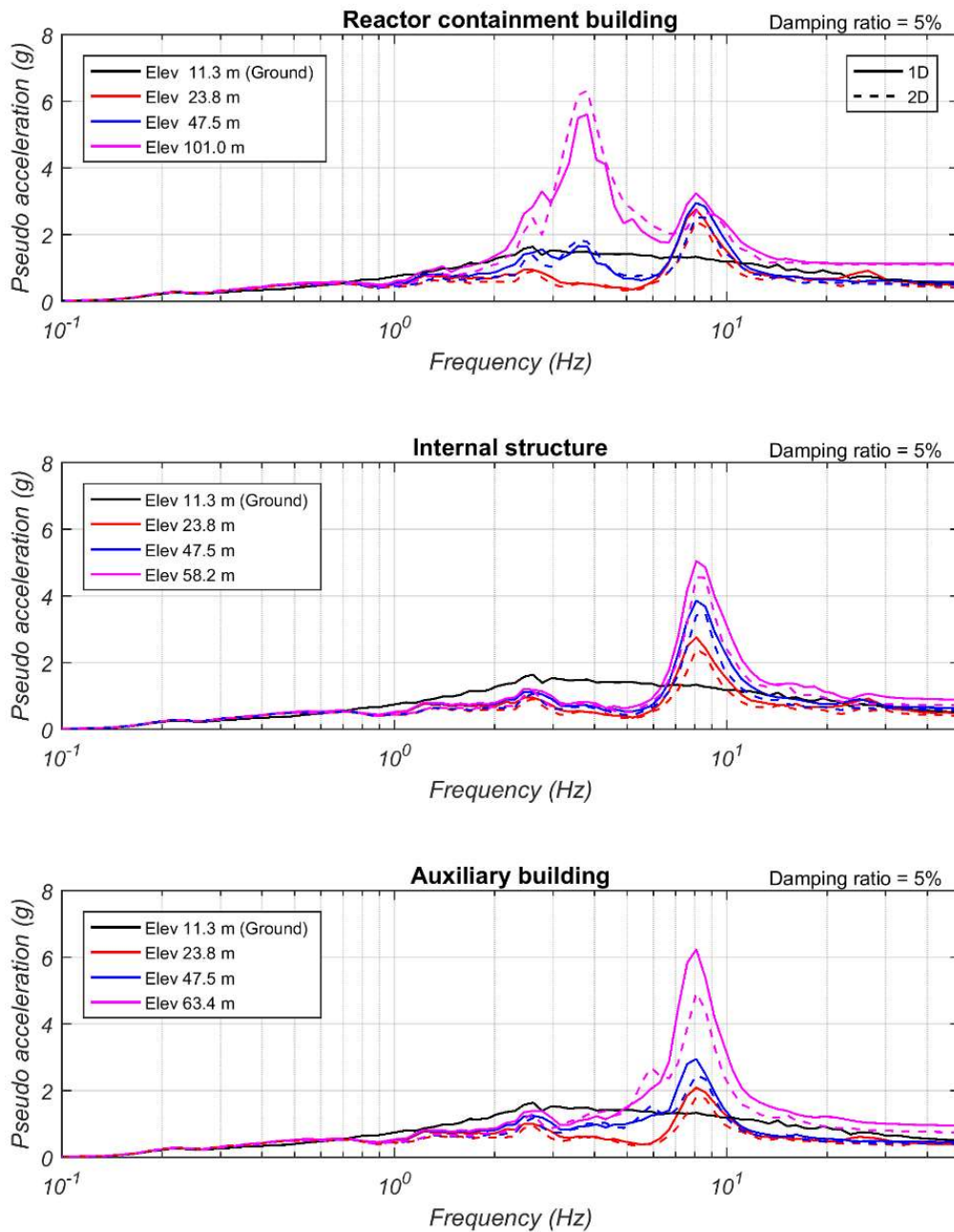


FIG. 145. Comparison of floor response spectra for 1D vs. 2D ground motion inputs. (Both hybrid simulations were conducted in real time using the EQSB 1-bearing equivalent model).

simulation results, experimental errors were fairly large for the real-time tests and affected floor response spectrum peaks, especially around 8 Hz. A careful investigation of FFTs for the displacement errors, force feedbacks as well as error monitors for these two test runs indicated that the tracking performance was indeed not very accurate. Significant average delays were observed: for the 1D test the delay in longitudinal direction was 14 ms, while for 2D test case the delay was 12 ms in longitudinal direction and 9 ms in lateral direction. Comparing Fourier amplitude plots of the displacement errors, one can identify amplitude spikes around 8 Hz for the 2D test which are not present in the 1D test. As for the LRB tests, we can conclude that even though average delays were a bit smaller in the 2D test, the displacement errors, especially at higher frequencies were worse than in the 1D test. This behaviour, which was caused by the tracking error of the SRMD, is likely the reason for the counterintuitive results observed in the floor response spectra.

b. Run 103 vs. 104 (2x-slower than real time, 1-bearing model)

To further assess differences between 1D and 2D hybrid simulation tests, a comparison is conducted based on tests that were executed at a rate 2x-slower than real time. Isolator responses are compared in Figure 146. In terms of longitudinal displacement demands, the two cases are very similar, for the 1D test a peak longitudinal displacement amplitude of 200 mm is observed, while for the 2D test the peak longitudinal displacement amplitude is 197 mm. The shapes of the longitudinal hysteresis loops are also quite similar, especially for the largest displacement cycle which drove the EQSB into the nonlinear hardening range. The main difference for the isolator response lies in the fact that for the 2D test shear forces again fluctuate noticeably more than for the 1D test which produced a smooth hysteresis loop for the 2x-slower than real time test rate. As before this behaviour is explained by the following two effects. Firstly, bidirectional sliding produces a circular yield surface which means that the horizontal friction forces in the longitudinal and lateral directions are coupled. Secondly, the longitudinal friction force at the ends of the lateral MER springs fluctuates as they are compressed and the normal force in that sliding interface fluctuates. Both effects are a bit less pronounced than in the real-time hybrid simulations because of somewhat reduced dynamic effects due to the slower test rate. For the 1D hybrid simulation the maximum horizontal shear force in the bearing is 4122 kN which is similar to the 4225 kN shear force from the 2D test. The shear force interaction surface for the 2D test case is mostly circular with a radius of approximately 1300 kN. However, two large cycles are clearly identified in the shear force interaction surface where the resisting force significantly exceeded the yield surface, meaning that the MER springs were compressed into their nonlinear range.

Comparisons of floor response spectra for the 2x-slower hybrid simulations are shown in Figure 147. Generally, response spectrum amplitudes from the 2D tests are slightly smaller as compared to the 1D hybrid simulation. This is true over the entire frequency range but especially around the fundamental frequencies of the three power plant superstructures. Experimental errors in these 2x-slower tests were much smaller as compared to the real-time tests and their effect on test results can therefore be neglected. The cause for the slightly larger response spectrum amplitudes in the 2D test case are the shear force fluctuations that were discussed above. So contrary to the LRB behaviour, bidirectional excitation of the EQSB increases floor response spectrum peaks and unidirectional testing of these types of bearings thus tends to underestimate in-structure responses.

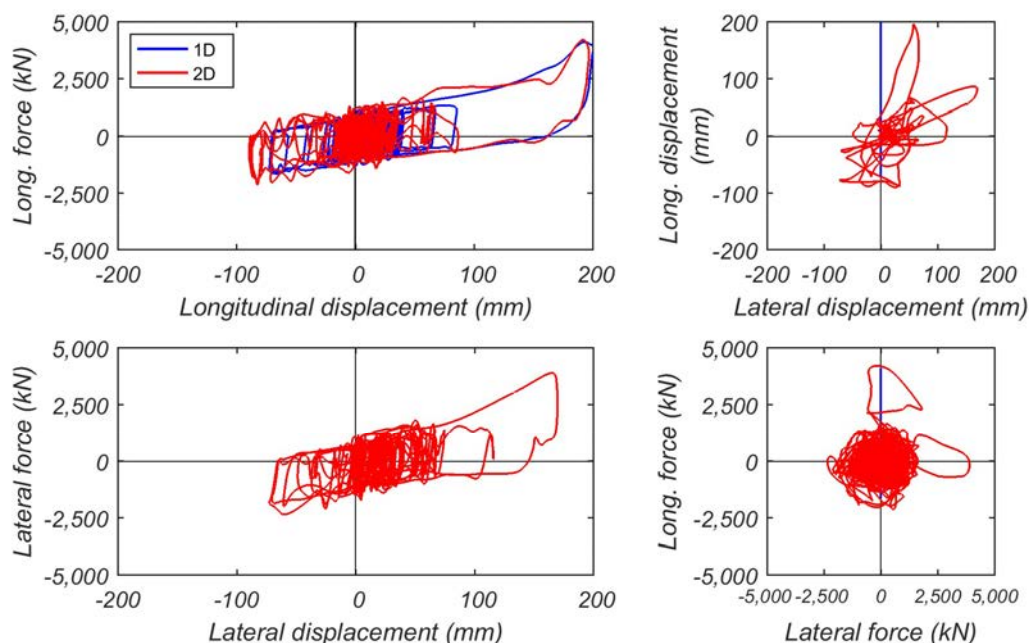


FIG. 146. Comparison of EQSB isolator response for 1D vs. 2D ground motion inputs. (Both hybrid simulations were conducted 2x-slower than real time using the 1-bearing equivalent model).

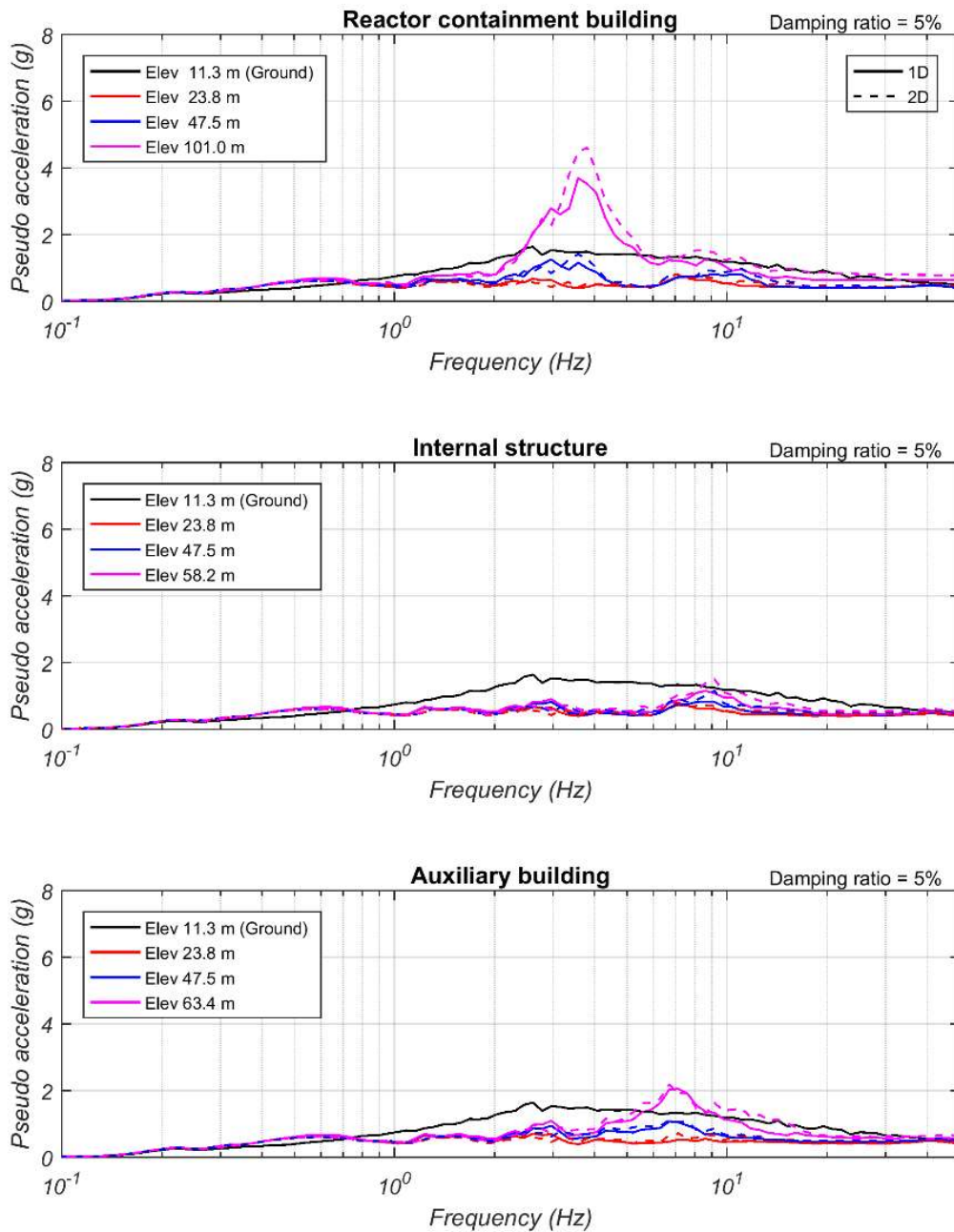


FIG. 147. Comparison of floor response spectra for 1D vs. 2D ground motion inputs. (Both hybrid simulations were conducted 2x-slower than real time using the EQSB 1-bearing equivalent model).

5.7.2.2 Comparison of different test rates

a. Run 98 vs. 103 (1D input, 1-bearing model)

In order to investigate the effect of different hybrid simulation testing rates, the response from a real-time hybrid test is compared with the response from a hybrid simulation conducted 2x-slower than real time. For both cases, 1D hybrid simulations in longitudinal direction are performed using the 1-bearing equivalent model. Isolator responses are shown in Figure 148. From the longitudinal force-deformation relation of the bearing, it can be observed that the maximum bearing displacement for the real-time hybrid test case is 138 mm, while the displacement demand from the 2x-slower test is 200 mm, which is significantly larger than the real-time case. By comparing the shapes of the longitudinal hysteresis loops, it is clear that for the 2x-slower test the loops are substantially thinner. Hence, the significantly larger isolator deformation observed in the 2x-slower hybrid simulation is caused by the smaller isolator

characteristic strength which is equal to the friction force. The smaller friction forces in the slower test are a direct result of the velocity dependence of the static and dynamic coefficients of friction which is typical for certain PTFE-stainless-steel sliding interfaces. For the 2x-slower test, smaller coefficients of friction are therefore expected in comparison with the real-time test, ultimately leading to larger isolator displacement demands. For the 2x-slower hybrid simulation, the displacement in longitudinal direction is larger than the design displacement of the EQSB bearing so that the MER springs exhibited nonlinear hardening behaviour.

Floor response spectra are shown in Figure 149. It is evident from the results that above a frequency of 1 Hz spectral accelerations are much smaller for the 2x-slower test in comparison to the real-time test. This is especially true for floor spectrum peaks at the fundamental frequencies of the RCB, INS, and ACB. It seems that the real-time hybrid simulation produced more high frequency response that got transmitted into the power plant superstructures. As discussed in the previous section, for the real-time hybrid simulations there is a clear excitation of all three superstructures at a frequency of about 8 Hz. To determine if these effects are caused by greater dynamic effects or larger experimental errors in the real-time test cases, it is necessary to evaluate and compare FFTs of displacement errors and force feedbacks as well as error monitors. Evidently, the tracking performance was significantly less accurate in the real-time test as compared to the 2x-slower test. An investigation of the delays in the longitudinal degree of freedom shows that the average delay in the real-time case was around 14 ms,

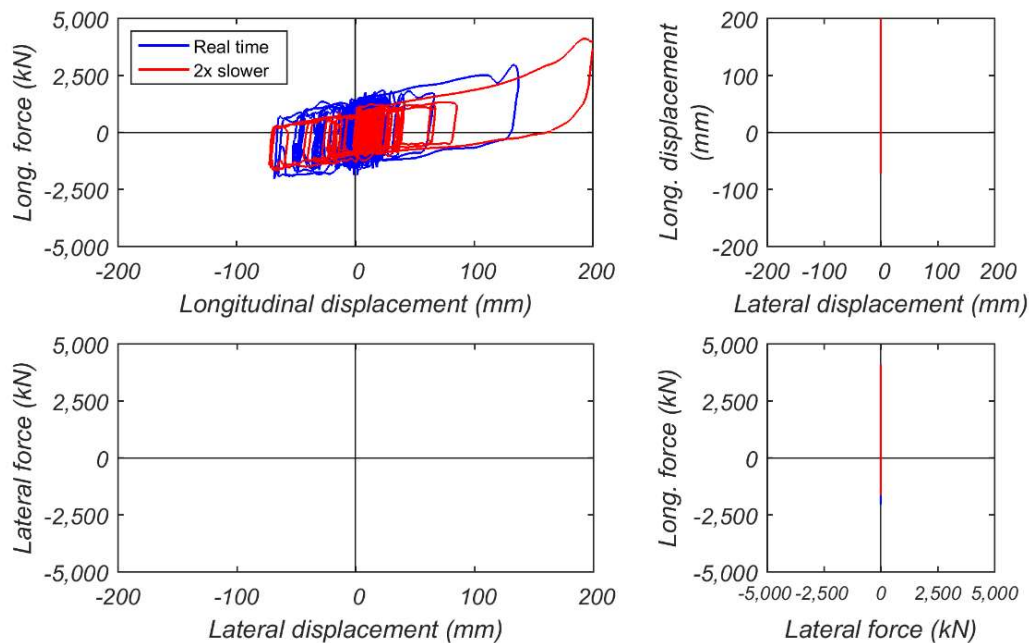


FIG. 148. Comparison of EQSB isolator response for real-time hybrid test and hybrid test executed 2x-slower than real time. (Both hybrid simulations were conducted with 1D longitudinal input using the 1-bearing equivalent model).

whereas in the 2x-slower case the delay was only 0.4 ms. In addition, the error monitors show approximately 6-times more error in the real-time test in relation to the 2x-slower test. Therefore, the large difference in the floor response spectrum amplitudes is caused by the combination of increased dynamic effects and much greater experimental errors in the real-time hybrid simulation. In conclusion, it seems that in the real-time hybrid simulation the experimental errors played a more important role on the in-structure response than the dynamic and inertial effects. Hence, the real-time hybrid simulation conducted with the EQSB likely produced unrealistically large floor response spectra for the power plant superstructures due to excessive experimental errors.

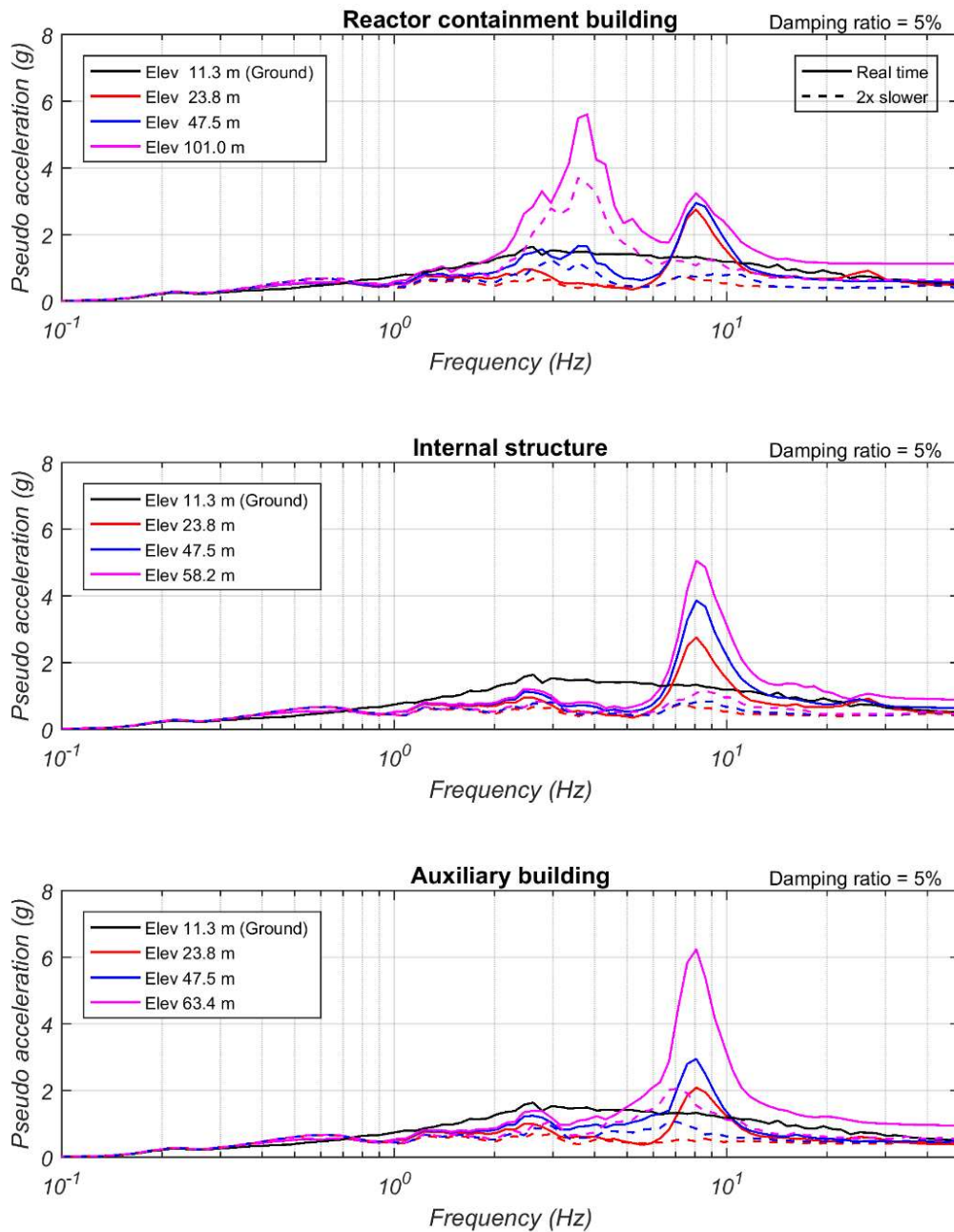


FIG. 149. Comparison of floor response spectra for real-time hybrid test and hybrid test executed 2x-slower than real time. (Both hybrid simulations were conducted with 1D longitudinal input using the EQSB 1-bearing equivalent model).

b. Run 96 vs. 104 (2D input, 1-bearing model)

To further investigate the effect of different hybrid simulation test rates, results from 2D bidirectional hybrid simulations are compared. One test was executed in real-time and the other was executed 2x-slower than real time. Both hybrid simulations were using the 1-bearing equivalent ANT model. Firstly, the isolator responses are shown in Figure 150. Evidently the 2x-slower test results in larger isolator displacement demands both in longitudinal and lateral directions in comparison with the real-time hybrid simulation. As discussed above, this is due to the lower coefficient of friction in the sliding interface when sliding velocities are low. Thus, for bidirectional excitation friction forces are smaller and displacement demands larger in both the longitudinal and lateral directions. The maximum longitudinal displacement demand from the real-time test is 137 mm, which is smaller than the 200 mm demand from the test conducted 2x-slower than real-time. As observed in previous sections when 2D tests are

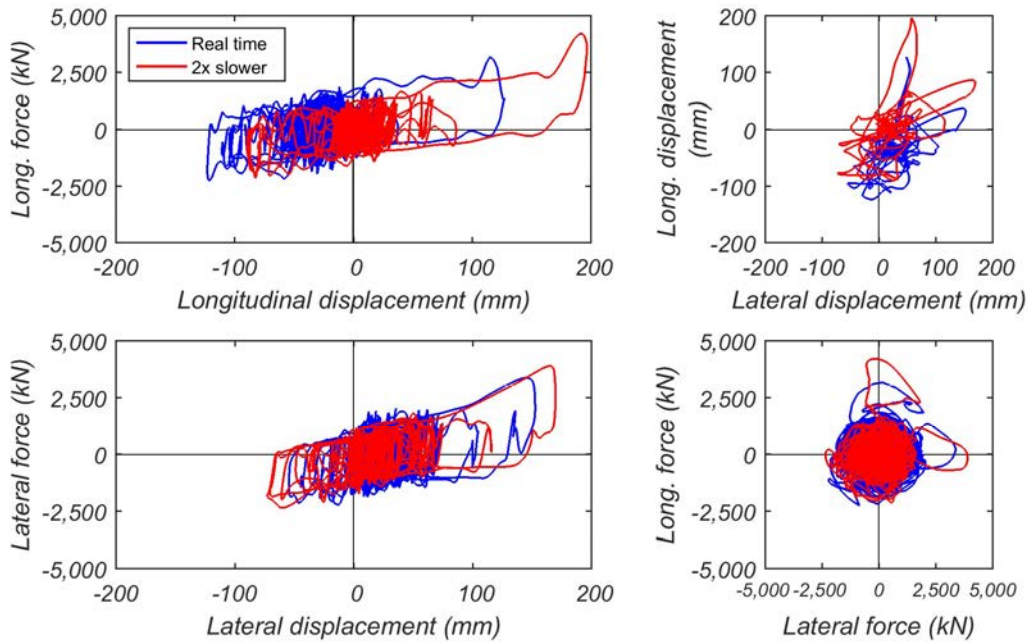


FIG. 150. Comparison of EQSB isolator response for real-time hybrid test and hybrid test executed 2x-slower than real time. (Both hybrid simulations were conducted with 2D bidirectional input using the 1 bearing equivalent model).

considered, isolator shear forces in the two horizontal directions fluctuate because of the perpendicular movement of the bearing and the coupling of both, the friction forces and the MER spring forces.

Floor response spectra are compared in Figure 151 for a real-time hybrid simulation and a 2x-slower test under 2D ground motion input. Investigating the effect of the hybrid simulation test rate on the in-structure response, similar conclusions can be drawn as in the 1D comparison above. The power plant response in the real-time test produces much larger floor response spectrum amplitudes, especially in the high frequency range, as compared to the 2x-slower test rate. A distinct peak located around 8 Hz is observed for the real-time hybrid simulation case, while for the 2x-slower case the amplification around the 8 Hz frequency is not present. As discussed above in the 1D comparison, this difference can mostly be attributed to experimental errors. For the real-time hybrid simulation investigated here, average delays were around 12.2 ms in longitudinal direction and 9.1 ms in lateral direction, whereas in the 2x-slower test they were around 1.0 ms and 2.4 ms, respectively. In addition, all the error monitors show approximately 2-times more error in the real-time test than in the 2x-slower hybrid simulation. Therefore, we can conclude that for the real-time hybrid simulation case, experimental errors played an important role and significantly affected the accuracy of the in-structure response in terms of floor response spectrum amplitudes. The distinct peak in the spectra around 8 Hz is primarily caused by experimental errors and resulted in unrealistically large spectral amplitudes for the real-time hybrid

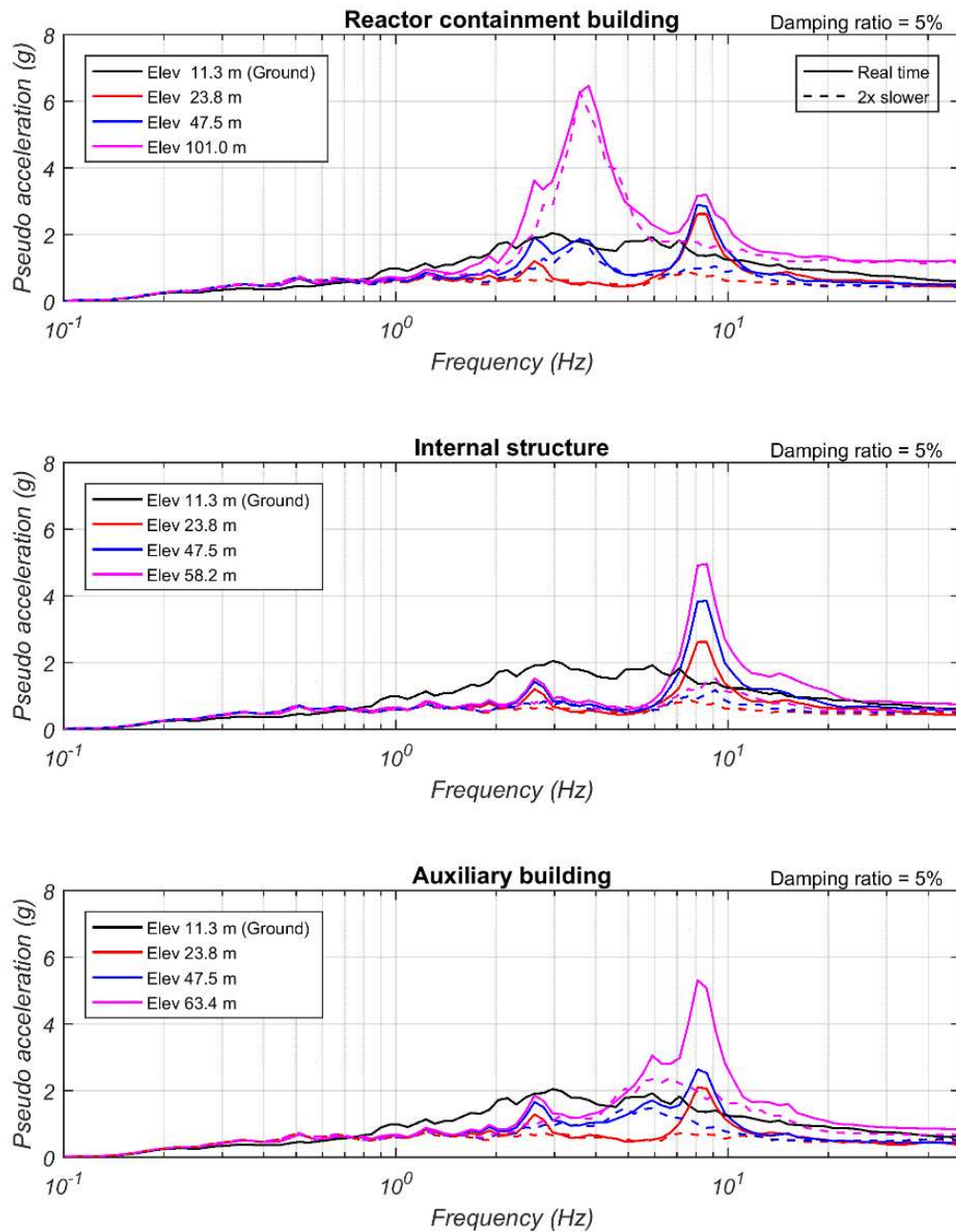


FIG. 151. Comparison of floor response spectra for real-time hybrid test and hybrid test executed 2x-slower than real time. (Both hybrid simulations were conducted with 2D bidirectional input using the EQSB 1-bearing equivalent model).

5.7.2.3 Effect of vertical excitation

a. Run 104 vs. 121 (2x-slower for 2D input, 10x-slower for 3D input, 1-bearing model)

In order to investigate effects of including the vertical ground motion input, test results considering 2-component input (Run 104) and 3-component input (Run 121) are compared. The 1-bearing equivalent ANT model was used for both cases and the hybrid simulation was executed 2x-slower than real time for the 2D case and 10x-slower than real time for the 3D case. Isolator responses are shown in Figure 152. Comparing horizontal hysteresis loops of the bearing from the two hybrid simulations, it can be

seen that displacement amplitudes are quite similar in both longitudinal and lateral directions except for an offset of the entire hysteresis loops in both directions.

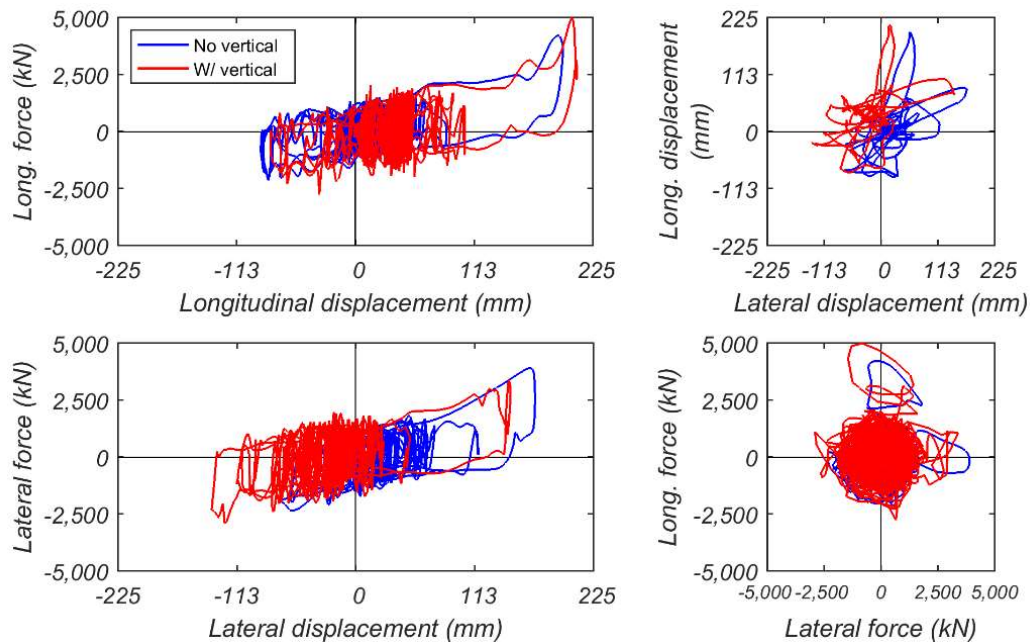


FIG. 152. Comparison of EQSB isolator response for 2D vs. 3D ground motion inputs. (The 2D test is executed 2x-slower and the 3D test 10x-slower than real time. Both hybrid simulations are using the 1-bearing equivalent model).

Shear force fluctuations in the horizontal hysteresis loops are observed for hybrid simulations, however, when vertical input is included, substantially more high frequency shear force fluctuations are observed, especially at smaller bearing deformations. Because the total horizontal resisting forces of the EQSB are a combination of sliding friction forces and MER spring forces, axial force fluctuations induced by the vertical ground motion result in increased oscillations of the sliding friction forces and hence the total resisting forces in the bearing. The shear force oscillations predominantly occur around frequencies between 8 Hz and 10 Hz. This corresponds to the first fundamental frequency of the isolated nuclear power plant in vertical direction. Thus, the higher frequency shear force oscillations are a result of the vertical-horizontal force coupling behaviour of the EQSB. Axial force fluctuations in the isolator caused by the vertical ground motion input affect the shear resistance of the bearing resulting in horizontal force fluctuations at the same frequency as the vertical force fluctuations.

Floor response spectra are compared in Figure 153 for the 2-component and 3-component input cases. It can be observed that the floor response spectrum amplitudes in the high frequency range are significantly larger for the 3D case in comparison with the 2D case, especially for the INS and ACB superstructures above frequencies of 7 Hz. As discussed above, this is due to the substantial shear force fluctuations induced by the vertical ground motion input in the 3D case. The high frequency oscillations are transmitted into the power plant superstructures, which results in large spectral accelerations spikes in the horizontal floor response spectra. Note that the fundamental vertical frequency of the plant is around 10 Hz and the fundamental horizontal frequencies of the INS and ACB are 8 Hz and 7.5 Hz, respectively.

Therefore, the increase of floor response spectrum amplitudes in the high frequency range is more pronounced for the INS and ACB since the fundamental horizontal frequencies are close to the vertical frequency of the plant. On the other hand, the horizontal fundamental frequency of the RCB is around 3.7 Hz, which is well separated from the frequency of the shear force fluctuations induced by the vertical-horizontal force coupling of the EQSB. Thus, the horizontal floor response spectra of the RCB are not significantly increased by the inclusion of the vertical ground motion input.

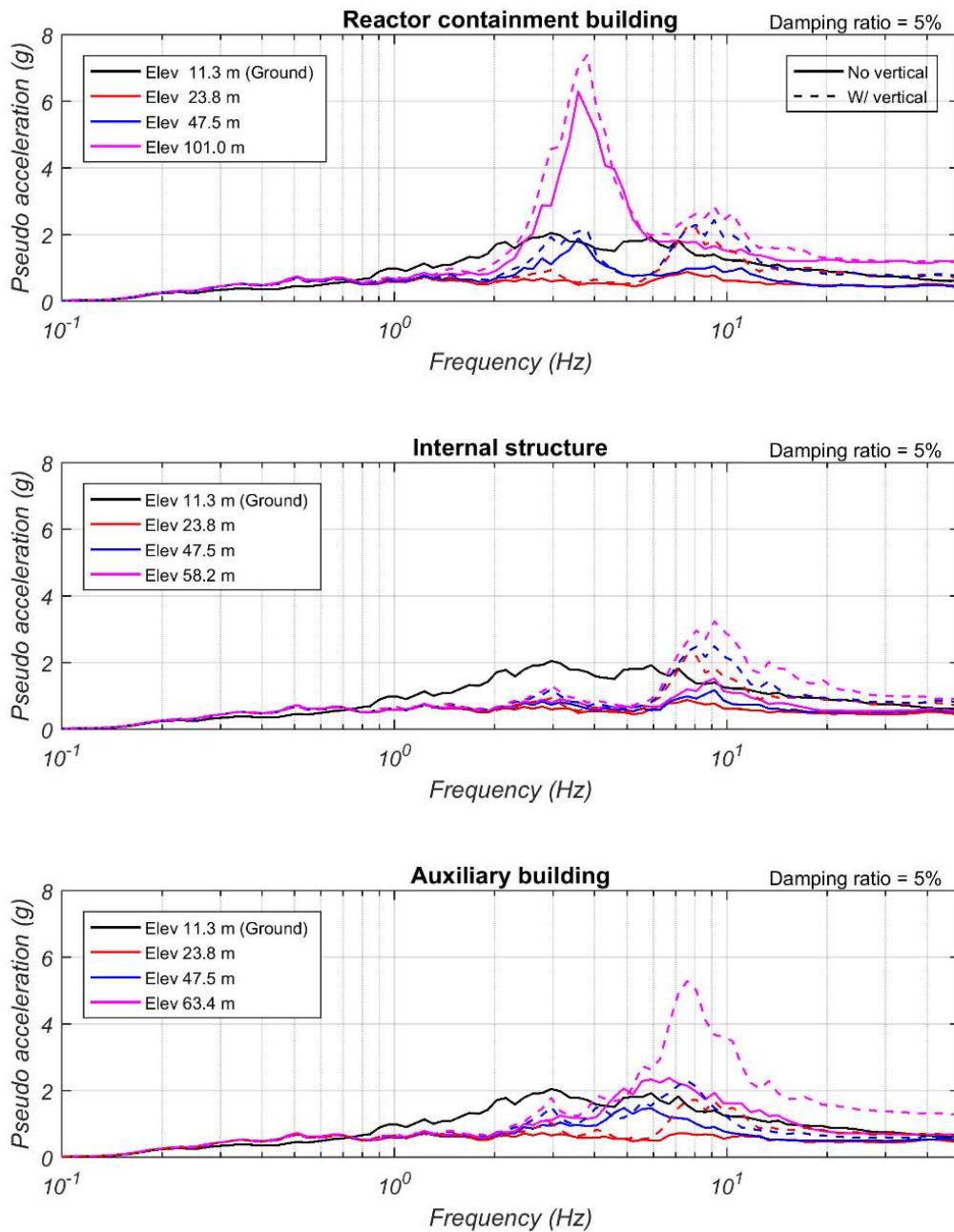


FIG. 153. Comparison of floor response spectra for 2D vs. 3D ground motion inputs. (The 2D test is executed 2x-slower and the 3D test 10x-slower than real time. Both hybrid simulations are using the EQSB 1-bearing equivalent model).

5.7.2.4 Variation due to bearing discretization models

a. Run 98 vs. 108 (1D input, real time)

Finally, the effect of different bearing discretization models is compared based on hybrid simulation results obtained using the 1-bearing equivalent model and the 5-bearing equivalent model. For the first test (Run 98), the 1-bearing equivalent model is used and the hybrid simulation was executed in real time. For the second case (Run 166), the 5-bearing equivalent model was used, with the experiment bearing located in the north-east quadrant of the ACB and the hybrid simulation was also conducted in real time. Both cases used a unidirectional ground motion input in longitudinal direction. Firstly, isolator responses are shown in Figure 154.

It can be seen that the response from the 5-bearing equivalent model exhibits slightly smaller isolator displacement demands with a maximum of 124 mm. In comparison, the 1-bearing equivalent model

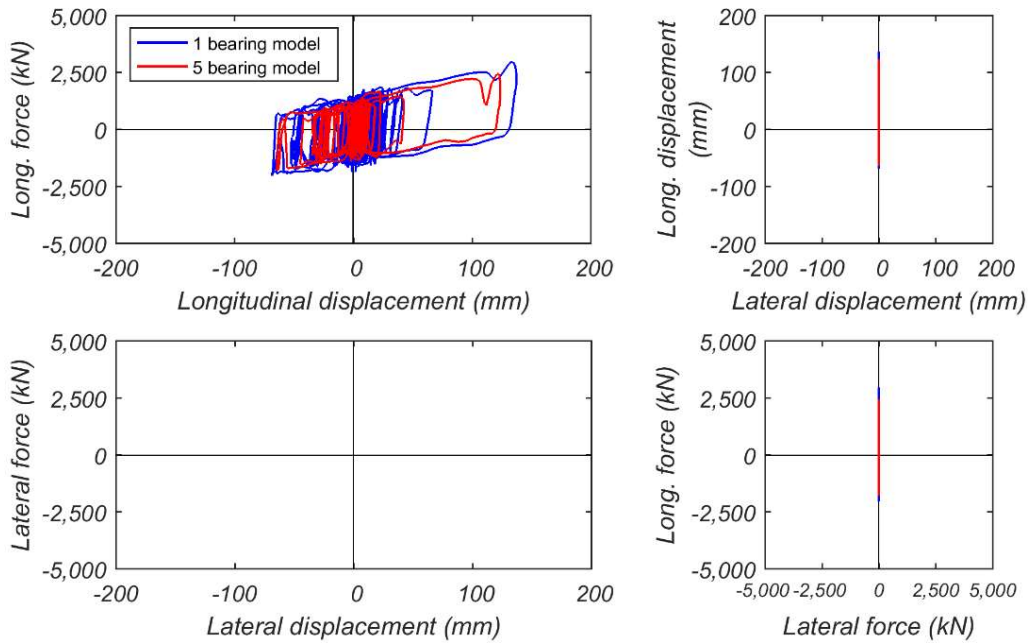


FIG. 154. Comparison of EQSB isolator response for different bearing discretization models. (Both hybrid simulations were executed in real time considering 1D longitudinal ground motion inputs).

experienced a peak isolator displacement of 138 mm. The isolator response for the 1-bearing equivalent model is entirely determined by the experimental specimen while for the 5-bearing equivalent model, the response is also affected by the behaviour of the four analytical isolators. Therefore, differences in the hysteresis loops of the experimental isolator are expected due to the influence of the analytical isolators on the displacement history of the entire isolation plane. Thus, it is essential that an accurate analytical isolator model is employed wherever analytical bearings are used to model some portion of the isolation plane. It is also important to be noted that during the hybrid simulation with the 5-bearing equivalent model the experimental isolator was affected by the fluctuation of the axial force due to overturning whereas in the case of the 1-bearing equivalent model the axial force on the experimental bearing remained constant.

Floor response spectra are shown in Figure 155 for the two hybrid models considered. The floor response spectra for the two cases are quite different, especially for the RCB and ACB. As discussed above, such differences are expected because the analytical isolator model might not capture the actual behaviour of the test specimen in every detail, particularly breakaway friction phenomena. This leads to different responses of the isolation plane and thus different in-structure responses in terms of floor response spectra.

Similar to the observations made from previous comparisons, when real-time hybrid simulations are conducted with the EQSB experimental specimen, distinct peaks in the horizontal floor response spectra (around 8 Hz) can be identified. As discussed previously, this behaviour was mainly caused by experimental errors and dynamic effects due to the real-time execution of the hybrid simulations. In addition, for the floor response spectra of the RCB a frequency shift occurs of the main spectral acceleration peak around the horizontal fundamental frequency of the RCB. For the 1-bearing equivalent model the main spectral acceleration peak is located at a frequency of 3.7 Hz, but for the 5-bearing equivalent the peak shifts to a frequency of about 3 Hz. At this point it is unclear why the frequency shift was larger than what was predicted by modal analyses (see Table 33). Further investigation of this phenomenon is necessary to determine the cause.

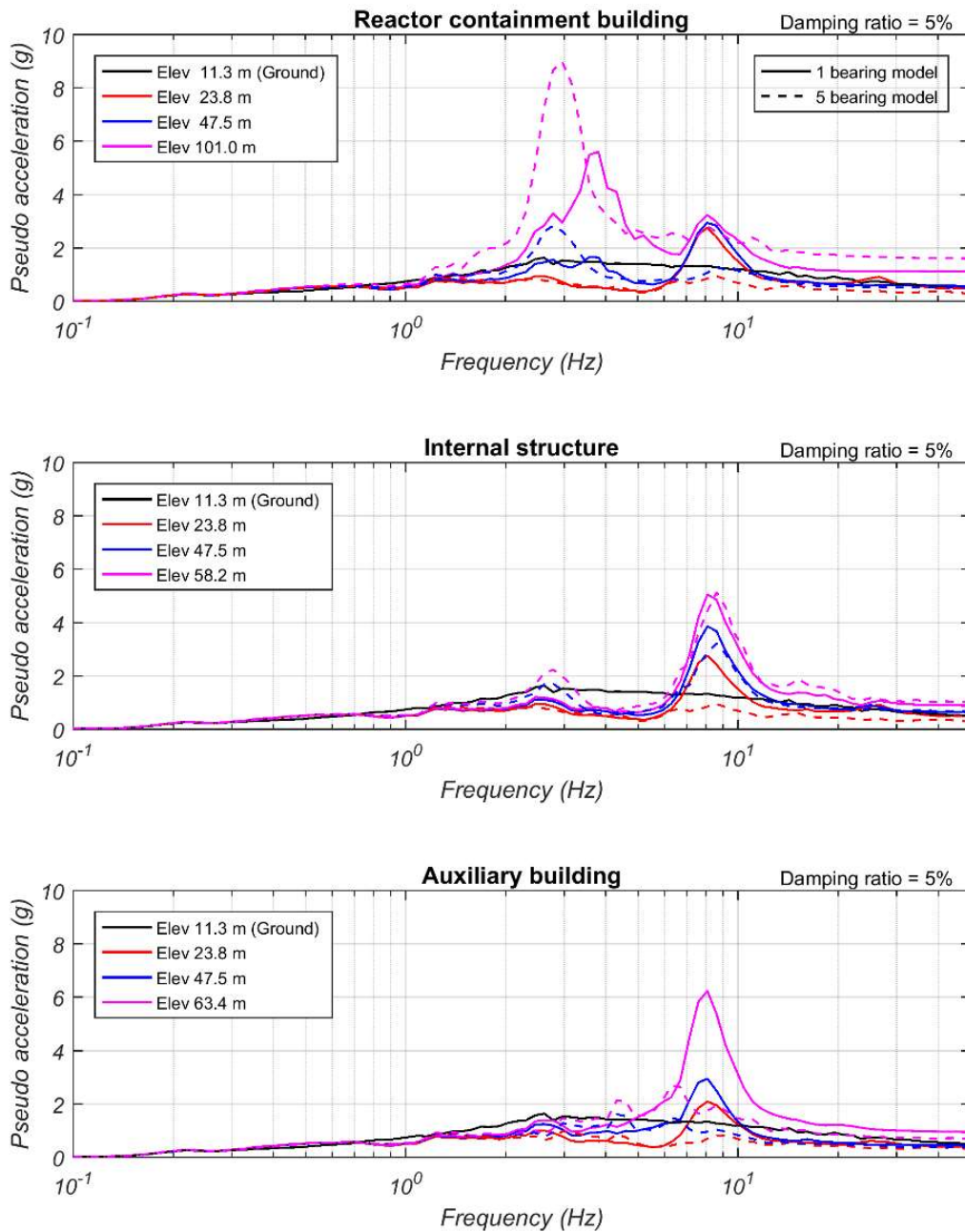


FIG. 155. Comparison of floor response spectra for different EQSB bearing discretization models. (Both hybrid simulations were executed in real time considering 1D longitudinal ground motion inputs).

b. Run 104 vs. 110 (2D input, 2x-slower than real time)

Another set of tests considering the 1-bearing equivalent model and the 5-bearing equivalent model are compared next. These two tests were conducted under bi-directional input motion rather than 1D motion as discussed above, however, they are executed at a rate 2x-slower than real time. Isolator response results are compared in Figure 156, which indicates that the 1-bearing equivalent model and the 5-bearing equivalent model produced fairly similar hysteresis loops in both the longitudinal and lateral directions. Looking more closely, it can be observed that the hysteresis loop of the 5-bearing equivalent model shows more shear force fluctuations in comparison with the hysteresis loop of the 1-bearing equivalent model. This is caused by the fluctuation of the axial force due to overturning effects in the 5-bearing equivalent model, which are not being captured in the 1-bearing equivalent model.

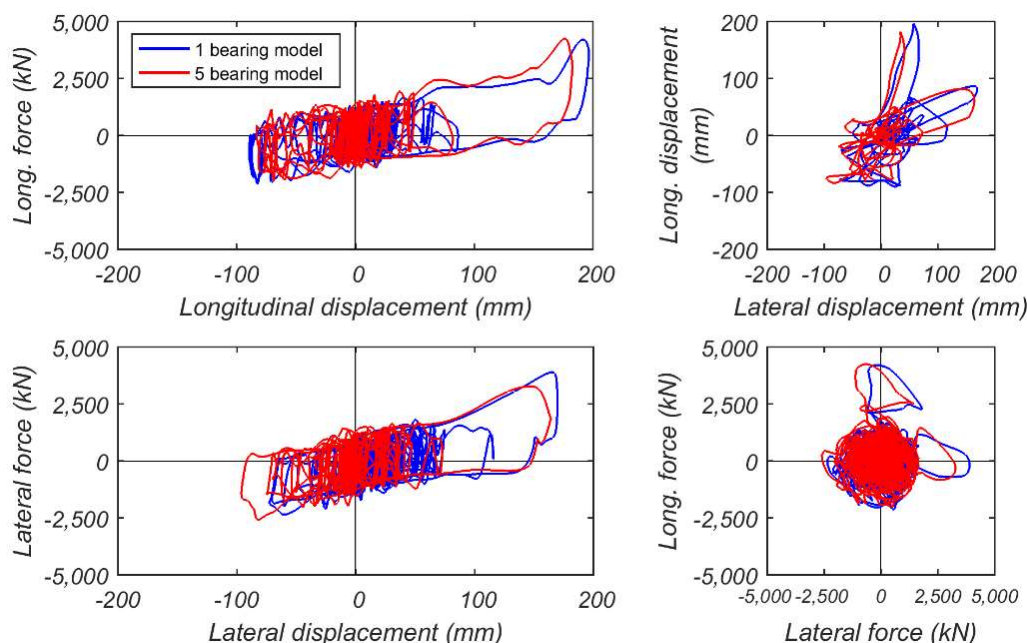


FIG. 156. Comparison of EQSB isolator response for different bearing discretization models. (Both hybrid simulations were executed 2x-slower than real time considering 2D bidirectional ground motion inputs).

Floor response spectra are compared in Figure 157. In general, similar conclusions can be drawn as discussed above. However, the increase of the response spectra for the 5-bearing equivalent model in the lower frequency range, especially around the fundamental horizontal frequency of the RCB, is caused by overturning effects. Unlike vertical excitation, overturning effects occur at the horizontal modal frequencies, meaning that the previously mentioned axial force fluctuations have similar frequency content. Hence, the floor spectra increase is most noticeable around the fundamental spectral peak of the RCB. As before, a frequency shift in the RCB floor response spectra is observed. For the 1-bearing equivalent model, the fundamental spectral peak is located at approximately 3.7 Hz but shifts to around 3 Hz for the 5-bearing equivalent model. Again, further investigation is needed to identify possible causes for this frequency shift.

5.7.3 TPFB isolator

5.7.3.1 Comparison of 1D and 2D horizontal input

a. Run 216 vs. 217 (2x-slower than real time, 1-bearing model)

Finally, similar comparisons as for the LRB and EQSB are made based on the hybrid simulation results using the TPFB experimental specimen. Firstly, in order to investigate the effect of the number of horizontal ground motion components a comparison is conducted between a 1D longitudinal hybrid simulation (Run 216) and a 2D bidirectional hybrid simulation (Run 217). Both hybrid tests used the 1-bearing equivalent model and were executed at a rate 2x-slower than real time.

Isolator responses are depicted in Figure 158. Comparing the horizontal force-deformation hysteresis loops in longitudinal direction, it can be seen that responses are quite similar. For the 2D case, a somewhat larger positive displacement demand of 450 mm is observed as compared to the longitudinal isolator displacement amplitude of 393 mm in the 1D test. Since the horizontal resisting force of the TPFB largely depends on the friction forces at each sliding interface, which in turn depend on the axial force on the bearing, small variations in the axial force will result in horizontal shear force fluctuations which can be seen even for the 1D loading case. The maximum horizontal bearing shear force in the 1D test is 1496 kN, while for the 2D test a slightly larger peak shear force of 1561 kN was obtained. Comparing these horizontal isolator shear force amplitudes to the ones obtained in the hybrid simulations with the LRB and EQSB (on the order of 2500-3000 kN), significantly lower isolator shear

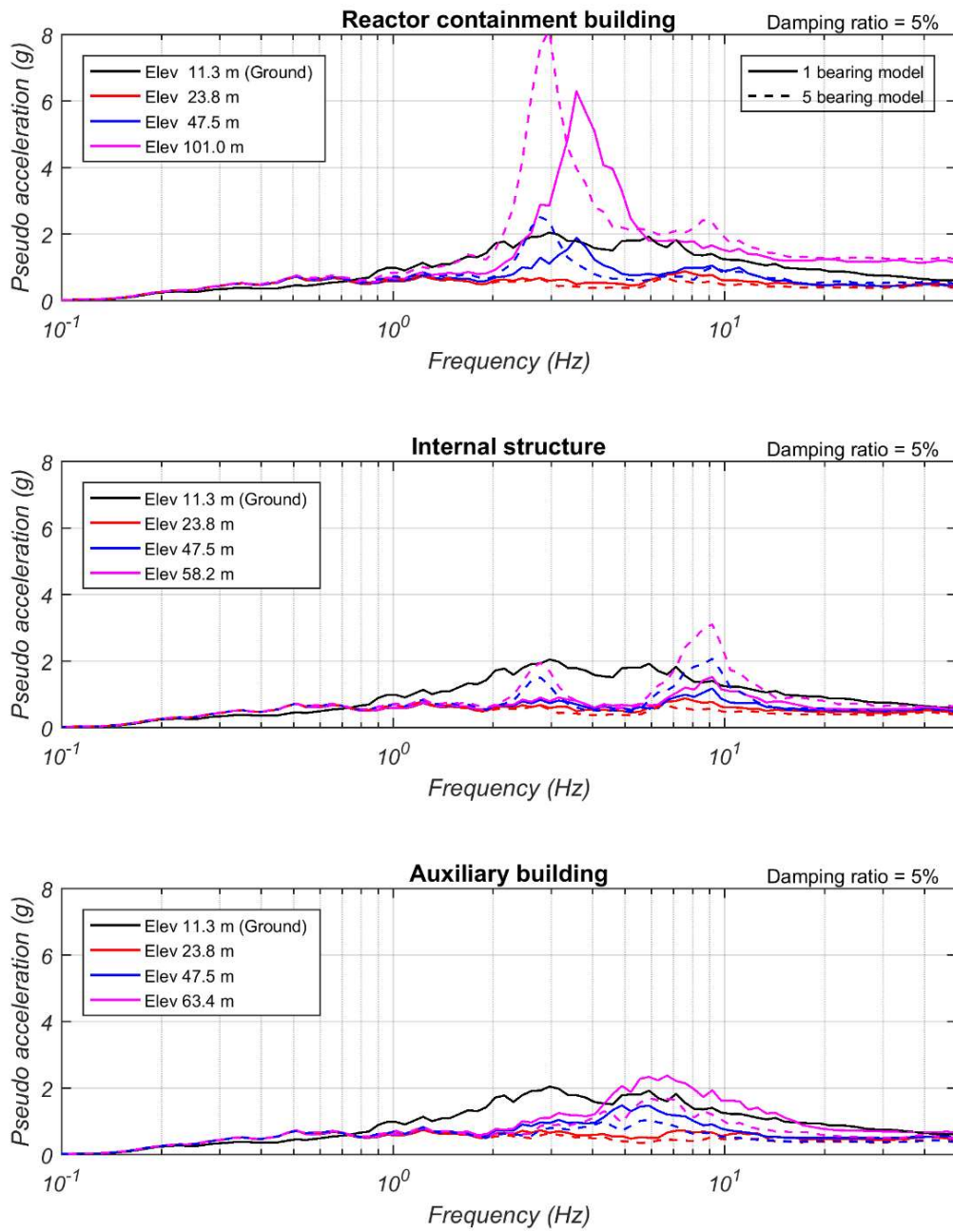


FIG. 157. Comparison of floor response spectra for different EQSB bearing discretization models. (Both hybrid simulations were executed 2x-slower than real time considering 2D bidirectional ground motion inputs).

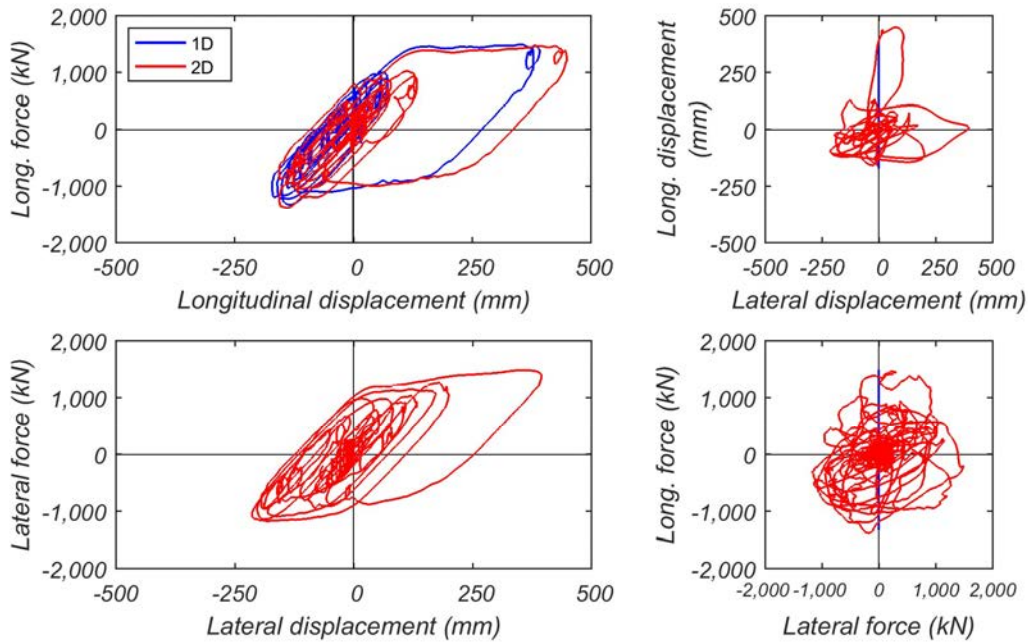


FIG. 158. Comparison of TPFB isolator response for 1D vs. 2D ground motion inputs. (Both hybrid simulations were conducted 2x-slower than real time using the 1-bearing equivalent model).

forces are obtained for the TPFB. This indicates that less force is transmitted into the power plant superstructure components, leading to an overall more efficient in-structure response reduction effect.

It is important to notice that for the main sliding stage of the TPFB in the first large loading cycle in positive direction, a smaller horizontal stiffness is observed during the test in relation to the theoretical isolator horizontal stiffness based on the radii of the concave sliding dishes. However, after unloading when the isolator movement reverses direction, the experimentally observed stiffness of the main sliding stage returns to the theoretically calculated value. This behaviour was also observed in the characterization test results of the TPFB and was discussed in Section 5.3.4.3. The main reason for this behaviour is the large break-away force that is required to initiate sliding for the main stage of the TPFB. The static (or initial) coefficient of friction is larger than the dynamic (or steady-state) coefficient of friction. Therefore, a larger force is needed to overcome the initial break-away friction force to start the sliding when the bearing initially moves into the main sliding stage. After the movement commences, the friction coefficient drops to the steady-state or dynamic value. The magnitude of the break-away force due to adhesion is dependent on velocity and jerk (derivative of acceleration) of the movement. Bondonet and Filiatrault [34], who have performed extensive studies on the frictional response of PTFE (Teflon) sliding surfaces similar to the ones used in the TPFB isolator, have found very similar behaviour. While Bondonet and Filiatrault [34] investigated and developed modelling approaches for PTFE sliding surfaces at the macroscopic level, several other studies investigated adhesion in PTFE sliding surfaces at the microscopic level. Thus, we can conclude that this behaviour is expected and is caused by adhesion in PTFE sliding surfaces.

The horizontal floor response spectra of the RCB, INS and ACB comparing 1D and 2D loading cases are shown in Figure 159. The response spectra are generally nearly identical over most of the plotted frequency range. Only minor differences can be observed for the peak values of the response spectra, with the 2D input case resulting in slightly smaller spectral accelerations. However, the differences are small and negligible. For the RCB superstructure, the largest response spectrum peak occurs around 3.7 Hz which corresponds to the fundamental horizontal frequency of the

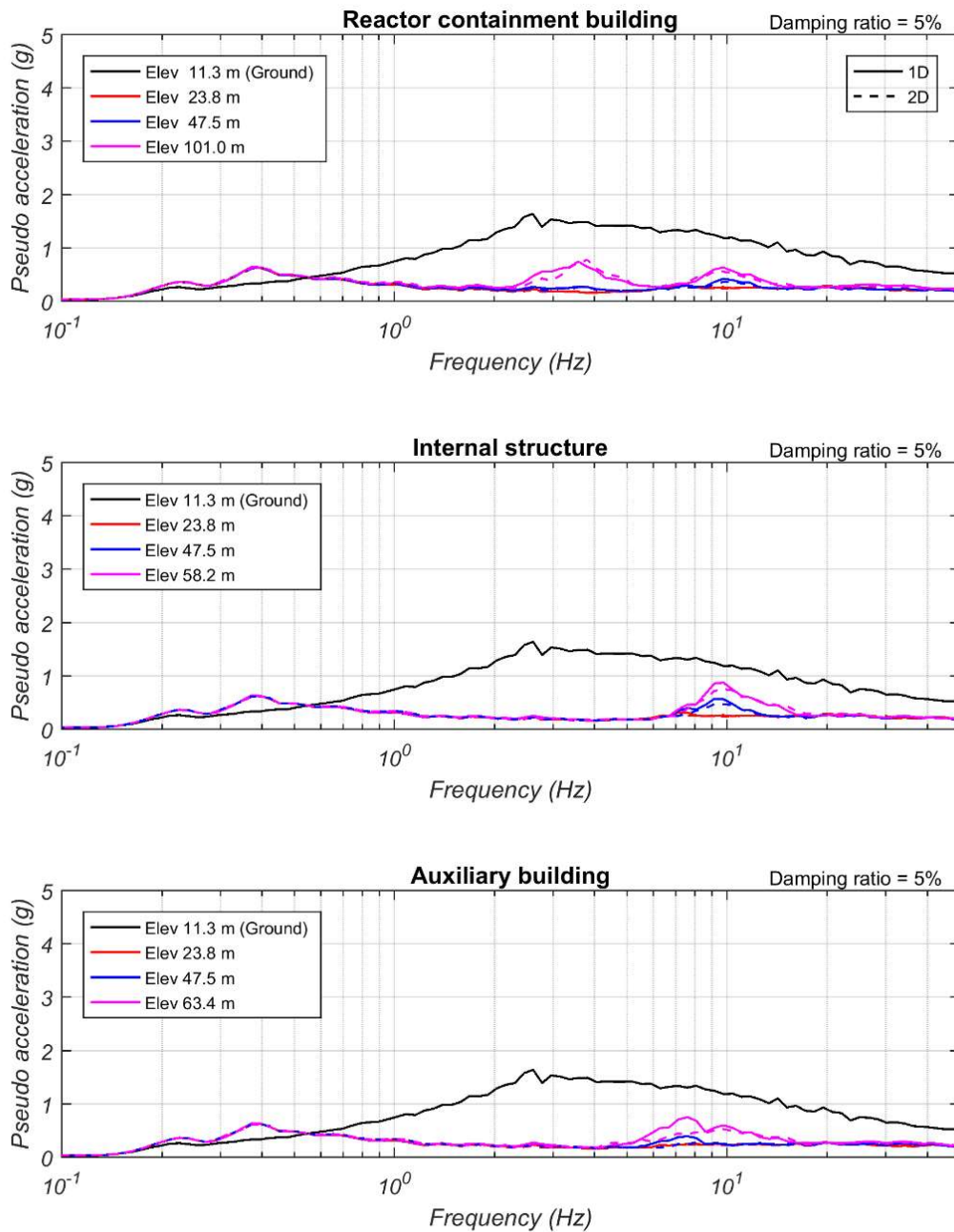


FIG. 159. Comparison of floor response spectra for 1D vs. 2D ground motion inputs. (Both hybrid simulations were conducted 2x-slower than real time using the TPFB 1-bearing equivalent model).

building. However, a second peak around a frequency of 10 Hz also exists in the floor response spectra of the RCB which is caused by the vertical-horizontal coupling behaviour of the axial and friction forces in the TPFB. For the INS and ACB, the peak responses in the floor spectra all occur around the fundamental frequencies of each building. For the INS, the spectral acceleration peak is around 0.9 g at 9.5 Hz, while for the ACB the spectral acceleration peak is around 0.8 g at 7.5 Hz. For all floor spectra for all three superstructures there is an additional peak around 0.37 Hz, which corresponds to the effective isolation frequency.

Finally, it is important to notice that for all elevations and over most of the frequency range from 0.1 Hz to 50 Hz spectral accelerations for the plant isolated with TPFB are significantly lower than for the plant isolated with LRB (up to 3.5 times higher) or EQSB (up to 5.5 times higher). The only place where spectral accelerations are larger for the TPFB is around the isolation frequency of 0.37 Hz. A detail comparison of the hybrid simulation results using the three different bearing types is made later, in Section 5.7.4.

5.7.3.2 Comparison of different test rates

a. Run 217 vs. 219 (2D input, 1-bearing model)

To investigate the effect of the hybrid simulation testing rate on the bearing and in-structure response for the TPFB, results from tests conducted at a rate 2x-slower than real time (Run 217) and 10x-slower than real time (Run 219) are compared. The two tests were both conducted using the 1-bearing equivalent model under bi-directional ground motion input. Isolator responses are shown in Figure 160 and are discussed first.

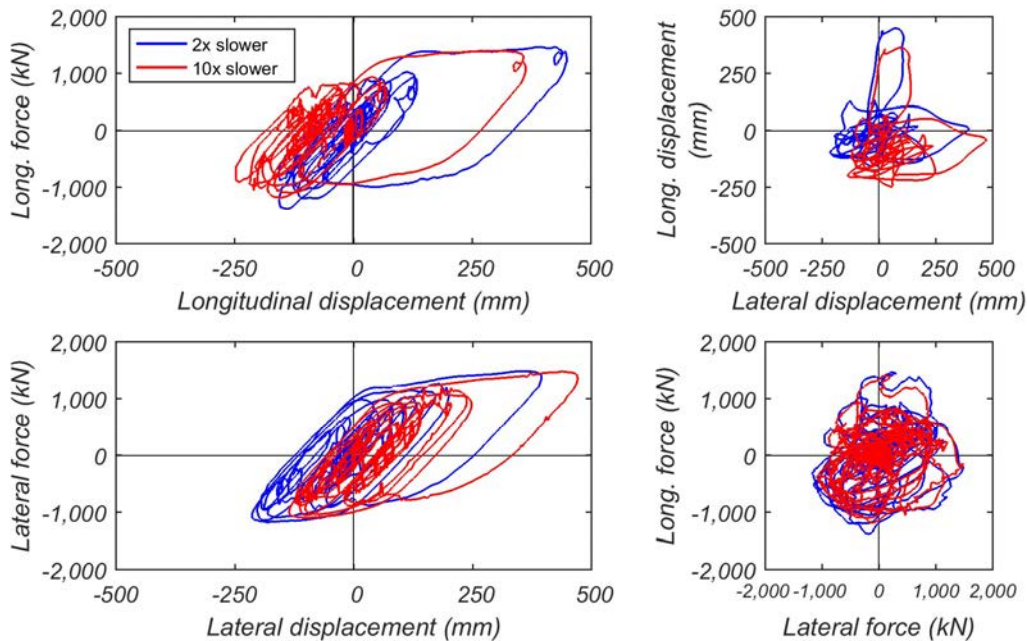


FIG. 160. Comparison of TPFB isolator response for hybrid test executed 2x-slower than real time and hybrid test executed 10x-slower than real time. (Both hybrid simulations were conducted with 2D bidirectional ground motion input using the 1-bearing equivalent model).

From the comparison of longitudinal and lateral shear force-displacement hysteresis loops, displacement offsets in both directions are observed. This was most likely caused by the inner slider not being perfectly re-centred after a previous run. Therefore, it is difficult to assess the maximum isolator displacement demands obtained in the two hybrid simulations. However, the shape of the hysteresis loops can be compared, and it is obvious that the loops are quite similar for the two tests executed at different testing rates. The maximum horizontal shear force for the 2x-slower test is 1561 kN which is larger than the shear force amplitude of 1491 kN in the 10x-slower test. Because the inertial forces and the coefficients of friction in the TPFB all depend on the sliding velocity, it is expected that minor differences exist for the isolator response when hybrid simulations are conducted at different speeds. However, overall the test rate does not have a significant effect on the horizontal hysteretic behaviour of the TPFB. Compared to the EQSB, the coefficients of friction in the TPFB are less velocity dependent.

Floor response spectra are depicted in Figure 161. It can be seen that at higher frequencies the response spectrum amplitudes for all three superstructures are larger for the 2x-slower test in comparison to the 10x-slower test. For example, the peak spectral acceleration amplitudes at the horizontal fundamental frequencies of the RCB, INS, and ACB for the 2x-slower test are 0.89 g, 0.81 g, and 0.64 g, respectively. However, for the hybrid simulation executed at a rate 10x-slower than real time, the peak amplitudes at the same frequencies are only 0.78 g, 0.45 g, and 0.42 g, respectively.

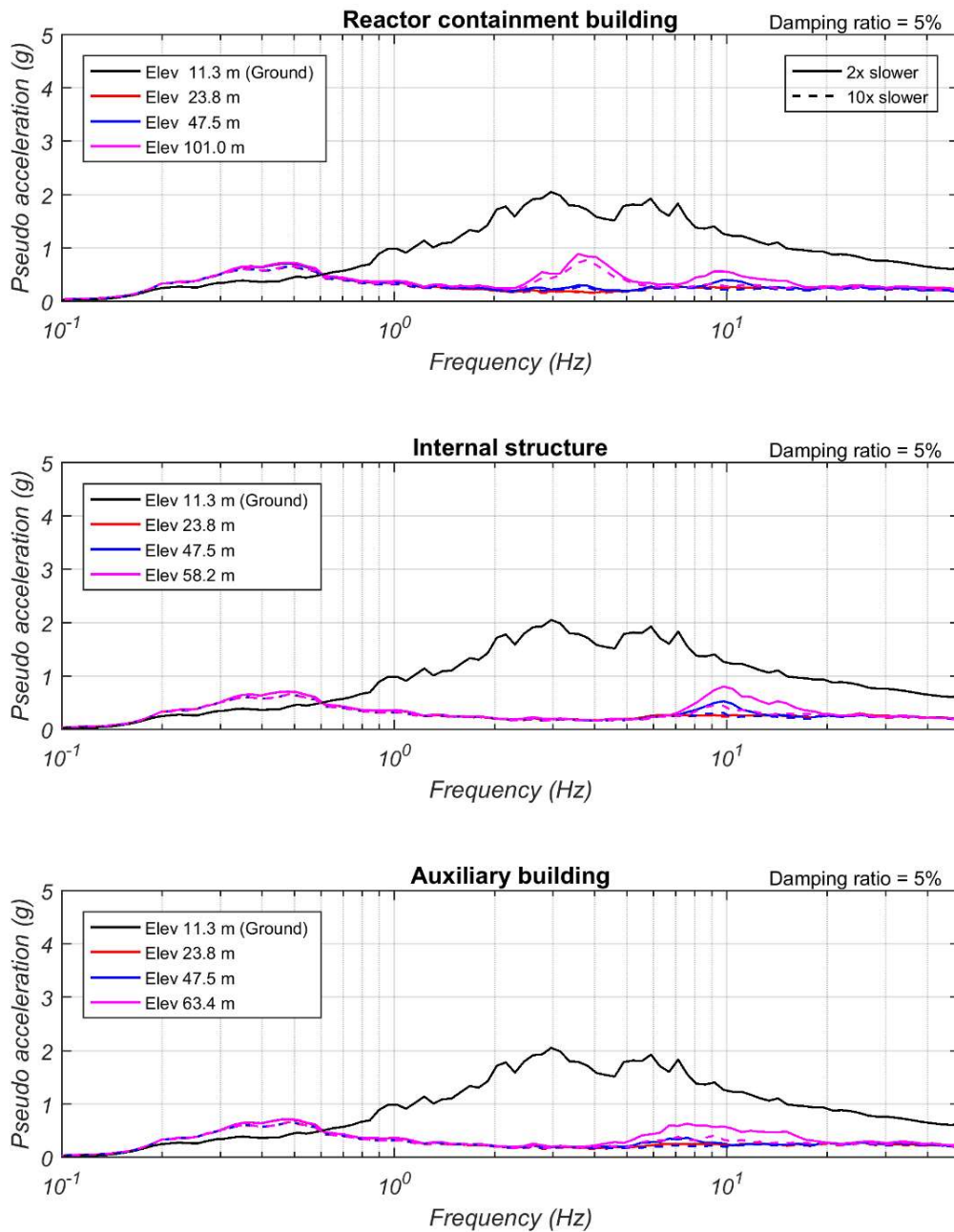


FIG. 161. Comparison of floor response spectra for hybrid test executed 2x-slower than real time and hybrid test executed 10x-slower than real time. (Both hybrid simulations were conducted with 2D bidirectional ground motion input using the TPFB 1-bearing equivalent model).

As discussed for other bearing cases, the larger floor spectra responses in the faster hybrid simulation are mostly caused by the larger dynamic and inertia effects in the test setup and test specimen. However, for the TPFB, this increase of horizontal floor response spectrum amplitudes has also a significant contribution from the increased vertical-horizontal coupling effects at faster testing rates. As explained above, for the TPFB, the horizontal shear force depends on the friction forces in the sliding interfaces, which are directly related to the axial compression force on the bearing during testing. Due to the concave shape of the sliding surfaces, the bearing extends by a significant amount in axial direction as it deforms horizontally. This required that the SRMD platen had to be moved accordingly in vertical direction to maintain a constant axial force on the bearing during the test. For the hybrid simulations at the larger test rate, the platen needs to move faster which reduces accuracy due to tracking performance difficulties in vertical direction at high velocities. Therefore, for the 2x-slower test, more axial force fluctuation in the bearing is expected due to the inability to move the SRMD platen fast enough in vertical direction. Increased axial force fluctuations in the faster tests also mean more horizontal shear

force fluctuation. These horizontal isolators resisting force fluctuations are transmitted into the power plant superstructures which in turn results in larger floor spectra responses. It is important to note that the frequency content of these vertical force oscillations is determined by the horizontal frequencies of the motion and the vertical tuning parameters of the control system. This is in contrast to the 3D ground motion input case where the frequency content of the vertical oscillations is based on the vertical ground motion and vertical superstructure frequencies.

5.7.3.3 Effect of vertical excitation

a. Run 197 vs. 198 (10x-slower, 1-bearing model, DBE excitation level)

In order to investigate effects of including the vertical ground motion input in 3D hybrid simulations, results of hybrid tests with 3-component ground motion input (Run 198) and 2-component input (Run 197) are compared. The 1-bearing equivalent ANT model was used and both hybrid simulations were executed 10x-slower than real time under design basis earthquake (DBE) excitation levels. Isolator responses are shown in Figure 162. Due to the inclusion of vertical excitation in the 3D hybrid simulation, significant isolator restoring force fluctuations can be observed in two horizontal hysteresis loops in comparison to the 2D hybrid simulation. In this case, the frequency of these shear force oscillations is determined by the frequency content of the horizontal and vertical ground motions, the vertical response of the numerical superstructure, and the vertical tuning parameters of the control system. The vertical ground motion input and the horizontal movement on the curved sliding surfaces of the TPFB both contributed to the axial force fluctuations in the bearing during the test. This resulted in significant high frequency horizontal isolator restoring force oscillations as shown for the 3-component ground motion input case in Figure 161.

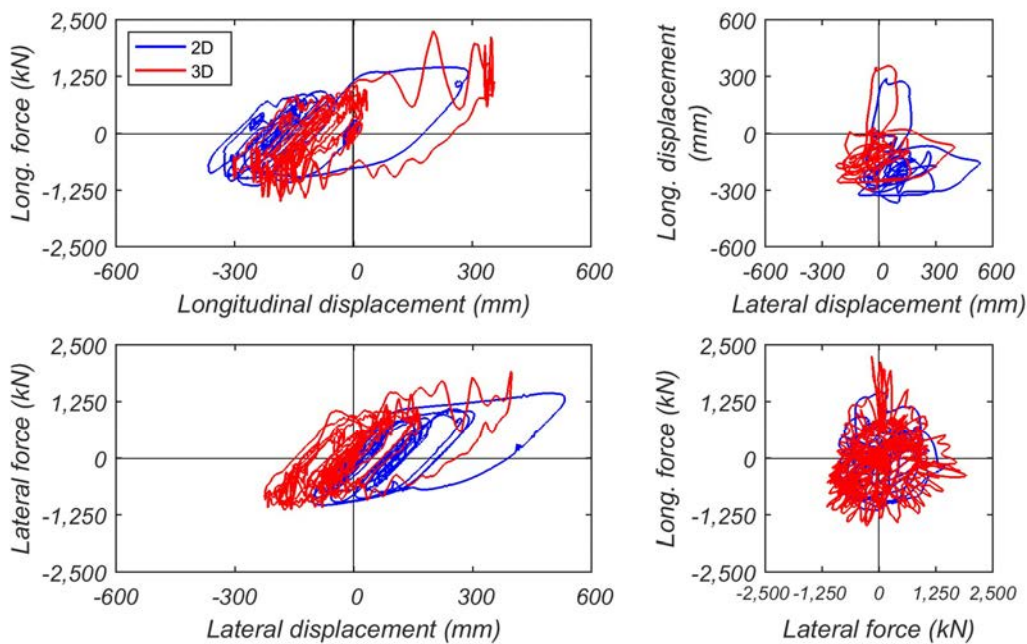


FIG. 162. Comparison of TPFB isolator responses for 2D vs. 3D ground motion inputs. (Both hybrid simulations were executed 10x-slower than real time using the 1-bearing equivalent model under DBE seismic excitation levels).

Floor response spectra are compared in Figure 163. It can be observed that the horizontal floor response spectra for all three buildings have significantly larger spectral acceleration amplitudes if the vertical seismic input is included. Comparing to the case without vertical input, the amplification of horizontal floor response spectrum peaks is as much as 10 times around the fundamental frequencies of the plant superstructure components. The amplification effect is greatest around 10 Hz, which corresponds to the vertical fundamental frequency of the isolated power plant. As discussed above, because of the kinematic and force vertical-horizontal coupling behaviour of the TPFB, the high frequency fluctuations of axial forces induced by the inclusion of the vertical ground motion input resulted in significant

horizontal isolator resisting force fluctuations. These fluctuations predominantly have similar frequency content as the vertical behaviour of the isolated nuclear power plant. Hence, a substantial increase of the horizontal floor response spectra is expected around a frequency of 10 Hz.

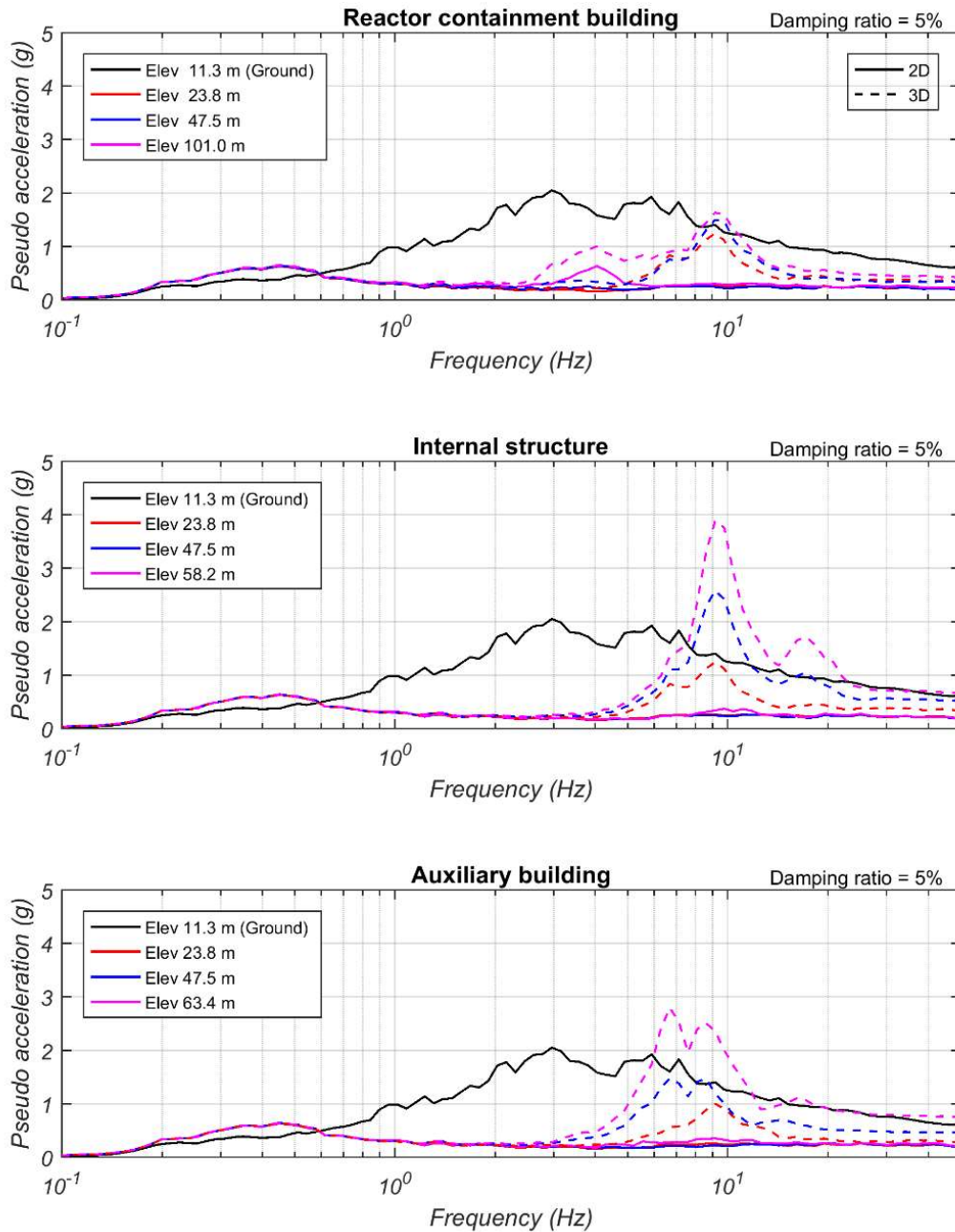


FIG. 163. Comparison of floor response spectra for 2D vs. 3D ground motion inputs. (Both hybrid simulations were executed 10x-slower than real time using the TPFB 1-bearing equivalent model under DBE seismic excitation levels).

b. Run 230 vs. 231 (10x-slower, 1-bearing model, OBE excitation level)

To further investigate the effect of vertical ground motion input on the behaviour of the TPFB and the corresponding in-structure response, an additional comparison between 2D input and 3D input is performed. However, in these two hybrid simulations, the operating basis earthquake (OBE) excitation level was used instead of the DBE excitation level as for all the previously discussed tests. The components of the OBE motion have 2/3 the amplitude of the DBE motion. The two hybrid simulations were again executed 10x-slower than real time using the 1-bearing equivalent model. Isolator responses

are shown in Figure 164. Ignoring the shift of the longitudinal horizontal hysteresis loop, the response of the isolator is similar for the two cases despite the large shear force fluctuations observed in the 3D

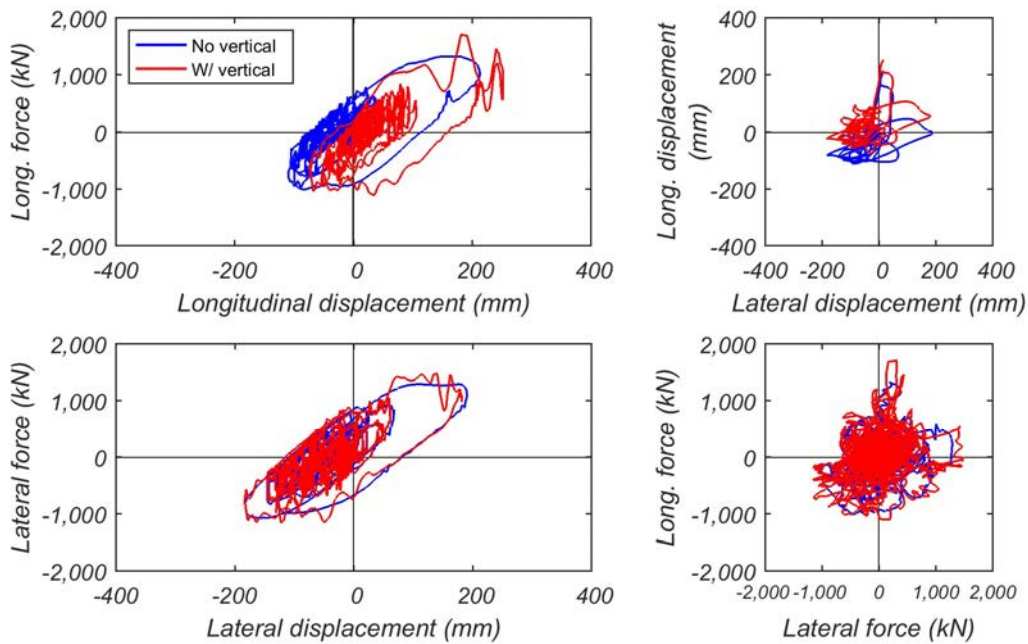


FIG. 164. Comparison of TPFB isolator responses for 2D vs. 3D ground motion inputs. (Both hybrid simulations were executed 10x-slower than real time using the 1-bearing equivalent model under OBE seismic excitation levels).

case, which have been discussed above. Due to the smaller intensity of shaking, the vertical-horizontal coupling effects of the TPFB are a little less pronounced as compared to the DBE shaking intensity; however, they are still clearly visible. Again, the kinematic and force vertical-horizontal coupling behaviour of the TPFB results in larger horizontal floor response spectrum amplitudes, especially in the high frequency range, as illustrated in Figure 165.

5.7.4 Comparison of results for all bearing types

Lastly, hybrid simulation results from the three isolator types (LRB, EQSB, and TPFB) are compared in order to investigate differences in the isolator behaviours and their effect on the in-structure response of the seismically isolated nuclear power plant superstructures.

5.7.4.1 2D tests: LRB (Run 56), EQSB (Run 104), TPFB (Run 217)

Firstly, results from hybrid simulations with 2-component ground motion input are compared for the three different isolator types. The three hybrid simulations were executed at a test rate 2x-slower than real time using the 1-bearing equivalent model excited by the same design basis earthquake (DBE) motions. The isolator responses are compared in Figure 166. Significant differences in the horizontal isolator displacement demands are observed for the three isolation systems. The peak displacement amplitude for the LRB is 254 mm, while for the EQSB, the maximum isolator displacement is 205 mm, which is somewhat smaller than the LRB displacement demand. However, because the design displacement of the EQSB is only 152 mm, nonlinear hardening behaviour of the MER springs in the EQSB is observed. This significantly increased the horizontal shear forces in the bearing. For the TPFB, the peak isolator displacement amplitude is 456 mm, almost twice the displacement demand obtained for the other two bearings. However, as stated before, the design displacement of the TPFB is 584 mm, therefore the displacement demand is only 78% of the displacement capacity and no stiffening behaviour is observed for the TPFB. Nevertheless, it is important to remember that the large displacement demand of the TPFB requires that the umbilical systems, which cross the seismic isolation gap, are designed based on this large possible deformation.

Due to the greatly different displacement amplitudes and horizontal force-deformation behaviours of these three bearings, the horizontal shear force amplitudes are also very different. For the LRB and EQSB, the characteristic strengths are similar (1010 kN vs. 1090 kN). However, as discussed earlier, nonlinear hardening is triggered in the EQSB due to its smaller design displacement, leading to a peak

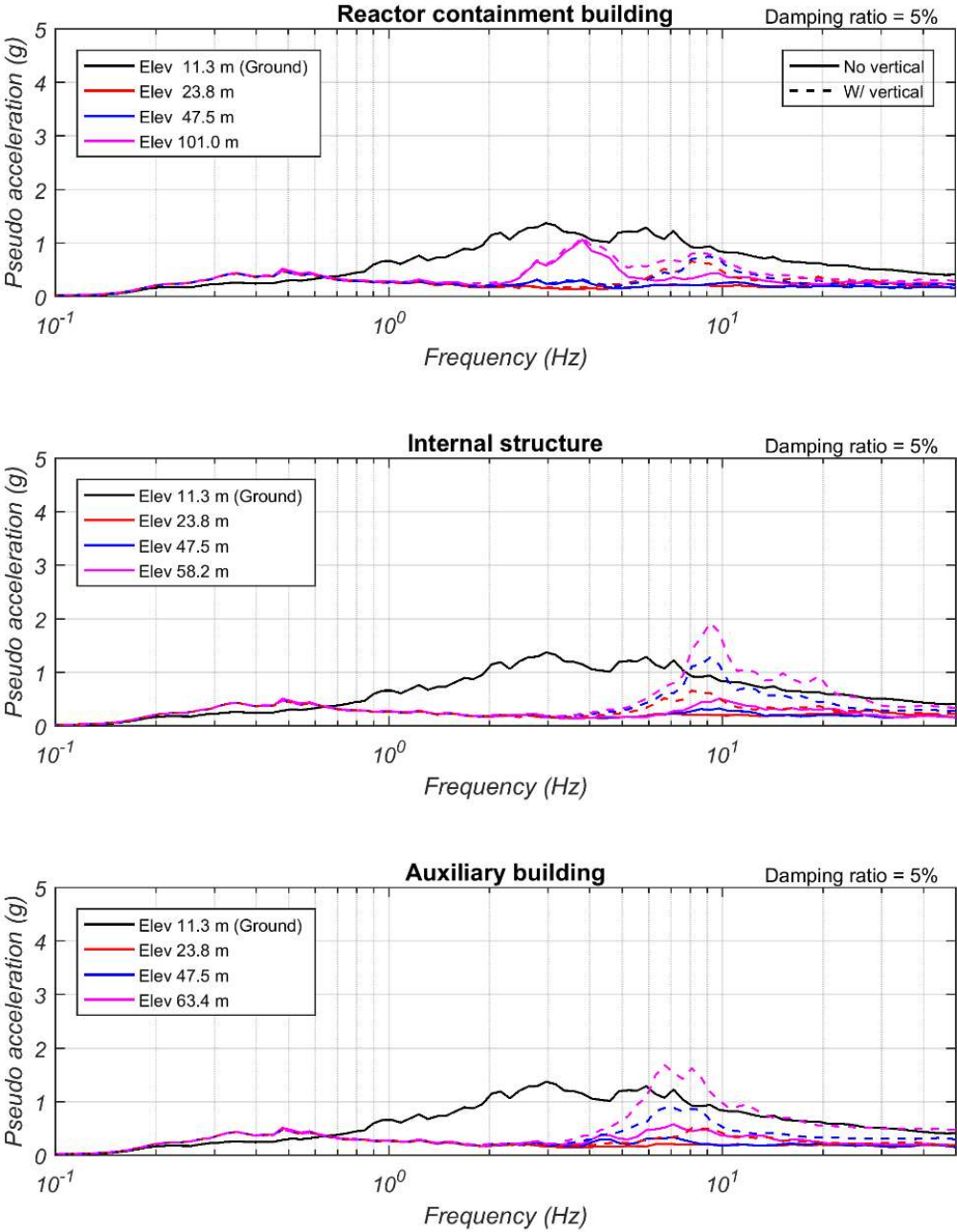


FIG. 165. Comparison of floor response spectra for 2D vs. 3D ground motion inputs. (Both hybrid simulations were executed 10x-slower than real time using the TPFB 1-bearing equivalent model under OBE seismic excitation levels).

horizontal resisting force in the EQSB which is almost twice that of the LRB (4227 kN vs. 2235 kN). For the TPFB, due to its low horizontal sliding stiffness of the main sliding stage, which is significantly smaller than the post-yield stiffness of the other two bearings, the maximum shear force is only 1561 kN. This is the case despite the much greater displacement demand of the TPFB in relation to the other two cases. The significantly smaller shear force amplitude of the TPFB is beneficial for reducing the in-structure response of the upper plant because a smaller force demand is being

transmitted into the superstructure. However, as a trade-off, the large displacement demand needs to be considered in the design of umbilical and other systems that cross the seismic isolation gap.

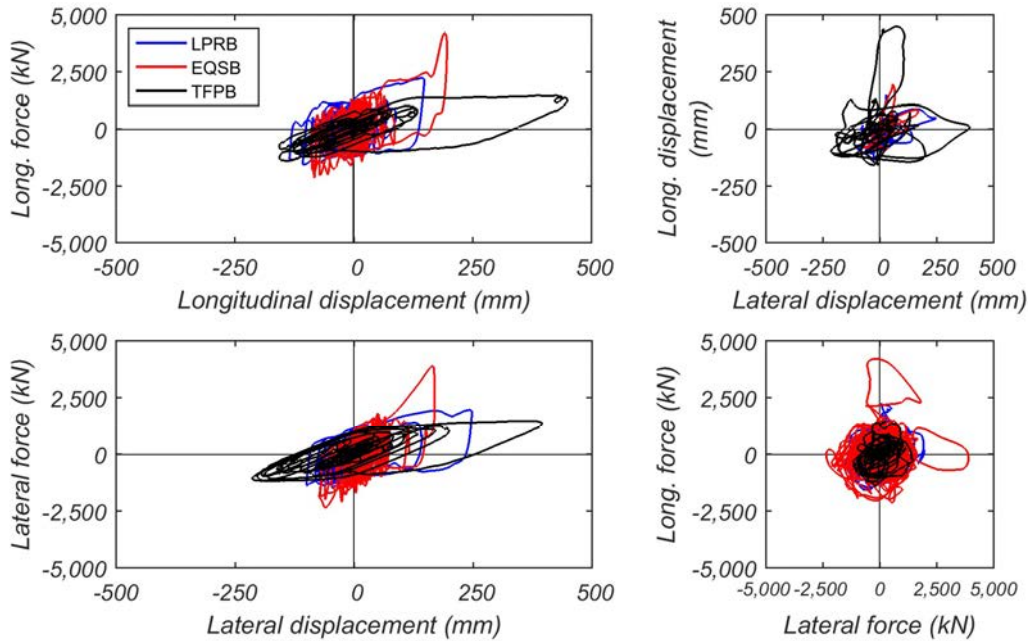


FIG. 166. Comparison of isolator response for three different isolator types. (All hybrid simulations were executed 2x-slower than real time with 2D bidirectional ground motion input using the 1-bearing equivalent model).

Floor spectra are compared in Figure 167. As can be observed, the in-structure responses are also significantly different for the three isolation systems. To provide a reference for the comparison and to better assess the benefits of the isolation systems, the original ground motion spectra and the fixed base spectra without isolators are also plotted. For the RCB, INS, and ACB buildings, above frequencies of 0.6 Hz spectral accelerations from the EQSB are up to two times larger than those from the LRB. Spectral accelerations from the TFPB are even lower than the ones from the LRB for frequencies above 0.6 Hz. The only frequency range where the response spectra of the TFPB are somewhat larger than the ones from the LRB and EQSB is between 0.3 Hz and 0.6 Hz, which corresponds to the post-sliding frequency range of the TFPB. Because most of the equipment in the power plant is sensitive to accelerations with frequencies above 1 Hz (except for possible fluid sloshing effects), the TFPB is the most effective isolation system among the three systems considered to reduce the in-structure response in the power plant superstructures. This in-structure response, assessed in terms of floor response spectra, is consistent with the conclusions drawn based on the isolator responses where it was observed that the TFPB transmits the lowest shear force demands into the superstructure, followed by the LRB and then the EQSB transmitting the largest shear force demands. Finally, it is important to notice that all three bearing types tremendously reduce in-structure responses above frequencies of 0.7 Hz compared to the fixed-base power plant design. Peak floor accelerations are reduced by up to a factor of 3 for the EQSB isolation design and by up to a factor of 6 for the LRB and TFPB designs. Only at very low frequencies, which correspond to the effective periods of the isolators, the spectral acceleration amplitudes of the seismically isolated plants are slightly larger than the ones of the fixed base plant.

5.7.4.2 3D tests: LRB (Run 57), EQSB (Run 121), TFPB (Run 198)

To further assess the effectiveness of the different isolation systems, an additional comparison between the LRB, EQSB, and TFPB systems is performed. However, for this comparison the hybrid models were subjected to 3-component ground motion input at the DBE level. The three hybrid simulations were executed at a test rate 10x-slower than real time using the 1-bearing equivalent model. Firstly, the isolator responses are compared in Figure 168. Similar to the 2-component ground motion input case discussed above, the horizontal behaviour of the isolation systems is significantly different for the three bearing types. The TFPB generated a displacement demand (405 mm) that is almost twice as large as

the LRB demand (254 mm) and the EQSB demand (211 mm). In comparison to the previously discussed 2D input case, much larger shear force fluctuations can be observed, especially for the EQSB and the TFPB. For the LRB the shear force fluctuations are somewhat less pronounced.

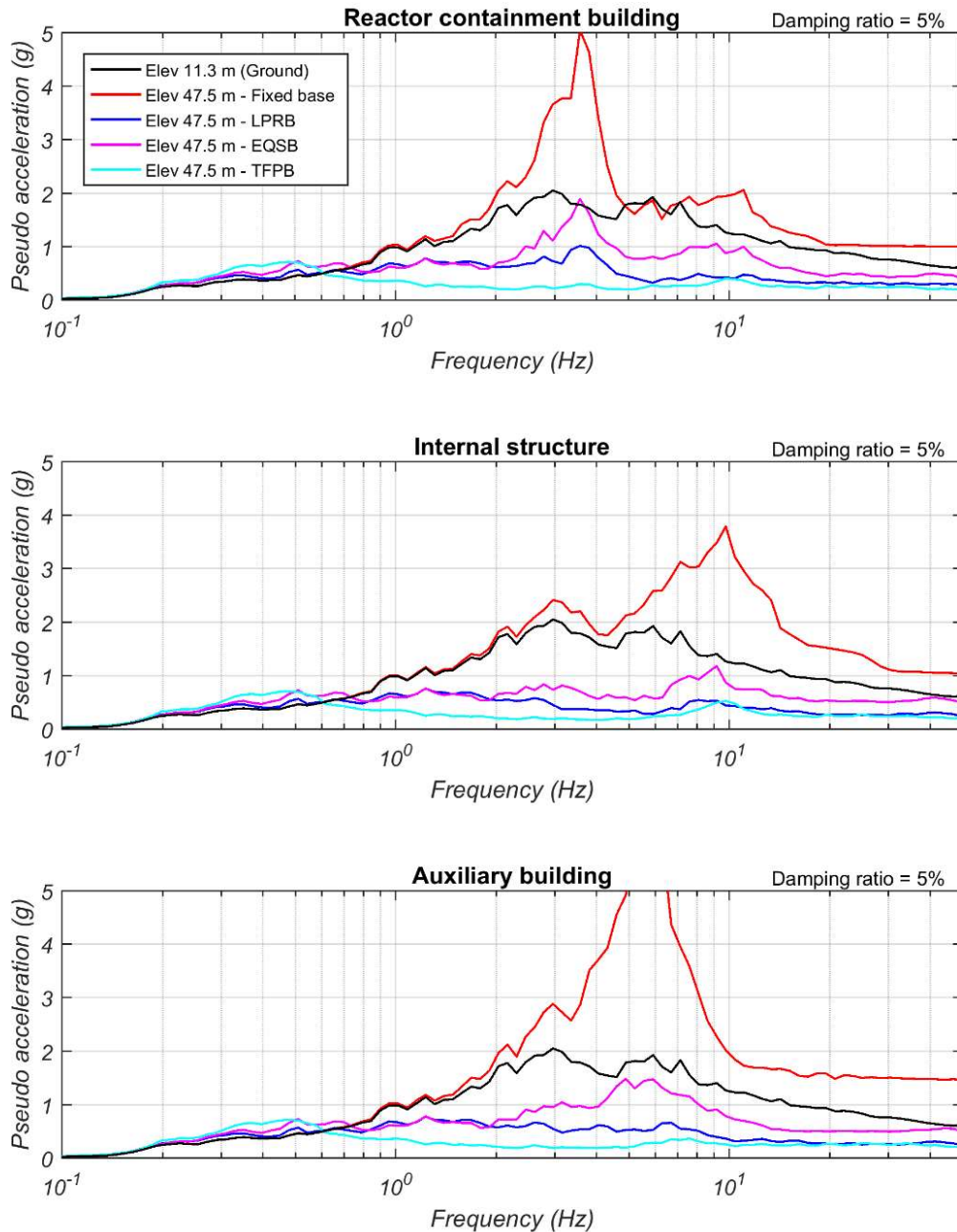


FIG. 167. Comparison of floor response spectra for three different isolator types. (All hybrid simulations were executed 2x-slower than real time with 2D bidirectional ground motion input using the 1-bearing equivalent model).

These shear force oscillations are mainly due to the vertical-horizontal force coupling of the TFPB and EQSB where the sliding friction force directly depends on the instantaneous axial force in the bearing. For the TFPB there is additional vertical-horizontal kinematic coupling due to the curved sliding surface. Hence, the frequency of the oscillations in the shear forces is related to the frequency content of the axial force fluctuations. Part of this depends on the frequency content of the horizontal and vertical ground motion components, but part of it also depends on the vertical frequency of the seismically isolated plant and the vertical tuning parameters of the SRMD control system. For the LRB, shear force fluctuations are also observed, but they are much less pronounced in comparison to the other two

isolation systems because the LRB only exhibits vertical-horizontal kinematic coupling effects. In addition, due to the poor vertical force tracking performance of the SRMD, the EQSB and TFPB behaviour is also greatly affected because of the pronounced vertical-horizontal coupling effects.

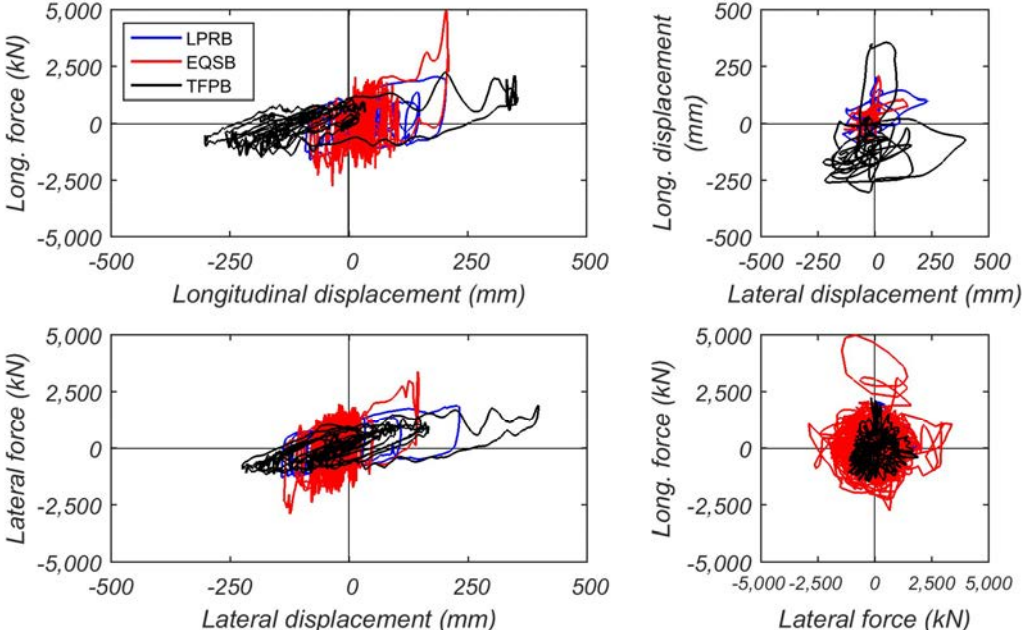


FIG. 168. Comparison of isolator response for three different isolator types. (All hybrid simulations were executed 10x-slower than real time with 3D ground motion input using the 1-bearing equivalent model).

The maximum horizontal resisting force also varies a lot for the three isolator types. For the LRB, the maximum shear force is only 2058 kN, while for the EQSB it is 5065 kN. The TFPB has a peak shear force amplitude of 2267 kN. Because the displacement demand of the EQSB was well beyond the design displacement of the bearing, nonlinear hardening behaviour of the MER springs was observed. This is the main cause for the very larger shear force demands produced by the EQSB. Because of the shear force fluctuation effects, the largest isolator force is greatly affected by the oscillation amplitudes. Unlike the 2-component ground motion input case discussed above, the TFPB isolator shear force amplitude is similar to the LRB in the 3-component input case. The main reason is that the significant shear force fluctuations due to vertical ground motion input result in spikes, which in turn increase the maximum value of shear. Therefore, the effectiveness of the TFPB system to reduce the in-structure response in the power plant superstructure is substantially affected when 3D excitations are considered.

Superstructure floor response spectra are compared in Figure 169. Similar to the results obtained for the 2-component ground motion input, for most of the frequency range above 0.6 Hz, the TFPB provides the greatest reduction of spectral acceleration amplitudes. The EQSB provides the smallest reduction in relation to the fixed base power plant. However, all three isolation systems deliver significant benefits in comparison to the fixed base case. Because of the strong vertical-horizontal coupling behaviour of the sliding bearings, when vertical ground motion input is included, the shear force oscillations in the EQSB and TFPB result in a significant increase of the spectral accelerations around 9-10 Hz. From the results shown in Figure 169, all three cases have a larger spectral response in the 9-10 Hz frequency range when vertical ground motion input is considered in comparison to the 2D input case discussed earlier. The amplification effect for the EQSB and TFPB systems is more pronounced than for the LRB system. As discussed, the vertical-horizontal coupling for these two sliding bearings is mainly a force coupling, while the vertical-horizontal coupling effect of the LRB is mainly a kinematic or second order effect, which is less pronounced than the friction effect in sliding bearings.

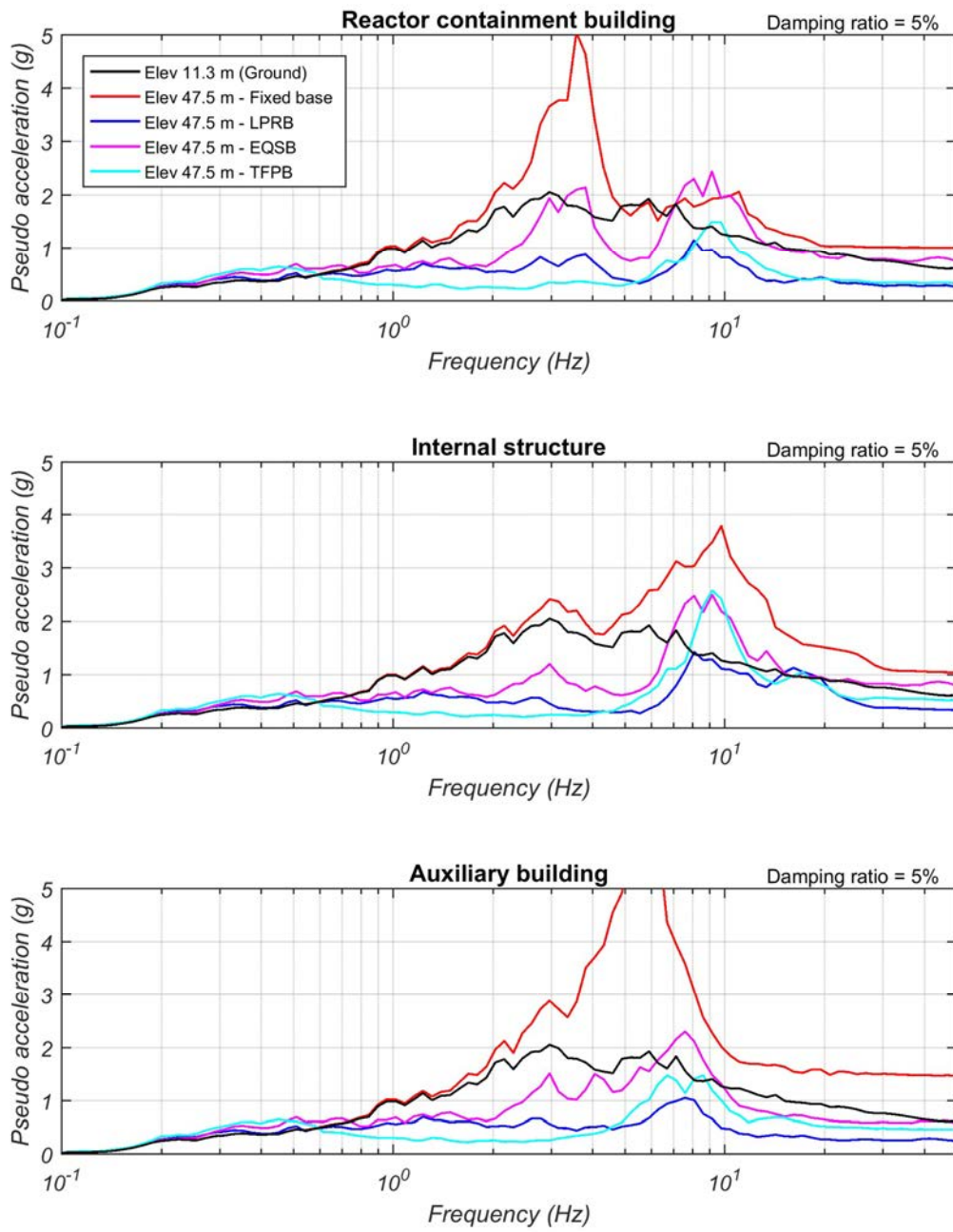


FIG. 169. Comparison of floor response spectra for three different isolator types. (All hybrid simulations were executed 10x-slower than real time with 3D ground motion input using the 1-bearing equivalent model).

5.8 REMARKS AND CONCLUSIONS

Conclusions and suggestions related to real-time hybrid simulation as a viable testing method for determining the mechanical influence of seismic isolators in nuclear power plants are reported. Observations and conclusions related to the assessed behaviour of the tested isolation systems and the numerically modelled plant superstructure follow in Section 6 and Section 7.

With regards to the real-time hybrid simulation testing method which was employed to experimentally test isolators in NPPs the following conclusions can be drawn:

- This research program confirmed that rapid and real-time (with limitations as summarized below) hybrid simulation is indeed a viable testing method to experimentally assess the behavior of large isolators at full-scale [33].
- The SRMD bearing test machine was successfully converted to perform rapid and real-time hybrid simulation tests for large hybrid models [33].
- A SCRAMNet+ network providing fast digital communication between different hardware components of the hybrid testing system was successfully implemented in an effort to enable real-time hybrid tests at the SRMD testing facility.
- Bearing forces could be successfully measured by indirect forces from actuator load cells. This new measuring technique requires a new model compensating inertia and friction force correction.
- During the experimental test program, the tracking performance (in terms of delays) was significantly improved by employing the Adaptive Time Series delay compensation on the xPC Target DSP and using feedforward-control in the SRMD control system. Employing these advanced delay compensation techniques enabled real-time hybrid testing for 1D and 2D excitations (controlling one or two horizontal displacement degrees of freedom).
- It was determined that it is currently not possible to conduct 3D real-time hybrid simulations with the SRMD due to insufficient vertical tracking performance. To achieve acceptable performance and accuracy in the force controlled vertical DOF a hybrid simulation needs to be performed at a minimum 10x-slower than real time.
- It was also determined that the SRMD has more difficulties in maintaining constant axial loads in 1D and 2D hybrid simulations for test specimens that change their height as they deform sideways in shear. This is again caused by the insufficient vertical tracking performance.
- High-performance computing algorithm can be also applied to real-time hybrid simulation testing based upon the large DOFs' structures.
- It was found, except for the EQSB, that rapid hybrid simulations (2x-slower than real time) are sufficient to accurately capture the response of the isolators and the in-structure response of the seismically isolated superstructure. Experimental errors due to insufficient tracking performance were significantly smaller for the rapid hybrid simulations than for the real-time hybrid simulations. Consequently, hybrid simulations executed at a test rate 2x-slower than real-time are the best representation of the overall response of the seismically isolated nuclear power plant.
- One equivalent bearing model represents the overall behaviors of all the bearing model, but also shows the limitation to simulate rocking of superstructure.
- Axial force fluctuations in the test bearing due to overturning can be simulated using five-equivalent bearing model, but some discrepancies of the simulated responses compared to the tests model should be lessened through developing more refined analytical bearing elements for other four bearing groups.
- The maximum speed of hybrid simulation tests using full bearing model plus high-performance computing platform was a 15x-slower than real time execution and can be improved by adding more parallel processing machines.

- It was realized that tracking errors to capture the motions of especially near-real-time hybrid simulations of seismic isolation systems can be minimized through improved control of horizontal and vertical directions.

6 COMPARISON BETWEEN HYBRID TESTS AND BENCHMARK RESULTS

6.1 COMPARISON FOR LRB ISOLATORS

6.1.1 Available data and selection of representative results

As presented in Table 16 (Section 4.2.1), hybrid tests were performed for the benchmark cases 1, 3 and 5, all corresponding to a RG 1.60 spectra excitation at DBE level (0.5 g peak ground acceleration). For each of these cases, two subcases are defined corresponding to:

- Excitation in real time but in the two horizontal directions only.
- Excitation in slowed time in the three directions simultaneously.

As identified in Section 5, the results obtained for Case 3 are close to those of Case 5. In both cases the effect of the tested isolator is overshadowed by the effect of the simulated isolators. Both of these tests are closer to pure simulation results. Therefore, and for clarity purpose, the following comparisons between hybrid tests and benchmark results on LRB isolation system will focus on Case 1 and they will refer to other cases only when relevant.

In the text and figures of the present Section, the different hybrid test results will be designated by concatenating the case number and the subcase number: “Test 1_1” corresponds to the benchmark Case 1 with two horizontal excitations only in real time and “Test 1_2” corresponds to the benchmark Case 1 with three directional excitations but with slow execution time.

6.1.2 Comparison of displacement time histories

Comparison of displacement time histories between hybrid simulation tests and benchmark numerical results are given in Figure 170.

In both horizontal directions, there is an excellent fit between all benchmark results and the hybrid simulation tests in terms of detecting the onset and end of lead yielding phases. The displacement time history shapes are always similar. This conclusion is equally valid for other cases not illustrated here.

The horizontal displacement test results are about 25% lower than those of the group of participants who predicted the highest displacements (P1, P2, P5, P6 and P7, see Section 4). For other cases, not analysed in detail here, the test results always lie below those obtained by this group of participants and are always higher than those of the second group (P3, P4, P8).

It can then be concluded that the group who predicted the higher displacements is generally conservative, in the sense that there is more energy dissipation in reality than in their uncalibrated isolator models. In Case 1, this conservatism is relatively small. It increases for cases where more isolators were simulated in the hybrid tests, pointing at the fact that the simulated isolators might be more dissipative.

On the other side, the group who predicted the lower displacements is non-conservative in all cases, meaning that their models dissipate more energy than what was observed during the tests.

Only a limited influence of the vertical excitation or of the test speed is observed on the test horizontal displacements obtained in Case 1. For other cases, there is absolutely no influence. It can then be inferred that the hybrid simulation horizontal displacement results are mostly unaffected by the tests conditions and do then constitute a reliable comparison basis for the benchmark numerical results.

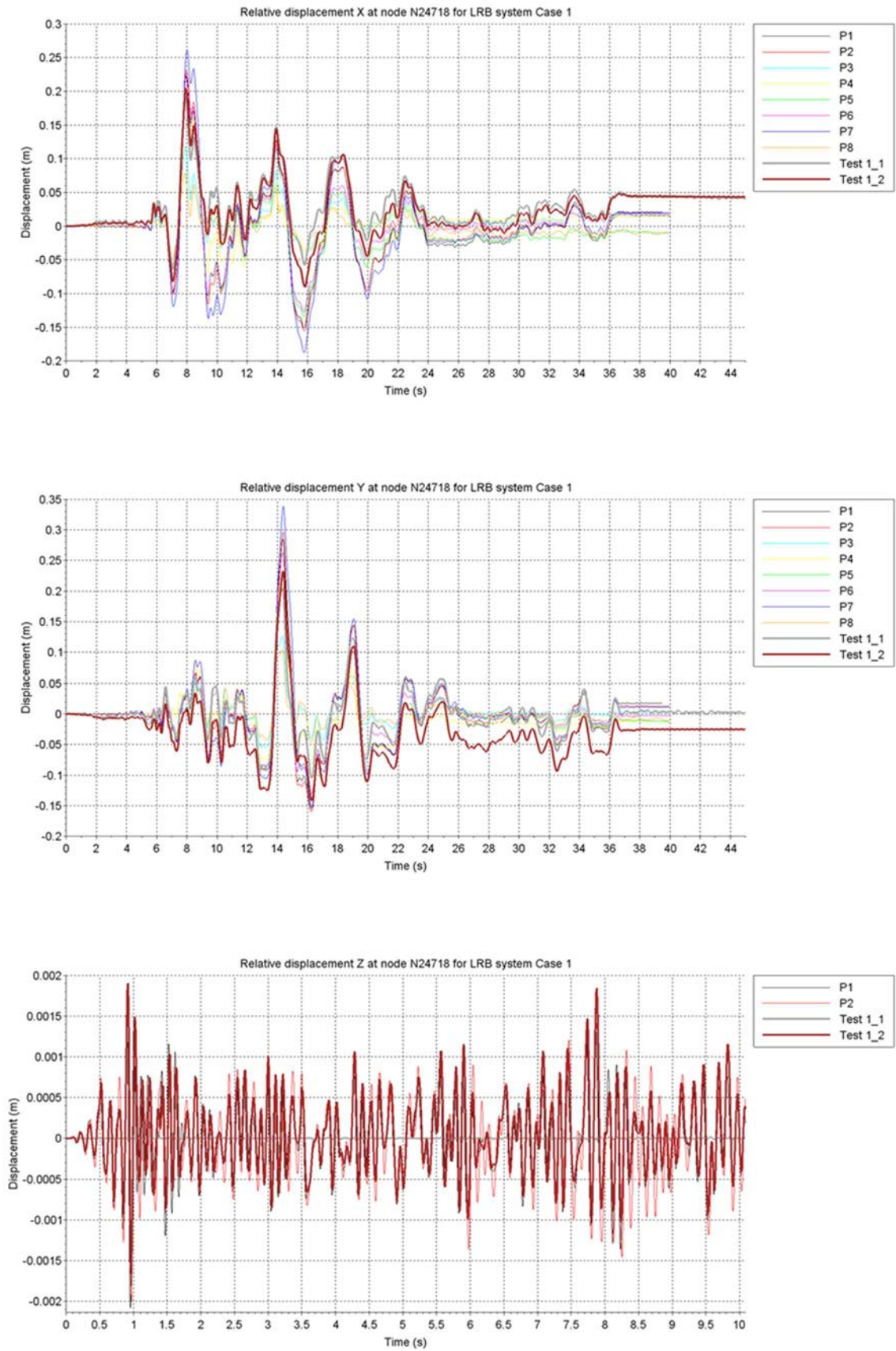


FIG. 170. LRB system - Comparison hybrid tests and benchmark results for Case 1 –Relative displacement at centre of upper basemat.

In the vertical direction, the comparison of test results is made only against those of participants P1 and P2. As explained in Section 4.1.2, participants P1 and P2 were the only ones to update the vertical stiffness of their isolator models, and, given the order of magnitude of the change it represents, it would not have made sense to compare results of other participants to tests results.

Participants P1 and P2 vertical displacements are similar to those obtained in hybrid testing, both in frequency and amplitude. It could then be said that participants P1 and P2 models give good representations of the actual bearing in this case.

6.1.3 Comparison of floor response spectra at centre of upper basemat

Comparison of floor response spectra at upper basemat central node between hybrid simulation tests and benchmark numerical results are given in Figure 171 for Case 1. In the horizontal directions:

- The test response spectra lie almost fully in the range of the benchmark participants response spectra. Its overall shape is also very similar. Since the results of Case 1 at the basemat level is the closest to a pure experiment, this can be considered as an excellent outcome.
- Below 0.5 Hz, the test results are enveloped by those of the first group of participants (P1, P2, P5, P6 and P7) while remaining above those of the second group of participants (P3, P4 and P8). In the frequency range from 0.5 and 2 Hz, the results of the second group of participants appear to be conservative, whereas results of the first group of participants are now below experimental results.
- At higher frequencies, where the structural responses are predominant, the hybrid tests results present a high peak, similar to the one of participant P2 in the X direction and even higher in the Y direction.
- The test results zero period acceleration is of the same order of magnitude as the highest ones predicted by participants and is located between 0.25 and 0.3 g.
- Finally, the differences between results of tests 1_1 and 1_2 are significant and of an order of magnitude similar to the differences between tests and benchmark participants results (up to 50% on the peak at 8 Hz in the X direction). This highlights the fact that uncertainties exist not only on the numerical model but also in the experimental procedure and that these uncertainties have to be acknowledged when designing a seismic isolation system.

For other cases (Case 3 and Case 5), in the horizontal directions, the test results tend to get closer to those of the second group of participants in the 0.5 to 2 Hz frequency range while exhibiting the same features as those described for the Case 1 elsewhere. It is then supposed that the damping attributed to the simulated isolators in the hybrid simulation lies closer to the one of the second group. As the influence of the only tested isolator tend to be overshadowed by the numerical ones in these other cases, there is almost no difference between floor response spectra obtained with the two different experimental approaches.

In the vertical direction, the test results are very close to the ones of participants P1 and P2 on the complete frequency range up to 15 Hz, where some phenomena seem to occur in experiment and produce a new peak and an increase zero period acceleration. This test spectra shape after 15 Hz share some similarities with the spectral shapes obtained by participants P1 and P2 with higher excitations (Case 2 and Case 6) and attributed to rubber cavitation in Section 4. Since cavitation limit is not expected to be reached in this case, it is possible that other local nonlinear effects occur in the bearing.

6.1.4 Comparison of floor response spectra at top of buildings

Comparison of floor response spectra at the top of the buildings for Case 1 are given in Figure 172, Figure 173 and Figure 174, respectively for internal structure building, containment building and auxiliary complex building.

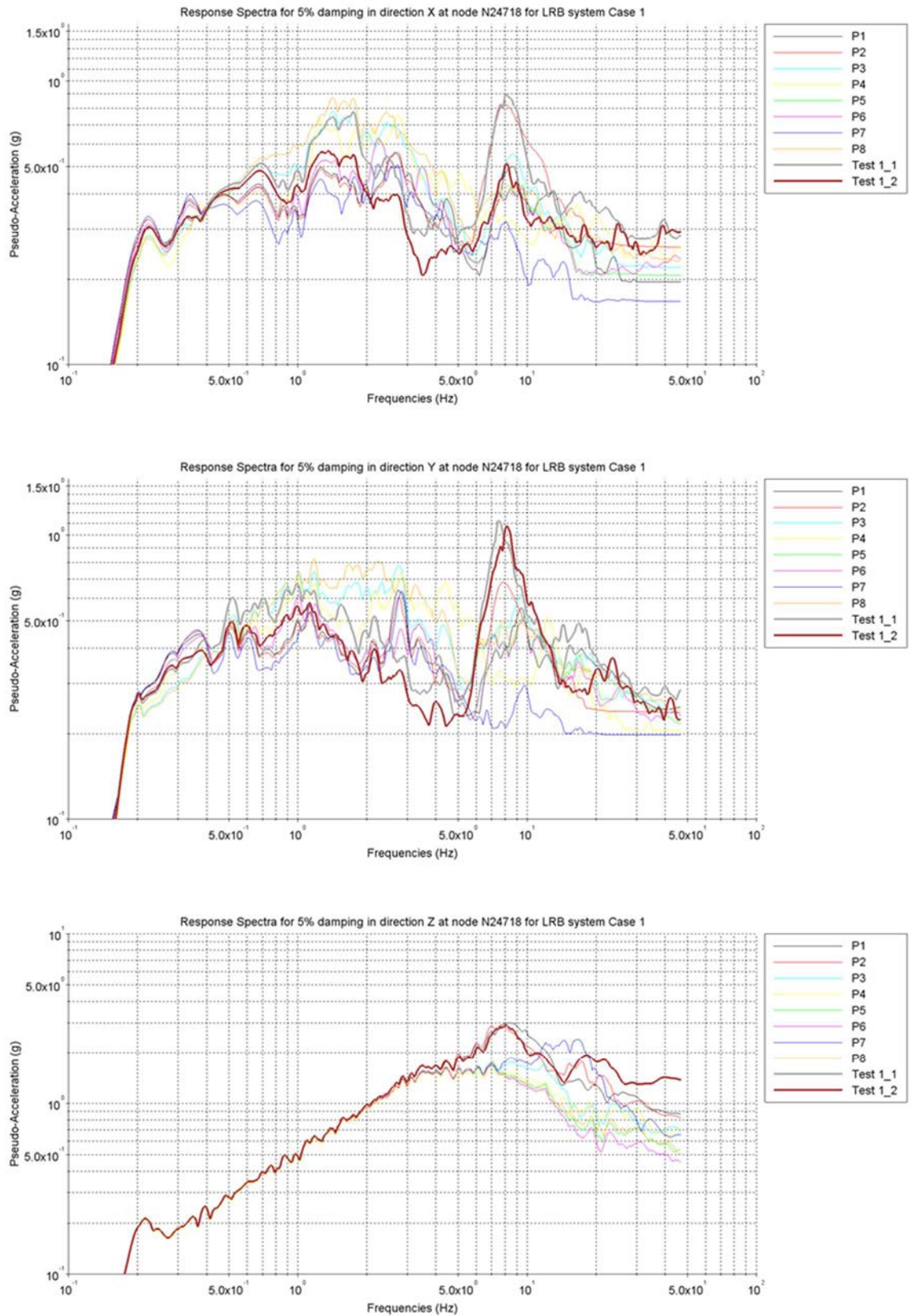


FIG. 171. LRB system – Comparison hybrid tests and benchmark results for Case 1 –Floor response spectra at center of upper basemat.

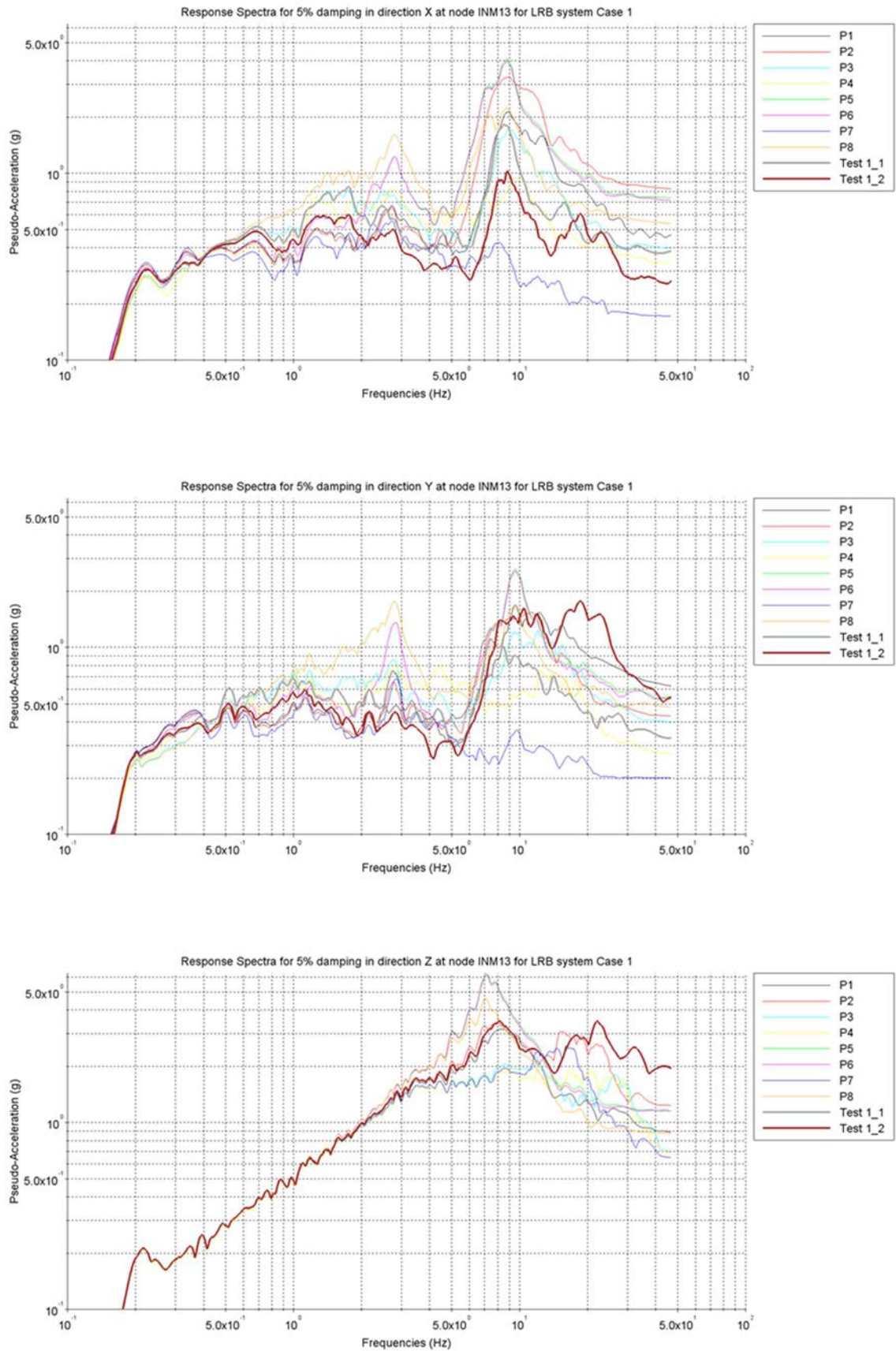


FIG. 172. LRB system – Comparison hybrid tests and benchmark results for Case 1 –Floor response spectra at top of internal structures.

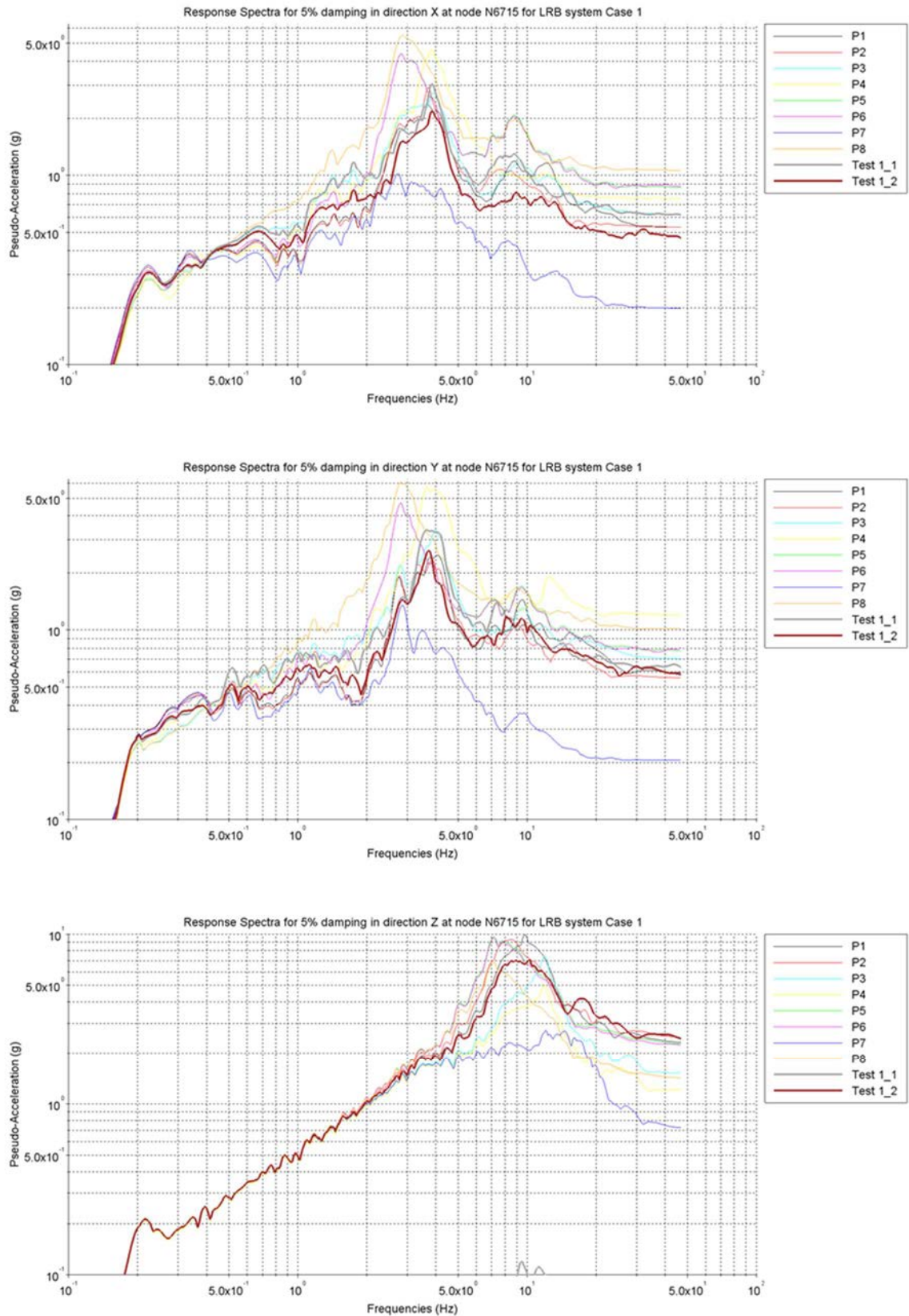


FIG. 173. LRB system – Comparison hybrid tests and benchmark results for Case 1 –Floor response spectra at top of containment building.

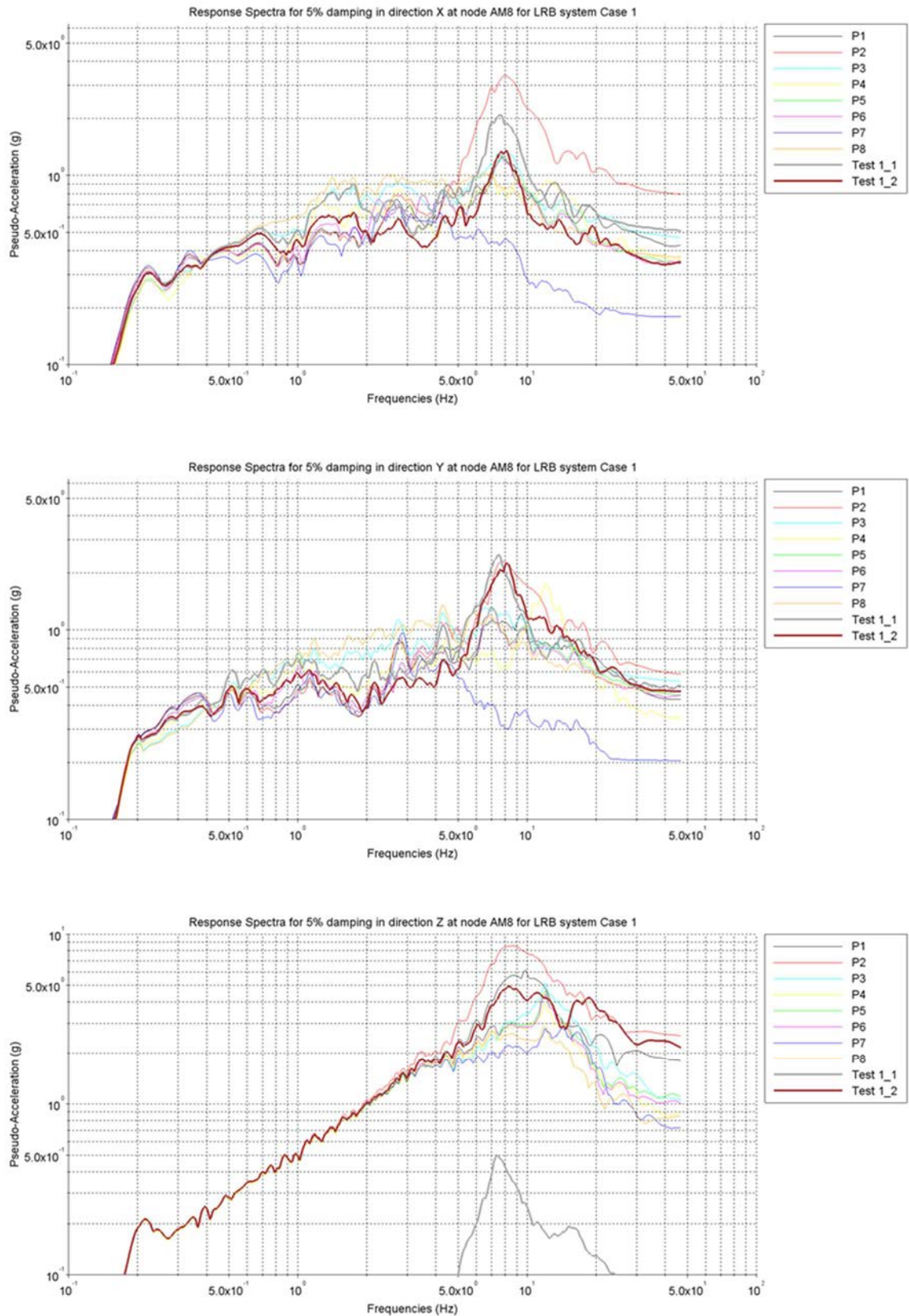


FIG. 174. LRB system – Comparison hybrid tests and benchmark results for Case 1 –Floor response spectra at top of auxiliary complex building.

In both horizontal directions and for all buildings, the test response spectra seem in good agreement with the average of the floor response spectra produced by the different participants. More specifically:

- In the frequency range from 0.5 to 5 Hz, and with exception of the containment building, the tests results lie in between those of the different participants.
- For the containment building, which structural response is located within the above-mentioned frequency range, most of the participants results are in complete agreement with the test response spectra. Results of participants with a not fully rigid basemat modelling, as identified in paragraph 4.2.2.3, are logically different. Results of participant P7, which never exhibit any structural response, is significantly below. It is expected that if all participants had a similar basemat modelling and no overdamping of structural modes, all results would be in good agreement with the test results at containment building top.
- After 5 Hz, for the reactor internal structure building as well as for the auxiliary complex building, the test results exhibit sharp peaks that are comparable to those obtained by most participants. Significant amplitude differences are sometimes observed but the variability of tests results themselves is high in this frequency range, with differences sometimes reaching a factor 2 between the two test results.
- The zero-period acceleration from test results always lie in the range of the benchmark participants results.

In the vertical direction:

- At top of the internal structure building, the test result is very close to the one predicted by participants P1 and P2 until approximately 15 Hz. After this frequency, the test spectrum globally follows the one predicted by participant P2 but with a second peak at a higher frequency.
- At top of containment building, the test results peak lies about 20% below the peaks predicted by both participants P1 and P2. Before and after this peak, participants P1 and P2 prediction perfectly follow the test spectra.
- At top of auxiliary complex building, the test results peak is close to participant P1 results peak and significantly below the one predicted by participant P2. After the peak, all three models converge to approximately the same zero period acceleration.

No comparison is made with results from other participants, who did not update their vertical stiffness, since the structural response is too heavily affected by this hypothesis.

6.1.5 Comparison of hysteresis loops

Force-strain curves corresponding to Case 1 in the X and Y directions are given in Figure 175. On this figure, all participants results are plotted as background to Test 1_1 and Test 1_2 results.

In the horizontal directions and for both tests results, there seem to be higher forces developing in the isolator during the main yielding phases than predicted by the participants, with the exception of participant P8. Still, the global apparent secondary stiffness observed in test results seems to be similar to the one used by participants. Moreover, the forces observed for the test in real time (Test 1_1) are noticeably larger than the ones obtained in slow time (Test 1_2), underlining that the increase in force values compared to the ideal bilinear behaviour is velocity dependant.

The larger forces measured on the actual isolator is associated to one or a combination of the following cause:

- Change in yield value of the lead with the loading velocity.
- Rubber scragging effect, making the isolator apparently stiffer during the first significant loading cycle.
- Other energy dissipation mechanisms acting in parallel with the lead yielding and producing additional resisting forces for a same displacement.

Typically, addition of an equivalent viscous damping to the isolator numerical models in the horizontal direction would produce such change of hysteresis loops as the one observed in Figure 175. Furthermore, the force increase dependency to the distortion velocity, would typically be reproduced with an additional equivalent viscous damping in the model.

Actually, such additional equivalent viscous damping forces might have been included by some participants in their model but, except for participant P8, they did not report their value in the isolator horizontal force values.

As it was predicted by participants P1 and P2 models, the test results show no significant lead heating effect in Case 1. No rubber hardening effect is visible either for the relatively small distortions obtained here.

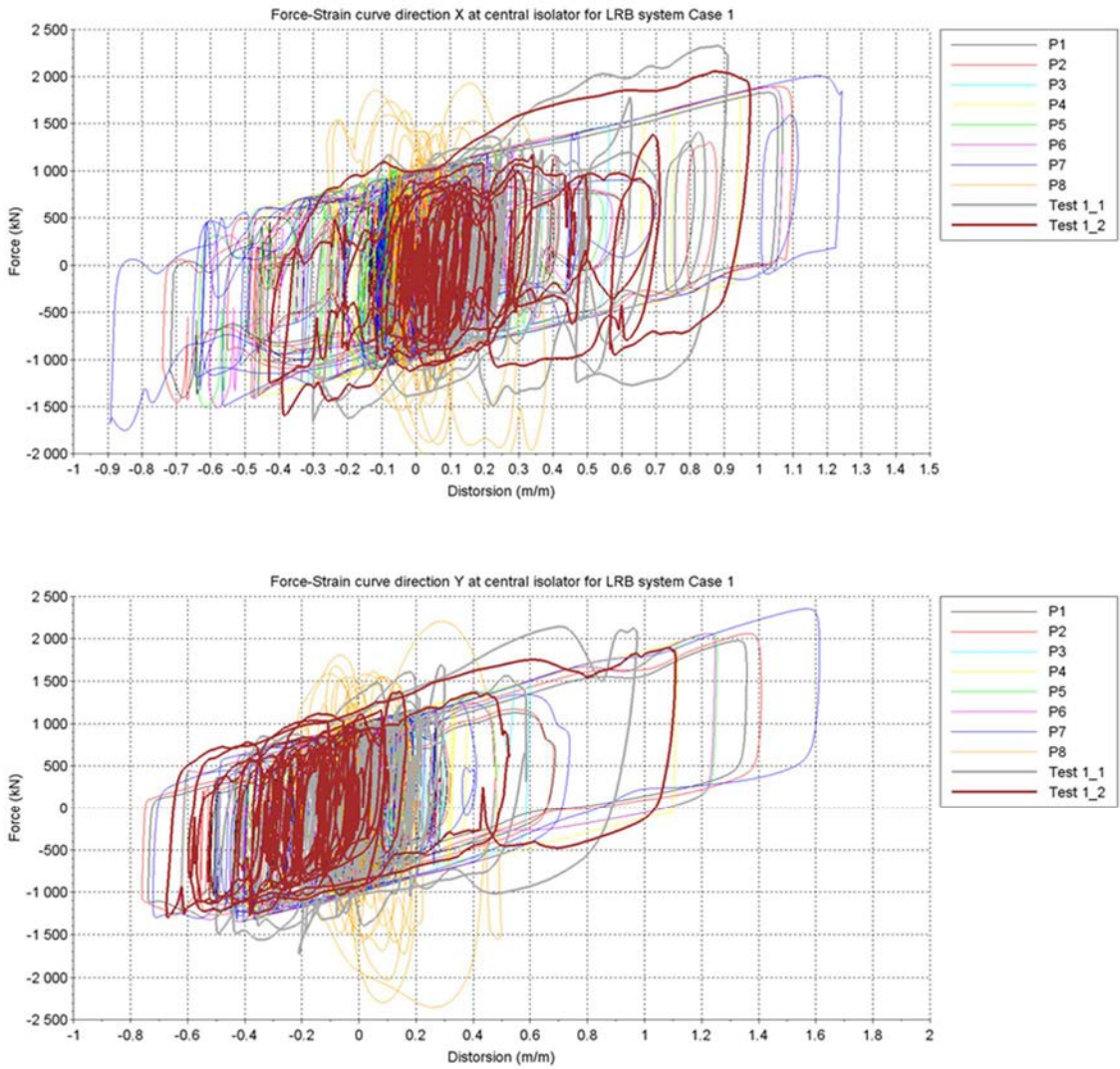


FIG. 175. LRB system – Comparison hybrid tests and benchmark results for Case 1 –Horizontal hysteresis curves.

Force-displacement curves for the vertical direction are given in Figure 176. In this direction, the test results give an initial isolator compression about 1.5 mm, higher than the one predicted by participants P1 and P2. This is explained by the gap filling during the initial LRB compression process on the test rig (see Section 5). Another noticeable difference is the curvature of the experimental curve, with an

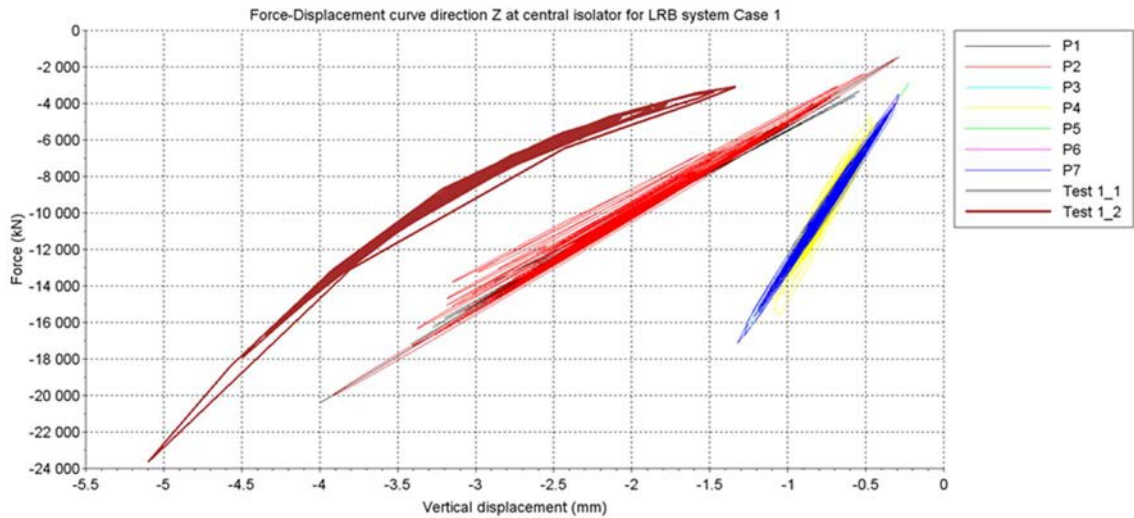


FIG. 176. LRB system – Comparison hybrid tests and benchmark results for Case 1 – Vertical force-displacement curves.

increasing bearing stiffness with increasing vertical load. None of the participants did reproduce such behaviour in their models. These differences seem to affect neither the seismic displacements nor the response spectra within the superstructure

The vertical excitation level in this case was too low to generate rubber cavitation phenomena or to induce significant reduction of vertical stiffness due to horizontal distortion.

6.2 COMPARISON FOR EQSB ISOLATORS

6.2.1 Available data and selection of representative results

As presented in Table 17 (Section 4.3.1), hybrid tests were performed for the benchmark cases 1 and 3 only, corresponding to RG 1.60 spectra excitation at DBE level (0.5 g peak ground acceleration) with, respectively, one and five macro-isolators. For each of these cases, two subcases are defined corresponding to:

- Excitation in real time but in the two horizontal directions only.
- Excitation in slowed time in the three directions simultaneously.

As for the LRB system in the previous section, and for the same reasons, the comparison will focus on the two tests representative of the Case 1 and noted Test 1_1 (two directions real time) and Test 1_2 (three directions slowed time).

In the vertical direction, and due to practical testing reasons, the excitation applied during the hybrid tests on the EQSB isolator was lower than the one specified for the numerical benchmark (see Section 5). This change can potentially affect both the vertical and the horizontal behaviour, because of the dependency of friction forces on the vertical loads. This fact is acknowledged when comparing simulation to tests results.

6.2.2 Comparison of displacement time histories

Comparisons of the experimental and numerical displacement time histories at the central node of the upper basemat are given in Figure 177 for the three directions X, Y and Z and for Case 1.

In both horizontal directions, and as it was observed for the LRB system, the main sliding phases occur at the same time in the simulation and in the experiments. On the other hand, and unlike what was

observed with LRB, some small sliding phases occurring at the beginning and at the end on the experiment seem not to be reproduced by any of the participants simulation. This phenomenon is

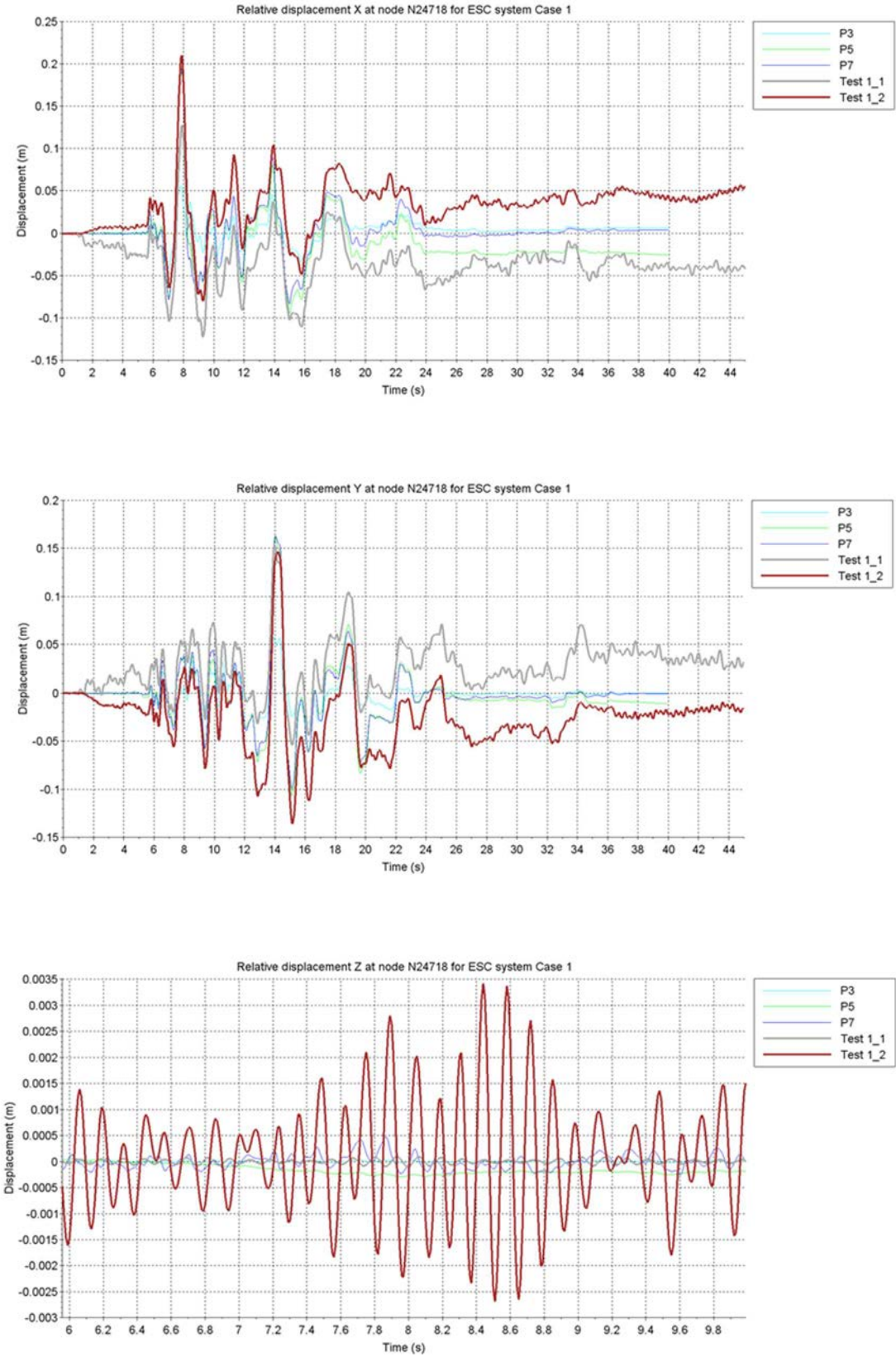


FIG. 177. EQSB system – Comparison of hybrid tests and benchmark results for Case 1 –Relative displacement at centre of upper basemat.

associated to the experimental process itself, as explained in Section 5 and it will not be further considered here.

The maximum amplitude of the sliding phase is correctly predicted by both participant P5 and P7. Unlike for the LRB system, no apparent conservatism is observed for this group of participants with the EQSB system. Participant P3 results are 2 to 3 times lower than the experimentally observed ones.

In the vertical direction, and even though the test excitation applied was lower than the one applied to the numerical models, all participants results are significantly lower than the experimental ones. For participants P3 and P5, this is clearly due to their rigid representation of the EQSB isolator in the vertical direction. For participant P7, who updated his vertical stiffness based on the isolator characterization tests, and whose results still seem to be one order of magnitude below the experimental one, it seems to be that the global vertical mode of the superstructure is affected by the same overdamping of all structural modes that was identified in all of these participants results.

The conclusions for Case 3 are strictly the same as those stated above for Case 1.

6.2.3 Comparison of floor response spectra at centre of upper basemat

Participants floor response spectra computed at the upper basemat central node are compared to the test ones for directions X, Y and Z in Figure 178.

In the horizontal directions, and up to 2 Hz, participants P5 and P7 (first group of participants) response spectra do fit the test response spectra rather well, highlighting a same globally well represented effect of the isolation system. For reasons that have already been explained in Section 4, results of participant P3 (second group of participants) are significantly different in this frequency range.

Around 3 Hz, a peak appears on the test response spectra, which exact frequency seems to be dependent on the loading rate. This peak occurs at different frequencies for Test 1_1 and Test 1_2 and it may partially be a side effect of the testing process. This peak is not observed on the participants response spectra.

For higher frequencies, where the influence of the internal structures and auxiliary building structural modes is felt at the basemat level, the peak appearing around 8 Hz on the test results is 2 to 3 times higher than the one predicted by participants P3 and P5. Participant P7 spectra, as in other cases, show no peak at all at the structural frequencies.

In the vertical direction, a clear peak appears in the test response spectra between 7 and 8 Hz, which is non-existent on the participant predicted response spectra. This shows the tremendous importance of not neglecting the isolators vertical stiffness calibration when defining a numerical model.

The comparison of floor response spectra at the upper basemat level for Case 3 leads to slightly different conclusions from the ones presented above for Case 1. For this reason, results for Case 3 are presented in Figure 179. The peak observed in Case 1 around 3 Hz and reaching 1 g is now smaller and its frequency does not vary with the test loading speed anymore. The peak at 8 Hz, which was largely above the participants predicted peak is now reduced to a comparable order of magnitude.

In the vertical direction the conclusions for Case 3 are identical to those for Case 1.

As a global conclusion, the test procedure itself has a significant effect on the upper basemat floor response spectra in the frequency range of the structural modes. Significant differences are observed between tests in real time and slowed time around 3 Hz and a 50% variability are observed on peaks resulting from the structural modes around 8 Hz.

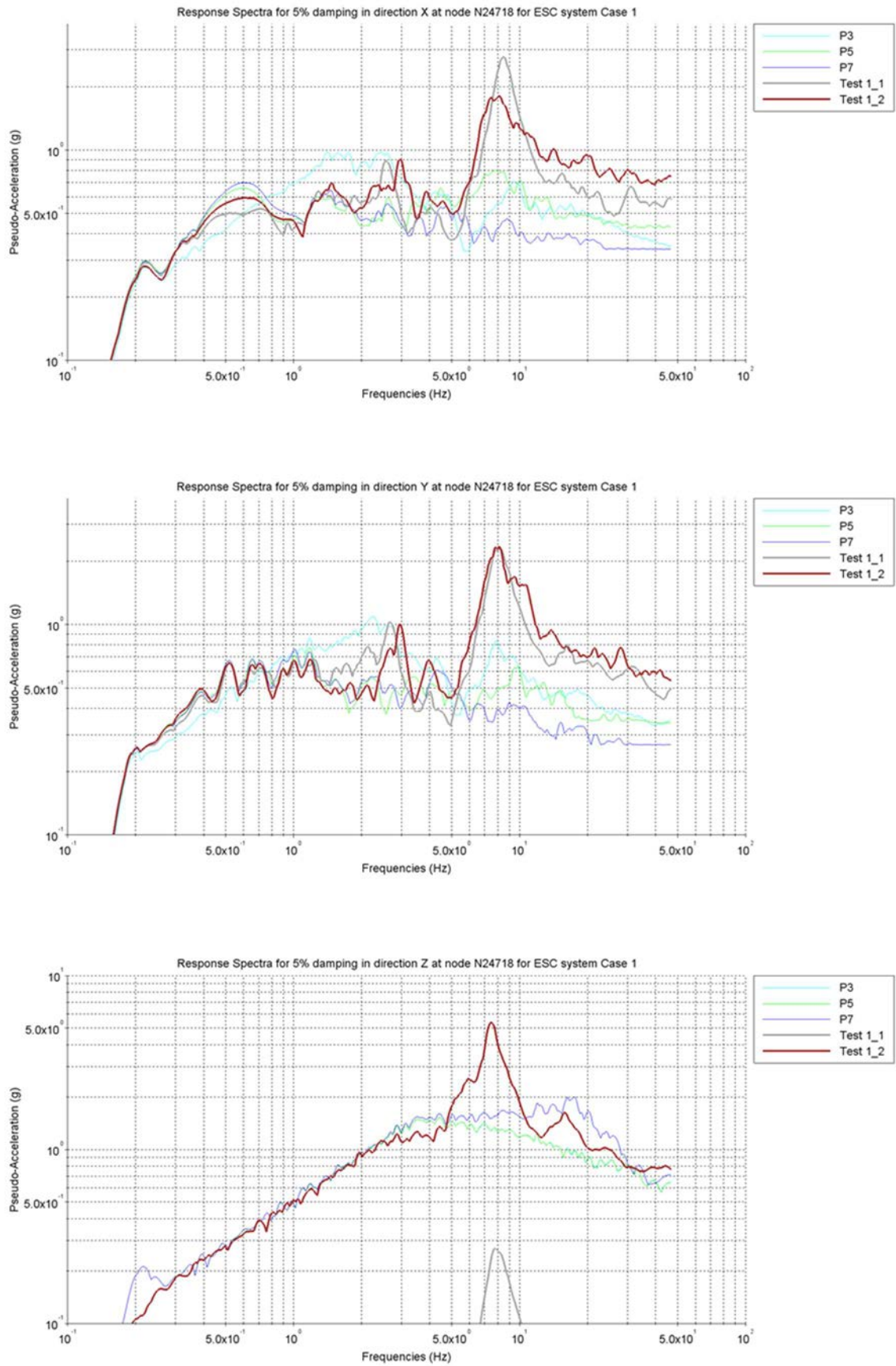


FIG. 178. EQSB system – Comparison of hybrid tests and benchmark results for Case 1 – Floor response spectra at upper basemat level.

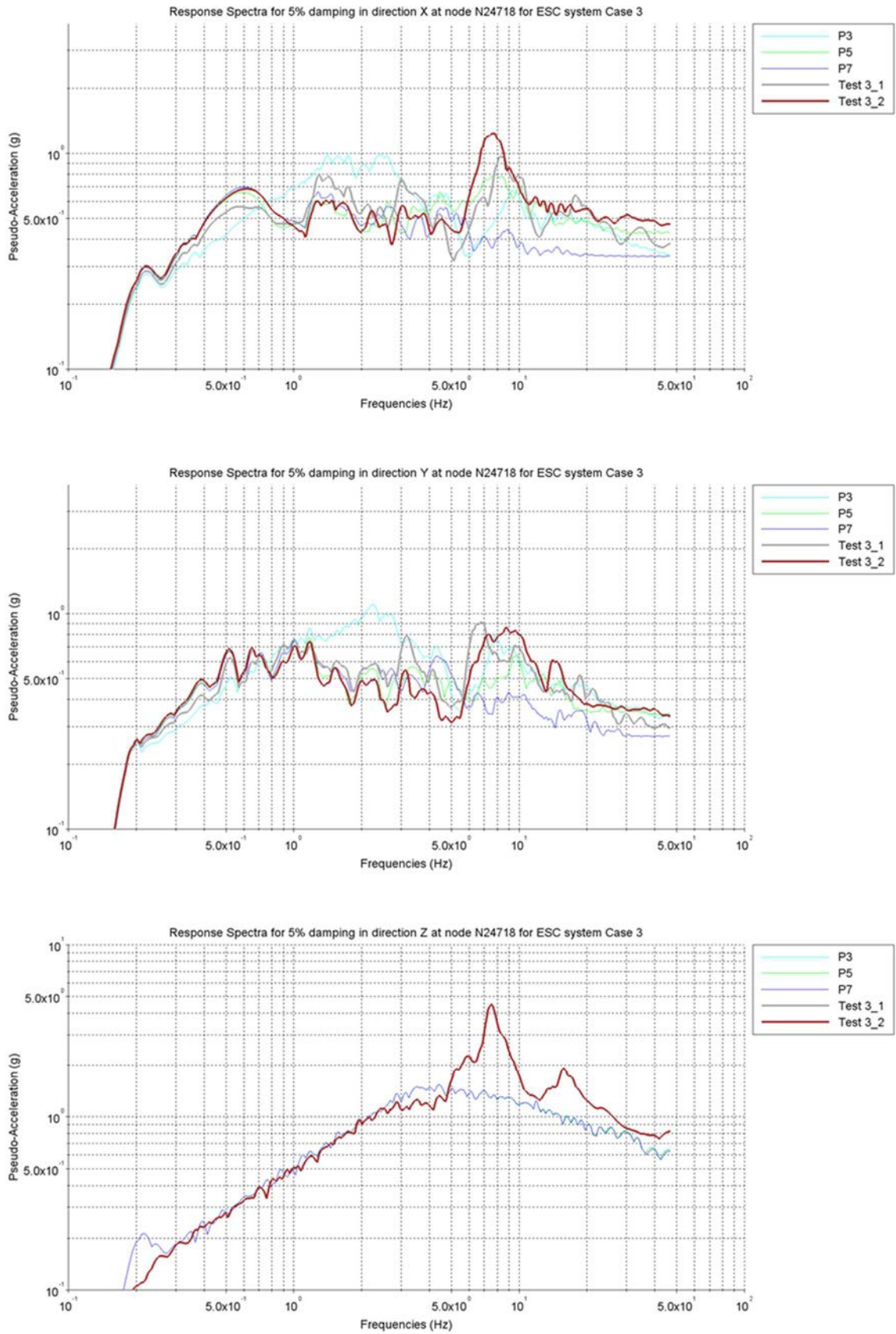


FIG. 179. EQSB system – Comparison of hybrid tests and benchmark results for Case 3 – Floor response spectra at upper basemat level.

6.2.4 Comparison of floor response spectra at top of buildings

Comparisons between participants and tests results floor response spectra at building top are given in Figure 180 for the internal structures building, Figure 181 for the containment building and Figure 182 for the auxiliary complex building. Each figure contains spectra in X, Y and Z directions.

In the horizontal direction, between 0 and 2 Hz, before any structural mode appears, the same conclusions as the ones stated for the upper basemat level still hold for all buildings.

Setting aside participant P7 results, for which no influence of structural modes is visible, results of participants P5 and P3 are closer to the test results at building top levels than they were at upper basemat level. For the internal structures building, participant P5 results are globally similar to the test results whereas the peak on participant P3 response spectra is slightly below the one of Test 1_2 in the X direction but significantly lower than both tests in the Y direction. For the containment building, spectral peaks of both participants P3 and P5 are about 20% below the test results. For the auxiliary complex building, participants P3 and P5 spectral peak is clearly twice lower than the experimental one.

In the vertical direction, since neither participant P3 nor participant P5 did update their vertical stiffness, their results cannot really be compared to the tests results. The high peak observed on participant P5 spectra for internal structures and containment building is due to the non-rigid basemat modelling of this participant, as explained in Section 4.1.1. The fact that these peaks occur at the same frequency as the one in the experimental results, which is due to the vertical stiffness of the EQSB, is purely fortuitous.

6.2.5 Comparison of hysteresis loops

Forces-displacement curves for tests and numerical results are plotted against each other in Figure 183 for the directions X, Y and in Figure 184, for the direction Z.

The effect of the vertical load variations on the horizontal hysteresis curves of the EQSB isolators are very clearly observable on both test results and their overall shape is comparable to the one obtained by participant P5, who explicitly modelled such effect. Unlike for LRB system, the test curves are this time significantly less smooth than the numerical curves obtained by participant P5. The many spikes appearing in these curves clearly results from some other non-linear effects not included in the model of participant P5.

On the horizontal hysteresis curves, it is noticeable that participant P7, without including the effect of vertical load variation into his model, predicts approximately the same distortion as participant P5 and the tests. Effect of vertical load variation are quickly reversing and are averaged over one full sliding cycle of the EQSB isolator.

For the vertical direction, it is clear that the very rigid linear model used by participants P3 and P5 is one order of magnitude apart from the actual EQSB vertical stiffness. With these models, the vertical displacement during the earthquake remains within about a tenth of millimetres. The model of participant P7, with an updated stiffness, also remains relatively far from the experimental results. This model predicts 3 mm of initial compression and less than 1 mm of variation around this value. The experimental results, on the other side, show 12 mm of initial compression and about 6 mm of variation about this value during the earthquake.

The underlining of the importance of correctly assessing the vertical stiffness of isolators, even when they might appear as rigid at a first glance, is a major lesson to be learn from these results.

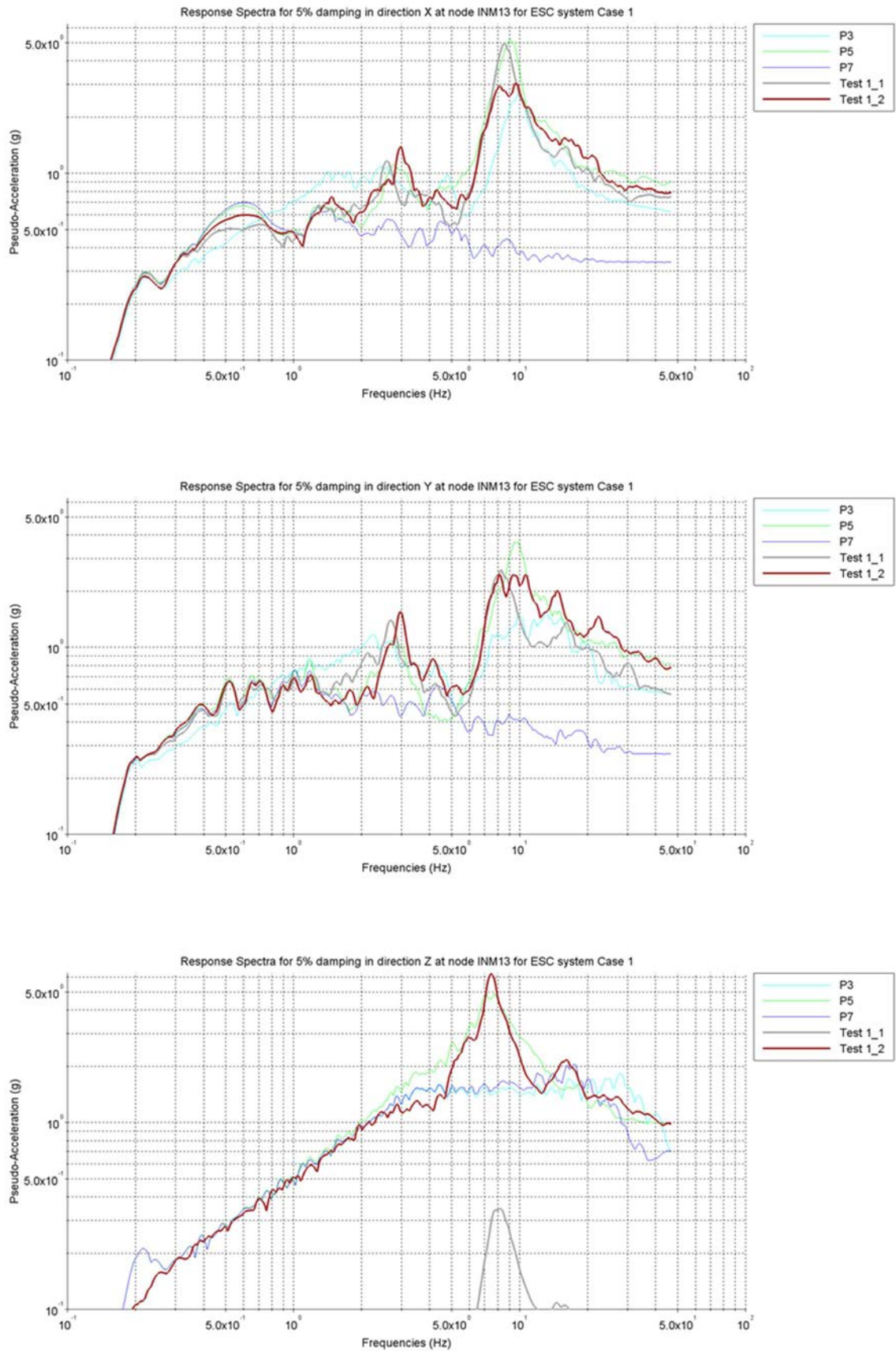


FIG. 180. EQSB system – Comparison of hybrid tests and benchmark results for Case 1 – Floor response spectra at top of the internal structures building.

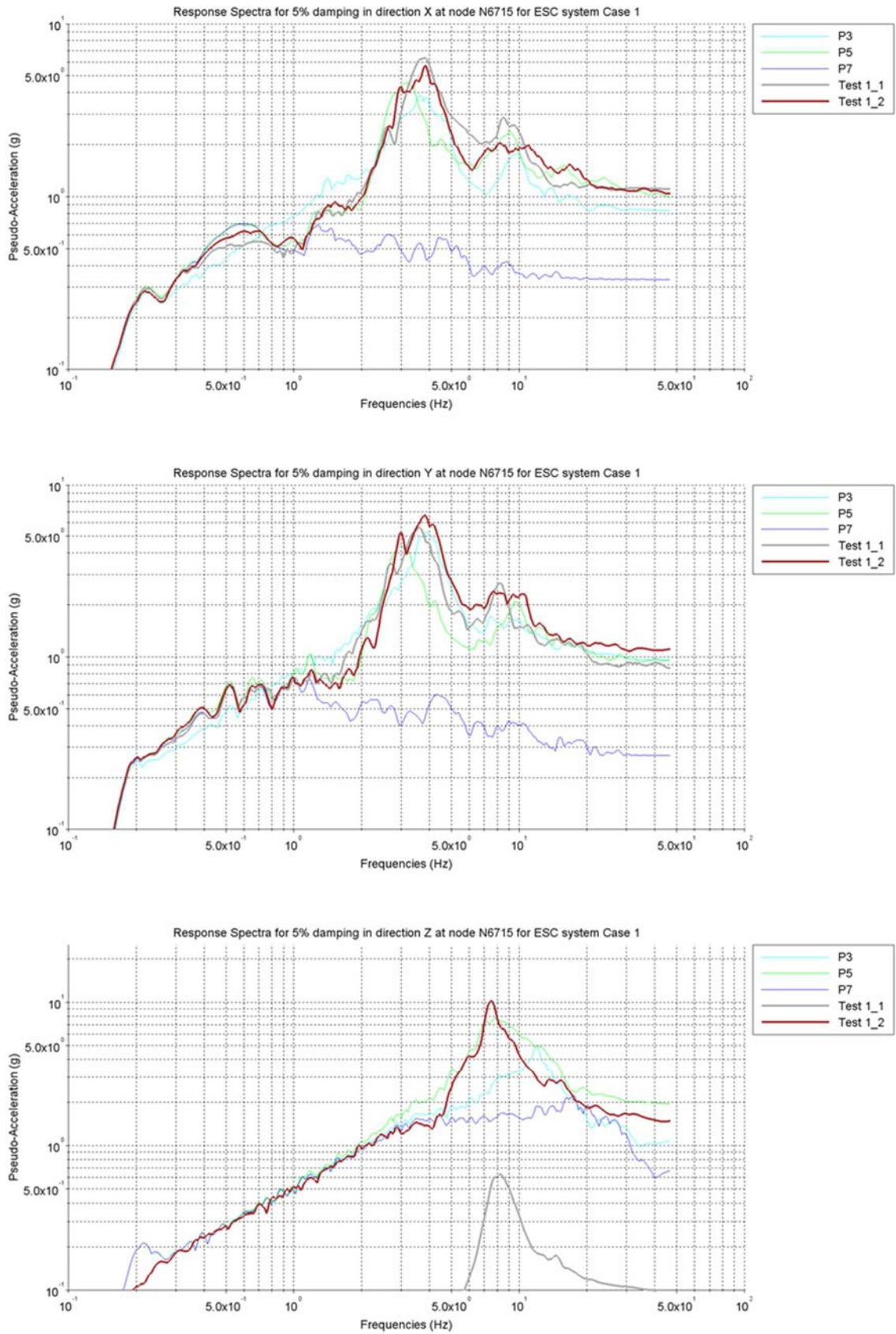


FIG. 181. EQSB system – Comparison of hybrid tests and benchmark results for Case 1 – Floor response spectra at top of the containment building.

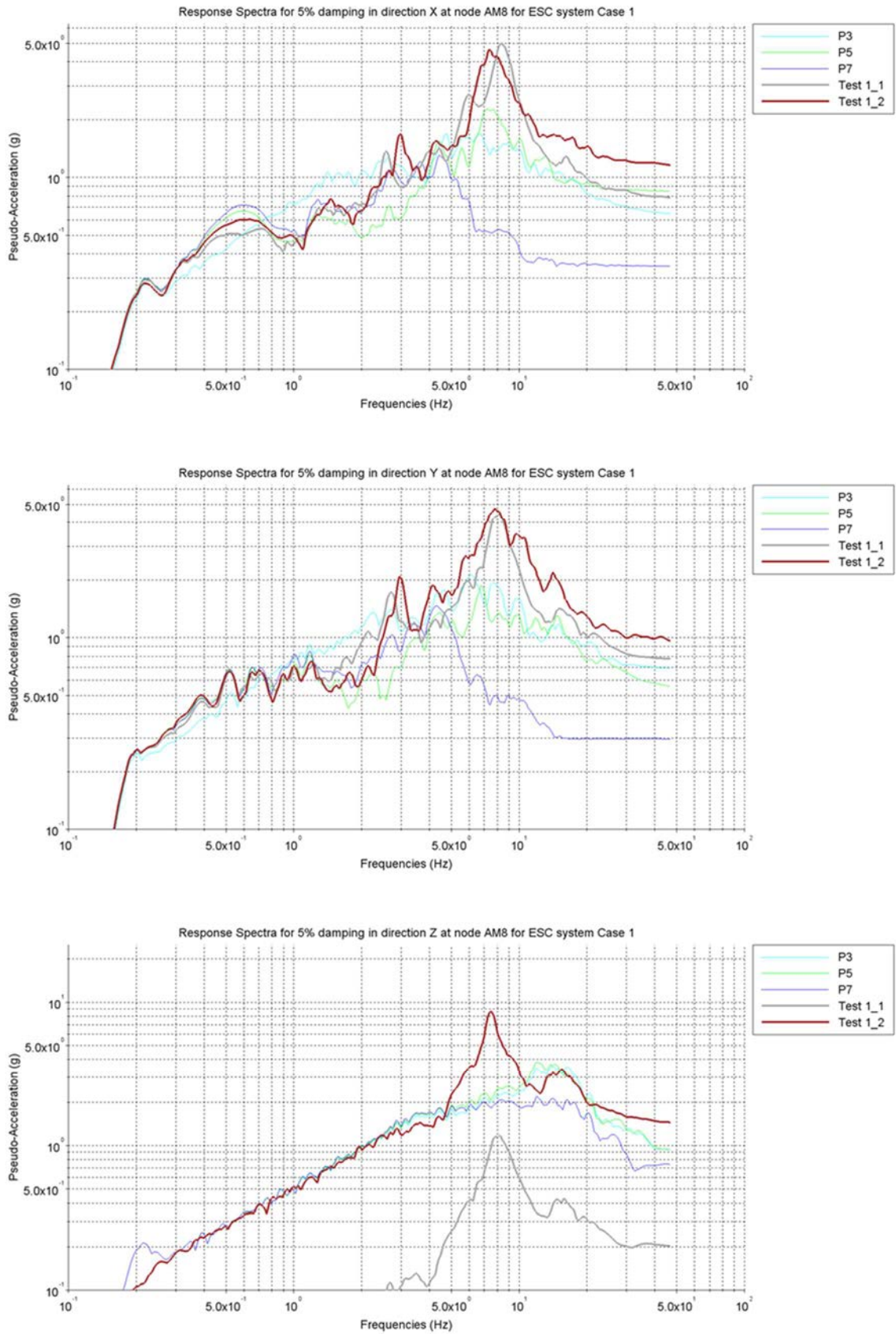


FIG. 182. EQSB system – Comparison of hybrid tests and benchmark results for Case 1 – Floor response spectra at top of the auxiliary complex building.

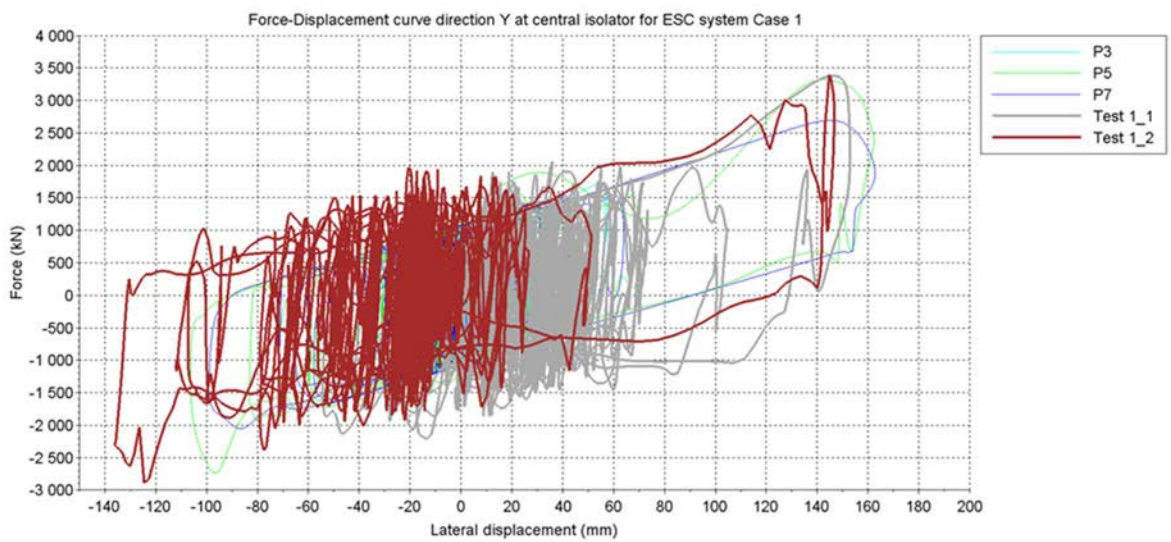
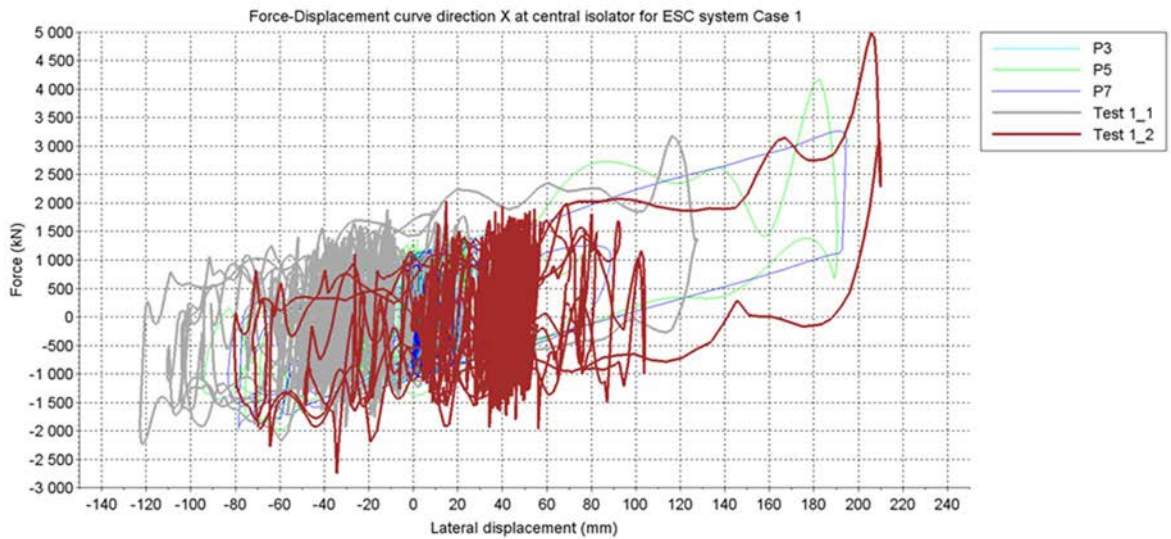


FIG. 183. EQSB system – Comparison of hybrid tests and benchmark results for Case 1 – Horizontal force-displacement curves.

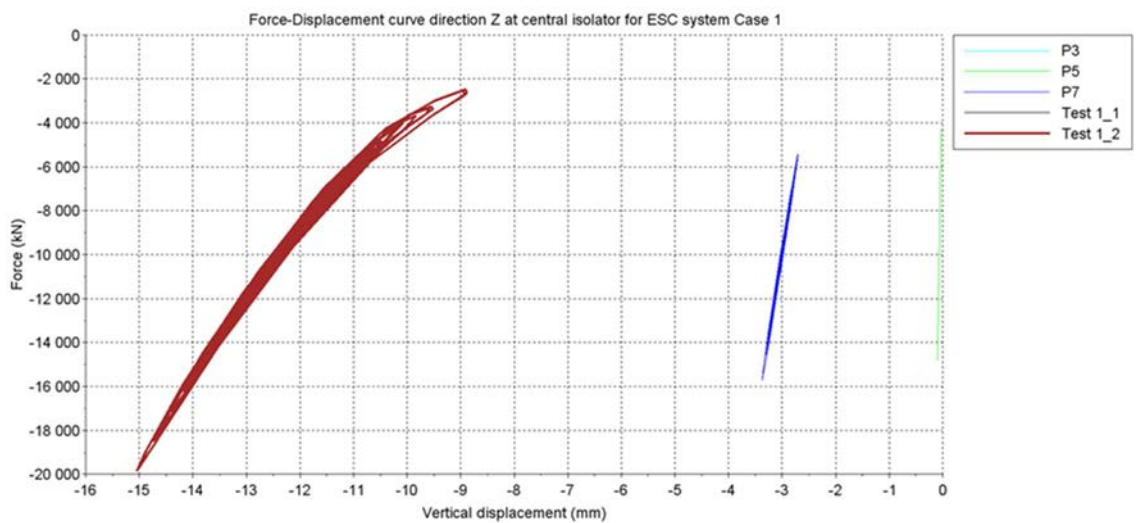


FIG. 184. EQSB system – Comparison of hybrid tests and benchmark results for Case 1 – Vertical force-displacement curves.

6.3 COMPARISON FOR TPFB ISOLATORS

As mentioned in Section 4, for the TPFB system, hybrid tests were performed only for benchmark Case 1, corresponding to a RG 1.60 spectrum excitation at DBE level (0.5 g peak ground acceleration) with one macro-isolators. Only participant P5 modelled the TPFB isolation system. Under these conditions, the Secretariat decided that no general conclusions could be drawn from the comparison between the experimental and the analytical results.

6.4 CONCLUSIONS

As a first conclusion, the results of the hybrid simulation tests are fully in line with those of the benchmark participants in predicting a high efficiency of the seismic isolation system for the reduction of horizontal in-structure response spectra in all cases. Although some variations are observed between participants results and tests results, none of these variations is large enough to put this conclusion into question.

In all cases and for all type of isolators, the onset and the end of lead yielding phases or sliding phases, which were found in Section 4 to always be in phase for all of benchmark participants, are also in phase with all hybrid tests results. Hence, all participants models, whatever their differences, are able to correctly predict the onset and end of yielding or sliding phases.

Setting aside a few outlier results, the order of magnitude of the results produced by the hybrid simulation test are globally similar to the ones of benchmark participants results. The hybrid test results do almost always lie in the range of results predicted by the different participants. Given the fact that none of the participants did calibrate their model on characterization test previous to the benchmark, this can be considered as an excellent outcome of the present exercise.

The horizontal displacements of the superstructure and the horizontal isolators distortion observed in the experiments were generally found to be either matched (for the EQSB system) or enveloped (for the LRB system) by the results of the first group of participants (P1, P2, P5, P6 and P7). The dispersion existing on the maximum displacement values predicted by these participants and those observed in the tests is about 30 %. This is illustrated Figure 185. As a conclusion, it is possible to state that the displacement or distortion values obtained by these participants with the RG 1.60 spectral shape at 0.5 g are always either realistic or on the safe side.

In all cases, results of the second group of participants (P3, P4, P8), predicting significantly lower displacement and distortion values than the first group, were found to be below those of the hybrid tests, and therefore not on the safe side with respect to the design of isolators design. For participant P4, this may be attributed to the use of unidirectional isolators elements, with no coupling of the plasticity in X and Y directions. For participants P3 and P8, this may be associated to a too high damping term acting in parallel of the isolation system and restricting de facto the rigid body motions of the superstructure.

On all horizontal response spectra, at both upper basemat level and buildings top level, the hybrid test results generally lie in the range of those of benchmark participants and share some common characteristics in terms of shape: peaks and valleys generally occur at the same frequencies. More specifically:

- In the frequency range from 0 to 2 Hz, the test spectra are globally in between to the ones of the first group of participants (P1, P2, P5, P6 and P7) and the one of the second group of participants (P3, P4, P8), highlighting the fact that the reduced damping of the first group, which proved conservative in terms of displacement, is not necessarily conservative in terms of response spectra. The damping forces themselves, transmit part of the excitation to the superstructure and it might be advised to systematically study the effect of additional damping on floor response spectra of an isolated superstructure.
- Between 3 and 4 Hz, for the containment building, which structural modes are located in this range, and setting aside results of participants affected by a non-rigid representation of the

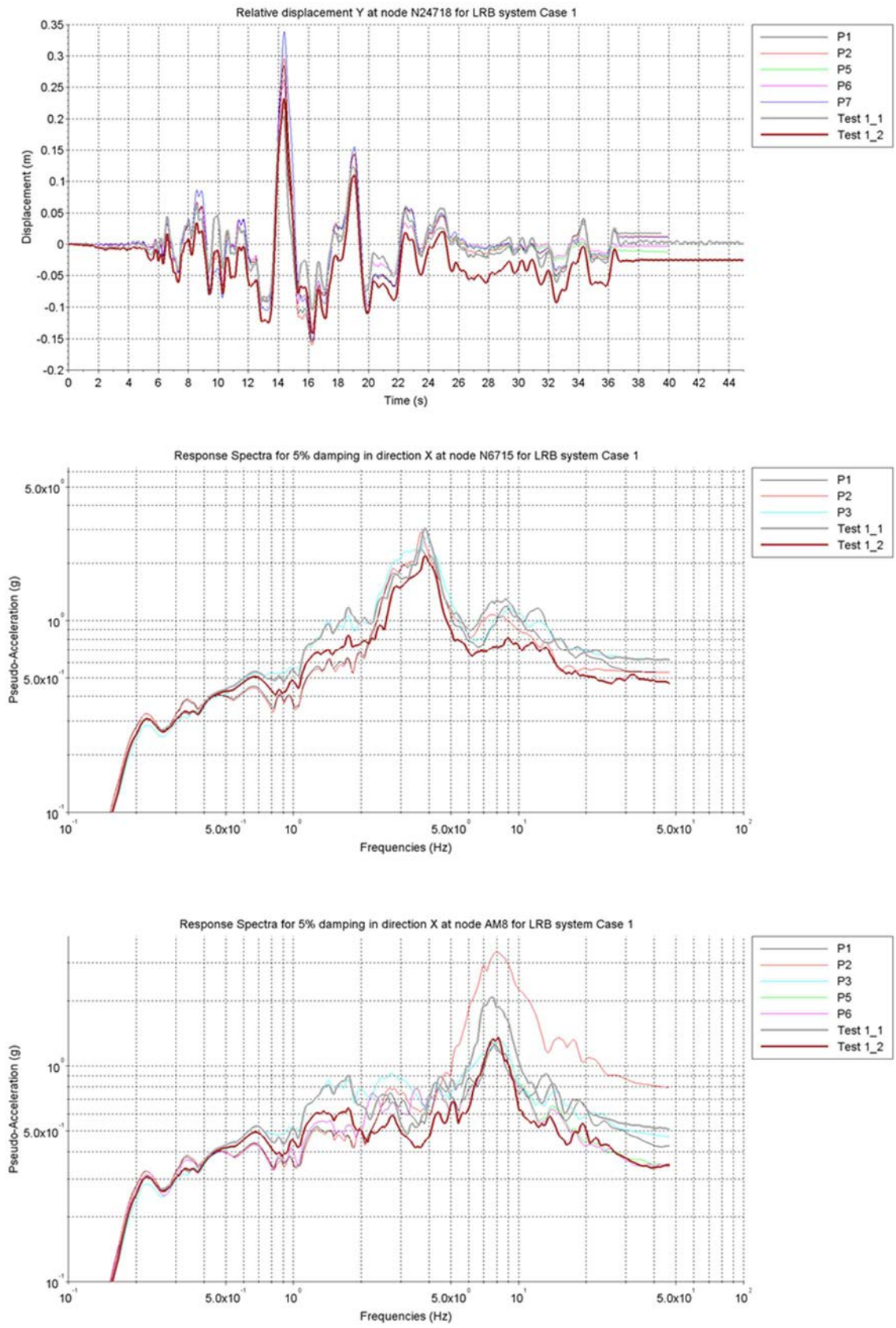


FIG. 185. Comparison of some representative participants' displacements at basemat and spectra at the top of auxiliary building (LRB system – Case 1).

basemat or by an overdamping of the structural modes, there is an excellent fit between most of participants results and tests results. The variability of the selected participant results is not

larger than the variability of the tests results themselves, when changing the test procedure. This is illustrated on Figure 185 for the LRB system, Case 1 and a selected set of participants results.

- Between 5 and 10 Hz, in the frequency range of the reactor internal structure building horizontal response, the auxiliary complex building horizontal response and the isolated superstructure vertical response, when the LRB or EQSB stiffness is properly accounted for, a significantly increased variability of both the benchmark results (up to factor 4 between two participants spectra) and the tests results (up to factor 2 between slow time and real time) is observed. An extreme example of such dispersion is illustrated on Figure 185 at the top of the auxiliary building with the LRB system for Case 1.

From a design point of view, it could be noted that this last range of frequencies, between 5 and 10 Hz, is typically important for equipment and safety systems located inside a nuclear island structure. In the frame of a design analysis this highlight the need for a proper 3D representation of the superstructure and its basemat when generating in-structure response spectra. Nowadays, this conclusion is already recognized, even in the absence of a seismic isolation system.

Finally, for the horizontal response spectra, no single participant set of results can be said to be either always envelop or always be similar to the hybrid test results, but several participants can be said to be relatively close to the hybrid test results in most cases (within 30% at low frequencies and within 50 % at high frequency).

It is expected that the coupling effect between horizontal, vertical and rocking modes, the different strategies used by different participant to fully, partially or not at all rigidify their basemat and the different simplifying hypotheses used to merge 486 isolators into one macro isolator are the root causes for the wide dispersion of results observed on auxiliary complex building and internal structures building horizontal spectra in the 5 to 10 Hz frequency range. As hybrid tests with one macro-isolator remain the most valuable to validate an isolator system model, and since such test would always require the kind of simplification that has led to the observed dispersion, it could be suggested, when performing such test:

- To always use an absolutely rigid basemat in the numerical model to validate as well as in the model used for the hybrid tests. This avoid the risk of frequency shift of the structural modes due to the presence of one single macro-isolator or simplified building representations.
- To block all basemat rotations, so that the excitation transmitted to the simplified superstructure model are pure translations. This avoid the need for defining rotation characteristics and damping for the macro-isolator.

In the vertical direction, the main conclusion is that only results of participants who updated their isolator model stiffness were able to approach the hybrid tests results. Some amplitude differences remain because the isolator vertical damping was not calibrated for these models. As a consequence, the numerical results tend to envelop those of the hybrid tests.

The hysteresis curves recorded during tests 1_1 and 1_2 on the LRB isolator show that other phenomena, on top of lead yielding, may contribute to dissipate energy when the isolator is distorted. Indeed, the recorded forces were shown to be higher than those calculated by the participants and exhibiting a shape that could be induced by an additional equivalent viscous damping and/or by rubber scragging effect. This equivalent apparent “additional damping” may explain why the first group of participants systematically predict higher distortion than what is observed during the experiment.

The hysteresis curves recorded during tests 1_1 and 1_2 on the EQSB isolator hinted at the fact that several additional non-linear effects may be superposed to those expected by the participants. Indeed, several sharp dents appear on these curves which are not reproduced by any participant. This could also explain the fact that participants response spectra were observed to be always significantly below the test ones in the frequency range of the structural response for this isolation technology. More in-depth analysis of the EQSB actual functioning would be required to further explain these phenomena.

For all types of isolation systems, the importance of calibrating the isolators characteristics with a set of proper characterization tests is underlined. Even though the superstructure behaviour, notably in the horizontal directions, was rather well approximated by some participants simulation with uncalibrated models, the behaviour in the vertical direction has only been captured by these participants that have updated their vertical stiffness values after receiving the first results of the characterization tests. This conclusion holds for all type of isolators, including those for which an analytical estimation of the vertical stiffness seems achievable.

It is also important to be noted that differences between results of hybrid tests 1_1 (2D, real time) and 1_2 (3D, slowed time) are significant and similar to the differences between tests and benchmark participants' purely analytical results. This highlights the fact that uncertainties exist not only on the numerical model but also in the experimental procedure and that these uncertainties have to be acknowledged when designing a seismic isolation system.

7 CONCLUSIONS AND SUGGESTIONS

7.1 CONCLUSIONS

7.1.1 General conclusions

The international benchmark described in the present publication demonstrates that the current state of the technological development allows modelling of highly dissipative bearings accurately enough for the purposes of the design of isolation systems intended for nuclear power plant buildings. Currently available analytical and experimental methods allow to understand, characterize, model and validate seismic isolation systems with highly dissipative bearings, in the of context nuclear power plant structures, and for design basis conditions and beyond design basis conditions.

For all cases, in analytical results as well as in hybrid test results, the seismic isolation systems were predicted to significantly reduce the horizontal response spectra at all elevations of the isolated superstructure. The scatter observed among different participants and between participants and test results always remains small in comparison to the clear benefit of the isolation system for all excitations studied in the present publication.

The results provided by the participants show as well that, at present, the nature of this type of analysis requires a high degree of specialization by the analysts. The 'outlier' results were produced by less experienced analysts. As the origin of the identified outlier deviations is understood, the benchmark highlights the absence of an international design code addressing this type of isolators and including detailed guidance for modelling assumptions and parameters. In the absence of such a code, the role of a carefully implemented peer review by knowledgeable engineers can be key to assure an acceptable reliability. An independent peer review will ensure that the results are not in a zone considered to be 'outlier' in the present exercise.

On the other hand, this research program confirmed that rapid and with some limitations real-time hybrid simulation is indeed a viable testing method to experimentally validate isolation systems in nuclear power plants, with consideration of the actual behaviour of large isolators at full-scale.

7.1.2 Specific conclusions

For both the LRB and EQSB systems, all participants models, even though not calibrated on characterisation tests and implemented differently on different tools, were able to detect the onset and the end of lead yield or friction phases at the same instants as in the experiments.

The yielding or sliding amplitudes are predicted differently by two groups of participants, the first one (P1, P2, P5, P6 and P7) predicting larger displacements than the second one (P3, P4 and P8). Comparing with hybrid tests results, the first group results were found to be either best estimate (for the EQSB system) or conservative (for the LRB system), while the second group results were always non-conservative. The main difference between the two groups was identified as being an additional damping, acting in parallel of the isolators, in the second group models. For the LRB system, a detailed

analysis of the hybrid tests hysteresis curves showed that some additional energy dissipation mechanism, with a dependency to the loading speed, seems to be indeed present in the isolator and leads to displacement values about 25 % lower than those of the first group. This effect remains small compared to the one present in the second group of participant models.

Different shapes and amplitudes of floor response spectra were predicted by different participants, essentially because of model simplification hypotheses and damping representations. The main sources of scatter were:

- The simplifications adopted to rigidify the basemat, which made it fully rigid for some participants, partially rigid for others and unrealistically flexible for the last ones.
- The simplifications adopted and to merge 486 isolators into one or five macro isolators. Especially the rotation behaviour and the vertical damping were modelled differently by different participants.
- The excessive damping of the superstructure rigid body motions in the second group of participant models was already identified as the source for too small displacement values.
- The excessive damping of the superstructure dynamic modes in one participant model.

Therefore, ‘raw’ dispersion found in the participants’ results is generally large. However, in cases where some modelling hypotheses are removed or rendered negligible, and when results of participants with excessive damping are set aside, the scattering is significantly reduced.

In general, response spectra originating from hybrid tests were found to be in the range of those predicted by the different participants, which is a very positive outcome of this work. It is important to be noted that differences between results of hybrid tests 1_1 (2D, real time) and 1_2 (3D, slowed time) are significant and similar to the differences between tests and benchmark participants’ purely analytical results. This highlights the fact that uncertainties exist not only on the numerical model but also in the experimental procedure. Once structural modelling differences, simplifying hypotheses differences and excessively damped results are set aside, the dispersion in the test results themselves was found to be only slightly smaller than the dispersion in the participant results. In the frequency range between 0 and 5 Hz, the variation range is typically around 30 %. Between 5 and 10 Hz, the variability goes up to more than 50%, because of the coupling between some structural horizontal modes, rocking modes and vertical modes at these frequencies.

As a supplement to the benchmark cases one participant conducted a parametric analysis increasing the seismic level to 2.25 times and 3 times the DBE for the LRB case. The exercise confirmed the feasibility of simulate earthquakes much larger than the DBE. At these large seismic motions, non-linear effects, such the lead heating effect or the strong reduction of vertical stiffness induced by the isolators’ distortion, have a strong influence in the response.

For the LRB isolation system, it was demonstrated that including the effects of lead heating, reduction of vertical stiffness due to horizontal distortion and rubber cavitation into the isolator models was not necessary with the design basis earthquake but becomes increasingly important as the seismic excitation level is increased. The structural modes frequencies themselves are observed to be affected by such effects for beyond design basis excitations. For predicting the ultimate capacity of the isolation system, including the effect of rubber hardening may also become necessary, although not considering it is conservative for the design of the isolators themselves. As the hybrid simulation tests were conducted only for design basis earthquake, they could only be used to validate the conclusion with this excitation level.

For the EQSB isolation system, it was found that the effect of the vertical load variation on the horizontal behaviour of the complete structure was affecting the horizontal hysteresis curves and the response spectra in a significant manner. The superstructure displacements, on the other side, seem not to be very affected since the variation of vertical load is averaged throughout a complete friction cycle. Even though no cases with superstructure uplift was calculated or tested in the present benchmark, it is thought that the onset of such behaviour would significantly affect the whole structure response and possibly generate impacts and high frequency vibrations.

The number of participants who selected the TPFB isolator for their simulations was not sufficient for having meaningful comparisons. However, the TPFB isolators were successfully tested and its behaviour compared with that of the other two. The TPFB isolators provided the greatest reduction of spectral acceleration amplitudes in the floor response spectra.

For all types of isolation systems, the importance of calibrating the isolator characteristics with a set of proper characterization tests was underlined. Even though the superstructure behaviour, notably in the horizontal directions, was rather well approximated by most participants with uncalibrated models, the behaviour in the vertical direction has only been captured by those participants who have updated their vertical stiffness values after receiving the first results of the characterization tests. This conclusion holds for all type of isolators, including those for which an analytical estimation of the vertical stiffness seems achievable.

7.2 SUGGESTIONS

7.2.1 General suggestions

The use of hybrid tests is a way of verification of adequacy of a seismic isolation system design. It is suggested to perform such tests after characterisation tests are conducted, proper isolator model is defined, and preliminary parametric numerical analyses are performed. The hybrid test results will then come as a confirmation that the previous steps did indeed result in a robust design.

In hybrid simulation tests, it is suggested to keep the representation of the superstructure simple and to run cases where the tested isolator alone represents all of the isolation system, not one among many simulated others. This requires running specific analyses to be compared to the results of hybrid tests, which may be significantly different, in terms of structural modelling, from the actual design analyses. For such simple analyses, it is suggested to:

- Keep the superstructure model simple, so that hybrid test remains feasible in real time.
- Keep the basemat absolutely rigid to avoid unexpected flexural effects due to either the superstructure simplifications or the isolation system merging into one macro-isolator.
- Restrict all basemat rotations in the model, so as to transmit only pure translational motions through the isolation system. An isolation system merged into one macro-isolator is not able anyway to adequately represent the rocking motions and such representation is not necessary in a model validation step.
- Pay special attention to the damping hypotheses on the model. Avoid the use of mass proportional damping on the superstructure, which is known to damp the rigid body motions. Avoid the use of any damping in the isolator element on top of what is strictly intended.

When building a structural model for the design justification analyses, following the calibration and the validation of the isolator model, it is suggested to:

- Represent all isolators individually and at their correct position.
- Model the superstructure with shell or 3D elements, representing its stiffness, and especially the basemat stiffness, in an accurate manner.

Simplifications on these aspects were indeed found to affect the final results and to be a significant source of discrepancies between participant's floor response spectra in the present benchmark.

Overall, given the nature of this type of analyses, the role of a carefully implemented peer review of the modelling assumptions and results by knowledgeable engineers, can be key to assure an acceptable reliability. A peer review by an independent group will assure that the results will not stay in a zone considered to be 'outlier' in the present exercise.

7.2.2 Specific suggestions

When defining a numerical isolator model, it is suggested to calibrate its behaviour on the result of comprehensive characterization tests in laboratory. It is indeed a lesson learned of the present benchmark that the manufacturer's data may sometimes not adequately represent the isolator behaviour in the conditions to which they are assumed to be submitted in the safety demonstration of a nuclear structure. Among others, the calibration of the following is thought to be necessary:

- The isolator vertical stiffness, including its environment (typically the pedestal) when relevant. As observed in the present work, this stiffness might be significantly non-linear.
- For the LRB system, the amount of equivalent viscous damping associated to the rubber and lead in shear. For high excitation level, calibrating the behaviour under cyclic loading (lead heating), tension (cavitation) and extreme shear (hardening) are also necessary.
- For the EQSB system, the variation of friction forces with the vertical loads and the loading speed.

When analysing a LRB isolation system for excitations that significantly distort it and/or that produces local tension in isolators (typically for Beyond Design Basis earthquake), it is suggested to include into the isolator model such effect as:

- Vertical stiffness reduction with horizontal distortion,
- Lead heating effect, and
- Rubber cavitation effects.

For the determination of isolator ultimate capacity, a representation of the rubber hardening is also suggested.

When analysing an EQSB isolation system, it is suggested to represent the friction forces variations with vertical loads and with the loading speed. This suggestion is valid whatever the level of earthquake applied. Furthermore, if significant vertical or rocking motion occur, the representation of uplift and return into contact of the isolator is necessary.

REFERENCES

- [1] MOUSSALLAM, N. et al, "Seismic Isolation of Nuclear Structures - Overview of the French Practice and Experience," in *SMiRT-22*, San Francisco, CA, 2013.
- [2] INTERNATIONAL ATOMIC ENERGY AGENCY, "Seismic Hazards in Site Evaluation for Nuclear Installations," Specific Safety Guide No. SSG-9, Vienna, 2010.
- [3] HALBERT, P.W., LANDAUER, J.P. and WITSENHAUSEN, H.S., "Hybrid simulation of adaptive path control," in *AIAA Proceedings of the Simulation for the Aerospace Conference*, Columbus, OH, USA, 1963.
- [4] HEARTZ, R.A. and JONES, T.H., "Hybrid simulation of space vehicle guidance system," in *Proceedings of the International Space Electronics Symposium*, Las Vegas, NV, USA, 1964.
- [5] TAKANASHI, K., UDAGAWA, K., SEKI, M., OKADA, T. and TANAKA, H., "Non-linear earthquake response analysis of structures by a computer-actuator online system," *Transactions of the Architectural Institute of Japan*, no. 229, pp. 77-83, 1975.
- [6] SHING, P.S.B. and MAHIN, S.A., "Rate-of-loading effects on pseudodynamic tests," *Journal of Structural Engineering - ASCE*, vol. 114, no. 11, pp. 2403-2420, 1988.
- [7] SHING, P.S.B. and MAHIN, S.A., "Experimental error effects in pseudodynamic testing," *Journal of Engineering Mechanics - ASCE*, vol. 116, no. 4, pp. 805-821, 1990.
- [8] C. R. THEWALT and S. A. MAHIN, "Hybrid solution techniques for generalized pseudodynamic testing," Earthquake Engineering Research Center, Berkeley, CA, USA, 1987.
- [9] MOSQUEDA, G., STOJADINOVIC, B. and MAHIN, S.A., "Implementation and Accuracy of Continuous Hybrid Simulation with Geographically Distributed Substructures," Earthquake Engineering Research Center, Berkeley, CA, USA, 2005.
- [10] NAKASHIMA, M., KATO, H. and TAKAOKA, E., "Development of real-time pseudo dynamic testing," *Earthquake Engineering and Structural Dynamics*, vol. 21, no. 1, pp. 79-92, 1992.
- [11] KWON, O.S., NAKATA, N., ELNASHAI, A. and SPENCER, B., "A framework for multi-site distributed simulation and application to complex structural systems," *Journal of Earthquake Engineering*, vol. 9, no. 5, pp. 741-753, 2005.
- [12] PAN, P., TOMOFUJI, H., WANG, T., NAKASHIMA, M. and OHSAKI, M., "Development of peer-to-peer (P2P) internet online hybrid test system," *Earthquake Engineering and Structural Dynamics*, vol. 35, no. 7, pp. 867-890, 2006.
- [13] TAKAHASHI, Y. and FENVES, G.L., "Software framework for distributed experimental-computational simulation of structural systems," *Earthquake Engineering and Structural Dynamics*, vol. 35, no. 3, pp. 267-291, 2006.
- [14] SCHELLENBERG, A.H., TAKAHASHI, Y., MAHIN, S.A. and FENVES, G.L., "Open Framework for Experimental Setup and Control," Pacific Earthquake Engineering Research Center, 2016. [Online]. Available: <http://openfresco.berkeley.edu>.
- [15] KIM, H.K., "Development and implementation of advanced control methods for hybrid simulation," University of California, Berkeley, CA, USA, 2011.
- [16] ELKHORAIBI, T. and MOSALAM, K.M., "Towards error-free hybrid simulation using mixed variables," *Earthquake Engineering and Structural Dynamics*, vol. 36, no. 11, pp. 1497-1522, 2007.
- [17] PAN, P., NAKASHIMA, M. and TOMOFUJI, H., "Online test using displacement-force mixed control," *Earthquake Engineering and Structural Dynamics*, vol. 34, no. 8, pp. 869-888, 2005.
- [18] SCHELLENBERG, A.H., MAHIN, S.A. and FENVES, G.L., "Advanced Implementation of Hybrid Simulation," Pacific Earthquake Engineering Research Center, Report No. PEER2009/104, Berkeley, CA, USA, 2009.
- [19] S. N. DERMITZAKIS and S. A. MAHIN, "Development of Substructuring Techniques for On-Line Computer Controlled Seismic Performance Testing," Earthquake Engineering Research Center, Berkeley, CA, USA, 1985.

- [20] N. NAKATA, "Acceleration trajectory tracking control for earthquake simulators," *Engineering Structures*, vol. 32, no. 8, pp. 2229-2236, 2010.
- [21] Y. CHAE, K. KAZEMIBIDOKHTI and J. M. RICLES, "Adaptive time series compensator for delay compensation of servo-hydraulic actuator systems for real-time hybrid simulation," *Earthquake Engineering and Structural Dynamics*, vol. 42, pp. 1697-1715, 2013.
- [22] P. S. B. SHING and S. A. MAHIN, "Pseudodynamic Test Method for Seismic Performance Evaluation: Theory and Implementation," Earthquake Engineering Research Center, Berkeley, CA, USA, 1984.
- [23] COMPUTERS AND STRUCTURES, INC., "SAP2000 version 18 – CSI Analysis Reference Manual," Berkeley, California, USA, 2015.
- [24] U.S. NUCLEAR REGULATORY COMMISSION, "Design Response Spectra for Seismic Design of Nuclear Power Plants," Regulatory Guide 1.60, Rev. 2, Washington, DC, 2014.
- [25] EUR PROMOTERS, "European Utility Requirements for LWR Nuclear Power Plants," Revision D, October 2012.
- [26] PARK, Y.J., WEN, Y.K and ANG, A.H.S., "Random vibration of hysteretic systems under bi-directional ground motions," *Earthquake Engineering and Structural Dynamics*, vol. 14, no. 4, pp. 543-557, 1986.
- [27] KUMAR, M., WHITTAKER, A. and CONSTANTINOU, M.C., "An advanced numerical model of elastomeric seismic isolation bearings," *Earthquake Engineering and Structural Dynamics*, vol. 43, pp. 1955-1974, 2014.
- [28] KALPAKIDIS, I.V., CONSTANTINOU, M.C. and WHITTAKER, A.S., "Modeling strength degradation in lead-rubber bearings under earthquake shaking," *Earthquake Engineering and Structural Dynamics*, vol. 39, pp. 1533-1549, 2010.
- [29] WARN, G.P., WHITTAKER, A.S. and CONSTANTINOU, M.C., "Vertical stiffness of elastomeric and lead-rubber seismic isolation bearings," *ASCE Journal of Structural Engineering*, vol. 133, no. 9, pp. 1227-1236, 2007.
- [30] KENNEDY, R.P. and RAVINDRA, M.K., "Seismic fragilities for nuclear power plant risk studies," *Nuclear Engineering and Design*, vol. 79, no. 1, pp. 47-68, 1984.
- [31] SHORTREED, J.S., SEIBLE, F., FILIATRAULT, A. and BENZONI, G., "Characterization and testing of the Caltrans Seismic Response Modification Device Test System," *Philosophical Transactions of the Royal Society London A*, vol. 359, no. 1786, pp. 1829-1850, 2001.
- [32] SCHELLENBERG, A.H., SAREBANHA, A., SCHOETTLER, M.J., MOSQUEDA, G., BENZONI, G. and MAHIN, S.A., "Hybrid Simulation of Seismic Isolation Systems Applied to an APR-1400 Nuclear Power Plant," Pacific Earthquake Engineering Research Center, Report No. PEER2015/05, Berkeley, CA, USA, 2015.
- [33] KASALANATI, A., "Velocity Dependency of Elastomeric Isolators," in *Proceedings of the 8th U.S. National Conference on Earthquake Engineering*, San Francisco, CA, USA, 2006.
- [34] BONDONET, G. and FILIATRAULT, A., "Frictional Response of PTFE Sliding Bearings at High Frequencies," *Journal of Bridge Engineering*, vol. 2, no. 4, pp. 139-148, 1997.
- [35] CURTISS-WRIGHT DEFENSE SOLUTIONS, "SCRAMNet Shared Memory," 2016. [Online]. Available: <https://www.curtisswrightds.com/products/cots-boards/io-communication/shared-memory/>.
- [36] IAEA, "Draft TECDOC on Seismic Isolation," IAEA.

ABBREVIATIONS

ACB	Auxiliary Complex Building
ANT	Archetype Nuclear Test model
ATS	Adaptive Time Series delay compensator
COV	Coefficient of Variation (ratio of standard deviation to mean)
DBE	Design Basis Earthquake
DSP	Digital Signal Processor
EBP	Extra-Budgetary Program
EESS	External Events Safety Section (part of Nuclear Safety Division of IAEA)
EQSB	Eradi Quake System [®] Bearing
FP	Friction Pendulum bearing
IAEA	International Atomic Energy Agency
LD	Low Damping elastomeric bearings
LDRB	Low Damping Rubber Bearings
LR	Lead Rubber elastomeric bearings
LRB	Lead Rubber Bearing
MER	Mass Energy Regulator
MIMO	Multiple-Input, Multiple-Output system
NPP	Nuclear Power Plant
PID	Proportional–Integral–Derivative (PID controller)
PTFE	Polytetrafluoroethylene (better known by its commercial name Teflon [®])
RCB	Reactor Containment Building
RTHS	Real-Time Hybrid Simulations
SRMD	Seismic Response Modification Device (testing machine at UC San Diego)
TCL	Tool Command Language (high-level, interpreted programming language)
TPFB	Triple Pendulum Friction Bearing
UCSD	University of California, San Diego
ZPA	Zero Period Acceleration

Annex

SUPPLEMENTARY FILES

The supplementary files for this publication can be found on the publication's individual web page at www.iaea.org/publications.

CONTRIBUTORS TO DRAFTING AND REVIEW

Alliard, P. M.	Tractebel Engineering, France
Altinyollar, A.	International Atomic Energy Agency
Beltran, F.	Belgar Engineering Consultants, Spain
Chu, M.	SNERDI, China
Dai, J.	IEM, China
El Hamimy, S. T.	ENRRA, Egypt
Haddad, J.	International Atomic Energy Agency
Henkel, F.	Wölfel Engineering GmbH + Co. KG, Germany
Hyun C.	KINS, Republic of Korea
Kostarev, V.	CKTI-VIBROSEISM, Russian Federation
Lee, E.	Chonnam National Univ., Republic of Korea
Lee, H.	Korea Hydro and Nuclear Power Co. Ltd., Republic of Korea
Lee, S.	KEPCO E&C, Republic of Korea
Lee, Y.	KINS, Republic of Korea
Morita, S.	International Atomic Energy Agency
Moussallam, N.	Framatome, France-Germany
Pan, R.	NSC, China
Politopoulos, I.	CEA, France
Poveda Solano, A.	International Atomic Energy Agency
Schellenberg, A.	UC Berkeley, United States of America
Sollogoub, P.	Consultant, France
Stoeva, N.	International Atomic Energy Agency

Consultants Meetings

Vienna, Austria: 10-12 April 2017, 26-28 February 2018

Busan, Republic of Korea: 24-25 August 2017



ORDERING LOCALLY

IAEA priced publications may be purchased from the sources listed below or from major local booksellers.

Orders for unpriced publications should be made directly to the IAEA. The contact details are given at the end of this list.

NORTH AMERICA

Bernan / Rowman & Littlefield

15250 NBN Way, Blue Ridge Summit, PA 17214, USA

Telephone: +1 800 462 6420 • Fax: +1 800 338 4550

Email: orders@rowman.com • Web site: www.rowman.com/bernan

Renouf Publishing Co. Ltd

22-1010 Polytek Street, Ottawa, ON K1J 9J1, CANADA

Telephone: +1 613 745 2665 • Fax: +1 613 745 7660

Email: orders@renoufbooks.com • Web site: www.renoufbooks.com

REST OF WORLD

Please contact your preferred local supplier, or our lead distributor:

Eurospan Group

Gray's Inn House

127 Clerkenwell Road

London EC1R 5DB

United Kingdom

Trade orders and enquiries:

Telephone: +44 (0)176 760 4972 • Fax: +44 (0)176 760 1640

Email: eurospan@turpin-distribution.com

Individual orders:

www.eurospanbookstore.com/iaea

For further information:

Telephone: +44 (0)207 240 0856 • Fax: +44 (0)207 379 0609

Email: info@eurospangroup.com • Web site: www.eurospangroup.com

Orders for both priced and unpriced publications may be addressed directly to:

Marketing and Sales Unit

International Atomic Energy Agency

Vienna International Centre, PO Box 100, 1400 Vienna, Austria

Telephone: +43 1 2600 22529 or 22530 • Fax: +43 1 26007 22529

Email: sales.publications@iaea.org • Web site: www.iaea.org/publications

International Atomic Energy Agency
Vienna
ISBN 978-92-0-162719-3
ISSN 1011-4289